

Electronic Signatures of Large Amplitude Motions

by

Adam H. Steeves

B.A., Williams College

Submitted to the Department of Chemistry
in partial fulfillment of the requirements for the degree of

Doctor of Philosophy

at the

MASSACHUSETTS INSTITUTE OF TECHNOLOGY

June 2009

© Massachusetts Institute of Technology 2009. All rights reserved.

Author
Department of Chemistry
May 13, 2009

Certified by.....
Robert W. Field
Haslam and Dewey Professor of Chemistry
Thesis Supervisor

Accepted by.....
Robert W. Field
Chairman, Department Committee on Graduate Students

This doctoral thesis has been examined by a Committee of the Department of Chemistry that included

Professor Sylvia Ceyer _____
(Thesis Chairperson)

Professor Troy Van Voorhis _____

Professor Robert W. Field _____
(Thesis Supervisor)

Electronic Signatures of Large Amplitude Motions

by

Adam H. Steeves

Submitted to the Department of Chemistry
on May 13, 2009, in partial fulfillment of the
requirements for the degree of
Doctor of Philosophy

Abstract

In this thesis, I demonstrate that measurements of electronic-structure-induced splittings in the rotational spectrum of a vibrationally excited state can identify the nature and extent of the distortion of the equilibrium electronic wavefunction and thereby provide a measure of progress along a reaction coordinate. One-dimensional models of the large amplitude bending reaction coordinates and their associated electronic signatures are constructed for two prototypical unimolecular isomerizations: acetylene \leftrightarrow vinylidene (HCCH \leftrightarrow CCH₂), and hydrogen cyanide \leftrightarrow hydrogen isocyanide (HCN \leftrightarrow HNC). The nuclear quadrupole hyperfine structures of HCN and HNC are distinct at their equilibrium geometries due to the dissimilar natures of bonding in the vicinity of the ¹⁴N nucleus. High resolution rotational spectroscopy has been used to determine the hyperfine coupling parameters for the ground and excited vibrational levels of HCN and HNC, with up to ten quanta of bending excitation in HCN and up to four quanta in HNC. These spectra reveal the evolution of electronic structure along the isomerization path. Large amplitude local-bending vibrational eigenstates of the $\tilde{X}^1\Sigma_g^+$ state of acetylene are shown to be unique in that they possess significant electric dipole moments as a result of the dynamical symmetry breaking in the local-mode limit. Stimulated emission pumping (SEP), through Franck–Condon-forbidden vibrational levels of the \tilde{A}^1A_u state, has been employed to populate the lowest few eigenstates that manifest large amplitude local-bending behavior. Locating appropriate SEP intermediate states has required thorough analysis of the \tilde{A} -state level structure, particularly the overtones and combination levels involving the nearly degenerate low frequency bending modes, ν'_4 and ν'_6 , that are directly related to two possible paths for *trans-cis* isomerization on the excited state surface. Recent developments in chirped-pulse rotational spectroscopy will enable identification of the higher energy local-bending eigenstates, which approach the acetylene \leftrightarrow vinylidene transition state, based on their predicted Stark coefficients.

Thesis Supervisor: Robert W. Field
Title: Haslam and Dewey Professor of Chemistry

Acknowledgments

The work contained in this thesis represents a period of intensely collaborative research. I owe a debt of gratitude to the many people who have made this document possible. Three deserve special thanks: my research advisor Bob Field, Anthony Merer, and Hans Bechtel.

I benefitted from collaborative work with other members of the Field Group: Bryan Wong, Barratt Park, Josh Baraban, and Annelise Beck.

Steve Coy, Mike McCarthy, and Carl Gottlieb introduced me to millimeter-wave spectroscopy.

I also enjoyed working with Bryan Lynch, Liam Duffy, Dave Oertel, Dan Byun, Kyle Bittinger, Wilton Virgo, Tony Colombo, Kirill Kuyanov, Huzeifa Ismail and Heather Kulik.

This work was supported by a National Defense Science and Engineering Graduate Fellowship and an MIT Presidential Graduate Fellowship.

Contents

1	Introduction	17
1.1	Motivation	17
1.2	Thesis Outline	20
2	Millimeter-wave spectroscopy of pulsed-jet sources	23
2.1	Introduction	23
2.2	Pulsed-jet millimeter-wave absorption spectrometer	25
2.2.1	Millimeter-wave source: Phase-locked Gunn oscillator	26
2.2.2	Millimeter-wave detection	29
2.2.3	Propagation of millimeter-wave radiation	30
2.2.4	Characterization of mm-wave spectrometer	31
2.3	Millimeter-wave–optical double resonance and millimeter-wave–detected, millimeter-wave–optical polarization spectroscopy	35
2.3.1	Motivation for millimeter-wave–optical double resonance	35
2.3.2	Experimental details	37
2.3.3	mmODR and mmOPS of carbon monosulfide	38
2.3.4	mmODR of vibrationally excited states	44
2.3.5	Rotational spectroscopy of laser-excited states	45
3	Laboratory measurements of the hyperfine structure of $\text{H}^{14}\text{N}^{12}\text{C}$ and $\text{D}^{14}\text{N}^{12}\text{C}$	49
3.1	Introduction	49
3.2	Origin of nuclear quadrupole hyperfine splitting	51

3.3	Implications for astrochemistry	53
3.4	Coaxial jet mm-wave spectrometer	54
3.5	Analysis of the hyperfine-resolved spectra	57
3.6	Comparison of laboratory and astronomical measurements of hyperfine coupling constants	64
4	Evolution of electronic structure during HCN↔HNC isomerization revealed though nuclear quadrupole hyperfine structure	67
4.1	Introduction	67
4.2	Experimental: Photolysis-jet spectrometer	69
4.3	Mm-wave spectroscopy of bend-excited HCN and HNC	73
4.4	<i>Ab initio</i> calculation of $(eQq)_N$	75
4.5	Chemical interpretation of the variation of the hyperfine structure . .	79
	4.5.1 Variation of $(eQq)_N$	79
	4.5.2 Variation of $(eQq)_D$	80
4.6	Variation of the HNC quadrupole hyperfine structure with excitation of stretching modes	81
4.7	Nuclear quadrupole hyperfine splitting reveals nascent bond breaking isomerization	82
5	Vibrational assignments in the S_1 state of acetylene, I:	
	Pure-bending polyads	85
5.1	Introduction	85
5.2	Experimental details	88
5.3	Theory	91
	5.3.1 Matrix elements of the rotational and Coriolis operators . . .	91
	5.3.2 Darling–Dennison resonance	95
	5.3.3 Structures of the Hamiltonian matrices	96
	5.3.4 Selection rules: Coriolis coupling and axis-switching	97
5.4	Results	98
	5.4.1 The $v'_4 + v'_6 = 2$ polyad (B^2)	99

5.4.2	The $v'_4 + v'_6 = 3$ polyad (B^3)	109
5.4.3	The B^4 and B^5 polyads	115
5.5	Discussion	121
6	Vibrational assignments in the S_1 state of acetylene, II:	
	Totally symmetric modes	131
6.1	Introduction	131
6.2	Experimental details	134
6.2.1	Hot band promotion	134
6.2.2	Absolute lower state J -numbering	135
6.3	Matrix elements for the interacting 1^1 and 2^1B^2 vibrational levels . .	137
6.4	Results	138
6.4.1	The 2^2 level	138
6.4.2	Deperturbation of the $1^1/2^1B^2$ interaction	140
6.4.3	Vibrational assignments up to $+4500\text{ cm}^{-1}$	143
6.5	Vibrational parameters for the totally symmetric modes	146
6.6	Vibrational assignment of previously observed levels	148
6.7	Impact of reassignment on our understanding of S_1 predissociation . .	149
7	Vibrational assignments in the S_1 state of acetylene, III:	
	Combination polyads and the approach to isomerization	155
7.1	Introduction	155
7.2	Appearance of the spectra	156
7.3	Combination polyads observed in IR-UV double resonance	159
7.3.1	The 2^1B^1 polyad	159
7.3.2	The interacting $2^13^1B^1$ and 3^1B^3 polyads	163
7.3.3	The 2^2B^1 polyad	172
7.4	Combination polyads observed in one-photon laser excitation	173
7.4.1	The 3^1B^2 polyad	174
7.4.2	The 3^2B^2 polyad	180
7.4.3	The 3^3B^2 polyad	185

7.4.4	The 2^1B^2 and 2^2B^2 polyads	188
7.4.5	The $2^13^1B^2$ and 3^1B^4 polyads	189
7.4.6	The 5^1B^1 polyad	196
7.4.7	^{13}C isotope shift of the $K' = 1$ sub-bands	198
7.5	Discussion	200
8	Observation of large amplitude bending eigenstates in S_0 C_2H_2	207
8.1	Motivation	207
8.2	A local-bender reaction coordinate	208
8.2.1	Local-bending energies from theory and experiment	210
8.2.2	Electronic signatures: Electric dipole moments	211
8.2.3	Symmetry considerations for dipole moments in the local-mode limit	213
8.3	Dipole moments from a full-dimensional <i>ab initio</i> description of acetylene vibrations	216
8.4	Experimental observation of the local-bending eigenstates	220
8.4.1	A local-bender pluck of \tilde{X} -state dynamics	221
8.4.2	Stimulated emission pumping from Franck–Condon forbidden vibrational levels	223
8.5	Chirped-pulse millimeter-wave spectroscopy	230
9	Ongoing work	235
9.1	Global vibrational structure of S_1 acetylene	235
9.2	Strong, unassigned perturbing levels in S_1	241
9.3	“Extra” levels and the <i>cis</i> well of S_1	244
A	Cavity-ringdown spectroscopy of the $\tilde{A} - \tilde{X}$ transition of C_2H_2	247

List of Figures

2-1	Schematic of the pulsed-jet millimeter-wave spectrometer	27
2-2	Initial spectrum of the OCS $J = 8 - 7$ transition recorded with the pulsed-jet millimeter-wave spectrometer	31
2-3	Rotational spectra of OCS isotopologues	33
2-4	Schematic of the mmOPS apparatus	37
2-5	Observed signals for the mmODR experiment	39
2-6	Comparison of mmODR and mmOPS	40
2-7	mmOPS spectra of nominally spin-forbidden electronic transitions to triplet states of CS	43
2-8	mmODR signal for vibrational excitation of the $2\nu_3$ band of HNC	45
2-9	Pure rotational mmOPS spectrum of CS in an excited triplet state	46
3-1	$J = 1 - 0$ transitions of (a) HCN and (b) HNC recorded in conventional spectrometer geometry	51
3-2	Schematic of the coaxial mm-wave jet spectrometer	55
3-3	Side-on view of the rooftop reflector mounted onto the discharge nozzle	55
3-4	Comparison of orthogonal and coaxial spectrometer geometries	57
3-5	Energy-level diagram for the $J = 1 - 0$ rotational transition of a molecule with a single quadrupolar nucleus with $I = 1$	58
3-6	Hyperfine-resolved rotational spectra of $\text{H}^{14}\text{N}^{12}\text{C}$ and $\text{D}^{14}\text{N}^{12}\text{C}$	60
3-7	Rotational spectra ($J = 2 - 1$ and $J = 3 - 2$) of HNC and DNC	63
4-1	Schematic of the laser-photolysis millimeter-wave spectrometer	70
4-2	Time-dependent absorption signals of photolysis-generated HCN	72

4-3	Millimeter-wave rotational spectra ($J = 1 - 0$) bend-excited ($0v_2^\ell 0$) vibrational levels of HCN and HNC	74
4-4	<i>Ab initio</i> (eQq) values as a function of Jacobi angle	78
4-5	Hyperfine-resolved $J = 1 - 0$ rotational spectrum of HNC in the ($00^0 1$) vibrational state.	82
4-6	Experimental and vibrationally averaged <i>ab initio</i> (eQq) _N values for HC ¹⁴ N and H ¹⁴ NC	83
5-1	Energy level schemes for one-photon and IR-UV LIF	89
5-2	One-photon LIF of the B^2 polyad	100
5-3	Hot band excitation spectra of the B^2 polyad	102
5-4	Energy level structure of the B^2 polyad	103
5-5	IR-UV double resonance spectrum of low energy end of the B^3 polyad	109
5-6	Central portion of the B^3 polyad	111
5-7	Energy level structure of the B^3 polyad	112
5-8	LIF spectrum of the low energy subbands of the B^4 polyad	117
5-9	IR-UV LIF of the two topmost $K' = 0$ subbands of the B^5 polyad	120
6-1	LIF of the 2^2 band of jet-cooled C ₂ H ₂	138
6-2	LIF spectrum of the $1^1/2^1 B^2$ polyad	142
6-3	Reduced term value plots for the $1^1/2^1 B^2$ polyad	144
7-1	Survey one-photon and IR-UV LIF spectra of jet-cooled acetylene	158
7-2	Reduced term value plot of the $2^1 B^1$ polyad	161
7-3	Energy levels of the interacting $2^1 3^1 B^1$ and $3^1 B^3$ polyads	165
7-4	Coriolis-induced structure in the $3^1 B^3$ polyad	166
7-5	IR-UV double resonance spectra of the $3^1 B^3$ polyad	168
7-6	Low frequency part of the $3^1 B^2$ polyad	175
7-7	Reduced term value plot of the perturbation between $K' = 3$ sublevels of $2^1 3^1$ and $3^1 B^2$	179
7-8	The lowest $3^2 B^2$, $K' = 1$ sub-band of acetylene	182

7-9	Triplet perturbations in 3^2B^2 and the weak 5^16^1 band	185
7-10	Interaction between $3^34^16^1$ and 2^13^3	187
7-11	Reduced term values for the 1^13^1 , $2^13^1B^2$ and 3^1B^4 vibrational states	194
7-12	Coriolis interactions in the 3^1B^4 polyad of acetylene	197
7-13	Comparison of the spectra of the 3^nB^2 polyads	203
8-1	One-dimensional potential for acetylene \leftrightarrow vinylidene isomerization . .	209
8-2	Comparison of effective frequencies from polyad and internal coordinate path Hamiltonians	212
8-3	Symmetrized and unsymmetrized local-bending <i>ab initio</i> wavefunctions at $N_{\text{bend}} = 20$	218
8-4	Transition dipole moments between <i>g</i> - and <i>u</i> -symmetry polyads at low and high vibrational excitation	220
8-5	DF spectra from normal and Franck–Condon forbidden intermediate levels	222
8-6	SEP spectra each member of the 3^2B^2 polyad	225
8-7	SEP spectra of the $N_b = 14$ local-bender state	227
8-8	SEP spectra of the lowest members of the $N_b = 10 - 16$ polyads . . .	231
8-9	Schematic of the chirped-pulse millimeter-wave spectrometer	233
8-10	UV-CPmmW double resonance spectra of CS $e^3\Sigma^-$	234
9-1	DVR wavefunctions of planar S_1 acetylene	238
9-2	Comparison of DVR and \hat{H}^{eff} wavefunctions	240
9-3	Effective frequencies of vibration for the <i>trans</i> - and <i>cis</i> -bending modes as a function of v'_3	243
9-4	IR-UV LIF spectra showing an “extra” vibrational level near 3^1B^3 . .	245
A-1	CRDS spectrum of $A^3\Sigma_u^+(v' = 11) - X^3\Sigma_g^-(v'' = 0)$	249
A-2	Pressure-broadening of the transitions observed by CRDS in the Herzberg I system	252

A-3	Broad CRDS spectra of the $V_0^1 K_0^1$ band of the $\tilde{A}^1 A_u - \tilde{X}^1 \Sigma_g^+$ transition of C_2H_2	254
A-4	CRD spectra of portions of the Q branches of the (a) $V_0^0 K_0^1$, (b) $V_0^1 K_0^1$, and (c) $2_0^1 V_0^1 K_0^1$ bands of acetylene	256

List of Tables

3.1	Transition frequencies of $\text{H}^{14}\text{N}^{12}\text{C}$	61
3.2	Transition frequencies of $\text{D}^{14}\text{N}^{12}\text{C}$	62
3.3	Molecular constants of $\text{H}^{14}\text{N}^{12}\text{C}$ for the ground vibrational state. . . .	64
3.4	Molecular constants of $\text{D}^{14}\text{N}^{12}\text{C}$ for the ground vibrational state. . . .	65
4.1	Hyperfine-resolved $J = 1-0$ transition frequencies (in MHz) of ground-state and bend-excited $\text{H}^{12}\text{C}^{14}\text{N}$, $\text{H}^{14}\text{N}^{12}\text{C}$, and $\text{D}^{15}\text{N}^{12}\text{C}$	75
4.2	Fitted hyperfine parameters for $\text{H}^{12}\text{C}^{14}\text{N}$, $\text{H}^{14}\text{N}^{12}\text{C}$, and $\text{D}^{15}\text{N}^{12}\text{C}$	76
4.3	Experimental and <i>ab initio</i> (eQq) _N values for $\text{H}^{14}\text{N}^{12}\text{C}$ and $\text{H}^{12}\text{C}^{14}\text{N}$	77
5.1	Rotational constants from least squares fitting of the B^2 polyad of the $\tilde{A} \ ^1A_u$ state of C_2H_2	107
5.2	Results of the from least squares fit of the B^3 polyad	114
5.3	Calculated $J = K$ rotational levels of the B^4 and B^5 polyads	118
5.4	Assigned rotational lines of the pure bending polyads of the $\tilde{A} \ ^1A_u$ state of C_2H_2	124
5.5	Upper state term values for the B^3 polyad from IR-UV double resonance	128
5.6	Assigned rotational lines of the higher pure bending polyads of the $\tilde{A} \ ^1A_u$ state of C_2H_2	129
6.1	Rotational constants for the 2^2 vibrational level	139
6.2	Least squares fit to the $1^1/2^1B^2$ interacting system	143
6.3	Rotational constants for the 2^3 vibrational level	145
6.4	Rotational constants for the 1^12^1 vibrational level	146

6.5	Vibrational parameters for the a_g symmetry vibrational modes of \tilde{A}^1A_u state of acetylene.	148
6.6	Line list for the 2^2 upper state, $K'_a = 0$ and 1	152
6.7	Line list for the 2^2 upper state, $K'_a = 2$	152
6.8	Line list for the $2^2(\text{H}^{13}\text{C}^{12}\text{CH})$ upper state, $K'_a = 1$	153
6.9	Line list for the 1^1 upper state, $K'_a = 0$ and 1	153
6.10	Line list for the 1^1 upper state, $K'_a = 2$	153
6.11	Line list for the $2^3 K'_a = 1$ upper state	154
6.12	Line list for the $1^1 2^1 K'_a = 1$ and 2 upper states	154
7.1	Least squares fit of the $2^1 B^1$ polyad	162
7.2	Least squares fit of the interacting $2^1 3^1 B^1$ and $3^1 B^3$ polyads	170
7.3	Least squares fit to the $3^1 B^2$ polyad	177
7.4	Least squares fit to the $3^2 B^2$ polyad	183
7.5	Band-by-band fits to miscellaneous levels	188
7.6	Calculated and observed K -structures of the $2^1 3^1 B^2$ and $3^1 B^4$ polyads	193
7.7	Band-by-band least squares fit to the members of the $2^1 3^1 B^2$ and $3^1 B^4$ polyads	195
7.8	^{13}C isotope shifts derived from LIF spectra	199
7.9	Summary of \tilde{A} -state triplet perturbations	206
8.1	1-D and 6-D <i>ab initio</i> dipole moments	219

Chapter 1

Introduction

1.1 Motivation

The vibrational spectra of molecules at high degrees of excitation are characterized by extraordinary complexity due to the high density of vibrational states and the strong mixing between states consistent with fast intramolecular vibrational redistribution. Yet, vibrational spectroscopy persists as the most direct probe of the forces acting between the atoms that make up a molecule. The relationship between the vibrational spectrum and the shape of the underlying potential energy surface is relatively straightforward for small displacements from the equilibrium geometry of the molecule. The areas of the potentials in which this relationship is valid are, however, those of least interest to the study of reaction dynamics. Chemical transformations necessarily occur far from equilibrium and give rise to products determined by the heights and shapes various reaction barriers. In order to approach the regions of the surface where the bonds between atoms are broken and reformed, we require new experimental techniques and interpretive concepts to bridge the gap between the small amplitude, normal-mode vibrations and large amplitude motions of chemical interest.

The primary difficulties in relating the spectra of vibrationally highly excited molecules to the underlying features of the potential energy surface are those of access and recognition. Spectroscopic selection rules generally favor small changes in vibrational quantum numbers, making it difficult to populate selected highly ener-

gized states. In the unusual situation where the design of an experiment permits the observation of transitions into highly excited states, construction of any mechanistic model of the dynamics requires us to label the states with quantities (i.e. vibrational quantum numbers) that describe that describe how the excited vibrations cause the molecule to distort from its equilibrium geometry. Without such labels, an explanation would be, at best, statistical.

Previous work on acetylene, and other small molecules, has demonstrated that certain large amplitude motions remain relatively stable, even at high degrees of excitation. Such a large amplitude motion is extremely valuable because it allows us to reduce the dimensionality of the problem to one (or a few) relevant degrees of freedom. This reduction means that the vast majority of the vibrational levels can be discarded from the model, but how are we to know which levels are relevant to the large amplitude motions?

In order to distinguish between large amplitude motion eigenstates and those that embody “ergodic” behavior, we seek experimentally observable quantities that are sensitive to both the class of motion as well as the magnitude of the vibration. By recognizing that large amplitude motions, particularly those directed along chemically interesting internal coordinates, must cause significant distortions of the electronic wavefunction, we choose to focus on electronic properties as reporters, or spectroscopic signatures, of vibrational motion. The spectroscopic signatures are informed by our intuition regarding the differences in the electronic structure of isomeric species. Furthermore, quantitative determination of useful electronic properties enables the experimenter to describe, in detail, the changes in electronic structure along an isomerization path.

The prescription of our method for the analysis for highly vibrationally excited states of systems capable of undergoing unimolecular isomerization, is as follows:

- We begin by examining the equilibrium electronic structure of the two isomers, endpoints of the isomerization reaction, for qualitative differences. If the isomerization takes place on a smoothly varying potential energy surface, the evolution of the electronic structure should serve as a measuring stick for how

far along the reaction coordinate the system has progressed.

- We choose an electronic property by which the two isomers may be distinguished, on the basis of their differing electronic structures. Such a property may be either local, related only to the bonding characteristics of a single atom, or global, describing some aspect of the complete electronic distribution. Properties of both classes will be used in this thesis, with the nuclear quadrupole hyperfine structure reflecting the distribution of valence electrons associated with a particular nucleus, and the electric dipole moment describing the global asymmetry of the charge density.
- A spectroscopic technique, capable of probing the selected electronic property, is identified. This is largely a question of experimental resolution, as minor electronic effects induce small shifts or splittings in the spectrum. In order to observe these minor, often overlooked, effects, we favor rotational spectroscopy as a means to record high resolution spectra of vibrationally excited states.
- The highly vibrationally excited states must be populated before they can be interrogated, and achieving this is often the most challenging aspect of the process. In this work, we take advantage of accessible (low) barriers on excited electronic surfaces in order to obtain access to the high barriers to bond-breaking isomerization on the ground state surface.
- The electronic properties are determined for each target vibrational state, and those whose properties indicate that they are unrelated to the desired large amplitude motion are discarded. Developing survey techniques to sample the electronic properties of many states simultaneously, or each state rapidly, will become increasingly important in regions of high state density.
- The energies of the large amplitude motion eigenstates are fed back into the construction of a low-dimension model for the reaction path.

This procedure is unique in that the standard spectroscopic picture dictates that vibrational excitation should cause a small perturbation to the electronic wavefunc-

tion. Therefore the electronic properties are typically viewed as weak functions of the vibrational degrees of freedom. While such an argument is reasonable for small amplitude vibrations, the nature of large amplitude motions dictate that they are capable of strongly distorting the electron distribution.

This work was inspired by work on the $\text{HCN} \leftrightarrow \text{HNC}$ isomerization system by Joel Bowman and Alec Wodtke[1]. They demonstrated that electronic properties could be exceedingly strong functions of vibrational excitation. Considering the electric dipole moment of each vibrational level of HCN and HNC, they noted that “delocalized states,” those vibrational wavefunction not localized in either well of the potential energy surface, had dipole moments on the order of three times smaller than those of localized vibrational levels. Here the interpretation is more physical than chemical: the delocalized hydrogen atom orbits around the CN fragment causing the dipole moments of the two equilibrium geometries to cancel one another. In this thesis, we focus on properties that do not necessarily differentiate localized vs. delocalized vibrational states, but rather properties that enable us to measure progress along the isomerization path.

1.2 Thesis Outline

- In **Chapter 2**, we introduce experimental techniques of millimeter-wave spectroscopy and describe an absorption spectrometer constructed to observe the rotational spectra of small molecules in the gas phase. We demonstrate the use of several laser–millimeter-wave double-resonance techniques on the diatomic molecule carbon monosulfide. Included here is a discussion of a novel double-resonance method in which the polarization rotation of the millimeter-waves is used to detect an optical transition.
- In **Chapter 3**, we describe modifications made to the millimeter-wave pulsed-jet spectrometer to enable the recording of spectra with superior resolution to that achievable in the conventional spectrometer geometry. The millimeter-waves are propagated along the axis of the pulsed expansion with the effect

of eliminating the contribution of the transverse velocity of the pulsed-source to the linewidth of the observed transitions. The ~ 30 kHz resolution of the coaxial spectrometer is used to record, for the first time in the laboratory, a hyperfine-resolved rotational spectrum of hydrogen isocyanide (HNC).

- In **Chapter 4**, we report high resolution millimeter-wave spectra of vibrationally excited states of HCN and HNC. The evolution of the nuclear quadrupole hyperfine structure along the isomerization coordinate is described in terms of the underlying changes in electronic structure.
- In **Chapters 5, 6 and 7**, we describe new laser-induced fluorescence and IR-UV double-resonance measurements of the vibrational level structure of the first electronically excited singlet state of acetylene. First, in **Chapter 5** we describe the pure-bending polyads, which consist of levels excited in the two low frequency bending modes, ν'_4 (torsion) and ν'_6 (in-plane *cis*-bend). Levels within a polyad are strongly coupled by Coriolis interactions, previously described in the analysis of the vibrational fundamentals[2], and by a newly described Darling–Dennison interaction due, in large part, to the effects of vibrational angular momentum. Importantly, an “extra” level first identified by Scherer *et al.*[3] is assigned conclusively as a specific member of the B^4 polyad, where $v'_B = v'_4 + v'_6$, and B^4 implies $v'_B = 4$.
- Then, in **Chapter 6**, we describe the observation of ν'_1 , the last remaining experimentally unobserved vibrational fundamental of the \tilde{A}^1A_u state of acetylene. The observation of this level is made possible by the understanding of the polyad level structures and by the use of population-labeling experiments to assign the rotational quantum numbers in the absence of clear ground state combination differences.
- In **Chapter 7**, we describe the vibrational levels of the S_1 state that contain excitation in the low frequency modes in combination with the Franck–Condon active modes. These combination polyads reveal a large anharmonicity between

the Franck–Condon active *trans*-bending mode, ν'_3 , and the low frequency *cis*-bending mode, ν'_6 . This anharmonicity is associated with the low barrier to *trans*–*cis* isomerization, which is calculated to proceed through a half-linear transition state.

- In **Chapter 8**, we approach the question of how to experimentally measure large amplitude motion along the acetylene↔vinylidene isomerization path. We identify the electronic signature of this motion by considering the vibrationally averaged electric dipole moments for local-bending wavefunctions in reduced- and full-dimension *ab initio* calculations. The large electric dipole moments of the local-bending states arise from dynamical symmetry breaking in the local mode limit and the large distortion of the electronic wavefunction that is characteristic of large amplitude motion along an isomerization path. We report the experimental observation, by SEP from the Franck–Condon-forbidden vibrational levels of the \tilde{A} state, of the lowest energy eigenstate that manifests local-bending behavior. Tentative assignment is provided for the second such eigenstate, but we argue that to continue to higher energy it will be necessary to implement the new experimental schemes to recognize the electronic signatures of these levels. Chirped-pulse millimeter-wave spectroscopy, a promising new technique for the rapid collection of rotational spectra of small molecules, is introduced, and we advocate its use in detecting electronic signatures of large amplitude vibrations at high resolution.
- In **Chapter 9**, we present ongoing research into the spectroscopic signatures of *trans*–*cis* isomerization on the S_1 surface of acetylene.

Chapter 2

Millimeter-wave spectroscopy of pulsed-jet sources

This chapter details the construction and use of a millimeter-wave spectrometer designed to interface with a pulsed-jet source. The second half of this chapter, dealing with millimeter-wave–optical double resonance techniques, has been published in the *Journal of Chemical Physics* (Ref. [4]), with the exception of section 2.3.4.

2.1 Introduction

Rotational spectroscopy may seem like an odd topic with which to begin a dissertation on large amplitude vibrational dynamics and isomerization. By far the most familiar use of rotational spectroscopy is the precise determination of equilibrium molecular geometries by establishing the three principal moments of inertia for isolated molecules or molecular complexes. However, the richness of detailed data obtainable in a “rotational” spectrum can hardly be overstated. The information encoded about the mass distribution is complemented by fine and hyperfine structure that report on the local and global electronic structure of the molecule. Intuitive chemical concepts such as ionic vs. covalent bonding character can be addressed by interpretation of the interaction of the electron distribution with the rotational motion of the molecule [5, 6].

Strategies to describe bonding character by the determination of fine and hyperfine properties are equally applicable to molecules in (highly) vibrationally excited states. Here, the determined quantities may not describe the equilibrium electronic structure, but rather that of the distorted nuclear configuration, where the bonds may be strained near the point of breaking. In addition, the onset of rapid intramolecular vibrational redistribution (IVR) in excited vibrational levels offers new possibilities for experimentation such as dynamic rotational spectroscopy [7, 8]. In contrast to the extensive body of knowledge accumulated on the rotational spectra of molecules in their ground electronic state, far fewer examples of spectra of vibrationally or electronically excited molecules are present in the literature. The recording of rotational spectra of molecules at high vibration has often relied on complicated experiments that require several lasers to shift the detection of the microwave transition into the optical regime (e.g. H_2CO [9]). Such a strategy is only viable for molecules with known, accessible electronically excited states. Deriving new, general methods for the accumulation of vibration-specific rotational spectra has been one of the goals of this work.

Rotational spectra of the type of molecules of we wish to investigate (small polyatomics, with at least one hydrogen atom) have their lowest frequency transitions in the millimeter-wave region of the electromagnetic spectrum, between 30 and 300 GHz. Unlike in the lower-frequency microwave region with the Balle–Flygare fourier-transform microwave spectrometer [10, 11], there is no single standard instrument design that dominates spectroscopy in the millimeter-wave region. Some modern spectrometers that promise extremely high data rate (Fast scan submillimeter spectroscopy technique, FASSST[12]) or extraordinary sensitivity (intracavity jet orotron [13]) have been described in the literature but are not discussed further here. In this chapter, we describe a a general purpose millimeter-wave spectrometer of extreme simplicity, designed to interface easily with laser excitation schemes. The ultimate

purpose of the spectrometer is the recording of rotational spectra of electronically or vibrationally excited states in order to assess how these excitations alter the electronic structure of the molecule. We seek to use the rotational spectra of vibrationally excited molecules to take snapshots of the electronic structure as the molecule traverses the barriers and valleys along the chemical reaction coordinate.

2.2 Pulsed-jet millimeter-wave absorption spectrometer

A pulsed jet millimeter-wave spectrometer was constructed with the goal of observing the rotational spectra of small polyatomic molecules at high resolution.¹ A schematic of the experiment is shown in Figure 2-1. The design of the spectrometer is similar to that of a robust free-space absorption instrument in use by several groups [14, 15, 16] to record the millimeter-wave spectra of a wide array of unstable molecules. This design has been subsequently extended to operate in conjunction with pulsed free jet sources, often with the particular aim of observing the spectra of van der Waals complexes [17, 18]. In addition, spectra of other classes of transient species such as molecular ions [19] and radicals have been investigated. Of particular note is one experiment [20] that has revealed the ground state proton tunneling splitting of the vinyl radical generated by ultraviolet photolysis in a supersonic jet environment, thereby demonstrating that the high resolution afforded by millimeter-wave rotational spectroscopy enables the experimenter to sample properties that report on the aspects of the potential energy surface most relevant to intramolecular isomerization.

Other possible designs for the geometry of jet millimeter-wave spectrometers exist in the literature. One alternative is the use of a parallel-plate waveguide, which can

¹In fact, the original goal of the spectrometer was more humble. It was intended to serve in an analytical function, as a monitor for the production of HNC via discharge, pyrolysis, or photolysis in a pulsed-jet environment for subsequent laser spectroscopic investigation.

extend the region of interaction between the molecular beam and the millimeter-wave probe with the effect of narrowing the observed linewidths considerably. Such a design has been demonstrated by Huiszoon[21]. However, we favor the free-space design due to its flexible nature, in particular the ability to introduce one or more lasers into the interaction region, which enables (among other experiments) the recording of laser–millimeter-wave double-resonance spectra.

2.2.1 Millimeter-wave source: Phase-locked Gunn oscillator

The first generation of our microwave spectrometer is based on a Gunn oscillator, which, relative to earlier frequency sources such as Klystrons, is characterized by superior frequency agility (i.e. a larger tuning range) but lower output power. The Gunn oscillator has a voltage-tuning characteristic that allows for continuous adjustment of the output frequency over a range of several hundreds of MHz. In addition, the oscillator can be mechanically tuned to provide coverage of nearly the entire W band.

The Gunn oscillator employed here (J.E. Carlstrom Co., H129) has been previously used as the frequency source for an electric resonance optothermal spectrometer employed in studies of the van der Waals complexes Ar-HCN[22] and He-HCN[23]. Useful output power is available from 73 to 106 GHz,² with a peak output of 90 mW at 78 GHz.

Frequency stability is achieved by phase locking the Gunn oscillator to a harmonic of the output of a microwave synthesizer (HP 8672A or 8673E) using a commercial phase-lock module (XL microwave 800A/801). The phase lock loop (PLL) requires two inputs, a low frequency stable reference, and an ‘intermediate’ frequency (IF). The stable reference frequency for the early experiments described in this chapter

²The nominal frequency range associated with the W band is 75–110 GHz. This frequency band is associated with a waveguide size denoted WR-10, where ‘10’ refers to the longer interior dimension of the waveguide in hundredths of an inch.

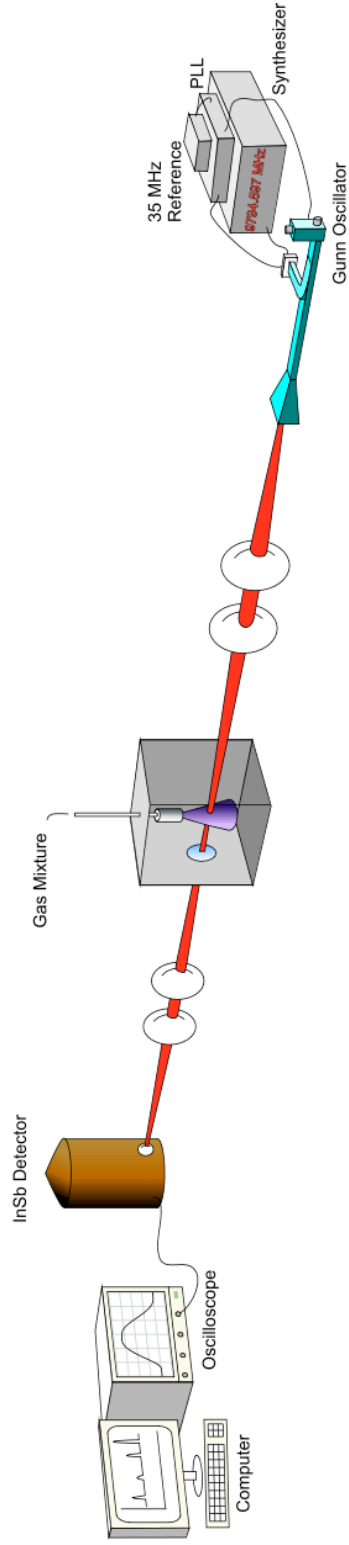


Figure 2-1: Schematic of the pulsed-jet millimeter-wave spectrometer. The millimeter-wave source is a Gunn oscillator (73–106 GHz), stabilized and scanned by a phase-locked loop (PLL). The millimeter-wave radiation is collimated and focused by a pair of PTFE lenses ($f = 40$ cm and $f = 30$ cm, respectively) into an unskimmed supersonic free-jet expansion produced by a pulsed valve. After exiting the chamber, the millimeter-waves are recollimated and focused with another pair of PTFE lenses ($f = 30$ cm and $f = 40$ cm, respectively) onto a liquid-helium-cooled InSb bolometer detector. The transient decrease in millimeter-wave power incident on the bolometer, when the radiation is on resonance with a molecular transition, is monitored by digitizing the output of the bolometer at each frequency step.

was provided by the output of a crystal oscillator at 35 MHz. The IF is generated by mixing a portion of the Gunn oscillator output (separated from the primary output by a directional coupler) with the output of the microwave synthesizer in a subharmonic mixer (Pacific Millimeter Products WM). The low frequency components of the mixer output are separated by a diplexer and routed to the PLL input. By adjusting the bias voltage to the Gunn oscillator, the PLL circuitry seeks to match the frequency (and phase) of the IF with that of the stable reference signal. Stated differently, the phase-lock condition is met when the frequency of the Gunn oscillator (F_{osc}) is offset from the frequency of a harmonic of the microwave synthesizer ($N \times F_0$) by an amount equal to the reference frequency (F_{REF}).

$$F_{\text{IF}} = (F_{\text{osc}} - N \times F_0) = F_{\text{REF}} \quad (2.1)$$

The Gunn frequency can be tuned by adjusting the frequency of either the reference source or that of the microwave synthesizer. In the applications described in this chapter, the microwave synthesizer is tuned via GPIB interface to scan the frequency of the Gunn oscillator. However, it is sometimes desirable to adjust the low frequency reference, and such a scenario will be described in Chapter 3. When locked, the uncertainty in the mm-wave frequency is better than 5 kHz, which is significantly less than the width of the narrowest lines observed with our instrument. The quality of the lock is monitored by displaying the IF on a spectrum analyzer. Successful phase-locking, apparent on the spectrum analyzer due to suppression of power at undesired frequencies near the lock reference, is achieved by optimizing the power input to the subharmonic mixer by both the Gunn oscillator and microwave synthesizer, in addition to adjusting the loop gain (V_{lg}) on the phase lock control module.

The output of the Gunn oscillator can be extended to shorter submillimeter wavelengths by the use of frequency multipliers. Specifically, the instrument can be

equipped with either a planar GaAs Schottky diode-based frequency doubler (Virginia Diodes WR5.1x2) or tripler (WR3.4x3) to extend the range of the spectrometer to 146–206 or 219–309 GHz. These modern multipliers are extremely convenient in comparison to whisker diode multipliers in that they require neither external bias nor any tuning mechanism. Their emergence in extending the techniques of millimeter-wave spectroscopy to the terahertz region has been reviewed in a recent paper[24].

In fact, direct multiplication of low-frequency microwave synthesizers has become an excellent alternative to millimeter-wave sources such as Gunn oscillators. This technology is used, among others, by our collaborator, Prof. Liam Duffy, in millimeter-wave experiments similar to our own[25]. The primary benefits of these alternative sources is that one does not need to phase lock the source at a relatively high frequency and that the tuning ranges can be extremely large, allowing nearly full-band scans without any adjustments to the apparatus. We have recently acquired broadband multipliers operating in the region previously accessible with the Gunn oscillator. The use of these multipliers is described briefly in Chapter 8.

2.2.2 Millimeter-wave detection

The second critical component of an absorption spectrometer is the detector of radiation. In the millimeter-to-submillimeter range, the most popular technology for the detection of broadband radiation is the Indium antimonide (InSb) hot-electron bolometer. This detector operates on the principle that absorption of millimeter-wave radiation by free carriers in a semiconductor leads to increased electron mobility, associated with a change in conductivity of the material [26]. In the millimeter-wave region, the detector is cooled to liquid-helium temperatures (~ 4.2 K) so that the energy absorbed from the incident millimeter-waves is not swamped by thermal noise.

In the experiment, the bolometer serves as a sensitive, linear power detector for millimeter-waves in the μW regime. As such, the bolometer enables straightforward

Beer's-law measurements of absorbance by a sample. In practice, the bolometer used in these experiments is equipped with a sensitive preamplifier (Cochise Instruments, WBLN 3) that filters out frequencies below 5 Hz. In order to measure the power incident on the detector and, therefore, establish a value for baseline intensity, (I_0), the millimeter-wave beam must be modulated. A square-wave modulation can be imposed on the millimeter-wave power using an optical chopper (Stanford Research System, SR540) with a large-aperture slotted blade. The amplitude of the square-wave signal output by the bolometer is proportional to the input power, up to the point where the preamplifier response begins to saturate ($V_{\text{out}} \sim 16$ V). When observing transient signals, such as those due to a pulsed-jet of molecules passing through the millimeter-wave beam, the amplitude of the millimeter-waves need not be externally modulated or chopped, as the decrease in the power due to molecular absorption is on the appropriate timescale to be passed by the preamplifier. The transient bolometer voltage is related, in a direct way, to the power absorbed by the molecular sample. It should be noted here that the bolometer output signal is inverted, such that a transient decrease in power incident on the bolometer leads to a positive output voltage.

2.2.3 Propagation of millimeter-wave radiation

The millimeter-wave beam is propagated using free-space quasioptical techniques that more closely resemble those for routing optical beams than they do the electrical and waveguide techniques typically used in microwave spectroscopy. The optical design follows the example of previous spectrometers (e.g. Ref. [14]), ignoring the complex radiation pattern output by a pyramidal gain horn. Optical elements, such as lenses, are typically fabricated from polymeric materials like polyethylene and polytetrafluoroethylene (PTFE, Teflon®), which are characterized by good transparency and relatively flat refractive index in the millimeter-wave region.

2.2.4 Characterization of mm-wave spectrometer

As an initial test, we recorded the millimeter-wave absorption spectrum of a sample of 1% OCS in Ne in the region of the OCS $J = 8 \leftarrow 7$ transition near 97.3 GHz. The first, unoptimized spectrum recorded with our jet spectrometer is shown in Figure 2-2. On resonance, the absorption is readily observable above the noise level of the bolometer in a single gas pulse.

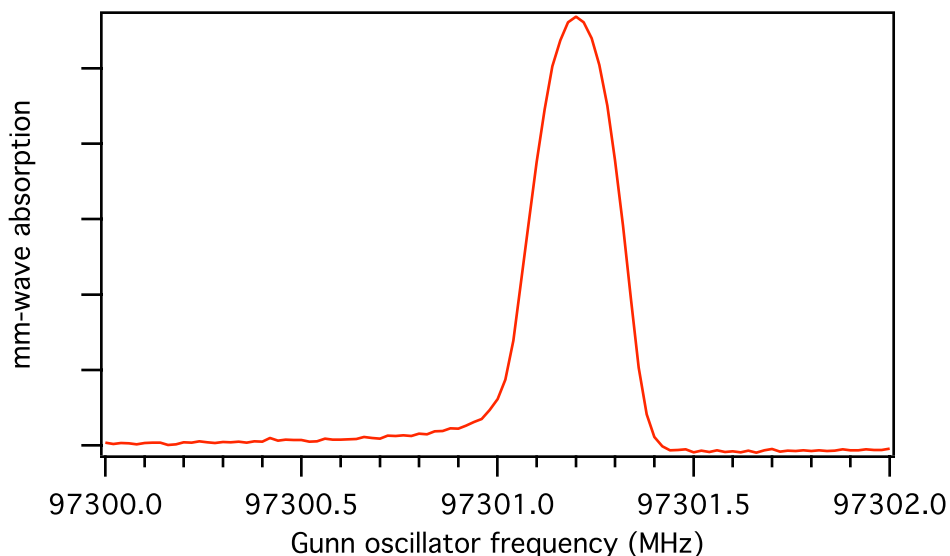


Figure 2-2: Initial spectrum of the OCS $J = 8 - 7$ transition recorded with the pulsed-jet millimeter-wave spectrometer. Each point is the average of 40 gas pulses.

It is apparent that the recorded lineshape suffers from significant asymmetry. This asymmetry persists, in the same sense, when scanning the spectrum in either direction, low frequency to high frequency, or vice versa. However, the degree and sense of the asymmetry are found to depend on the millimeter-wave alignment. Similar observations were made by Hepp *et al.*[17], who describe how such an asymmetry can be thought of as the admixture of absorptive and dispersive lineshapes that arises when a portion of the millimeter-wave probe does not intersect the absorbing sample. The asymmetry of the lines is detrimental to precise determination of the transition frequencies. Fitting our initial OCS spectrum to a simple gaussian shape results in

a center frequency that deviates from the best measurement of this transition by just over 5 kHz. In order to achieve the most accurate measurements, care is taken to align the spectrometer to minimize the effects of dispersion on the experimental lineshapes.

The ability to record much weaker signals is demonstrated in Figure 2-3, which shows an optimized spectrum of the same $^{16}\text{O}^{12}\text{C}^{32}\text{S}$ transition as in Figure 2-2 and the analogous transitions in two of the less abundant isotopologues, $^{16}\text{O}^{12}\text{C}^{34}\text{S}$ ($\sim 4\%$ natural abundance) and $^{16}\text{O}^{13}\text{C}^{32}\text{S}$ ($\sim 1\%$). In these spectra, the asymmetry is much less pronounced due to optimization of the alignment. The observed lineshapes are primarily gaussian, with a 280 kHz linewidth (FWHM). This is consistent with the Doppler effect serving as the dominant line-broadening mechanism, in contrast to traditional (non-jet) millimeter-wave spectroscopy where, in the typical range of pressures employed in spectroscopic experiments, pressure broadening typically dominates, leading to Lorentzian lineshapes. Transit-time effects, as well as power broadening, may also have an effect on our observed lineshapes. These mechanisms will be considered further in Chapter 3.

In Figure 2-3, the absorption spectra are shown with corresponding traces recorded using frequency modulation of the millimeter-wave source. In principal, there are a number of different ways in which the frequency may be modulated. The simplest implementation is the use the frequency modulation capability of the microwave synthesizer. The instantaneous frequency of the synthesizer is swept around the carrier frequency, ω_c , at a modulation rate, ω_m . This has the effect of adding sidebands to the carrier frequency, separated from it by ω_m . In the absence of an absorbing species, the power reaching the detector is constant. Near a resonance, the upper and lower sidebands will be differentially absorbed, and this difference will result in a time-dependent signal modulated at ω_m . Demodulation of the detector output at ω_m by a lock-in amplifier produces a derivative lineshape. This condition has some

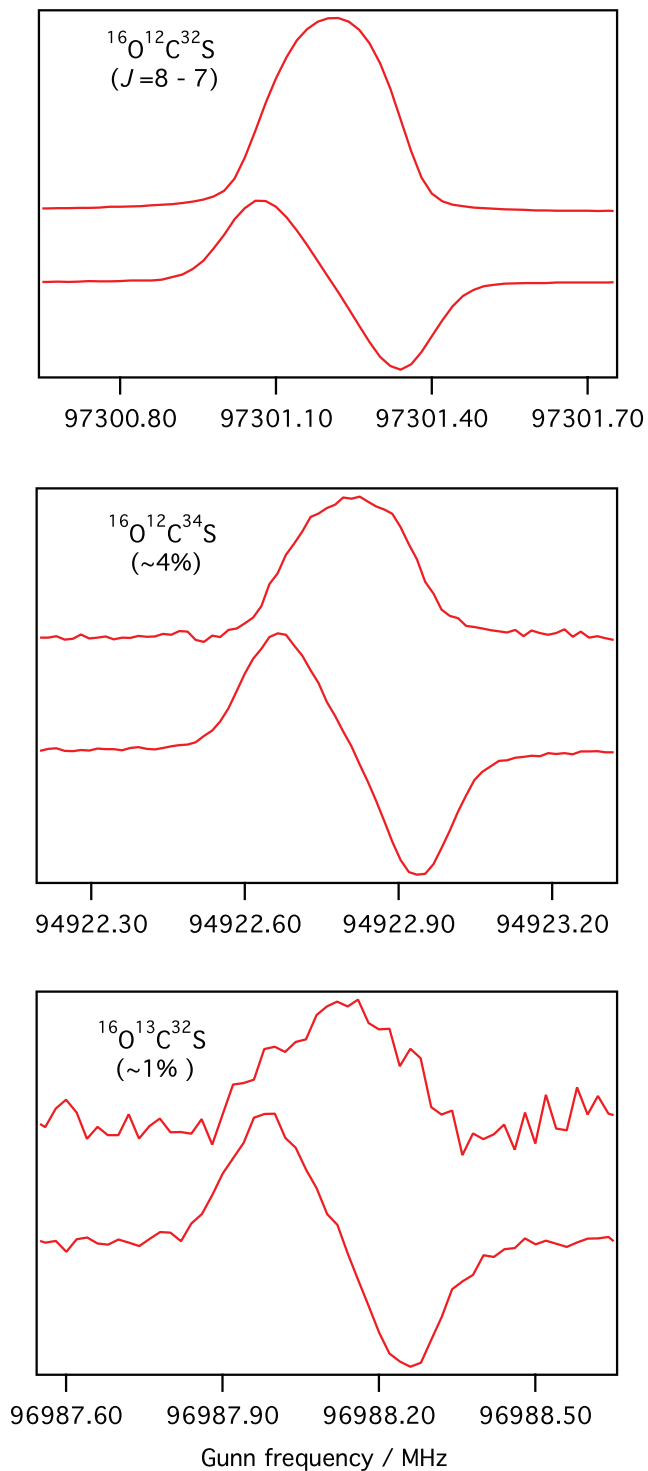


Figure 2-3: Rotational spectra of OCS isotopologues, recorded with the pulsed-jet millimeter-wave spectrometer. The sample is a 1% mixture of OCS in Ne, expanded from a backing pressure of 25 psi. The weaker isotopes are present at their natural abundance. The output of the Gunn oscillator is attenuated -21 dB in order to prevent saturation of the bolometer response. The Gunn frequency is stepped in 20 kHz increments. Each point is the average of 60 gas pulses for the traces recorded in absorption mode and 5 gas pulses for the spectra recorded using frequency modulation (derivative lineshape). As a result of shifting the detection frequency to higher frequencies, where the impact of technical noise is less, the signal-to-noise ratio for the FM spectra are superior to the absorption-detected spectra by approximately one order of magnitude. Taking into account the increased averaging time for the absorption-detected spectra, frequency modulation provides a sensitivity enhancement in the range of 10–30.

benefits, primarily that the line center can be identified with the zero-crossing point in the spectrum.

As is clear from the spectra of the less abundant isotopologues, the signal-to-noise ratio for the frequency modulated spectra is superior to that of the unmodulated absorption spectra. The advantage of this technique lies in the fact that the detection frequency is shifted away from DC into a frequency region where there is less technical noise. Isolation of the signal at the detection frequency is particularly effective when the signal can be demodulated with a long time constant, corresponding to a very narrow detection bandwidth. A further advantage is that the FM signal is related to the differential absorption of multiple frequency components of the probe beam. As a result, the experiment has an internal reference to compensate for power fluctuations of the source and does not require a dual-beam setup for maximum sensitivity.

In our pulsed-jet experiments, there is also a second modulation frequency present, that of the pulsed nozzle source, typically 10 or 20 Hz. This frequency of the molecular beam is not demodulated with a second lock-in but rather, due to the very low duty cycle of the pulsed expansion, gated in software to give the final plotted signal. This is accomplished by routing the output of the lock-in to a digital oscilloscope, which digitizes each averaged transient and transfers it to a personal computer for analysis. The second modulation may be termed “source modulation,” since it is the presence of the molecular absorbers that varies in time. However, in more typical usage, source modulation usually refers to the time-varying production of transient molecules by application of a modulated voltage to the electrodes in a discharge apparatus. Modulation techniques are often used in combination, in order to further isolate the desired signal from disparate sources of noise, and the resulting techniques are referred to as “double modulation.”

As is demonstrated above for the case of the OCS isotopologues, frequency modulation can provide significantly enhanced sensitivity over unmodulated absorption.

However, FM will not be used significantly in the remainder of this thesis. The primary reason for this is that FM detection necessarily requires convolving the detector response with some time constant because the lock-in must demodulate the signal over several periods of the modulation frequency, therefore reducing the range of dynamical timescales observable. This is a particular disadvantage for signals with durations shorter than tens of microseconds, including laser–mm-wave multiple resonance signals and absorption by transiently produced molecules.

2.3 Millimeter-wave–optical double resonance and millimeter-wave–detected, millimeter-wave–optical polarization spectroscopy

2.3.1 Motivation for millimeter-wave–optical double resonance

Because the frequencies of pure rotational transitions are easily calculated with high precision, the < 1 MHz resolution of microwave sources makes rotational transitions straightforward to resolve and assign even in complex chemical environments, such as discharges, where spectral congestion can hinder assignments of optical transitions. As a consequence, microwave transitions have been measured and tabulated [27, 28] for a vast number of transient species, many of which have unknown optical transitions. Microwave-detected, microwave–optical double-resonance (MODR) techniques [29, 30, 31, 32, 33], which monitor resonant changes in the microwave signal induced by optical pumping out of the lower or upper state of the rotational transition, are a convenient method of identifying optical transitions in these molecules. By labeling the molecule and the lower rotational level of the optical transition, microwave-detected MODR schemes provide a “rotational handle” to simplify tremendously the spectrum, allowing easier assignments and species identification. Moreover, microwave-detected

MODR techniques are widely applicable; they can be applied to weak vibrational and electronic transitions and to transitions that have poor fluorescence quantum yields arising from nonradiative processes, such as collisional quenching, predissociation, intersystem crossing, or internal conversion. Once optical transitions are identified, microwave-detected MODR can then be used to measure the pure rotational spectra of optically populated vibrationally and electronically excited molecules, with the resolution limited only by the radiative decay rate. Then, by monitoring the excited state rotational transition, additional optical transitions from this state can be identified. Thus, microwave-detected MODR not only provides a rotational handle for identifying optical transitions, but it can also be used to map out the energy-level structure of the molecule by systematically bootstrapping through different vibrational and electronic transitions, with each vibronic level unambiguously labeled by its characteristic pure rotational transition.

The following section describes a new microwave-detected MODR technique applicable to the millimeter-wave frequency region called millimeter-wave-detected, millimeter-wave optical polarization spectroscopy (mmOPS). mmOPS is analogous to optical polarization spectroscopy [34], polarization labeling [35], and microwave-optical polarization spectroscopy (MOPS) [36, 37, 38], in which the polarization of a probe beam is rotated by the angular anisotropy (unequal population in M_J sublevels) created by a polarized pump beam. Unlike previously reported polarization-detected techniques, however, in the current implementation of mmOPS the polarization rotation is in the millimeter-wave beam, rather than in an optical beam. We apply mmOPS to the well-known $A\ ^1\Pi - X\ ^1\Sigma^+$ electronic band system [39] of the diatomic molecule carbon monosulfide, CS, which is produced in a pulsed discharge supersonic nozzle. We find that the near-zero background of mmOPS makes it more sensitive than the millimeter-wave-detected, millimeter-wave optical double-resonance (mmODR) technique, [31] especially when using a liquid-helium-cooled InSb detector.

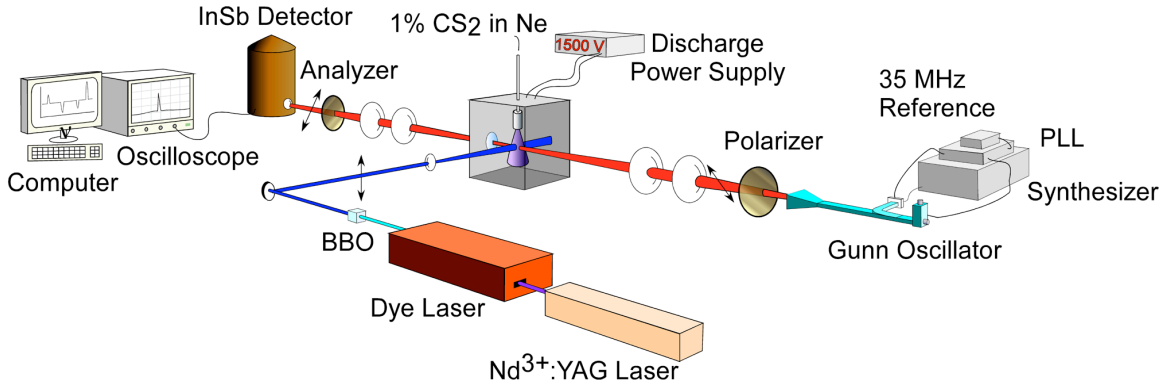


Figure 2-4: Schematic of the mmOPS apparatus. In the mmODR and mmOPS experiments, a pulsed laser interacts with the molecules while they are being probed by the always-on millimeter-waves. In the mmOPS experiment, the laser-induced polarization rotation of the millimeter-waves is detected with nominally crossed freestanding wire-grid polarizers.

2.3.2 Experimental details

Figure 2-4 is a schematic of the mmOPS apparatus. The experiment is performed in a $12 \times 12 \times 12$ in.³ vacuum chamber, which is evacuated by a 6 in. diffusion pump (Diffstak 160, Edwards) backed by a rotary mechanical pump. CS is generated in a supersonic expansion by passing a mixture of 1% CS₂ in Ar through a pulsed discharge nozzle (1-mm.-diameter orifice) that is similar to the design of Sanz *et al.*[40] The optimal conditions for detection of the CS $X^1\Sigma^+(v = 0, J = 2 - 1)$ rotational transition are backing pressure (3 atm), nozzle pulse duration (350 μ s), negative discharge voltage (1.4 kV), and discharge pulse duration (1 ms).

The millimeter-wave radiation is produced by a W-band (75-110 GHz) Gunn oscillator (J.E. Carlstrom Co.) that is phase-locked (XL Microwave 800A) to a harmonic of a microwave synthesizer (8672A) and coupled through waveguide components to a calibrated attenuator (Hitachi W9513). The radiation is emitted into free space through a standard gain horn (TRG Control Data, 15 dB) with a linear polarization of 45° relative to the pump-laser polarization and focused by a pair of PTFE lenses ($f_1 = 40$ cm, $f_2 = 30$ cm) to a spot size of ~ 1 cm diameter at the point of inter-

section with the molecular beam, ~ 2 cm downstream from the nozzle. After exiting the chamber, the millimeter-wave beam is refocused by a second pair of PTFE lenses ($f_3 = 30$ cm, $f_4 = 40$ cm) onto a liquid-helium-cooled InSb hot-electron bolometer (Cochise Instruments). The bolometer output is digitized with a 500 MHz oscilloscope (Lecroy LC334A) and transferred to a computer for storage. In the mmOPS version of the experiment, the rotation of the millimeter-wave polarization is detected by a pair of nearly crossed, freestanding, wire-grid polarizers. The polarizing grids are composed of 25- μm -diameter gold-plated tungsten wire with center-to-center wire spacings of 100 μm [41]. When perfectly crossed, the polarizers have an extinction ratio of $\sim 10^{-3}$.

The ultraviolet radiation is produced by frequency doubling the output of a Nd^{3+} :YAG-pumped dye laser (Quanta Ray DCR-3/Lambda Physik 3002) in a β -barium borate (β -BBO) crystal. The doubled radiation ($\sim 1-1.5$ mJ/pulse) is scanned ~ 10 cm^{-1} by pressure tuning the etalon-narrowed oscillator cavity and is calibrated to ± 0.02 cm^{-1} using a small amount of the residual fundamental to record an I_2 fluorescence spectrum[42]. As shown in Figure 2-4, the vertically polarized ultraviolet radiation enters the vacuum chamber in a direction orthogonal to both millimeter-wave and molecular beams. The overlap of the optical field with the millimeter-wave radiation is optimized by expanding the optical beam to ~ 2 cm in diameter in the overlap region.

2.3.3 mmODR and mmOPS of carbon monosulfide

In the mmODR technique, the millimeter-wave frequency is locked onto a ground-state rotational transition—here the $\text{CS } X^1\Sigma^+$ ($v'' = 0, J'' = 2 - 1$) transition—and the absorption of the millimeter-wave radiation is monitored while the laser frequency is scanned. When the lower state of the optical transition is one of the two levels connected by the millimeter-wave transition, the sudden change in the ground-state

population induced by the laser pulse creates a millimeter-wave transient nutation signal [29, 30, 31].

If the optical transition is out of the upper millimeter-wave connected level, then the transient nutation signal is absorptive (positive), whereas if the optical transition is out of the lower state, the transient nutation signal is emissive (negative)[see Figure 2-5].

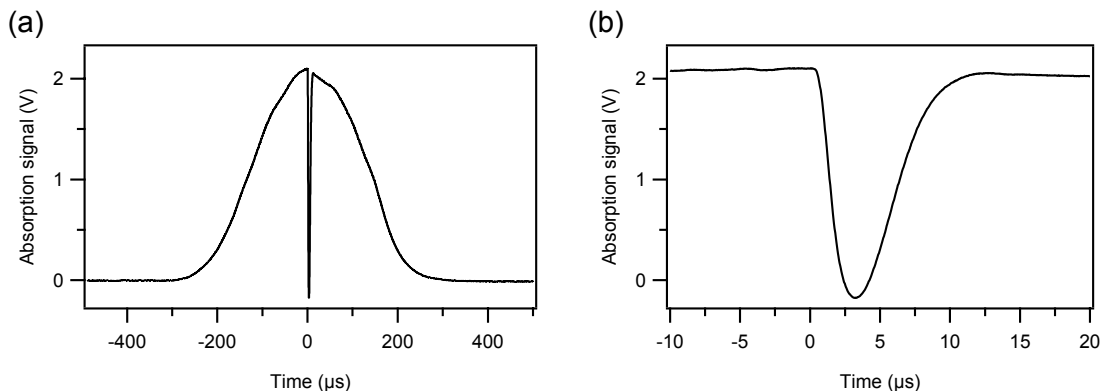


Figure 2-5: (a) In the mmODR experiment, the gas pulse passes through the millimeter-wave interaction region, resulting in an increase in the absorption signal between the -200 and $+200 \mu\text{s}$. The laser interaction occurs near $t = 0$, resulting in a transient disruption of the equilibrium population difference. (b) The signal is recorded by gating the laser-induced feature and comparing it to the background absorption signal, usually after fitting a portion of the background to a polynomial curve in order to remove the effects of the varying absorption due to the temporal profile of the gas pulse. The disruption of the population difference is so large that the millimeter-wave beam is transiently amplified.

Figure 2-6 shows selected rotational transitions from the CS $A \ ^1\Pi - X \ ^1\Sigma^+ (1 - 0)$ vibrational band, obtained using mm-wave-detected mmODR (upper trace) and mmOPS (lower trace) techniques. In addition to the five expected optical transitions originating from $J'' = 1[Q(1), R(1)]$ and $J'' = 2[P(2), Q(2), R(2)]$, the spectrum in Figure 2-6(a) contains a negative-going transition at the expected position of the $R(0)$ line. The sign of the extra signal indicates that the optical transition out of $J'' = 0$ causes a preferential depopulation of the $J'' = 1$ level relative to the $J'' = 2$, which is most likely due to collisional ($J'' = 0$ hole filling from $J'' = 1$) population

transfer following optical excitation. The optical pumping can significantly alter the thermal population difference between the $J'' = 2$ and $J'' = 1$ levels because the CS $A^1\Pi - X^1\Sigma^+ (1 - 0)$ transition is fully allowed and the Franck-Condon factor is 0.14 [39]. As a consequence, both negative and positive mmODR signals are observed that are considerably larger than the original absorption signal in the absence of optical pumping. The signal displayed in Fig. 2-5, the largest observed to date, dips below the 0 V baseline that represents the power transmitted to the detector when no molecules are present. That is, the equilibrium population is disrupted to the extent that the population is inverted and the millimeter-wave probe beam experiences some small gain.

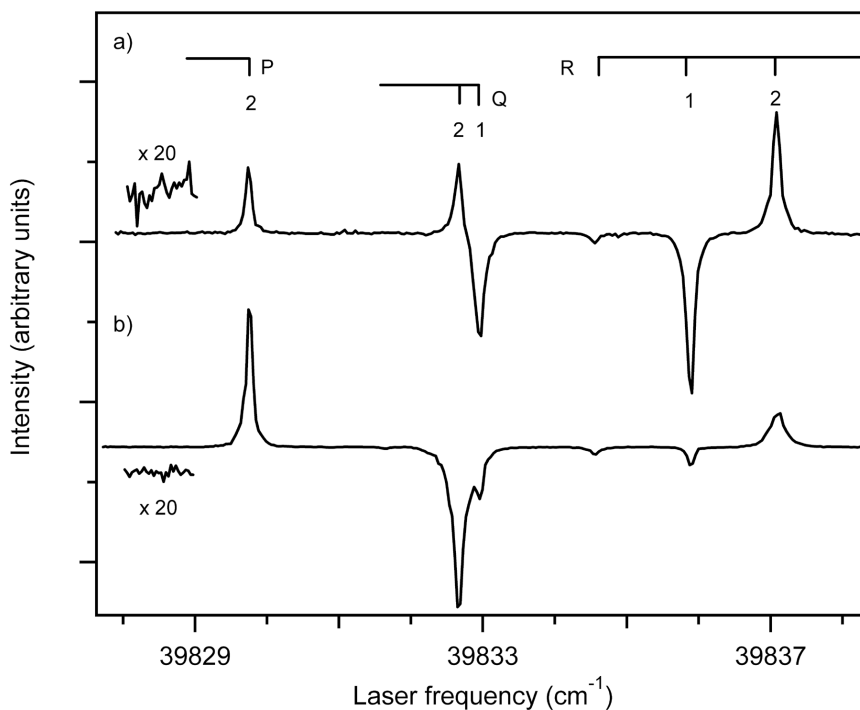


Figure 2-6: Comparison of (a) the millimeter-wave-detected mmODR technique with (b) the millimeter-wave-detected mmOPS technique. The spectra are obtained by scanning a laser over the $A^1\Pi - X^1\Sigma^+ (1 - 0)$ band, while the millimeter-wave frequency is locked to the CS $X^1\Sigma^+ (v'' = 0, J'' = 2 - 1)$ rotational transition. The laser was scanned at the same rate for both spectra and each point is an average of 20 laser shots. The expanded baselines in the region of $39\,829\text{ cm}^{-1}$ indicate that the baseline noise is improved by a factor of 4 for mmOPS relative to mmODR.

The sensitivity of the mmODR experiments is limited primarily by the large and fluctuating CS absorption background caused by instabilities in the CS number density produced in the pulsed-discharge supersonic expansion. This CS production noise can be largely removed by using the mmOPS technique. When the vertically polarized pump laser is resonant with a CS electronic transition, it creates an anisotropic sample of CS molecules by preferentially pumping certain M_J states. If one of the levels of the millimeter-wave transition is in common with the pump-laser transition, then the vertical and horizontal components of the millimeter-wave probe are differentially absorbed, causing a polarization rotation of the millimeter-waves. By using a pair of crossed polarizers, the unrotated millimeter-wave radiation can be blocked, while only the rotated millimeter-wave radiation strikes the detector. Thus, the polarization-detected experiment can have a background level that is limited only by the imperfect extinction of the polarizers and the birefringence of the millimeter-wave transmission optics.

When the polarizers are perfectly crossed, all mmOPS signals should have the same sign because millimeter-wave radiation strikes the detector only when the optical pump transition originates from one of the linked levels of the millimeter-wave transition. The signal levels in this case are often too small to be observed above the noise level of the current detector. As in optical-polarization-based experiments [43], however, the signal-to-background ratio can be improved by imperfectly crossing the polarizers to heterodyne the weak polarization-rotated signal field with the much stronger nonrotated field. Here, the spectra are collected at relatively large uncrossing angles ($\sim 5^\circ$) to obtain the best signal-to-noise ratio. Although the background level at 5° is approximately twice the background level when the polarizers are perfectly crossed, the cross-term between the signal and carrier millimeter-wave electric fields is much larger, which ultimately increases the signal-to-background ratio. The heterodyne term leads to both positive and negative feature in the mmOPS spectrum.

In contrast to the mmODR spectra, however, the sign and intensity of the observed features contain information about the rotational branch excited by the optical field, rather than simply the lower state of the optical transition. The spectra in Figure 2-6 have been normalized so that the strongest transition in each spectrum has the same peak intensity. The baseline in the region of $39\,829\text{ cm}^{-1}$ is expanded to show that baseline noise is suppressed by a factor of 4 for mmOPS relative to mmODR.

The enhancement in sensitivity (signal-to-background ratio) afforded by the mmOPS technique has enabled us to record nominally spin-forbidden transitions into triplet states of CS, as shown in Figure 2-7. Although the sensitivity enhancement of mmOPS is largely due to the reduction of the CS production noise present in the CS ground-state mmODR signal, it is also improved because the millimeter-wave power incident on the molecular beam can be increased without saturating the millimeter-wave detector. In the absorption-detected technique the power of the Gunn oscillator is attenuated by approximately 15 dB to $600\ \mu\text{W}$ to avoid saturation of the detector/preamplifier, while in the polarization-detected technique the full power of the oscillator (nominally 18 mW at 98 GHz) is incident on the molecular beam, but is attenuated by the crossed polarizers to $<1\text{ mW}$ on the detector.

Use of these higher mm-wave powers is somewhat problematic in that the characteristic transient nutation signals become evident, and, by varying line to line, cause difficulties in recording a spectrum with a uniform time gate.³ The ideal mm-wave power for the detection of one transient may cause the transient induced by another optical transition to oscillate one or more times, resulting in partial cancellation of the gated signal. Use of such a non-ideal gate (chosen to optimize gated signal for

³mmODR without polarization is largely immune to these factors, as all lines generally give rise to a similar transient profile. The exception is collisionally-induced lines, which have maxima occurring at later times due to the delay in transmitting the population hole in one state to its neighboring states via collisions. Unexplained transients are observed in mmODR, primarily when there is incomplete overlap of the laser and the mm-wave beam. However, once the anomalous time-dependent behavior is corrected for one optical transition, transient mm-wave signals for all transitions become well-behaved.

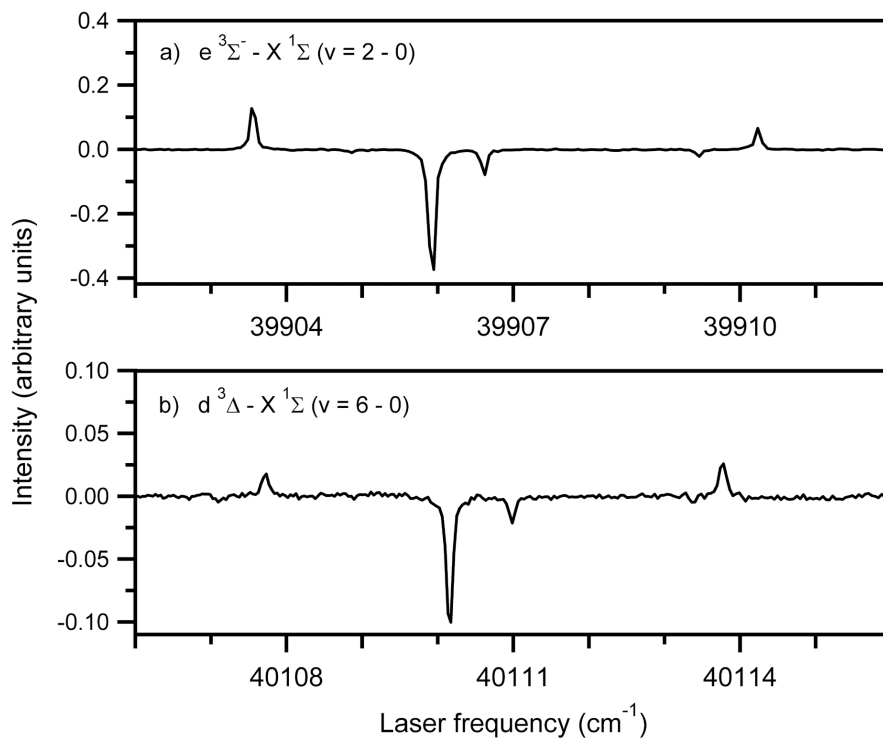


Figure 2-7: mmOPS spectra of nominally spin-forbidden electronic transitions to triplet states of CS, which borrow their intensity via spin-orbit interactions with the $A^1\Pi$ state. The millimeter-wave frequency is locked to the CS $X^1\Sigma^+$ ($v'' = 0, J'' = 2 - 1$) rotational transition and the laser is scanned over the (a) $e^3\Sigma^- - X^1\Sigma^+$ ($2 - 0$) and the (b) $d^3\Delta - X^1\Sigma^+$ ($6 - 0$) bands. The $e^3\Sigma^-$ ($v' = 2$) and the $d^3\Delta$ ($v' = 6$) states have 17% and 1% nominal $A^1\Pi$ character, respectively for the rotational levels accessed. Each point is an average of 20 laser shots.

the $Q(2)$ line) is the likely cause of the non-observation (or strange line shape) of the $R(1)$ line in the spectra shown in Figure 2-7(b).

2.3.4 mmODR of vibrationally excited states

We have shown in the previous section that mmODR techniques provide an alternative to traditional methods of electronic spectroscopy, such as laser induced fluorescence or multiphoton ionization, and provide the species- and rotational-selectivity characteristic of multiple resonance experiments. In general, mmODR techniques may provide advantages for the spectroscopy of states that undergo non-radiative processes, rendering them dark in emission. Another class of states, vibrationally excited levels of ground electronic states, which are effectively dark in emission due to their long radiative lifetimes and the relative insensitivity of typical detectors to infrared photons as compared to visible photons, should benefit from study by mmODR techniques. This is especially true for vibrationally excited states of molecules that resist characterization by other means, particularly those which do not have a known or accessible electronic spectrum. One significant molecule lacking such a spectrum is hydrogen isocyanide (HNC), which will be discussed in great detail in Chapters 3 and 4. The vibrational spectrum of HNC has been obtained by other means [44, 45, 46, 47], but HNC is used here as an example of a transient molecule that is often present in complex mixtures and may therefore benefit from the selectivity of double resonance spectroscopy.

The ground state $J = 1 - 0$ rotational transition of HNC, produced in a pulsed discharge of acetonitrile (CH_3CN) in Ar, is readily observed in our millimeter-wave jet spectrometer (see Chapter 3). A digitized transient, similar to that shown in Fig. 2-5 for CS, is given in Fig. 2-8(a). Here the background absorption due to the HNC rotational transition is much weaker than in the CS experiments, however, the sensitivity of the mmODR experiment is sufficient to record spectra as shown in Fig.

2-8(b). The spectrum shown is recorded by pumping the $R(0)$ line of the $2\nu_3$ band of HNC. Similar mmODR spectra have been recorded of the ν_1 and $\nu_1 + \nu_2$ bands of HNC (not shown).

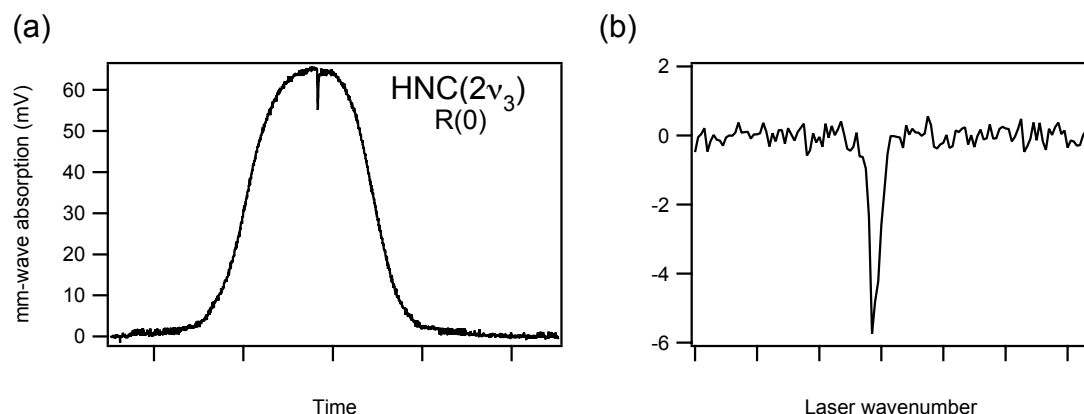


Figure 2-8: mmODR signal for vibrational excitation of the $2\nu_3$ band of HNC near 4026 cm^{-1} . (a) The digitized absorption transient from the bolometer output for the HNC $J = 1 - 0$ transition. The small dip near the center of the absorption envelope is due to laser excitation of the $2\nu_3$ band ($R(0)$ line) of HNC. The IR laser radiation is generated by difference frequency mixing in lithium niobate of the output of a dye laser operating with LDS 751 and the 1064 nm fundamental output of an injection-seeded Nd:YAG laser. The power is approximately 1.5 mJ/pulse . (b) Uncalibrated laser scan over the $R(0)$ line, demonstrating that the dip in (a) is a resonant feature associated with a relatively weak vibrational overtone transition.

2.3.5 Rotational spectroscopy of laser-excited states

To demonstrate further the capabilities of the mmODR and mmOPS techniques, we have measured a pure rotational transition in one of the optically populated triplet states of CS. Figure 2-9 shows the mmOPS spectrum recorded with the laser populating the $J' = 1, N' = 1$ level of the $e^3\Sigma^- (v' = 2)$ state. The trace is the average of four scans, each recorded by stepping the Gunn oscillator output in 50 kHz steps and averaging the bolometer output for ten laser shots at each frequency. The center frequency of the triplet rotational transition $J' = 2, N' = 2 \leftarrow J' = 1, N' = 1$ is

determined to be 76 229.027(20) MHz.⁴ The measured linewidth is 1.3 MHz, which is significantly broader than the ground-state linewidth [~ 240 kHz full width at half maximum (FWHM)]. We attribute the additional linewidth to the radiative lifetime of the triplet state, which is expected to be $\sim 1.2 \mu\text{s}$, assuming that the lifetime is dominated by the $\sim 17\%$ singlet character [39] of the populated nominal triplet level and the 198 ns lifetime for the $A \ ^1\Pi (v = 1)$ state [48].

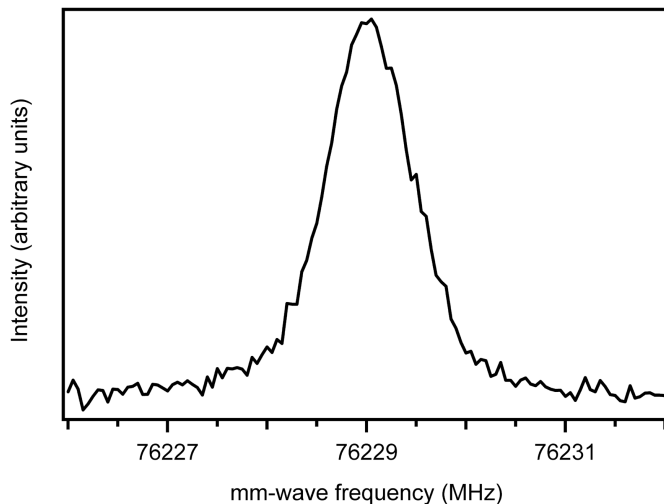


Figure 2-9: Pure rotational mmOPS spectrum of an excited triplet electronic state. The laser frequency is fixed to populate the $J' = 1, N' = 1 \leftarrow J'' = 1$ transition of the $e \ ^3\Sigma^- - X \ ^1\Sigma^+ (2 - 0)$ vibrational band. The center frequency of the pure rotational transition $J' = 2, N' = 2 \leftarrow J' = 1, N' = 1$ in the electronically excited state is 76 229.027(20) MHz.

In contrast to millimeter-wave transitions in the CS ground state, measurements of mmODR signals in the excited state are not compromised by fluctuations in the background absorption of ground-state CS molecules. Rather, the main contributor to the baseline noise is the millimeter-wave detector noise, which is larger than the amplitude noise of the millimeter-wave source. Because the most significant advantage

⁴Recent measurement of this transition with a chirped-pulse mm-wave spectrometer, described briefly in Chapter 8, has revealed that this measurement may be in error. In that experiment, the millimeter-wave transition is observed at a frequency almost exactly 35 MHz away from that observed in the bolometer-detected experiment. This 35 MHz frequency offset is likely caused by improper locking of the Gunn oscillator to a harmonic of the 35 MHz low-frequency reference. The experiment has not yet been repeated in bolometer-detected mode to confirm this hypothesis.

of the polarization-detected technique with the current millimeter-wave detector is the suppression of the CS source noise, the excited-state mmODR and mmOPS spectra are nearly identical in quality. In addition to detector noise, both the mmODR and mmOPS techniques are artificially limited by the bandwidth (5 Hz–500 kHz) of the millimeter-wave detector. This limitation attenuates transient nutation signals with periods shorter than 2 μ s and is particularly disadvantageous for the mmOPS technique, which would otherwise use the full power of the millimeter-wave source to induce the fastest possible transient nutation signals.

We have demonstrated that millimeter-wave-detected mmOPS is capable of being used to record selected rotational lines of an electronic transition with high sensitivity and to detect pure rotational transitions in electronically excited states, with resolution limited by the radiative decay rate. In addition, the development of sensitive new techniques such as millimeter-wave-detected mmOPS makes it possible to observe and identify optical transitions in complex environments, such as discharges, where traditional one-color measurements can be limited by spectral congestion.

As is briefly discussed in the introduction to this chapter, measurements of rotational spectra are often of particular value due to the fact that they can reveal details of molecular electronic structure. One property that is accessible in high-resolution rotational spectra, the nuclear quadrupole hyperfine splitting, is described in the following chapter. The hyperfine splitting is apparent in field-free spectra, but many other electronic properties are most readily measured by recording the absorption spectra in the presence of an external (DC) electric or magnetic field. The millimeter-wave techniques described in this chapter are capable of being extended to measure electric and magnetic moments of electronic and highly vibrationally excited states with Stark and Zeeman spectroscopy.

The chief advantage of making these measurements in the microwave/mm-wave regime lies in the inherently high resolution of the spectroscopic techniques used at

these frequencies. In order to measure the response of a system to a static external field (neglecting alternative strategies involving quantum beats), the field must be of sufficient intensity to shift or split an observed transition by an amount greater than the experimental resolution. In optical/ultraviolet experiments a typical resolution is 0.06 cm^{-1} ($\sim 2 \text{ GHz}$), determined by either the resolution of an etalon-narrowed pulsed dye laser or the residual Doppler-width (at 200 nm) of an unskimmed free-jet expansion. The observed lines in the spectra must be shifted by an amount larger than 2 GHz in order to extract a meaningful value for the electronic property sampled by the experiment. For a small molecule, with a typical dipole moment of 1 Debye, a Stark shift of several GHz will require an electric field of 10–100 kV/cm (see Ref. [49] for an example of a pulsed-laser optical Stark effect measurement), depending on whether the Stark effect is in a linear or quadratic regime. Maintaining such large fields is exceedingly problematic, and requires careful experimental design in order to prevent arcing and discharge. In contrast, the millimeter-wave experiments demonstrated in this chapter have typical linewidths on the order of 300 kHz, nearly 10^4 times smaller than those in pulsed optical experiments. Similar transitions will thus require fields on the order of $10^2 - 10^4$ times smaller than those required for optical Stark measurements, on the order of only 10-100 V/cm. The experimental tradeoff is that, in order to maintain a high resolution, the applied field must be very homogeneous as to not broaden the transitions. Relatively low field Stark measurements are common in FTMW spectroscopy, and several designs for electrodes to produce a homogenous field of large spatial extent exist in the literature [50]. It will be possible to adapt the strategies from the microwave region designs to our pulsed-jet millimeter-wave spectrometer, enabling the measurement of electronic properties of laser-excited states.

Chapter 3

Laboratory measurements of the hyperfine structure of $\text{H}^{14}\text{N}^{12}\text{C}$ and $\text{D}^{14}\text{N}^{12}\text{C}$

The work in this chapter resulted from a collaborative effort between myself and Dr. Hans A. Bechtel. The majority of the results in this chapter have been published in *Astrophysical Journal Letters* (Ref. [51]).

3.1 Introduction

In the analysis of the vibrational spectra of small organic molecules, the details of electronic structure are typically ignored. The simple reason for this is that the effects of the electronic structure (e.g. hyperfine splittings, electric dipole moments, etc.) in these molecules generally do not manifest themselves as observable splittings in a vibrational spectrum recorded at Doppler-limited resolution.¹ Such a situation is in stark contrast to that of radicals and transition-metal-containing molecules, the spectra of which are often littered with fine and hyperfine structure associated with

¹The electronic structure does, of course, determine the shape of the potential energy surface and, therefore, the frequencies of vibration.

unpaired or otherwise reactive electrons. The majority of stable organic molecules have a singlet Σ (in general totally symmetric) ground electronic state, i.e. $S = 0$, $\Lambda = 0$, and, as such, have no fine structure and exceedingly weak magnetic effects due to quenched electronic angular momentum. It is only at the level of nuclear quadrupolar hyperfine structure that the rovibronic levels of many small, stable molecules are split by interactions between the non-spherical charge distribution of some $I \neq 0$ nuclei and the anisotropic nature of the electric field at these nuclei.

Quadrupolar hyperfine splittings are rarely large enough to be directly observed in a Doppler-limited infrared or visible spectrum. However, by virtue of the relatively low frequencies used in rotational spectroscopy, even Doppler-limited spectra are often of sufficient resolution (< 1 MHz) to resolve hyperfine structure of many molecules. The spectra of one such molecule, hydrogen cyanide (HCN), is illustrated in Figure 3-1(a). The corresponding splitting in molecules with smaller hyperfine interactions may still remain unresolved, as is illustrated for the isomeric species hydrogen isocyanide (HNC) in Figure 3-1(b).² It is therefore often desirable to push the already high resolution of mm-wave spectroscopies into the sub-Doppler regime.

In this chapter, high-resolution (~ 50 kHz) is achieved by a spectrometer design in which the mm-waves are propagated coaxially with respect to the supersonic expansion. The enhanced resolution, relative to the conventional geometry described in Chapter 2, results from reduced contributions to the width from Doppler and transit-time broadening and enables resolution of the hyperfine structure of HNC, which is $\frac{1}{20}$ th the size of that in HCN.

²The reason for the qualitative difference between the spectra of these two isomeric species is discussed in the following chapter.

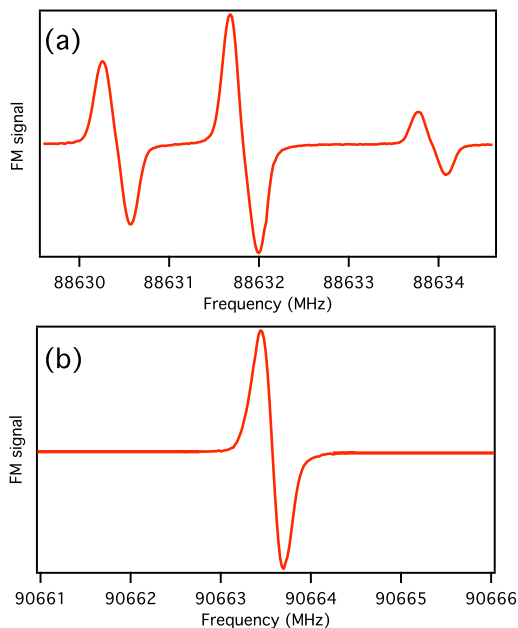


Figure 3-1: (a) $J = 1 - 0$ rotational transition of HCN, recorded with the spectrometer design described in Chapter 2. The transition is split into several components by the nuclear quadrupolar hyperfine interactions due to the ^{14}N nucleus. (b) The analogous structure in the $J = 1 - 0$ transition of HNC is not resolved in the conventional spectrometer geometry due to the much smaller splitting.

3.2 Origin of nuclear quadrupole hyperfine splitting

The distribution of charge in the nucleus of an atom may be non-spherical. It is quite reasonable, then, that the energy of the system will depend on the orientation of the nucleus relative to all of the extra-nuclear charges. While no nuclei have yet been observed to possess an electric dipole, all nuclei with nuclear spin $I \geq 1$ possess an electric quadrupole moment. A quadrupole moment represents a deviation from spherical shape by flattening or elongating the charge distribution preferentially along one axis.

Following Gordy & Cook[6], the classical electromagnetic interaction energy between the nuclear charge distribution, ρ_n , and the electric field at the nucleus, V , that results from extra-nuclear charges, is given by

$$E = \int \rho_n V d\tau_n. \quad (3.1)$$

Expansion of the field as a Taylor series about the center of charge results in the

quadrupole interaction energy

$$E_Q = \frac{1}{4} \left(\frac{\partial^2 V}{\partial z^2} \right)_0 \int \rho_n (3z_n^2 - r_n^2) d\tau_n. \quad (3.2)$$

For a given atom, the nuclear charge distribution is constant, so Eq. 3.2 is rewritten as

$$E_Q = \frac{1}{4} \left(\frac{\partial^2 V}{\partial z^2} \right)_0 eQ^*, \quad (3.3)$$

where the intrinsic quadrupole moment, Q^* , is taken as

$$Q^* = \frac{1}{e} \int \rho_n (3z_n^2 - r_n^2) d\tau_n. \quad (3.4)$$

While this quantity is constant for a given atom, it is variable across different isotopes of the same element. Nuclear charge distribution can vary both quantitatively and qualitatively, isotope to isotope. In fact, those elements for which the most abundant isotope has $I \geq 1$ (i.e. has a non-zero electric quadrupole moment), it is common that another stable isotope will exist with $I < 1$ (i.e. $Q^* = 0$). For the current study, the most important quadrupolar nucleus is ^{14}N , which has $I = 1$. The other stable isotope of nitrogen, ^{15}N , has $I = \frac{1}{2}$, and therefore will give rise to no quadrupole coupling in a spectrum.

In order to calculate the effects of the quadrupole on the energy levels of a molecule, the expression for the classical quadrupole energy must be expressed in a quantum mechanical form, and the rotation-dependence of the field gradient at the coupling nucleus must be taken into account. The resulting quantum mechanical Hamiltonian for the quadrupole, originally derived by Casimir [52], is

$$H_Q = \frac{(eQq_J)}{2I(2I-1)(2J-1)(2J+3)} \times [3(\mathbf{I} \cdot \mathbf{J})^2 + \frac{3}{2}(\mathbf{I} \cdot \mathbf{J}) - \mathbf{I}^2 \mathbf{J}^2] \quad (3.5)$$

where q_J depends on the form of the rotational wavefunction, and therefore on whether

the molecule is a linear, symmetric, or asymmetric top. Only linear molecules will be considered in this work, and for these

$$q_J = -\frac{qJ}{2J+3}. \quad (3.6)$$

From hyperfine-resolved measurements of rotational transitions, it is possible to derive a value for eQq and, therefore, the gradient of the electric field at the coupling nucleus, q . Because the electric field gradient is determined by the distribution of charged species, it reports on the electronic wavefunction of the molecule. The chemical interpretation of the field gradient is left for the following chapter.

3.3 Implications for astrochemistry

The 1971 discovery [53] of the U90.7 interstellar millimeter-wave emission line, which was later assigned to the $J = 1 - 0$ rotational transition of $\text{H}^{14}\text{N}^{12}\text{C}$ [54, 55, 56] (see Figure 3-1b), stimulated considerable interest in the astronomical community. Subsequent measurements of $[\text{HNC}]/[\text{HCN}]$ and $[\text{DNC}]/[\text{HNC}]$ abundance ratios have provided insights into the astrochemistry of dark clouds. In particular, measurements of the $[\text{HNC}]/[\text{HCN}]$ abundance ratio imply that the abundance of HNC in some regions is comparable to that of HCN [57, 58, 59, 60, 61, 62, 63], which is unexpected based on thermodynamics alone (HNC is 0.62 eV less stable than HCN). Those measurements suggest that the $\text{HCNH}^+ + e^-$ dissociative recombination reaction is a major source of HNC, although a decisive explanation for the relative overabundance of HNC remains to be established. The $[\text{DNC}]/[\text{HNC}]$ abundance ratio is also significant: in dark cloud cores, $[\text{DNC}]/[\text{HNC}]$ abundance ratios range from 0.008 to 0.122 [64, 65, 66, 67], which is considerably higher than the cosmic $[\text{D}]/[\text{H}]$ abundance ratio of about 10^{-5} [68]. Deuterium fractionation into various molecules has been shown to be sensitive to a variety of physical conditions, including temperature and the degree

of ionization.

Accurate measurements of abundance ratios require precise rest frequencies for observed transitions. Indeed, Turner [67] has shown that neglect of hyperfine structure can lead to significant errors in astronomical observations of abundance ratios. Although precise rest frequencies are typically obtained in the laboratory, laboratory measurements on the chemically unstable HNC molecule are challenging. In 1963, Milligan and Jacox [44] observed HNC in an argon matrix, but it was not until 1975 that Arrington and Ogryzlo [45] observed a laboratory gas phase spectrum. Since then, numerous groups have recorded microwave [69, 54, 55, 70, 71, 56, 72] and infrared spectra [73, 47, 74, 75, 46, 76] of HNC. The laboratory measurements, however, are not nearly as comprehensive as those for the more stable HCN isomer, and in none of them is the HNC hyperfine structure resolved.

3.4 Coaxial jet mm-wave spectrometer

These measurements are performed in a coaxial mm-wave pulsed discharge jet spectrometer, which provides better resolution than the conventional orthogonal geometry, described in Chapter 2, by minimizing Doppler and transit time broadening. A schematic of the spectrometer is given in Figure 3-2. The design is similar to that of Walker and McKellar[77] and McElmurry *et al.*[78] with the addition of a pulsed discharge nozzle, which extends the capabilities of the coaxial mm-wave jet spectrometer to rotationally cold transient species. An analogous spectrometer design is popular in the microwave region, referred to there as COBRA (coaxial beam-resonator arrangement)[79].

In our experiments, HNC (DNC) is generated with a mixture of 2% CH₃CN (CD₃CN) in Ne. The pulsed valve operates at 10 Hz with a backing pressure of 3 atm, a pulse duration of approximately 300 μ s, a negative discharge voltage of 1.5 kV,

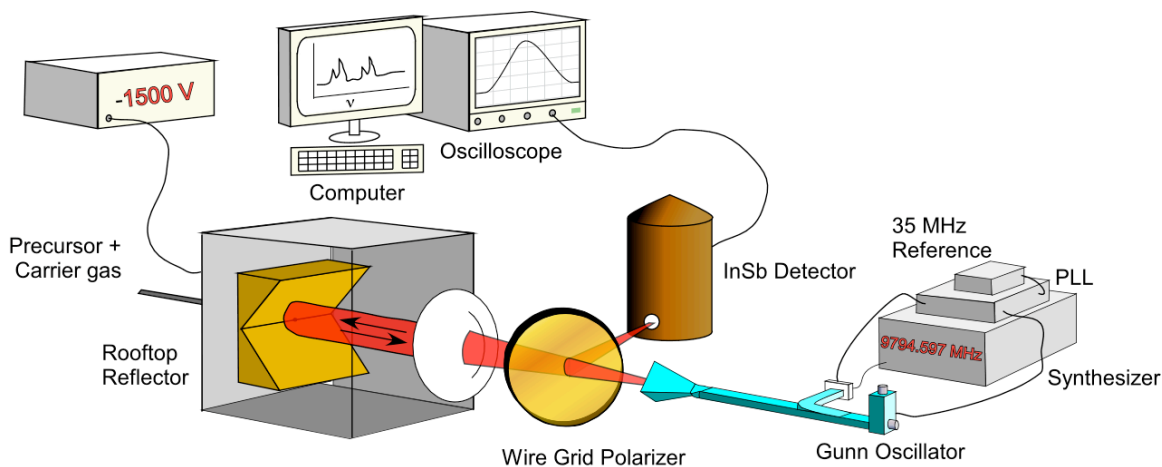


Figure 3-2: Schematic of the coaxial mm-wave jet spectrometer. The mm-wave radiation entering the chamber is polarized 45° relative to the vertical axis of the chamber. The returning polarization is rotated 90° by the rooftop reflector, causing it to be selectively routed to the bolometer for detection.

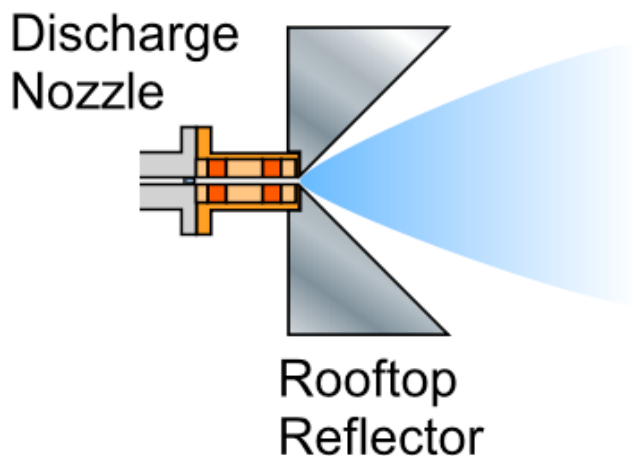


Figure 3-3: Side-on view of the rooftop reflector mounted onto the discharge nozzle.

and a discharge pulse length of $200 \mu\text{s}$ centered on the gas pulse. Shown in Figure 3-3, the discharge nozzle is mounted at the rear of an aluminum rooftop reflector that has a small hole ($\sim 4 \text{ mm}$ diameter) at the center to permit the passage of the molecular beam.

As in the experiments using the orthogonal geometry, the mm-wave radiation is produced by a W-band (72–106 GHz) Gunn oscillator that is phase-locked to the tenth harmonic of a microwave synthesizer (HP 8673E) and coupled through waveguide components to a calibrated attenuator (Hitachi W9513). Higher frequencies

are generated by doubling (144–212 GHz) and tripling (216–318 GHz) the output of the Gunn oscillator in Schottky diode multipliers (Virginia Diodes). The radiation is emitted into free space through a standard gain pyramidal horn and passed through a wire-grid polarizer oriented to pass the linearly polarized mm-wave radiation. A PTFE lens ($f = 30$ cm) is used to roughly collimate the mm-wave radiation, which is counterpropagated with the molecular beam and directed onto the rooftop reflector oriented at 45° with respect to the polarization of the mm-waves. The rooftop reflector rotates the mm-wave polarization by 90° and reflects the mm-wave radiation back onto itself, making a second pass of the vacuum chamber. The mm-wave radiation is focused by the PTFE lens, and finally reflected by the polarizer onto a liquid helium-cooled InSb hot electron bolometer. The bolometer output is digitized with a 500 MHz oscilloscope (Lecroy LC334A) and transferred to a computer for storage.

Unlike in the earlier experiments, it is necessary in the high-resolution case to scan the low-frequency phase-lock reference rather than the local oscillator to tune the frequency of the mm-wave source. The high-frequency synthesizer used as the LO has a (frequency-dependent) minimum step-size of 4 kHz, corresponding to a minimum Gunn oscillator step-size of 40 kHz (as the Gunn is typically locked to the 10th harmonic of the synthesizer), which is larger than the resolution of the experiment. Such undersampling is undesirable, so the high-resolution spectra are recorded by scanning the phase-lock loop reference (HP 3336B) in 2 kHz steps around a center frequency of 35 MHz. In addition, spectra recorded at the powers used in the conventional spectrometer geometry appear to be power broadened. The attenuation is increased by an additional 10 dB to a power of $\sim 50\mu\text{W}$, at which point the spectra do not get narrower with further attenuation.

The coaxial geometry of the mm-wave radiation and the molecular beam results in two Doppler-split peaks, the frequencies of which are averaged to determine the rest frequency. The separation of the peaks (~ 540 kHz at 90 GHz) indicates that

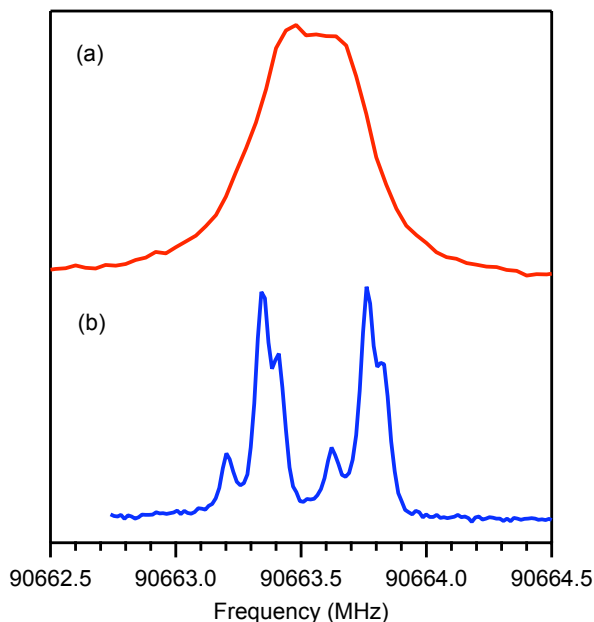


Figure 3-4: Comparison of (a) orthogonal (*upper trace*) and (b) coaxial (*lower trace*) spectrometer geometries for the $J = 1 - 0$ transition of HNC. The resolution of the spectra recorded in the coaxial geometry is superior by one order of magnitude, revealing nuclear quadrupolar hyperfine structure due to the ^{14}N nucleus.

the molecular beam speed is about 890 m/s for a beam composed primarily of neon. The lighter gas neon is used here, rather than argon, in order to create a large enough separation such that the hyperfine components of the associated with co- and counterpropagating molecules do not overlap.³

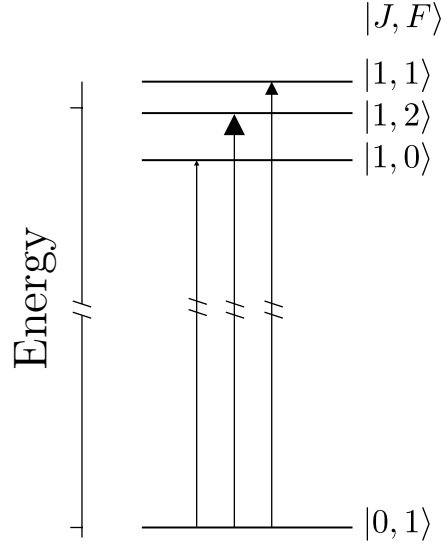
The spectrometer was calibrated by measuring several rotational transitions of OCS and HCN [28]. The uncertainty in the absolute frequencies for the measured transitions is ± 5 kHz for the $J = 1 - 0$ transitions and ± 10 kHz for the $J = 2 - 1$ and $J = 3 - 2$ transitions, whereas the uncertainty of the hyperfine splitting in a single rotational transition is ± 2 kHz.

3.5 Analysis of the hyperfine-resolved spectra

The hyperfine structure in $\text{H}^{14}\text{N}^{12}\text{C}$ is dominated by the interaction of the valence shell electrons with the electric quadrupole moment of the ^{14}N ($I_{\text{N}}=1$) nucleus. Although generally much smaller, the nuclear spin-rotation interaction, which is caused

³Using helium as the carrier gas for the expansion would again increase the separation, but we find that helium creates a very poor and unstable discharge at the voltages used.

Figure 3-5: Energy-level diagram for the $J = 1 - 0$ rotational transition of a molecule with a single quadrupolar nucleus with $I = 1$. The energetic ordering of the $|J, F\rangle$ levels is appropriate for a molecule with a positive value for eQq , as is the case for HNC. The size of the arrowheads is proportional to the transition intensity. The ticks on the vertical axis represent the quadrupole-free energies for $J = 0$ and 1.



by the interaction of rotating charged particles (electrons and nuclei) with the magnetic moment of the ^{14}N atom, also contributes to the hyperfine structure. These interactions cause the lowest rotational transition $J = 1 - 0$ of $\text{H}^{14}\text{N}^{12}\text{C}$ to be split into three components and the higher rotational transitions to be split into six components. An energy level diagram is given in Figure 3-5.

The hyperfine structure of $\text{D}^{14}\text{N}^{12}\text{C}$, on the other hand, is substantially more complicated because of the additional coupling of the D ($I_{\text{D}}=1$) nucleus. This coupling gives rise to a septet in the $J = 1 - 0$ transition and over 40 incompletely resolved lines in the higher J rotational transitions. The Hamiltonian for the hyperfine structure of $\text{D}^{14}\text{N}^{12}\text{C}$ is

$$\begin{aligned}
 H_{hfs} = & \frac{(eQq)_{\text{N}}}{2I_{\text{N}}(2I_{\text{N}} - 1)(2J - 1)(2J + 3)} \\
 & \times [3(\mathbf{I}_{\text{N}} \cdot \mathbf{J})^2 + (3/2)(\mathbf{I}_{\text{N}} \cdot \mathbf{J}) - \mathbf{I}_{\text{N}}^2 \mathbf{J}^2] + C_{\text{N}}(\mathbf{I}_{\text{N}} \cdot \mathbf{J}) \\
 & + \frac{(eQq)_{\text{D}}}{2I_{\text{D}}(2I_{\text{D}} - 1)(2J - 1)(2J + 3)} \\
 & \times [3(\mathbf{I}_{\text{D}} \cdot \mathbf{J})^2 + (3/2)(\mathbf{I}_{\text{D}} \cdot \mathbf{J}) - \mathbf{I}_{\text{D}}^2 \mathbf{J}^2] + C_{\text{D}}(\mathbf{I}_{\text{D}} \cdot \mathbf{J}),
 \end{aligned} \tag{3.7}$$

where $(eQq)_{\text{N}}$ and $(eQq)_{\text{D}}$ are the nuclear quadrupole coupling constants and C_{N}

and C_D are the spin-rotation constants of nitrogen and deuterium, respectively. Although analytical expressions for hyperfine energy levels are well known for molecules containing a single coupling ($I \geq 1$) nucleus [6], such as $\text{H}^{14}\text{N}^{12}\text{C}$, the full secular determinant must be solved for molecules containing multiple $I \geq 1$ nuclei, particularly when the values of the quadrupole coupling constants are comparable in magnitude, as in $\text{D}^{14}\text{N}^{12}\text{C}$ [80, 81]. Here, we have used the SPFIT program [82] to perform a global fit of the rotational transitions of $\text{H}^{14}\text{N}^{12}\text{C}$ and $\text{D}^{14}\text{N}^{12}\text{C}$. In this global fit, we used the data obtained from the present work, which includes resolved and partially resolved hyperfine lines up to 275 GHz. For the $\text{H}^{14}\text{N}^{12}\text{C}$ rotational transitions above 275 GHz, we used the hyperfine free data of Okabayashi and Tanimoto[70] for the $J = 4 - 3$ transition, the data of Amano and Zellinger[69] for the $J = 7 - 6$ transition, and the data of Thorwirth *et al.*[72] for the $J = 5 - 4$, $J = 6 - 5$, $J = 8 - 7$, $J = 9 - 8$, $J = 10 - 9$, and $J = 22 - 21$ transitions. For the $\text{D}^{14}\text{N}^{12}\text{C}$ transitions above 275 GHz, we used the data of Brünken *et al.*[83]. The experimental transition frequencies from the present work are shown in Tables 3.1 and 3.2, and the derived spectroscopic constants are shown in Tables 3.3 and 3.4 along with previously published values. In analogy to the hyperfine assignments of $\text{D}^{12}\text{C}^{14}\text{N}$ [84], we have used the sequential spin-coupling scheme to label the $\text{D}^{14}\text{N}^{12}\text{C}$ transitions:

$$\mathbf{J} + \mathbf{I}_N = \mathbf{F}_N \quad (3.8)$$

$$\mathbf{F}_N + \mathbf{I}_D = \mathbf{F}. \quad (3.9)$$

The experimental data were not sufficient to accurately determine C_D . Previous measurements of C_D in $\text{D}^{12}\text{C}^{14}\text{N}$ [84] have shown that it is small (-0.6 ± 0.3 kHz), and we do not expect it to change significantly in $\text{D}^{14}\text{N}^{12}\text{C}$. As a consequence, we have omitted it from the fit. The omission of C_D did not affect the quality of the fit.

Figure 3-6a shows the experimental mm-wave spectrum of $\text{H}^{14}\text{N}^{12}\text{C}$ ($J = 1 - 0$)

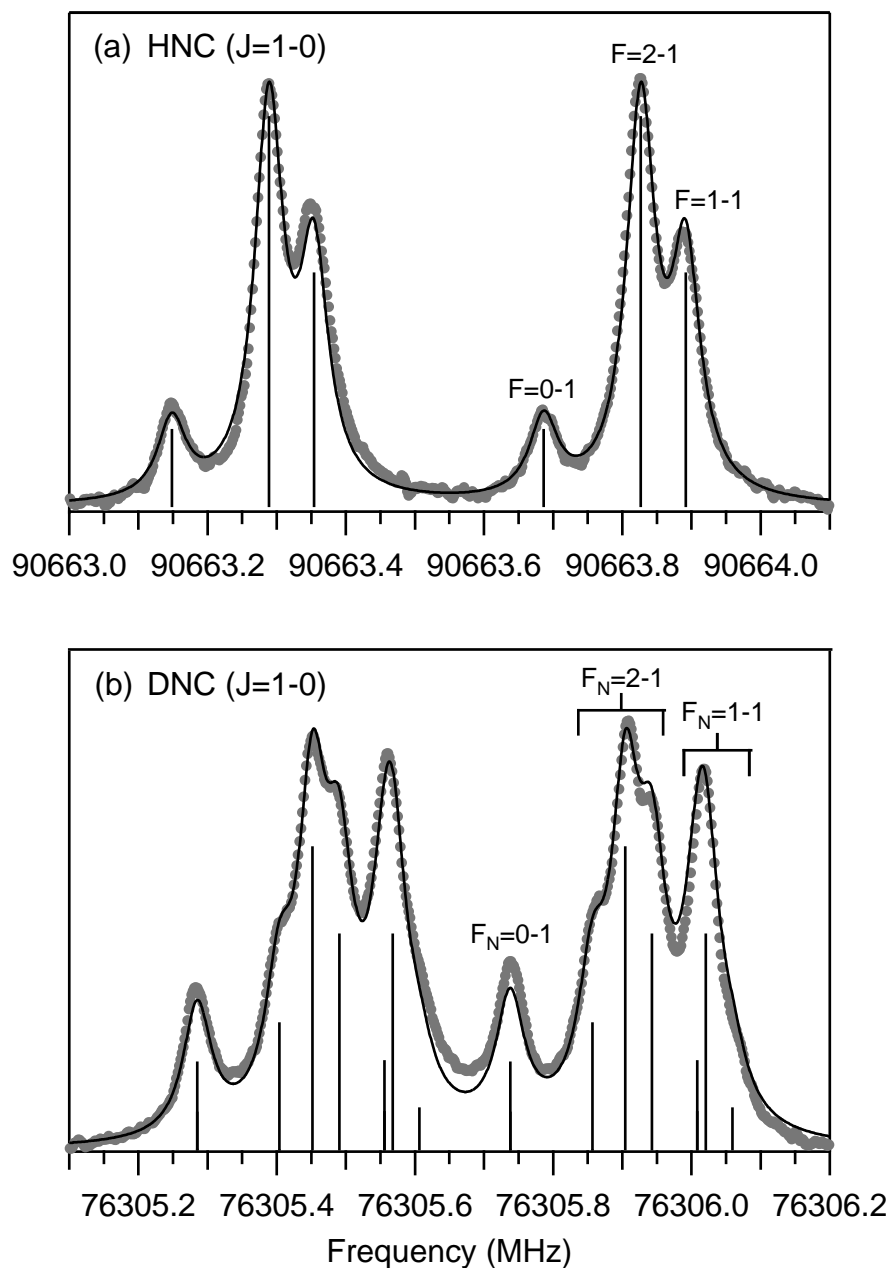


Figure 3-6: (a) $\text{H}^{14}\text{N}^{12}\text{C}$ ($J = 1-0$) and (b) $\text{D}^{14}\text{N}^{12}\text{C}$ ($J = 1-0$) experimental spectra (*circles*). The coaxial geometry results in two Doppler-split peaks, the frequencies of which are averaged to determine the rest frequency. The stick spectrum and simulation (*solid line*) are based on the molecular constants determined from the fit, assuming Lorentzian line shapes of 50 kHz and a molecular beam speed of 890 m/s.

Table 3.1: Transition frequencies of H¹⁴N¹²C.

$J' - J''$	$F' - F''$	Obs.	Obs.-Calc.
1 - 0	0 - 1	90663.417	0.000
	2 - 1	90663.556	-0.002
	1 - 1	90663.622	-0.001
2 - 1	1 - 1	181324.585	-0.001
	2 - 1	181324.729*	-0.005
	3 - 2	181324.729*	-0.005
	1 - 0	181324.792*	-0.002
	2 - 2	181324.792*	-0.002
3 - 2	3 - 2	271981.111*	-0.003
	4 - 3	271981.111*	-0.003
	2 - 1	271981.111*	-0.003

*Unresolved feature

and a simulation based on the molecular constants determined from the fit. Positive and negative Doppler shifts, corresponding to a molecular beam speed of 890 m/s, are added to the calculated line positions, and the doubled lines are convoluted with a Lorentzian lineshape of 50 kHz width. The experimental resolution is sufficient to resolve all three hyperfine components in the H¹⁴N¹²C ($J = 1 - 0$) rotational transition. However, the hyperfine transitions of the $J = 2 - 1$ and $J = 3 - 2$ rotational transitions, shown in Figure 3-7, are not fully resolved. This failure to resolve fully all of the hyperfine components is due in part to the decreased separation between hyperfine lines in higher rotational levels and the presence of six lines rather than three. The primary reason, however, is the degradation of experimental resolution caused by the linear frequency dependence of the Doppler linewidth. Thus, at 90 GHz, the experimental lineshapes are nearly Lorentzian with linewidths of about 50 kHz, whereas at 180 GHz and 270 GHz, the lineshapes are predominantly Gaussian with linewidths of about 100 kHz and about 180 kHz, respectively (see Figure 3-7).

The experimental mm-wave spectrum of D¹⁴N¹²C ($J = 1 - 0$) and the corresponding simulation is shown in Figure 3-6b. As noted above, the nuclear spin of deuterium

causes additional splitting, resulting in seven lines instead of three for the $J = 1 - 0$ rotational transition. Although the experimental resolution is not sufficient to fully resolve all members of the $F_N = 1 - 1$ triplet, the remaining lines can be distinguished. For the $J = 2 - 1$ and $J = 3 - 2$ transitions, the increased Doppler broadening at higher frequencies conceals all deuterium splitting effects and the profiles of the higher rotational transitions are similar to those of $\text{H}^{14}\text{N}^{12}\text{C}$.

Table 3.2: Transition frequencies of $\text{D}^{14}\text{N}^{12}\text{C}$.

$J' - J''$	$F'_N - F''_N$	$F' - F''$	Obs.	Obs.-Calc.
1 - 0	0 - 1	1 - 0, 1, 2	76305.511	0.000
	2 - 1	1 - 0, 1, 2	76305.630	0.000
	2 - 1	3 - 2	76305.678	0.001
	2 - 1	2 - 1, 2	76305.717	0.000
	1 - 1	1 - 0, 1, 2	76305.790*	-0.002
	1 - 1	2 - 1, 2	76305.790*	-0.002
	1 - 1	0 - 1	76305.836	0.002
2 - 1	1 - 1	2 - 2	152609.569*	0.005
	1 - 1	2 - 1	152609.569*	0.005
	1 - 1	1 - 2	152609.569*	0.005
	1 - 1	1 - 1	152609.569*	0.005
	2 - 1	3 - 2	152609.746*	-0.002
	3 - 2	4 - 3	152609.746*	-0.002
	3 - 2	2 - 1	152609.746*	-0.002
	3 - 2	3 - 2	152609.746*	-0.002
	2 - 1	2 - 2	152609.746*	-0.002
	2 - 1	2 - 1	152609.746*	-0.002
	1 - 0	1 - 1	152609.845*	-0.003
	2 - 2	3 - 3	152609.845*	-0.003
	1 - 0	1 - 1	152609.845*	-0.003
	2 - 2	1 - 1	152609.845*	-0.003
3 - 2	3 - 2	2 - 1	228910.481*	0.001
	3 - 2	4 - 3	228910.481*	0.001
	4 - 3	5 - 4	228910.481*	0.001
	4 - 3	3 - 2	228910.481*	0.001
	4 - 3	4 - 3	228910.481*	0.001
	3 - 2	3 - 2	228910.481*	0.001
	2 - 1	3 - 2	228910.481*	0.001

*Unresolved feature

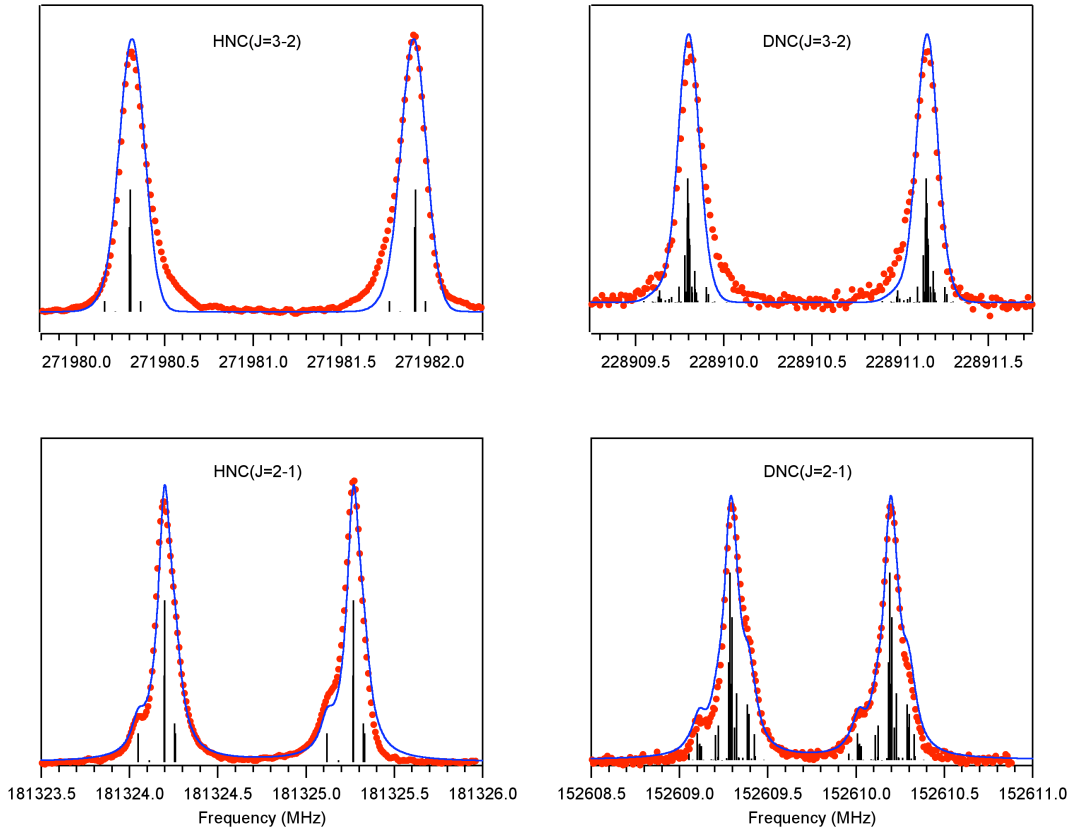


Figure 3-7: Higher- J rotational transitions for HNC (*left*) and DNC (*right*). The spectra shown here have twice the frequency width as those shown in Figure 3-6. As a consequence of the linear dependence of the Doppler effect on frequency, the splitting between the peaks due to the co- and counter-propagating components of the mm-wave beam increases from the lower- J to higher- J transitions. Additionally, the Doppler width of each hyperfine component increases, while the intensity distribution associated with the hyperfine structure becomes more compressed. Therefore, the determination of the hyperfine parameters is best made at the lowest possible value of J .

3.6 Comparison of laboratory and astronomical measurements of hyperfine coupling constants

The nuclear quadrupole constant of $\text{H}^{14}\text{N}^{12}\text{C}$ ($v = 0$), as measured in this work, is $(eQq)_{\text{N}} = 264.5 \pm 4.6$ kHz. It has the opposite sign and is considerably smaller than the nuclear quadrupole constant of the more stable $\text{H}^{12}\text{C}^{14}\text{N}$ isomer ($v = 0$), $(eQq)_{\text{N}} = -4709.03 \pm 1.62$ kHz [85]. The small value of $(eQq)_{\text{N}}$ for $\text{H}^{14}\text{N}^{12}\text{C}$ arises from the decreased electric field gradient at the central ^{14}N nucleus and is typical of other isonitriles, such as CH_3NC and HCCNC , which have nuclear quadrupole constants of 489.4 ± 0.4 kHz [86] and 946.4 ± 1.9 kHz [87], respectively. Recent *ab initio* calculations [88] on $\text{H}^{14}\text{N}^{12}\text{C}$ also predict a small nuclear quadrupole coupling constant, $-313 \geq (eQq)_{\text{N}} \geq -288$ kHz, but of the wrong sign.

Table 3.3: Molecular constants of $\text{H}^{14}\text{N}^{12}\text{C}$ for the ground vibrational state.

Parameter	$\text{H}^{14}\text{N}^{12}\text{C}$	$\text{H}^{14}\text{N}^{12}\text{C}$	$\text{H}^{14}\text{N}^{13}\text{C}$
	Present Work	Hyperfine Free	(Ref. [67])
B (MHz)	45331.98160(52)	45331.98415(79)	-
D (kHz)	99.8097(45)	99.8286(63)	-
H (Hz)	0.1458(57)	0.1682(78)	-
$(eQq)_{\text{N}}$ (kHz)	264.5(46)	-	276(21)
C_{N} (kHz)	7.15(109)	-	10.5(43)

Values in parentheses represent one standard deviation (1σ) in the units of the last digit. The uncertainties produced by the SPFIT program were converted to standard errors using the PFORM program from <http://info.ifpan.edu.pl/~kiesel/prospe.htm>.

Although the hyperfine structure of $\text{H}^{14}\text{N}^{12}\text{C}$ has not until now been resolved in the laboratory, partially resolved hyperfine structure has been observed in millimeter emission measurements of $\text{H}^{14}\text{N}^{12}\text{C}$ in interstellar dark clouds. Snyder *et al.*[89] first estimated the quadrupole coupling constant of $\text{H}^{14}\text{N}^{12}\text{C}$ from those observations, but self-absorption [90] of the strongest component, $F = 2 - 1$, led to incorrect assignments of the hyperfine structure and a quadrupole coupling constant with the wrong

Table 3.4: Molecular constants of D¹⁴N¹²C for the ground vibrational state.

Parameter	D ¹⁴ N ¹² C	D ¹⁴ N ¹² C	D ¹⁴ N ¹² C
	Present Work	Ref. [83]	(Ref. [67])
B (MHz)	38152.98807(36)	38152.98692(156)	-
D (kHz)	68.97119(281)	68.9649(87)	-
H (Hz)	0.1984(37)	0.1925(82)	-
$(eQq)_N$ (kHz)	294.7(131)	-	378.7(260)
C_N (kHz)	5.02(99)	-	-
$(eQq)_D$ (kHz)	261.9(145)	-	111(154)

Values in parentheses represent one standard deviation (1σ) in the units of the last digit. The uncertainties produced by the SPFIT program were converted to standard errors using the PFORM program from <http://info.ifpan.edu.pl/~kiesel/prospe.htm>.

sign. Later, Frerking *et al.*[91] gave improved estimates of the hyperfine transition frequencies and the nuclear quadrupole constant of H¹⁴N¹²C and H¹⁴N¹³C. Those estimates have been updated by the more recent measurements of Turner[67], which are shown in Table 3.3. Although the H¹⁴N¹³C astronomical value for $(eQq)_N$ is in good agreement with our laboratory measurements, the D¹⁴N¹²C astronomical values for both $(eQq)_N$ and $(eQq)_D$ are not (Table 3.4). The discrepancy is most likely a consequence of insufficient resolution in the astronomical spectra, which prevents an accurate determination of the nuclear quadrupole constants.

Also shown in Tables 3.3 and 3.4 are the H¹⁴N¹²C and D¹⁴N¹²C molecular constants determined from the most precise hyperfine-free data in the literature. A comparison of the B , D , and H rotational constants indicate that the D¹⁴N¹²C constants from the present work agree within 1σ with the values obtained by Brünken *et al.*[83]. The rotational constants of H¹⁴N¹²C, however, lie just outside of the 1σ ranges of the fit to the hyperfine free data set. The discrepancy arises primarily from the difference between our value of the $J = 3 - 2$ rotational transition and that of Okabayashi and Tanimoto[70], as well as the increased weighting of the lower rotational transitions in the fit that reflect the reduced uncertainty in our measurements.

The improved resolution of the coaxial mm-wave discharge jet spectrometer has

permitted the hyperfine structure of $\text{H}^{14}\text{N}^{12}\text{C}$ and $\text{D}^{14}\text{N}^{12}\text{C}$ to be resolved for the first time in the laboratory. The updated rest frequencies should aid astronomical measurements of $[\text{HCN}]/[\text{HNC}]$ and $[\text{DNC}]/[\text{HNC}]$ abundance ratios, particularly when the observed hyperfine structure is incompletely resolved or is distorted by self-absorption.

Measurement of the nuclear quadrupole hyperfine structure provides a direct measurement of the electronic structure in the vicinity of the coupling nucleus. The chemical interpretation of the field gradient provides insight into local bonding and hybridization that is complementary to that offered by measurement of the molecular electric dipole moment. Such interpretation is provided in the following chapter.

Chapter 4

Evolution of electronic structure during $\text{HCN} \leftrightarrow \text{HNC}$ isomerization revealed through nuclear quadrupole hyperfine structure

The work in this chapter resulted from a collaborative effort between myself and Dr. Hans A. Bechtel, with *ab initio* calculations performed by Bryan Wong. The majority of the results in this chapter have been published in *Angewandte Chemie International Edition* (Ref. [92]), with the exception of the stretch-excited spectrum in section 4.6.

4.1 Introduction

The making and breaking of bonds in chemical reactions necessarily involve changes in electronic structure. Therefore, measurements of a carefully chosen electronic property can serve as a marker of progress along a reaction coordinate and provide detailed mechanistic information about the reaction. In this chapter, we demonstrate through high-resolution spectroscopic measurements and *ab initio* calculations that nuclear

quadrupole hyperfine structure, an indicator of electronic structure near the nitrogen nucleus, is highly sensitive to the extent of bending excitation in the prototypical $\text{HCN} \leftrightarrow \text{HNC}$ isomerization system. Thus, measurements of hyperfine structure show how the nature of a chemical bond is altered when a large amplitude vibration that is coupled to the isomerization reaction coordinate is excited.

As described in the previous chapter, nuclear quadrupole hyperfine structure arises from the interaction of the electric quadrupole moment of a nucleus with the gradient of the electric field at that nucleus. This interaction causes rotational levels to split into multiple hyperfine components. The magnitude of the splitting is determined by eQq , in which e is the proton charge, Q is the quadrupole moment of the nucleus, and q is the gradient of the electric field ($\partial^2 V / \partial z^2$) at the nucleus. The electric quadrupole moment, Q , is a measure of the departure of the nuclear charge distribution from spherical symmetry and is nonzero for $I \geq 1$ nuclear spins. Although Q is constant for a particular nucleus, q can (and generally does) vary in different molecules. These values of q , and hence eQq , report on the local electronic environment of the nucleus, in contrast to Stark effect measurements of the electric dipole moment [1], which report on the global electron distribution within the molecule.

The $\text{HCN} \leftrightarrow \text{HNC}$ isomerization is a prototypical system for high-barrier, bond-breaking isomerization, a process fundamental to many areas of chemistry, including combustion. As described in the previous chapter, the hyperfine structure of HCN and HNC are qualitatively different, reflecting the different electronic environments of the nitrogen atom in the two isomeric structures. Therefore, the evolution of the hyperfine structure as the molecule is excited along the isomerization coordinate should reveal how the bonding motif in the vicinity of the nitrogen changes during the chemical transformation. In this chapter, we present the first laboratory measurements of HNC hyperfine structure in vibrationally excited states and extend the measurements of HCN hyperfine structure to higher vibrational levels.

4.2 Experimental: Photolysis-jet spectrometer

The goal of the experiments described in the current chapter is to record pure rotational spectra of highly vibrationally excited states of the HCN/HNC system. It is therefore necessary to produce a molecular sample that is characterized simultaneously by a high vibrational temperature and a low rotational temperature. The low rotational temperature is crucial for the sensitivity of the millimeter-wave absorption experiment, which has a $\frac{1}{T^2}$ dependence [93]. One possible method of accessing highly vibrationally excited states is direct optical pumping, as described in Chapter 2. Optical pumping gives rise to an inherently non-thermal rotational distribution if the transitions used are rotationally resolved. That is, all of the population is put into a single rotational level, so the population difference, ΔN_{ab} , a factor in the transition intensity, is equal to the number of molecules in the pumped state, N_a .

Single-photon optical pumping methods for populating highly vibrationally excited levels are, however, limited by the exceedingly weak absorption cross-sections for all vibrations apart from the overtones of X-H stretching modes. Multiple-resonance optical techniques, such as stimulated emission pumping (SEP)[94, 95], can bypass the restrictive vibrational selection rules by exploiting significant changes in molecular geometry upon electronic excitation. These methods require a well-characterized excited electronic state to use as a multiple-resonance intermediate. Despite attempts by several research groups [96], including our own, no bound vibrational levels of any electronically excited states of HNC have been definitively identified. Therefore, optical pumping strategies may prove useful for accessing highly vibrationally excited states of HCN but cannot universally access the relevant states of the HCN/HNC system.

Alternative strategies for the production of vibrationally excited HCN/HNC include discharge, pyrolysis, and photolysis. Of these, the pulsed discharge is the easiest to implement and has, as described in Chapter 3, proven to be a reliable source of

ground-state HNC. Although it is possible to generate vibrationally excited states in a pulsed-discharge coupled to a supersonic expansion [40], very little vibrational excitation of the HCN/HNC products is observed in our apparatus. In laser photolysis, an ultraviolet photon excites a molecule into a dissociative state. The partitioning of excess energy among rotational, vibrational, and translational degrees of freedom in the photoproducts depends upon the details of the dissociation mechanism. Despite some controversy over the mechanism [97], we find that photolysis of acrylonitrile (vinyl cyanide, CH_2CHCN) at 193 nm (the wavelength of the ArF excimer emission) is effective at producing observable quantities of HCN and HNC, highly excited in the bending mode.¹

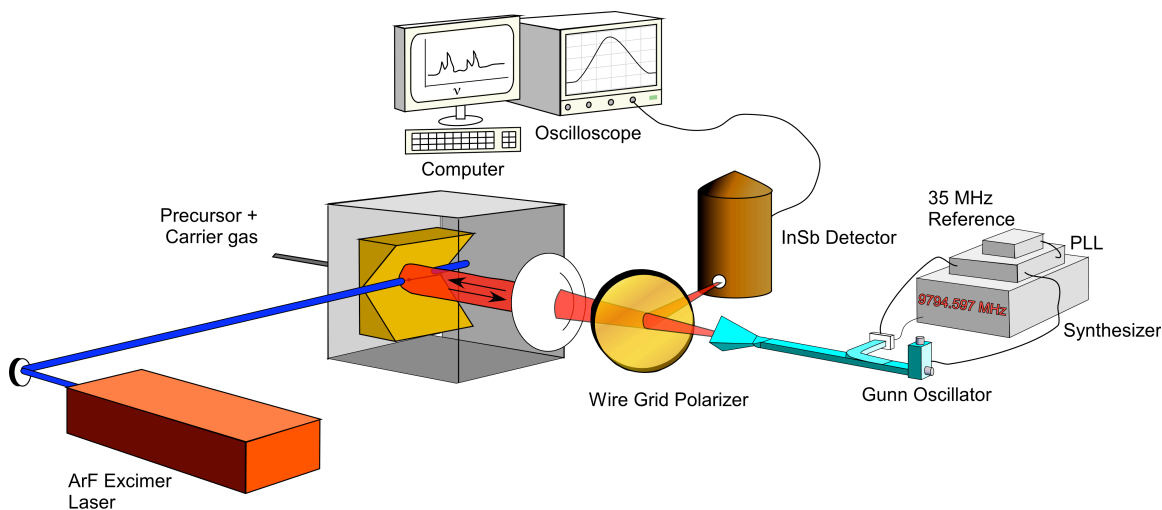


Figure 4-1: Schematic of the laser-photolysis millimeter-wave spectrometer.

The absorption measurements are performed in the coaxial mm-wave jet spectrometer described in the previous chapter. The modifications made to the spectrometer to incorporate a photolysis laser are depicted in Figure 4-1. The photolysis beam is routed along the notch in the rooftop reflector so as to cause the precursor molecule to fragment while it is still in the region of the jet expansion where there are sufficient collisions with the inert atoms of the gas mixture to cause significant rotational

¹Experiments monitoring the intensity of HCN and HNC signals as a function of excimer laser intensity indicate that the species studied here are likely due to multiphoton dissociation processes.

cooling. Under typical experimental conditions, the measured intensity ratios of the several observed transitions ($J = 1 - 0$, $2 - 1$, and $3 - 2$) indicate a cooled rotational temperature of ~ 5 K for both HCN and HNC.

The cooling dynamics are relevant to the data acquisition in the coaxial spectrometer geometry because the mm-waves are spatially overlapped with the complete expansion including the photolysis region. The recorded transients for photolysis-produced HCN (00^0_0), as a function of mm-wave frequency, are plotted in Figure 4-2. Directly after the photolysis pulse, the absorption signals are relatively broad in frequency, on the order of those observed in the orthogonal spectrometer geometry (see Figure 3-4). While the HCN photoproduct is still spatially localized in the region of the rooftop reflector, the molecules interact with the portion of millimeter-wave field passing between the two walls of the rooftop reflector. Spectra time-gated to detect only this absorption do not benefit from the narrowing associated with the coaxial geometry.

Additionally, the photolysis products may have large translational velocities that are not initially directed along the axis of the jet expansion but, instead, are relatively isotropic as they would be in a static cell. It is only after experiencing sufficient collisions with the buffer gas that the photoproducts become fully entrained in the expansion and become transitionally cold enough to give spectra with the highest resolution. This is evident in the bowing of the absorption transients of each of the three hyperfine components displayed in Figure 4-2. The initial isotropic distribution of velocities gives rise to broad Doppler profile. As the photoproducts experience collisions, their velocity in the laboratory frame increases and becomes highly directed along the beam axis. The experimental consequence is that the splitting between the two Doppler components becomes larger. After further collisions, the translational temperature, the velocity distribution of the molecules in the moving frame of the molecular beam, decreases and the frequency width of each of the Doppler components

narrows. As a consequence, the desired portion of the signal can only be collected once the asymptotic velocity has been reached. If the spectra are integrated over the full v-shaped time-evolution of the signal shown in Figure 4-2, the Doppler-split peaks are skewed towards each other, and there is an intense and broad ‘zero-velocity’ peak that obscures much of the hyperfine structure. In practice, the best, i.e. translationally coldest, portion of the signal is selected by adjusting the gate to later times in order to observe the broadest Doppler splitting and the narrowest absorption features.

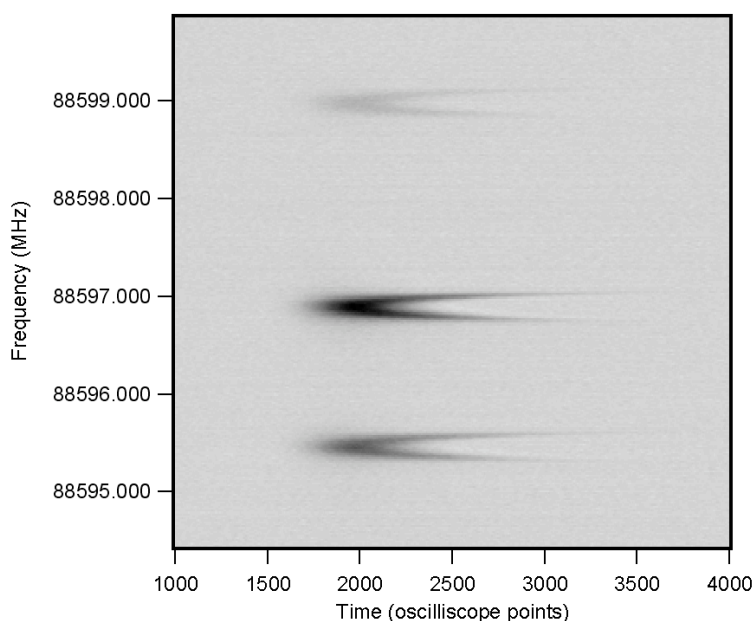


Figure 4-2: Time dependence of hyperfine-resolved absorption signals of photolysis-generated HCN (00^0_0), $J = 1 - 0$. The color scale reflects the bolometer output signal: darker color reflects larger absorption signals. As the photolysis products become entrained in the supersonic expansion, the detected absorption transition frequency shifts and narrows. The time-dependence of each hyperfine component of the absorption is equivalent.

For the spectra described in this chapter, vibrationally excited HCN and HNC are generated either by an electric discharge of a 2% acetonitrile/Ar mixture (for the ground vibrational states and lowest few vibrational states) or by 193 nm photolysis of a 2% acrylonitrile/Ar mixture (for the higher vibrational states). Methyl azide (CH_3N_3) was also tested as a photolysis precursor and was found to produce significant

quantities of HNC, however this route was discarded due to safety concerns associated with its synthesis and handling. Excimer laser powers for the photolysis experiments were in the range of 60–90 mJ/pulse.

4.3 Mm-wave spectroscopy of bend-excited HCN and HNC

In HC^{14}N and H^{14}NC , the only nucleus with a nonzero quadrupole moment, Q , is ^{14}N . The interaction of the nuclear spin ($I_{\text{N}} = 1$) with the rotational angular momentum (\mathbf{J}) causes the $J = 1 - 0$ rotational transition for both HC^{14}N and H^{14}NC to split into three lines that are labeled according to the total angular momentum $\mathbf{F} = \mathbf{I} + \mathbf{J}$ and have an intensity ratio of 3:5:1. Figure 4-3 shows the $J = 1 - 0$ rotational absorption spectrum of several bend-excited levels of HC^{14}N and H^{14}NC .

As shown in Figure 4-3, the hyperfine structure patterns of HCN and HNC are qualitatively different. First, the sign of the splitting for the ground vibrational level (00^0_0) of HNC is reversed with respect to that of HCN: the weak HNC $F = 0 - 1$ component is on the low frequency side of the strong $F = 2 - 1$ component rather than on the high frequency side, as in HCN. Second, the magnitude of the splitting is an order of magnitude smaller for HNC than for HCN. Indeed, the hyperfine structure of HNC cannot be resolved under normal Doppler-broadened conditions (Chapter 3). Finally, bending excitation in HCN increases the splitting of the hyperfine components, whereas bending excitation in HNC causes the splitting to decrease initially in magnitude and to reverse sign.

The observed transition frequencies are recorded in Table 4.1. As in Chapter 3, the line positions are fitted to a hyperfine Hamiltonian of the form given in Eq. 3.7, including the spin-rotation interaction. Higher rotational levels are not uniformly recorded, so the rotational constants are not determined. Instead the “hyperfine-

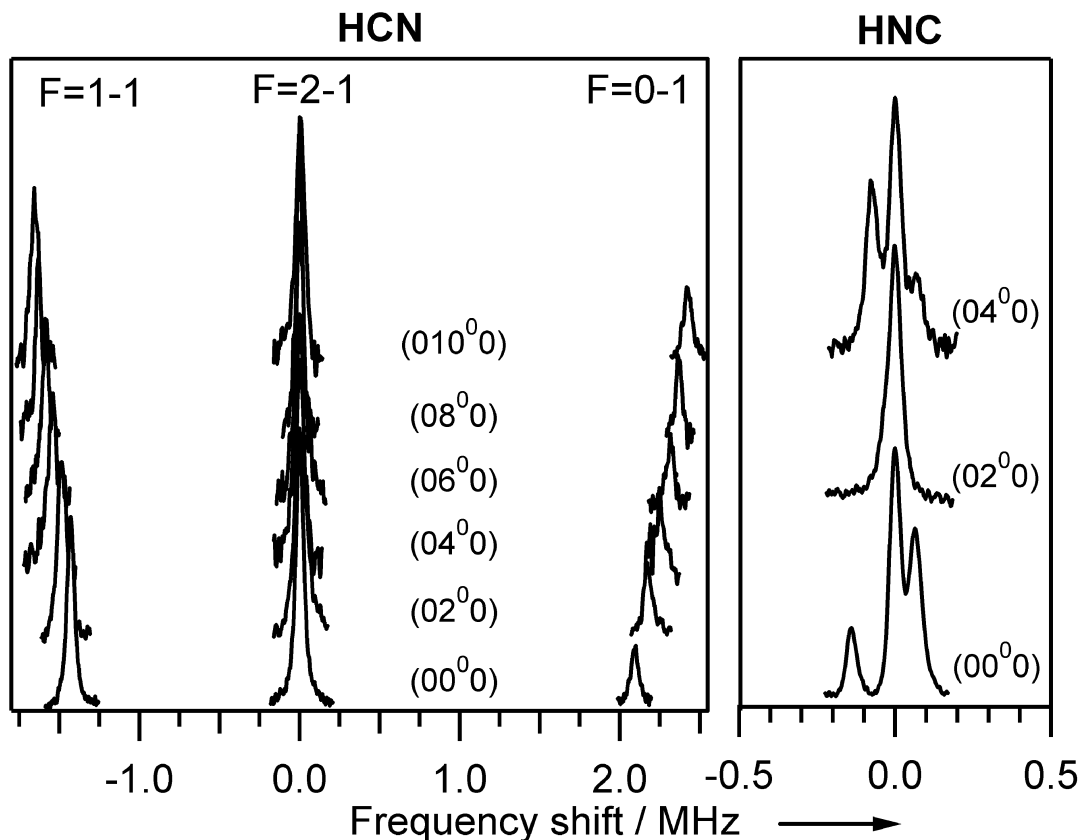


Figure 4-3: Millimeter-wave rotational spectra ($J = 1 - 0$) of several bend-excited, $(0v_2^\ell 0)$ vibrational levels of HCN and HNC, where v_2 is the number of quanta in the bending vibrational mode and ℓ is the vibrational angular momentum. Only one member of each pair of Doppler-split peaks is shown. The frequencies have been shifted such that the $F = 2 - 1$ components are aligned at zero frequency shift.

free” value for the $J = 1 - 0$ transition is determined by the fit. The fit results for the observed vibrational levels are listed in Table 4.2.

Table 4.1: Hyperfine-resolved $J = 1 - 0$ transition frequencies (in MHz) of ground-state and bend-excited $\text{H}^{12}\text{C}^{14}\text{N}$, $\text{H}^{14}\text{N}^{12}\text{C}$, and $\text{D}^{15}\text{N}^{12}\text{C}$.

	Vibrational level	$F' - F'' = 1 - 1$	$F' - F'' = 2 - 1$	$F' - F'' = 0 - 1$
$\text{H}^{14}\text{N}^{12}\text{C}$	(00 ⁰ 0)	90663.622(3)	90663.556(3)	90663.417(3)
	(02 ⁰ 0)	91341.926(3) ^a	91341.911(3) ^a	91341.883(3) ^a
	(04 ⁰ 0)	92066.079(3)	92066.155(3)	92066.226(3)
$\text{H}^{12}\text{C}^{14}\text{N}$	(00 ⁰ 0)	88630.414(3)	88631.846(3)	88633.935(3)
	(02 ⁰ 0)	89086.423(3)	89087.914(3)	89090.085(3)
	(04 ⁰ 0)	89567.869(3)	89569.413(3)	89571.660(3)
	(06 ⁰ 0)	90080.003(3)	90081.591(3)	90083.904(3)
	(08 ⁰ 0)	90628.340(3)	90629.629(3)	90632.339(3)
	(0 10 ⁰ 0)	91221.973(3)	91223.634(3)	91226.054(3)
$\text{D}^{15}\text{N}^{12}\text{C}$	(00 ⁰ 0)	75286.821(3)	75286.742(3)	75286.631(3)

Values in parentheses represent the experimental uncertainty, in units of the last digit.

^aResults determined from lineshape analysis of unresolved spectral features; single line fit yields 91341.914(3) MHz.

4.4 *Ab initio* calculation of $(eQq)_\text{N}$

To explain the observed trends, we performed *ab initio* calculations at the CCSD(T)/cc-pCVQZ level. By choosing a grid of 24 angles between the HCN ($\theta = 0^\circ$) and HNC ($\theta = 180^\circ$) isomers and optimizing all other internal coordinates to minimize the total energy, we obtained a one-dimensional potential from which $(eQq)_\text{N}$ values are calculated. Further details of the approach to solving for the energies and wavefunctions of the resulting one-dimensional vibrational potential can be found in Ref. [99]. Here, θ is the Jacobi angle between the Jacobi vectors \mathbf{r} and \mathbf{R} , where \mathbf{r} is the N–C displacement vector and \mathbf{R} is the displacement vector between the C–N center of mass and the H atom. As shown in Figure 4-4, the trends in the *ab initio* $(eQq)_\text{N}$ values agree with the experimental observations: $(eQq)_\text{N}$ for HCN is large and negative, and

Table 4.2: Fitted hyperfine parameters for H¹²C¹⁴N, H¹⁴N¹²C, and D¹⁵N¹²C.

	Vibrational level	$\nu_0(J = 1 - 0)/\text{MHz}$	eQq_N/MHz	C_N/kHz
H ¹⁴ N ¹² C	(00 ⁰)	90663.5627(7)	0.2641(10)	6.79(10)
	(02 ⁰)	91341.9156(11) ^a	0.0451(17) ^{a,b}	6.77(20) ^a
	(04 ⁰)	92066.1372(7)	-0.2066(8)	7.05(40)
H ¹² C ¹⁴ N	(00 ⁰)	88631.6010(16)	-4.7084(11) ^c	9.99(43)
	(02 ⁰)	89087.6577(18)	-4.8966(21) ^d	10.33(82)
	(04 ⁰)	89569.1480(40)	-5.0699(63)	11.52(151)
	(06 ⁰)	90081.3185(112)	-5.2175(68)	11.52(82)
	(08 ⁰)	90629.6887(11)	-5.3485(41)	11.78(208)
	(0 10 ⁰ 0)	91223.3489(40)	-5.4579(107)	11.77(141)
D ¹⁵ N ¹² C	(00 ⁰)	75286.7557(16)	0.2550(38)	-1.34(26)

Values in parentheses represent 95% confidence intervals of repeated measurements in units of the last digit.

^aMolecular constants based on results of lineshape analysis.

^bInstrumental resolution and lack of resolvable hyperfine components indicate $-0.060 < (eQq)_N < 0.060$ MHz.

^cLiterature value is -4.70903(162) [85].

^dLiterature value is -4.8990(21) [98].

$(eQq)_N$ for HNC is small and positive. Bending on the HCN side causes $(eQq)_N$ to increase initially in magnitude, whereas bending on the HNC side causes $(eQq)_N$ to decrease in magnitude and then change sign.

To make quantitative comparisons with the experimental data, the *ab initio* values of $(eQq)_N$ were averaged over the one-dimensional vibrational wavefunctions. To obtain the experimental $(eQq)_N$ values, the frequencies of the three $J = 1-0$ hyperfine components from each spectrum were fit with the SPFIT program [82]. As shown in Table 4.3, the agreement between the experimental and *ab initio* $(eQq)_N$ values is better than 35 kHz, which is remarkable considering our approximation of the motion to a single coordinate.

Table 4.3: Experimental and *ab initio* $(eQq)_N$ values for $\text{H}^{14}\text{N}^{12}\text{C}$ and $\text{H}^{12}\text{C}^{14}\text{N}$.

	Vibrational level	Experimental/MHz ^a	<i>ab initio</i> /MHz
$\text{H}^{14}\text{N}^{12}\text{C}$	(00 ⁰ 0)	0.2641(10)	0.2961
	(02 ⁰ 0)	0.0451(17) ^b	0.0611
	(04 ⁰ 0)	-0.2066(8)	-0.1915
$\text{H}^{12}\text{C}^{14}\text{N}$	(00 ⁰ 0)	-4.7084(11)	-4.6764
	(02 ⁰ 0)	-4.8966(21)	-4.8771
	(04 ⁰ 0)	-5.0699(63)	-5.0561
	(06 ⁰ 0)	-5.2175(68)	-5.2157
	(08 ⁰ 0)	-5.3485(41)	-5.3578
	(0 10 ⁰ 0)	-5.4579(107)	-5.4843

^aValues in parentheses represent 95% confidence intervals of repeated measurements in units of the last digit.

^bValue based on lineshape analysis; lack of resolvable hyperfine components and instrumental resolution indicate that $-0.060 < eQq_N < 0.060$ MHz.

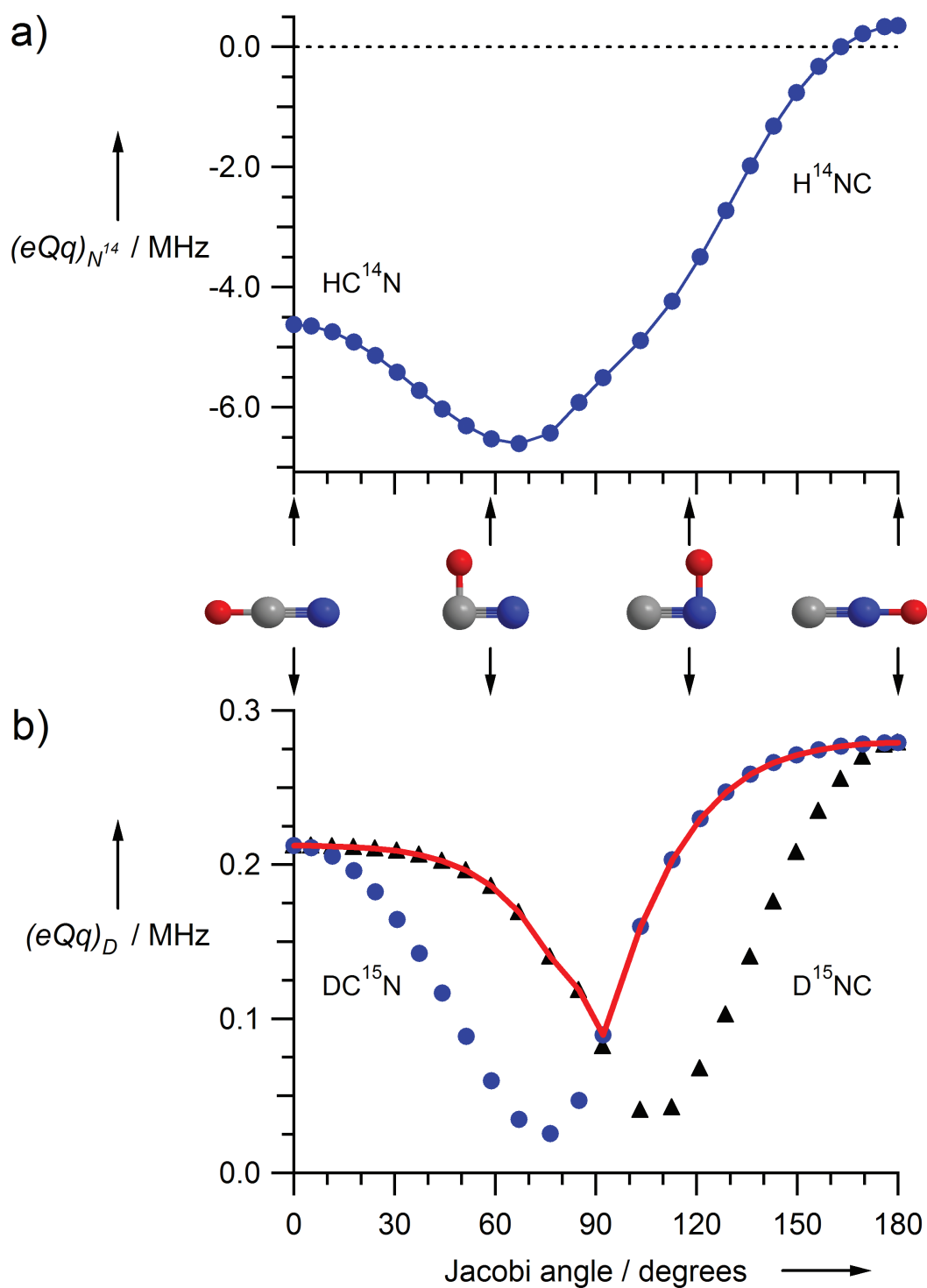


Figure 4-4: (a) *Ab initio* $(eQq)_N$ values in the C–N bond axis frame as a function of Jacobi angle. (b) *Ab initio* $(eQq)_D$ values in the C–D bond axis frame (triangles) and the N–D bond axis frame (circles). The red line follows the $(eQq)_D$ values in the C–D bond axis frame for $\theta < 90^\circ$ and follows the $(eQq)_D$ values in the N–D bond axis frame for $\theta > 90^\circ$.

4.5 Chemical interpretation of the variation of the hyperfine structure

4.5.1 Variation of $(eQq)_N$

According to the model of Townes and Dailey[5], the primary contribution to q in most molecules is the unequal filling of p orbitals in the valence shell of the coupling atom. In $\text{H}-\text{C}\equiv\text{N}:$, the bonding associated with the N nucleus consists of one electron in an sp-hybridized orbital that contributes to a σ bond, two electrons in a counter-hybridized sp orbital to make up the lone pair, and one electron in each of the p_x and p_y orbitals for the two π bonds. The lone pair creates an excess of electrons along the C–N axis, resulting in a large negative quadrupole coupling constant. In contrast, the N bonding for the primary resonance structure of $\text{H}-\overset{+}{\text{N}}\equiv\overset{-}{\text{C}}:$ consists of one electron in an sp-hybridized orbital that contributes to the N–C σ bond, and one electron in each of the p_x and p_y orbitals for the two π bonds. In this case, the four covalent bonds leads to a balanced occupancy of p orbitals, thus an $(eQq)_N$ near zero. The small positive value arises from the contribution of the secondary resonance structure $\text{H}-\overset{\cdot\cdot}{\text{N}}=\overset{\cdot\cdot}{\text{C}}:$, which has a lone pair in the p_x orbital, causing an excess of electrons perpendicular to the C–N axis.

As Figure 4-4 demonstrates, the values of $(eQq)_N$ do not follow a simple linear function as the bend angle increases. Instead, bending of HCN initially causes the magnitude of $(eQq)_N$ to increase before eventually decreasing during the isomerization process. Yarmus[100] suggested that the effect of bending on $(eQq)_N$ was caused by a decrease in the sp hybridization of the N–C σ bond. A natural bond orbital[101] analysis of our *ab initio* calculations shows, however, that the hybridization changes associated with the N atom are too small to account for this initial increase. Rather, the increase in magnitude of $(eQq)_N$ is caused by a partial localization of the in-plane π bond on the C atom that removes some of the electron density in the N-atom p_x

orbital. Because the lone-pair electrons on the N atom remain primarily along the C–N axis, an even larger p-electron imbalance is created, causing $(eQq)_N$ to increase. In the region around $\theta = 90^\circ$, however, the C–H bond breaks and the N–H bond forms. This rearrangement of the chemical bonding shifts the lone-pair electrons off the C–N axis and involves them in four covalent bonds, ultimately leading to a balance of the p electrons and a decrease in $(eQq)_N$.

4.5.2 Variation of $(eQq)_D$

The nature of the bonding may also be observed from the perspective of the hydrogen nucleus. Although hydrogen does not have a nuclear quadrupole moment ($I_H = 1/2$), deuterium ($I_D = 1$) does. The Townes-Dailey model is not directly applicable for predictions of $(eQq)_D$ because deuterium does not have any p electrons and its one electron is in a spherically symmetric 1s orbital. Instead, the electric field gradient q arises from the nuclear charge and the electron density of the atom to which the deuterium is bound [102]. To simplify the experimental analysis, we examined the $D^{15}NC$ isotopologue instead of the $D^{14}NC$ isotopologue, because ^{15}N ($I = 1/2$) does not have a nuclear quadrupole moment; thus, the hyperfine structure of $D^{15}NC$ gives a direct measure of $(eQq)_D$. The experimental and *ab initio* values for the ground vibrational state of $D^{15}NC$ are 255.0(38) and 270.4 kHz, respectively. The $J = 1 - 0$ transition of $DC^{15}N$ is just outside the range of our spectrometer, but the literature value[103] of $(eQq)_D = 200.9(8)$ kHz is in good agreement with our *ab initio* calculation of $(eQq)_D = 208.9$ kHz.

Unlike $(eQq)_N$, $(eQq)_D$ is similar in sign and magnitude for the two isomers. Moreover, as shown in Figure 4-4, the *ab initio* values of $(eQq)_D$ remain relatively unchanged as the molecule bends, except for the region around $\theta = 90^\circ$ where the C–D and N–D bonds are not well defined. The lack of change in $(eQq)_D$ indicates that the chemical bond involving deuterium remains relatively unaltered until isomeriza-

tion begins, when the D nucleus bridges the C and N nuclei. The angular region over which this ‘bridged’ bonding arrangement exists can be related to the features of the $(eQq)_D$ plot in Figure 4-4b. When the deuterium is involved with bonding interactions with both the carbon and nitrogen nuclei, $(eQq)_D$ will be significantly distorted from its linear-molecule values in both the C–D and N–D bond-axis frames of reference. This is observed to occur, relatively symmetrically, over a range of 70° to 110° in the Jacobi angle. The variation of $(eQq)_N$ provides further support for a qualitative change in bonding character over this region; 70° and 110° are both points where the $(eQq)_N$ curve is kinked.

Because q originates primarily from the interaction with the nucleus to which deuterium is bound, we expect q to be largely dependent on the bond length [104]. Indeed, the *ab initio* $(eQq)_D$ values are strongly anticorrelated with the bond length: the smallest $(eQq)_D$ value occurs at $\theta = 90^\circ$, which corresponds to the largest separation between D and C or N. The analysis of the *ab initio* values of the hyperfine coupling constants has recently been extended by our colleague, Bryan Wong [105].

4.6 Variation of the HNC quadrupole hyperfine structure with excitation of stretching modes

To this point, the HCN/HNC system has been treated as one dimensional, exclusively dependent on bond angle. The other degrees of freedom have been discarded due to the fact that they do not directly project along the isomerization reaction coordinate. Since the stretching motions do not lead to isomerization, excitation of the stretching modes is expected to have little effect on the electronic structure and, therefore, on the value of $(eQq)_N$.²

²It is likely that excitation of stretching modes will give rise to interesting changes as one approaches the dissociation limits for bonds involving the nitrogen atom, but this has not been explored.

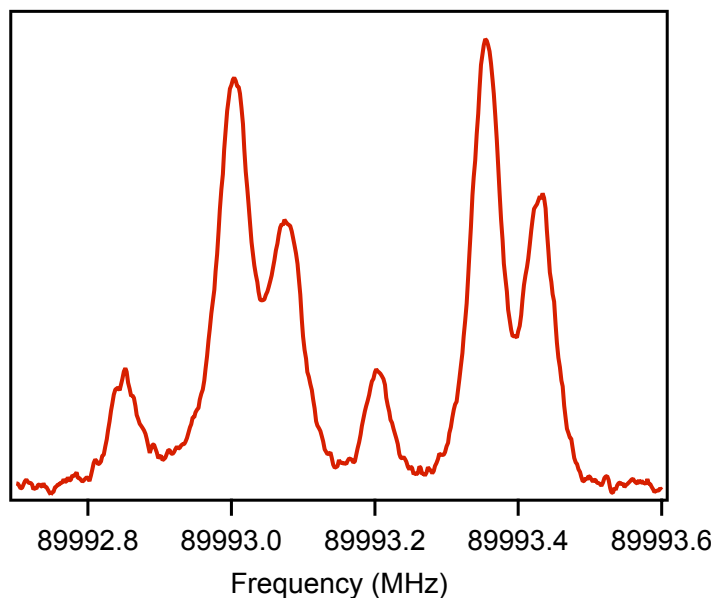


Figure 4-5: Hyperfine-resolved $J = 1 - 0$ rotational spectrum of HNC in the (00^0_1) vibrational state.

The $J = 1 - 0$ rotational spectrum of HNC (00^0_1), where ν_3 is a predominately C-N stretching vibration, is shown in Figure 4-5. As anticipated, the qualitative appearance of this spectrum is the same as that of the vibrationless level of HNC. The derived value for $(eQq)_N$ increases from the vibrationless value by approximately 10% to a value of 294 kHz.

4.7 Nuclear quadrupole hyperfine splitting reveals nascent bond breaking isomerization

We have demonstrated that nuclear quadrupole hyperfine structure is altered by the extent of bending excitation in HCN and HNC. As shown in Figure 4-6, the *ab initio* $(eQq)_N$ values of HC^{14}N and H^{14}NC follow the patterns experimentally established at low excitation and change smoothly as a function of increasing energy in the bending coordinate. Near the isomerization barrier (above $15,000\text{ cm}^{-1}$), however, the $(eQq)_N$ values of HC^{14}N and H^{14}NC deviate dramatically from their respective trends before

approaching a nearly constant value at above-barrier energies.

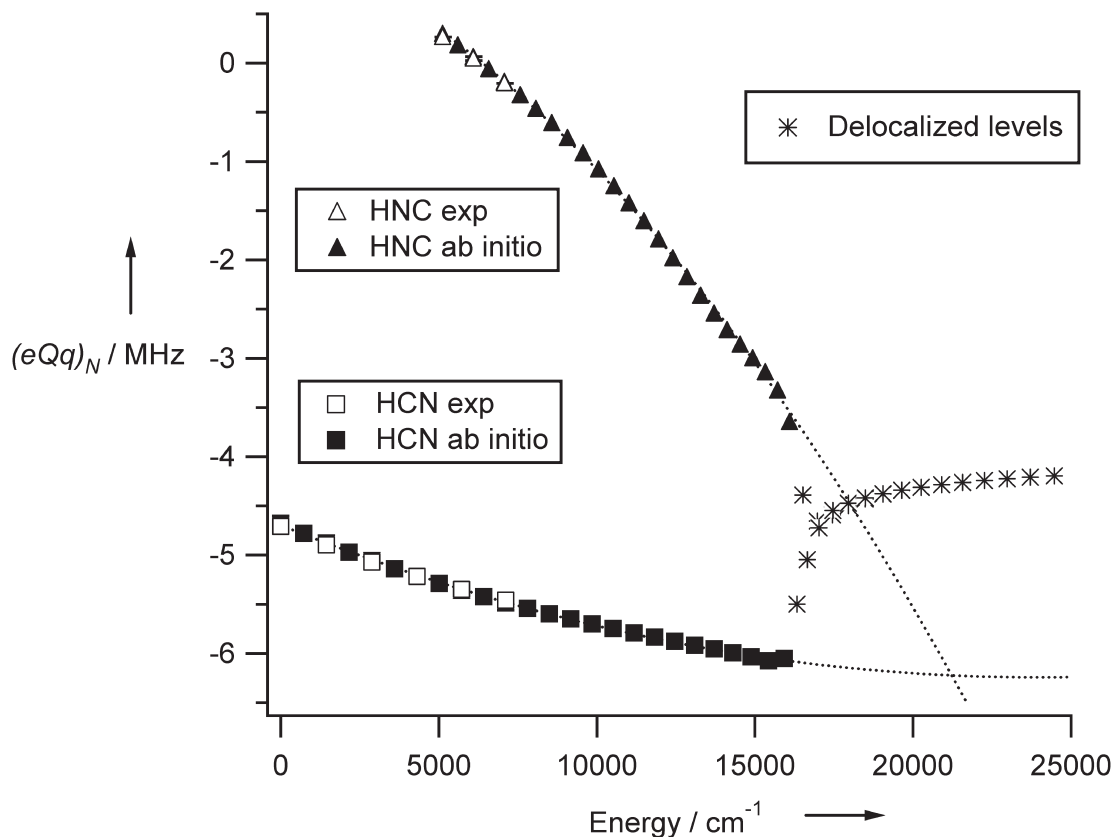


Figure 4-6: Experimental and vibrationally averaged *ab initio* $(eQq)_N$ values for HC^{14}N and H^{14}NC in the principal inertial axis frame, which is approximately aligned with the C–N bond. The *ab initio* energies are referenced to the HCN (00⁰) level, and the experimental $(eQq)_N$ values are matched to the *ab initio* energies according to vibrational level. The $(eQq)_N$ values for HC^{14}N and H^{14}NC vary smoothly as a function of energy until the onset of delocalization, at which point they deviate dramatically.

This deviation is caused by the onset of delocalization of the vibrational wavefunction into the regions above both the HCN and HNC potential energy wells. Bowman *et al.*[1] proposed the use of the electric dipole moment, another electronic structure indicator, as a diagnostic for delocalized states, because the HCN and HNC isomers have large dipole moments of nearly equal magnitude, but opposite sign, and the delocalized states have dipole moments near zero. Stark effect measurements of the

dipole moment can consequently characterize the degree of localization in a vibrational state of HCN or HNC. Although a single measurement of nuclear quadrupole hyperfine structure is not as useful as a single Stark effect measurement in terms of identifying a delocalized level, hyperfine structure can determine whether the wavefunction is localized in the HCN or HNC potential well, which is not possible with a single Stark effect measurement. Moreover, the dramatic deviation from the $(eQq)_N$ trend along a progression of bending vibrational levels provides a useful indicator of the onset of delocalization and provides a means of identifying pre-delocalized levels. Thus, Stark effect and nuclear quadrupole hyperfine structure measurements are complementary indicators of electronic structure that can be used as diagnostics for detecting and assigning delocalized states. Because the lowest energy delocalized state is the isomerization transition state, the detection of this state is tantamount to catching the molecule in the act of bond-breaking isomerization.

Chapter 5

Vibrational assignments in the S_1 state of acetylene, I: Pure-bending polyads

The work in this chapter resulted from a collaborative effort between myself and Prof. Anthony Merer, with contributions from Dr. Nami Yamakita and Soji Tsuchiya. The majority of the results in this chapter have been published in the *Journal of Chemical Physics* (Ref. [106]).

5.1 Introduction

The $\tilde{A}^1A_u - \tilde{X}^1\Sigma_g^+$ electronic transition of acetylene is one of the most widely studied of all polyatomic spectra. The principal reason is that acetylene is the simplest compound containing a C \equiv C triple bond, so that the analysis of the spectrum gives a clear picture of what happens on $\pi^* \leftarrow \pi$ electronic excitation of such a bond. As is well known, acetylene is linear in its ground electronic state, but, as was shown by Ingold and King[107, 108] and by Innes[109] over 50 years ago, it becomes *trans*-bent in its first excited singlet state \tilde{A}^1A_u . This was one of the first demonstrations that a molecule can change its point group on electronic excitation. In fact, it is more

complicated than this. The first excited singlet state (S_1), which corresponds to a ${}^1\Sigma_u^-$ state of the linear molecule, has potential minima corresponding to both *cis*- and *trans*-bent isomers [110, 111, 112, 113, 114, 115, 116], but transitions from the ground state are only permitted to levels of the *trans* isomer by the dipole selection rules. The S_1 state of the *cis*-isomer, $\tilde{A} {}^1A_2$, has never been observed, though it is calculated to lie about 3000 cm^{-1} higher than the $\tilde{A} {}^1A_u$ state of the *trans*-isomer [113, 116] or roughly 1000 cm^{-1} below the dissociation limit [117]. Interesting dynamics will occur at the barrier to *cis*-*trans* isomerization, and a search for the spectroscopic signatures of these dynamics has been one of the motivations of this work.

A second reason for the interest in the $\tilde{A} {}^1A_u - \tilde{X} {}^1\Sigma_g^+$ transition of acetylene is the wealth of detail it contains. The Franck–Condon pattern in absorption [118, 119] consists of a long progression in the *trans*-bending (or “straightening”) vibration, ν'_3 , each member of which is the origin of a short progression in the C=C stretching vibration, ν'_2 . This is consistent with the rotational analysis, which shows [120] that the equilibrium HCC angle is 122.5° , and that the C–C bond length has increase from 1.208 to 1.375 Å, which is greater than that in C_2H_4 . One of the results of the change in point group symmetry on electronic excitation, which was found in the spectrum of acetylene for the first time, is “axis-switching” [121] where a small rotation of the principal inertial axis system upon excitation causes the appearance of unexpected $K' - \ell'' = 0$ and ± 2 subbands in an otherwise perpendicular ($K' - \ell'' = \pm 1$) transition. Although predissociation sets in [117] just below the 3^4 level, its effects are minimal at first. Very extensive rotational analyses have therefore been possible, leading to a detailed description of the level structures of the ν'_2 and ν'_3 progressions and, from hot bands, of the ground state ν''_4 (*trans*-bending) vibration [118, 119, 122].

With a detailed understanding of the upper-state level structure available, the $\tilde{A} {}^1A_u$ state has been a valuable stepping stone for emission studies [123, 124, 125, 126, 127, 128] and particularly for double resonance experiments. Among these are

many comprehensive studies of the high vibrational levels of the ground state using stimulated emission pumping[129, 130, 131, 132] and of the level structures of various Rydberg and valence states[133, 134] and of the acetylene cation [135, 136].

Interestingly, although the Franck-Condon active (*gerade*) vibrational levels are fairly well understood, much less is known about the *ungerade* vibrations of the \tilde{A}^1A_u state. IR-UV double resonance experiments via the ground state $3\nu_3''$ level[2, 137] have allowed analyses of the three *ungerade* fundamentals, ν_4' (a_u , torsion), ν_5' (b_u , antisymmetric CH stretch), and ν_6' (b_u , in-plane *cis*-bend), together with the combination 3^15^1 . The ν_4' and ν_6' fundamentals of the \tilde{A}^1A_u state are almost degenerate [2], with wavenumbers of 764.9 and 768.3 cm^{-1} , respectively; they are also extremely strongly coupled by Coriolis interactions. Further double resonance experiments via the ground state ν_3'' fundamental have allowed analyses[138] of the combinations 3^24^1 , 3^26^1 , 3^34^1 and 3^36^1 , where again the structure is massively distorted by Coriolis effects. The only other information about the *ungerade* vibrations comes from one-photon laser-induced fluorescence (LIF) studies of the excitation spectrum[139] where, with the help of supersonic-jet cooling, some weak bands in among the strong Franck-Condon progression were identified as combinations involving overtones of the ν_4' and ν_6' vibrations.

The assignment of these weak combination bands[139] suggested that many other bands involving the low-lying *ungerade* vibrations ν_4' and ν_6' should be observable given sufficiently sensitive experiments. These bands would be highly forbidden according to the Franck-Condon principle but could obtain small amounts of intensity through anharmonic interactions of their upper levels with the Franck-Condon allowed levels. The purpose of the present chapter is to describe the successful observation of a number of such bands belonging to overtones of the ν_4' and ν_6' vibrations with up to five vibrational quanta. The *gerade* members have been observed in one-photon LIF experiments, and the *ungerade* members in IR-UV double resonance experiments via

the ground state ν_3'' and $\nu_3'' + \nu_4''$ levels.

The rotational and vibrational structures of these bands are highly unusual. Because the ν_4' and ν_6' vibrations have very nearly the same frequency, many of the features of a doubly degenerate vibration, with its associated vibrational angular momentum, appear in the overtone spectra. The strong Coriolis coupling of the ν_4' and ν_6' vibrations is one of these. Another is the strikingly large Darling–Dennison resonance that occurs between the overtones of ν_4' and ν_6' , and which causes the vibrational levels to be grouped into what looks like the vibrational angular momentum level structure of a degenerate vibration. As far as we are aware, this type of pattern has not been seen before in the bending vibrations of an asymmetric top molecules. The combination of a - and b -axis Coriolis coupling with the Darling–Dennison resonance distorts the spectra very severely. The K -structure is totally disorganized, and local rotational perturbations occur in the J -structure at many places where appropriate sets of levels happen to lie close to each other. For $K > 0$, all the members of an overtone polyad appear in the spectra, whatever their nominal vibrational symmetries. Specifically, the distinction between a and b irreducible representations is lost, although g/u symmetry remains valid (in the energetic region sampled by our experiments).

5.2 Experimental details

The c -axis polarization of the $\tilde{A}^1A_u - \tilde{X}^1\Sigma_g^+$ transition implies the rotational selection rule $K' - \ell'' = \pm 1$. Taking into account the g/u symmetry properties of the levels, it has been necessary to carry out four sets of experiments in order to map the $K' = 0 - 2$ structure of the \tilde{A} state, as illustrated in Figure 5-1. In one-photon jet-cooled experiments from the ground vibrational level, which has $\ell'' = 0$, only the vibrationally *gerade* $K' = 1$ levels are accessible in the absence of Coriolis- or axis-

switching-induced “forbidden” subbands. To get at the *gerade* $K' = 0$ and 2 levels, it is necessary to use a warmed sample that has a sufficient population in the ground state ν_4'' fundamental, where $\ell'' = 1$. Similarly, for the *ungerade* vibrational levels observed in IR-UV double resonance experiments, only the *ungerade* $K' = 1$ levels can be reached if the intermediate level is a Σ_u^+ ($\ell'' = 0$) ground state vibrational level, such as the ν_3'' fundamental; a Π_u vibrational intermediate ($\ell'' = 1$) is needed in order to reach the *ungerade* $K' = 0$ and 2 levels.

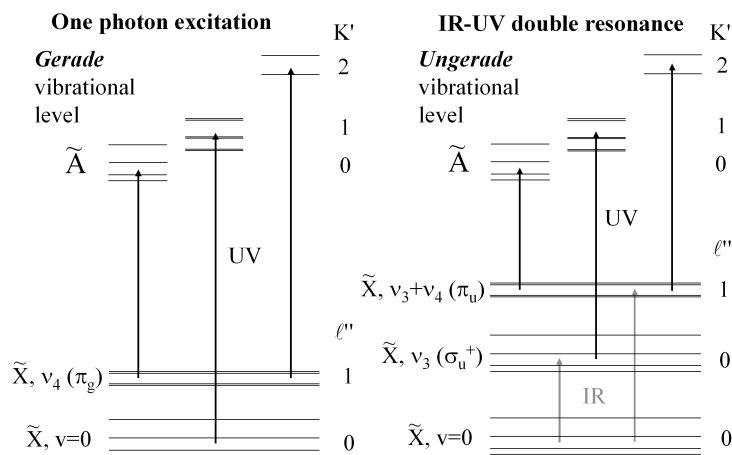


Figure 5-1: Schematic energy level diagram showing how the $K' - \ell'' = \pm 1$ selection rule necessitates two experiments, both in one-photon excitation and in IR-UV double resonance, in order to observe the complete set of upper state levels with $K' = 0 - 2$.

Laser-induced fluorescence spectra of neat acetylene have been recorded in an unskimmed pulsed jet expansion. The gas was expanded through a pulsed valve (General Valve, Series 9) with a 0.5 mm orifice from a backing pressure of 200 kPa. The ultimate vacuum achieved in the apparatus was 2×10^{-7} Torr, which rose to 5×10^{-5} under normal gas load.

The laser radiation was the frequency-doubled output of a Lambda Physik 3002E dye laser, pumped by the third harmonic of a Nd:YAG laser (Spectra-Physics DCR-3). A small amount of the portion of the dye laser power was passed through a

heated gas cell containing $^{130}\text{Te}_2$ vapor for calibration ($\pm 0.02 \text{ cm}^{-1}$ accuracy), while the remainder was doubled in a β -barium borate crystal, and sent to the molecular beam chamber. The laser radiation crossed the pulsed jet about 3 cm from the orifice.

Fluorescence from the excited acetylene was observed at right angles to both the laser beam and the jet axis. The fluorescence was collected by a lens system and detected by a Hamamatsu R331 photomultiplier after passing through a UG-5 or UG-11 colored glass filter.

To observe the $K' = 0$ and 2 levels belonging to *gerade* vibrational states it has been necessary to record hot band transitions from the ground state ν_4'' fundamental. In order to induce hot bands in the jet spectra while maintaining reasonably low rotational temperatures, the distance between the nozzle and the intersection of the laser with the pulse of molecules was reduced from ~ 30 to ~ 5 mm. Additionally, the relative timing of the pulsed valve and the laser was adjusted so that the laser radiation intersects the leading edge of the gas pulse, which is characterized by higher effective vibrational temperatures.

The *ungerade* vibrational states have been observed by IR-UV double resonance, using the ν_3'' and $\nu_3'' + \nu_4''$ IR bands as intermediates. The infrared radiation was generated in a two-step difference frequency generation/optical parametric amplification process. A portion of the 1064 nm output of an injection-seeded Nd:YAG laser (Spectra-Physics PRO-270) was mixed, in a lithium niobate (LiNbO_3) crystal, with the output of a dye laser (Lambda Physik FL 2002) operating with either LDS 798 or LDS 751. The resulting infrared radiation was then passed through a second LiNbO_3 crystal, which was pumped by the remainder of the 1064 nm beam. The amplified IR radiation had an energy of approximately 3 mJ/pulse and a spectral width of 0.15 cm^{-1} , which is limited by the resolution of the grating-tuned dye laser.

A small fraction of the IR beam was sent to a photoacoustic cell containing 10 Torr of acetylene gas. The observed photoacoustic signal was used to ensure that

the IR frequency stayed in resonance with the desired vibrational transition. The remaining IR radiation entered the chamber through a CaF₂ window in the opposite direction to the UV laser. The relative timing of the two lasers was adjusted so that the beams were temporally overlapped, with the precise timing adjusted to maximize the observed double-resonance fluorescence signals.

5.3 Theory

The energy level pattern for the coupled ν'_4 and ν'_6 bending fundamentals of the \tilde{A}^1A_u state of C₂H₂ has been described by Utz *et al.*[2] and is similar to that analyzed by Hegelund *et al.*[140] in the infrared spectrum of the *trans*-bent molecule diimide, N₂H₂. The overtones of ν'_4 and ν'_6 , which are the subject of the present work on C₂H₂, require, in addition, considerations of anharmonicity and Darling–Dennison resonance [141]. A summary of the relevant theory follows.

5.3.1 Matrix elements of the rotational and Coriolis operators

For an asymmetric top molecule such as C₂H₂ in its \tilde{A}^1A_u state, the general rotational Hamiltonian[142, 143, 144] simplifies to

$$\hat{H}_{\text{rot}} = A(\hat{J}_a - \hat{G}_a)^2 + B(\hat{J}_b - \hat{G}_b)^2 + C(\hat{J}_c - \hat{G}_c)^2, \quad (5.1)$$

where A , B , and C are the rotational constants, \hat{J} is the total angular momentum, \hat{G} is the vibrational angular momentum, and a , b , and c refer to the principal inertial

axes. When the squares are expanded, this equation becomes

$$\begin{aligned}\hat{H}_{\text{rot}} = & A\hat{J}_a^2 + B\hat{J}_b^2 + C\hat{J}_c^2 \\ & - 2A\hat{J}_a\hat{G}_a - 2B\hat{J}_b\hat{G}_b - 2C\hat{J}_c\hat{G}_c \\ & + A\hat{G}_a^2 + B\hat{G}_b^2 + C\hat{G}_c^2.\end{aligned}\tag{5.2}$$

The first three terms are the familiar rigid rotator Hamiltonian, followed by the three first-order Coriolis terms, and finally three terms involving the squares of the components of the vibrational angular momentum. These components are defined[145, 146] as

$$G_\alpha = \mathbf{Q}^{\text{tr}}\boldsymbol{\zeta}^\alpha\mathbf{P},\tag{5.3}$$

where \mathbf{Q} and \mathbf{P} are the vectors of vibrational normal coordinates and their conjugate momenta, and $\boldsymbol{\zeta}^\alpha$ is a skew-symmetric matrix of Coriolis coupling constants. Multiplying this out, and considering just the vibrations ν'_4 and ν'_6 ,

$$G_\alpha = Q_4\zeta_{46}^\alpha P_6 - Q_6\zeta_{46}^\alpha P_4.\tag{5.4}$$

For the $\tilde{A} \ ^1A_u$ state of C_2H_2 the only nonvanishing coupling constants between ν_4 and ν_6 are ζ_{46}^a and ζ_{46}^b , which are related by the sum rule[118, 144]

$$(\zeta_{46}^a)^2 + (\zeta_{46}^b)^2 = 1.\tag{5.5}$$

The terms in \hat{G}_c can be ignored, since there is no c -axis coupling.

The matrix elements of the vibrational angular momentum operators follow from

the matrix elements of the Q and P operators in a harmonic basis,[143]

$$\begin{aligned}\langle v_4 + 1 \ v_6 | \hat{G}_\alpha | v_4 \ v_6 + 1 \rangle &= -i\zeta_{46}^\alpha \hbar \Omega [(v_4 + 1)(v_6 + 1)]^{1/2}, \\ \langle v_4 \ v_6 + 1 | \hat{G}_\alpha | v_4 + 1 \ v_6 \rangle &= i\zeta_{46}^\alpha \hbar \Omega [(v_4 + 1)(v_6 + 1)]^{1/2},\end{aligned}\tag{5.6}$$

where Ω is Mills' abbreviation,[147]

$$\Omega = \frac{1}{2} \left[\sqrt{\frac{\nu_4}{\nu_6}} + \sqrt{\frac{\nu_6}{\nu_4}} \right].\tag{5.7}$$

Since the highest J values in either our jet-cooled spectra or our double resonance spectra are never more than 9, centrifugal distortion effects can be ignored. In a signed- k basis the matrix elements of the rigid rotator and first-order Coriolis terms are then

$$\begin{aligned}\langle v_4 \ v_6 \ J \ k | \hat{H} | v_4 \ v_6 \ J \ k \rangle &= [A - \frac{1}{2}(B + C)] k^2 + \frac{1}{2}(B + C)J(J + 1), \\ \langle v_4 \ v_6 \ J \ k \pm 2 | \hat{H} | v_4 \ v_6 \ J \ k \rangle &= \frac{1}{4}(B - C)[J(J + 1) - k(k \pm 1)]^{1/2}[J(J + 1) - (k \pm 1)(k \pm 2)]^{1/2}, \\ \langle v_4 + 1 \ v_6 \ J \ k | \hat{H} | v_4 \ v_6 + 1 \ J \ k \rangle &= 2iA\zeta_{46}^a \Omega k [(v_4 + 1)(v_6 + 1)]^{1/2}, \\ \langle v_4 + 1 \ v_6 \ J \ k \pm 1 | \hat{H} | v_4 \ v_6 + 1 \ J \ k \rangle &= iB\zeta_{46}^b \Omega [J(J + 1) - k(k \pm 1)]^{1/2} [(v_4 + 1)(v_6 + 1)]^{1/2}, \\ \langle v_4 \ v_6 + 1 \ J \ k | \hat{H} | v_4 + 1 \ v_6 \ J \ k \rangle &= -2iA\zeta_{46}^a \Omega k [(v_4 + 1)(v_6 + 1)]^{1/2}, \\ \langle v_4 \ v_6 + 1 \ J \ k \pm 1 | \hat{H} | v_4 + 1 \ v_6 \ J \ k \rangle &= -iB\zeta_{46}^b \Omega [J(J + 1) - k(k \pm 1)]^{1/2} [(v_4 + 1)(v_6 + 1)]^{1/2}.\end{aligned}\tag{5.8}$$

The matrix elements of the terms in \hat{G}_α^2 can be obtained by matrix multiplication from Eq. 5.6. There are nine possible expressions, but the only important ones are the diagonal element and the elements that act within a given vibrational polyad, defining this as one where the levels have the same value of $v'_4 + v'_6$,

$$\begin{aligned}
\langle v_4 v_6 | A\hat{G}_a^2 + B\hat{G}_b^2 | v_4 v_6 \rangle & \quad (5.9) \\
& = [A(\zeta_{46}^a)^2 + B(\zeta_{46}^b)^2](2v_4v_6 + v_4 + v_6), \\
\langle v_4 v_6 | A\hat{G}_a^2 + B\hat{G}_b^2 | v_4 + 2 v_6 - 2 \rangle & \\
& = -[A(\zeta_{46}^a)^2 + B(\zeta_{46}^b)^2][(v_4 + 1)(v_4 + 2)v_6(v_6 - 1)]^{1/2}, \\
\langle v_4 v_6 | A\hat{G}_a^2 + B\hat{G}_b^2 | v_4 - 2 v_6 + 2 \rangle & \\
& = -[A(\zeta_{46}^a)^2 + B(\zeta_{46}^b)^2][v_4(v_4 - 1)(v_6 + 1)(v_6 + 2)]^{1/2}.
\end{aligned}$$

In deriving these elements, the factors of \hbar^2 are absorbed into the rotational constants, and Ω^2 has been taken as exactly 1; terms involving $[(\nu'_4/\nu'_6)^{1/2} - (\nu'_6/\nu'_4)^{1/2}]^2$ were ignored since ν'_4 and ν'_6 are very nearly the same. The approximation of retaining only the matrix elements of \hat{G}_α^2 acting within a given polyad is not expected to cause problems, since the closest polyads must differ by two units of $v'_4 + v'_6$, as a result of the g/u symmetry properties of the levels, and will be separated by about 1500 cm^{-1} .

It can be seen from the first line of Eq. 5.9 that one of the effects of the vibrational angular momentum is to add a quantity $[A(\zeta_{46}^a)^2 + B(\zeta_{46}^b)^2]$ to the vibrational frequencies ν'_4 and ν'_6 . With the values of the parameters taken from the least squares analysis of the $v'_4 + v'_6 = 2$ polyad, described below, this quantity is 7.06 cm^{-1} .

The vibrational angular momentum also adds twice this quantity, i.e. 14.12 cm^{-1} , to the anharmonicity parameter x'_{46} . This is slightly larger than the observed value, $x'_{46} = 11.39 \text{ cm}^{-1}$ (described below), and implies that the anharmonic force field contributes a mere -2.73 cm^{-1} to x'_{46} . The dominance of the angular momentum contribution to x'_{46} is unusual and somewhat surprising. It also emphasizes that

the role of vibrational angular momentum, in generating what looks like vibrational anharmonicity, should not be neglected.

5.3.2 Darling–Dennison resonance

The off-diagonal elements in Eq. 5.9 have the same vibrational quantum number dependence as those responsible for the Darling–Dennison resonance [141]. This is a well-known effect [148, 149, 150] in the overtone spectroscopy of molecules such as H₂O and the ground state of C₂H₂. Provided that certain definite relationships between the Darling–Dennison resonance parameter and the anharmonicity constants are satisfied [151], the Darling–Dennison resonance converts the normal mode energy level pattern of low-lying stretching vibrational levels into a local mode pattern at higher energy [148]. This represents how the vibrational structure changes from the low energy pattern, where the two bonds vibrate in phase, to the high energy pattern approaching dissociation, where just one of the two bonds breaks. The strong Darling–Dennison resonance involving nearly degenerate bending vibrations in an asymmetric top appears to be a new phenomenon. Some aspects of the resulting vibrational level structure resemble what is found for stretching vibrations, but there are also differences; research into the various effects is continuing. It should be pointed out that the motions resulting from considering the combinations of modes ν'_4 and ν'_6 are not ‘local,’ because these vibrations are not the symmetric and antisymmetric motions of a pair of two symmetry-related internal coordinates. In the small amplitude rectilinear limit, the resulting motions are in directions 45° with respect to the *ab* plane.

Darling–Dennison resonance has been considered in some detail by Lehmann [152]. He gives the matrix element as

$$\langle n_a + 2 \ n_b - 2 | \hat{H} | n_a \ n_b \rangle = \frac{1}{4} K_{aabb} [(n_a + 1)(n_a + 2)n_b(n_b - 1)]^{1/2}, \quad (5.10)$$

where

$$\begin{aligned}
K_{aabb} = & \frac{1}{4}\phi_{aabb} + \sum_{\alpha} -B_{\alpha}(\zeta_{ab}^{\alpha})^2 \frac{(\omega_a + \omega_b)^2}{\omega_a\omega_b} \\
& + \frac{1}{8} \sum_k \phi_{kaa}\phi_{kbb}\omega_k \left(\frac{1}{4\omega_a^2 - \omega_k^2} + \frac{1}{4\omega_b^2 - \omega_k^2} \right) \\
& - \frac{1}{2} \sum_k \phi_{kab}^2 \frac{\omega_k}{\omega_k^2 - (\omega_a - \omega_b)^2}.
\end{aligned} \tag{5.11}$$

Although the notation is different, the term involving the ζ_{ab}^{α} parameters in Eq. 5.11 corresponds exactly to the coefficient in the off-diagonal elements of Eq. 5.9. Allowing for the factor $\frac{1}{4}$ in Eq. 5.10, this term contributes an amount $-4[A(\zeta_{46}^a)^2 + B(\zeta_{46}^b)^2] = -28.24 \text{ cm}^{-1}$ to the parameter K_{4466} . Although this is a surprisingly large amount, which (as shown below) outweighs the effects of cubic and quartic anharmonic potential constants, ϕ . It is remarkable that the vibrational angular momentum should make such a large contribution to what is usually thought of as anharmonicity, both for the x'_{46} and K_{4466} parameters.

5.3.3 Structures of the Hamiltonian matrices

A complication in using the elements of Eq. 5.8 for a matrix calculation of the energy levels is that the first order Coriolis terms are imaginary. This can be overcome by multiplying the $|v_6\rangle$ harmonic oscillator basis functions by a phase factor $(i)^{v_6}$. To implement this, the Hamiltonian matrices for each J -value from Eq. 5.8 are subjected to a similarity transformation, $\mathbf{H}' = \mathbf{S}^{\dagger}\mathbf{H}\mathbf{S}$. The \mathbf{S} matrix consists of blocks for each vibrational level that take the sums and differences of the signed- k basis function, converting them to an unsigned- K basis [6], but with all the elements in the blocks for the various vibrational levels multiplied by $(i)^{v_6}$. The transformation factorizes the matrix for each J -value into two submatrices, which can be given e and f symmetry labels. Further factorization is not possible because of the $\Delta K = \pm 1$ form of the

b -axis Coriolis elements.

After the transformation the matrix elements are all real, but any element off-diagonal in the vibrational quantum numbers carries a negative sign. The energy matrices can then be constructed directly from Eqs. 5.8 and 5.10, taking into account of the signs and the vibrational symmetries. Writing the basis functions as $|K^\pm x\rangle$, where \pm indicates the sum or difference and x is the irreducible representation label a or b , the e matrix contains the functions $|0^+a\rangle, |1^-a\rangle, |1^+b\rangle, |2^+a\rangle, |2^-b\rangle, |3^-a\rangle, \dots$, while the f matrix has the same structure but with the a and b labels reversed. As is well known [6], the $\langle k = -1 | H | k = 1 \rangle$ asymmetry element is added to or subtracted from the $|K = 1\rangle$ diagonal element by the similarity transformation, and any element connecting a $|k = 0\rangle$ basis function to a $|k = \pm 1\rangle$ or $|k = \pm 2\rangle$ basis function gets multiplied by $2^{1/2}$.

5.3.4 Selection rules: Coriolis coupling and axis-switching

In the absence of Coriolis and axis-switching[121] effects, the rotational selection rules for the c -axis polarized $\tilde{A}^1A_u - \tilde{X}^1\Sigma_g^+$ transition are $K' - \ell'' = \pm 1$, $\Delta J = 0, \pm 1$. Both Coriolis and axis-switching effects act to destroy the strictness of the first rule, giving rise to additional $K' - \ell'' = 0, \pm 2$ subbands. Because of this fact, it is difficult to distinguish between the two effects. In this work, the term axis-switching will be used to describe forbidden subbands of the Franck–Condon-allowed 3^n and $2^m 3^n$ progressions. These are easily recognized since the K -structures of the upper levels follow the normal asymmetric top energy level expressions, because there is no competing Coriolis coupling. The forbidden subbands in the bending polyads are best described as Coriolis-induced since this is the principal mechanism for their appearance. These forbidden subbands are mostly fairly weak, but a few are suprisingly strong, particularly when two sets of levels with zero-order K values differing by one unit happen to lie close to each other.

As for the vibrational selection rules, these are found to be obeyed strictly only for the $K = 0$ levels of the $\nu'_4 + \nu'_6 = \text{even}$ polyads, where $K' = 0$ levels with b_g vibrational symmetry are not seen. For the $\nu'_4 + \nu'_6 = \text{odd}$ polyads, the $K' = 0$ levels with both a_u and b_u vibrational symmetry appear in the double resonance spectra via Π_u intermediate levels ($\ell'' = 1$). They can be distinguished by their different rotational selection rules. For instance, in transitions from f -symmetry rotational levels of a Π_u intermediate level, $K' = 0$ levels with a_u vibrational symmetry (which have e rotational symmetry) give only Q branches, while those with b_u vibrational symmetry (f rotational symmetry) give R and P branches. The pattern is reversed in transitions from e -symmetry intermediate levels. The relative strengths of double resonance transitions to $K' = 0$ levels with a_u and b_u vibrational symmetry are found to depend on which Π_u intermediate state is chosen. Transitions to b_u levels dominate when $\nu''_3 + \nu''_4$ is used as the intermediate, though experiments with other polyads have shown that transitions to a_u levels dominate when $\nu''_1 + \nu''_5$ is used as the intermediate. It is not clear why this should be so. For $K \neq 0$ levels the a -axis Coriolis mixing is so strong that that every vibrational level appears in the spectrum, with the only restriction being that $K' - \ell'' = \pm 1$ transitions are usually the most intense.

For simplicity in what follows, the distinction between K for the $\tilde{A} \ ^1A_u$ state and ℓ for the $\tilde{X} \ ^1\Sigma_g^+$ state will not always be made. The two quantities describe the projection of the total angular momentum along the linear or near-linear inertial axis and are essentially equivalent.

5.4 Results

The structures of the bending polyads are highly irregular because of the interplay of Coriolis coupling and the Darling–Dennison resonance. Both of these are very large effects, with the experimental Darling–Dennison parameter K_{4466} found to be about

-50 cm^{-1} and the Coriolis parameter $2A\zeta^a$ (which is the coefficient of K in the a -axis coupling elements) about 18 cm^{-1} . It is not possible to separate them or to understand the structures of the polyads without data from levels with several K -values. For instance, it is essential to have data from as many of the $K = 0$ stacks as possible, because these contain no a -axis Coriolis effects and allow the vibrational origins to be established. Even so, these vibrational origins are not the fully deperturbed origins, because they represent the levels that result after the Darling–Dennison resonance has acted between harmonic basis levels of the same symmetry. The higher- K stacks suffer from both Darling–Dennison and Coriolis effects, but the effects can be separated because the a -axis Coriolis coupling depends linearly on K , whereas the Darling–Dennison resonance is independent of K . This means that a successful least squares analysis of a bending polyad requires data from $K = 0, 1$ and 2 stacks, at a minimum. It is, of course, necessary to use the the deperturbed band origins to calculate the higher- K levels correctly, since the Coriolis coupling and the Darling–Dennison resonance are both perturbations on the rigid rotator–harmonic oscillator basis.

5.4.1 The $v'_4 + v'_6 = 2$ polyad (B^2)

The first overtone polyad ($v'_4 + v'_6 = 2$, or B^2 , where B means “bending”) lies near $43\,700 \text{ cm}^{-1}$. It consists of three vibrational levels: 4^2 , 4^16^1 , and 6^2 . In room temperature absorption spectra it is completely buried under very intense hot band structure from the Franck–Condon allowed 3^24_1 band, but in jet-cooled LIF experiments the hot bands are sufficiently reduced to make analysis possible. Two regions of structure can be recognized: a confused group of lines centered at $43\,715 \text{ cm}^{-1}$ and an elegantly simple $K' - \ell'' = 1 - 0$ subband at $43\,796 \text{ cm}^{-1}$. The $43\,715 \text{ cm}^{-1}$ group is illustrated in Figure 5-2. In this figure, the lines of an overlapping hot band have been colored light gray.

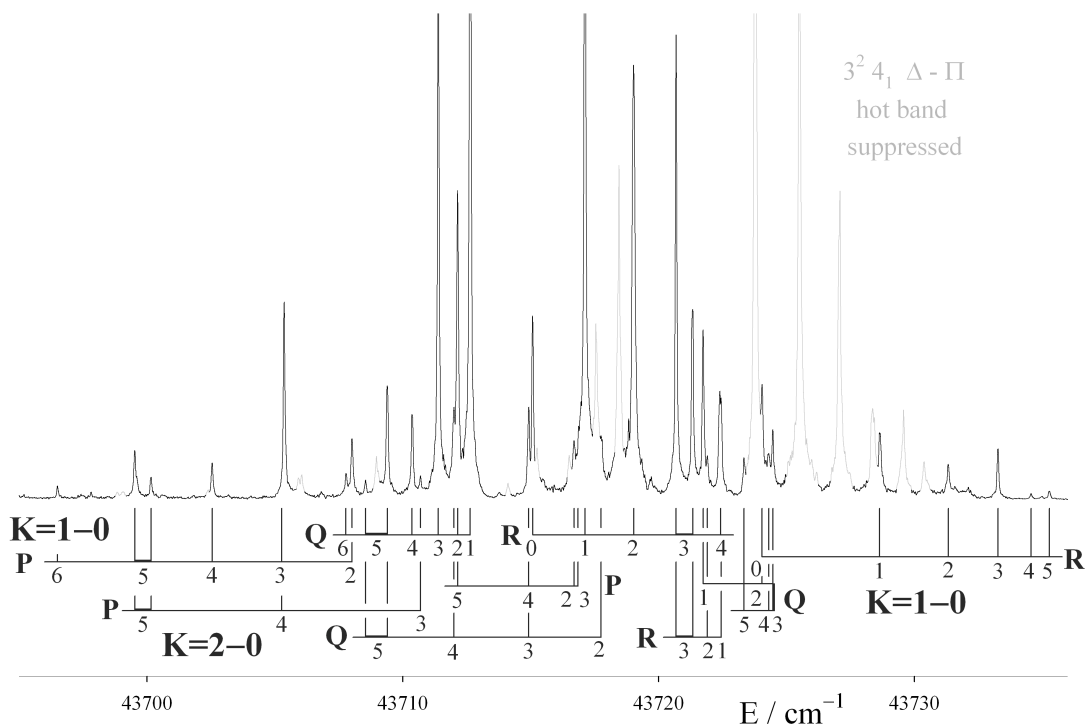


Figure 5-2: Low frequency part of the $v'_4 + v'_6$ (B^2) polyad of the \tilde{A}^1A_u state of C_2H_2 , observed in one-photon laser excitation. Three subbands are present, representing three interacting K -stacks, two with $K' = 1$ and one with $K' = 2$. The lines of an overlapping hot band ($3^2 4_1, \Delta - \Pi$) have been colored gray.

The bands shown in Fig. 5-2 represent transitions from the ground vibrational level of the molecule to the lower two of the three $K' = 1$ levels of the polyad, together with a Coriolis-induced $K = 2 - 0$ subband. One of the $K = 1 - 0$ subbands, with Q head at $43\,712\text{ cm}^{-1}$, is easily assigned and accounts for most of the strong lines. Somewhat surprisingly for a level so low in the vibrational manifold, it contains perturbations at $J' = 4e$ and $5f$. Because of the unexpectedly large Coriolis perturbations and the severe blending, the remaining structure could not be assigned until the $\nu'_4 + \nu'_6 = 3$ (B^3) polyad had been analyzed, and the Darling–Dennison resonance recognized. Calculations of the rotational structure then allowed the remaining lines, and the perturbations, to be assigned immediately.

Experiments with a warmed beam gave the spectrum shown in Fig. 5-3. The energy range illustrated lies below that of Fig. 5-2 by the amount of the ground state ν''_4 fundamental, and shows four of the $K' = 0$ and 2 stacks as hot bands from ν''_4 . The $K' = 0$ subbands belong to the two overtones, namely 4^2 and 6^2 , which have a_g vibrational symmetry. Although the ν''_4 and ν''_6 fundamentals lie only 3 cm^{-1} apart, the two overtones are 52 cm^{-1} apart, as a result of the Darling–Dennison resonance. The third $K' = 0$ hot band, going to the combination level 4^16^1 (b_g vibrational symmetry), is not seen. It would be observable if it lay close enough to one of the $K' = 1$ levels to obtain some intensity by b -axis Coriolis coupling, but such is not the case here. It is calculated to lie at $43\,131\text{ cm}^{-1}$.

The $K' = 1$ and 2 subbands near $43\,110\text{ cm}^{-1}$ in Fig. 5-3 are hot bands with the same upper states as the cold bands near $43\,720\text{ cm}^{-1}$ in Fig. 5-2. In Fig. 5-2 the intensity is carried by the $K' = 1$ level, with the $K' = 2$ level getting its intensity by b -axis Coriolis coupling. In Fig. 5-3 the roles of the two levels are reversed. Consistent with the line strengths for a $K = 2 - 1$ band, the P branches of both bands are expected to be much weaker than the rest of the structure, and are not seen. The intense $K = 2 - 1$ hot band at $43\,138\text{ cm}^{-1}$ in Fig. 5-3 goes to the middle $K' = 2$

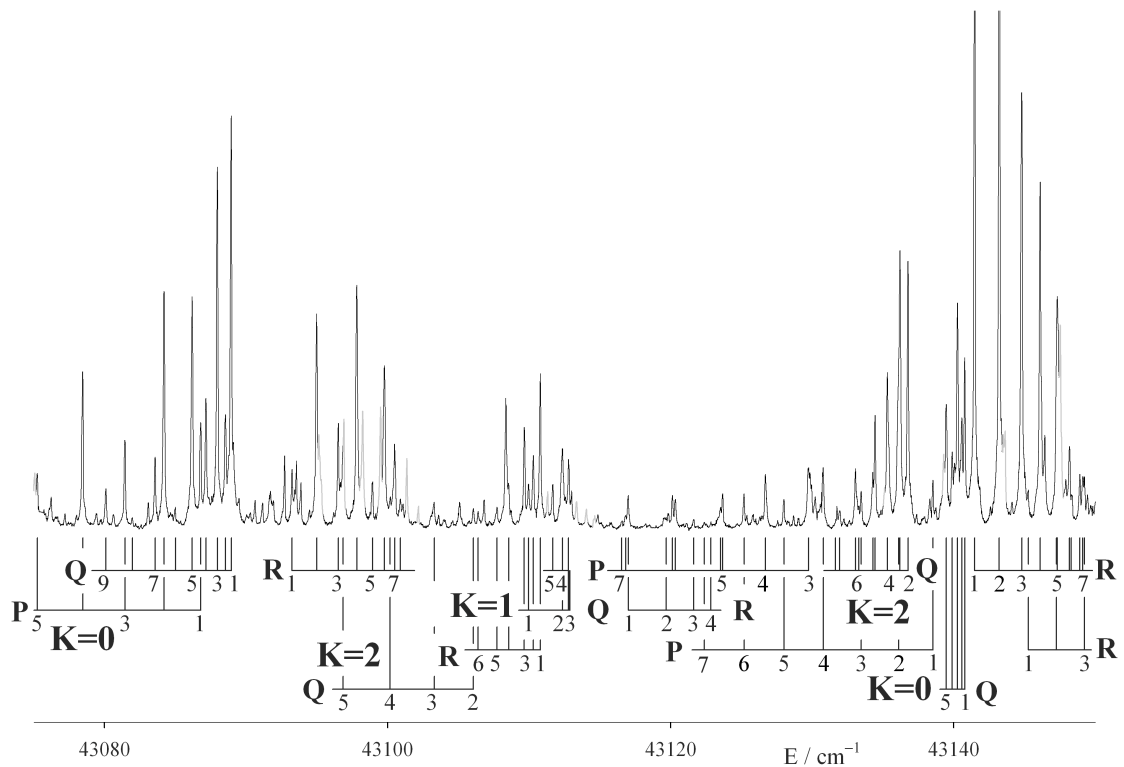


Figure 5-3: Hot bands of the $v'_4 + v'_6 = 2$ (B^2) polyad of the \tilde{A}^1A_u state of C_2H_2 . The region shown lies to the red of that shown in Fig. 5-2 by the amount of the ground state ν''_4 fundamental (π_g , 612 cm^{-1}). Overlapping lines from bands with $\nu''_4 = 2$ have been colored gray.

level. The uppermost $K = 2 - 1$ hot band is calculated to lie at $43\,258\text{ cm}^{-1}$, exactly as the position of the strong Franck–Condon allowed 3_0^1 band. It will be totally buried and has not been searched for.

The assignments of the $K' = 0$ and 2 hot bands near $43\,140\text{ cm}^{-1}$ are confirmed by the observation of some very weak lines near $43\,750\text{ cm}^{-1}$ in the cold spectra, corresponding to Coriolis-induced $K = 0 - 0$ and $2 - 0$ cold bands. These had been noted during the analysis of the cold spectra, but could not be assigned initially. The line assignments of the various subbands are given in Table 5.4. In this table the subbands are labeled for convenience by Roman numerals in order of increasing energy for each K value.

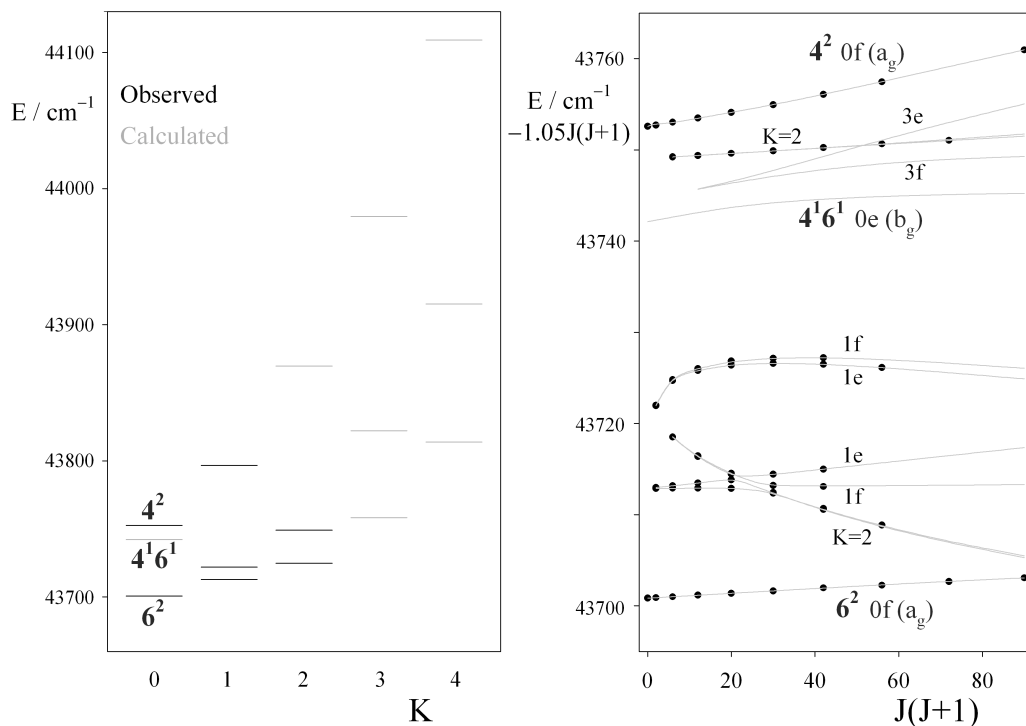


Figure 5-4: (a) K -structure of the $v'_4 + v'_6 = 2$ polyad. Observed levels are shown in black, calculated levels in gray. (b) J -structure of the eight lowest K -stacks of the B^2 polyad, with observed levels shown as black dots and calculated structure as gray lines. A quantity $1.05 \times J(J + 1)$ has been subtracted in order to reduce the term energies to approximately flat lines.

The level structure of the B^2 polyad is illustrated in Fig. 5-4. The left-hand side of Fig. 5-4 shows the K -structure. The two overtones, 4^2 and 6^2 , are almost degenerate in zero-order, with 4^2 lying 2.1 cm^{-1} above 6^2 . However, as a result of the Darling–Denison resonance, they give rise to two well-separated $K = 0$ levels, whose wavefunctions are very nearly the normalized sum and difference of $|4^2\rangle^{(0)}$ and $|6^2\rangle^{(0)}$. The $K = 0$ level of 4^16^1 lies above the midpoint of the two overtones because of the x'_{46} term. For $K = 1$, the a -axis Coriolis coupling complicates the picture. The 4^16^1 level interacts essentially only with the upper of the mixed overtone levels, whose approximate (sum) wavefunction is $2^{-1/2} [|4^2\rangle^{(0)} + |6^2\rangle^{(0)}]$. The lower mixed overtone (difference) is almost unaffected. The result is that the two upper $K = 1$ levels are pushed apart, with one of the dropping almost to the energy of the lower mixed overtone. For $K \geq 2$ the Coriolis coupling between the upper mixed overtone and 4^16^1 is so large that the Coriolis-coupled levels become the top and bottom levels for their K -value. It is possible to view these effects as an interference between the Coriolis and Darling–Denison interactions, which allows the sign of the Darling–Denison parameter to be determined.

The right-hand side of Fig. 5-4 shows the observed and calculated J -structure plotted against $J(J+1)$. Only the low energy levels are illustrated, so that the highest observed $K = 1$ level lies off the top of the figure. The most obvious irregularity is the very strong b -axis Coriolis perturbation between the lowest $K = 2$ level and the second $K = 1$ level. The two levels are almost exactly degenerate in zero-order, such that the splitting between the rises to over 20 cm^{-1} at $J = 7$. The lower level, nominally $K = 2$, is pushed down so strongly that the R branch going to it (see Fig. 5-2) degrades entirely to the red, in contrast to the usual pattern. This level also cuts through the lowest $K = 1$ level, causing the small perturbations mentioned at the beginning of the section.

An unexpected feature in Fig. 5-4 is the presence of an unseen $K = 3$ level

between the two uppermost $K = 0$ levels. It appears not to perturb the nearby $K = 2$ level, despite the possibility of b -axis Coriolis coupling (following $\Delta K = \pm 1$ selection rules), but to interact strongly with the two $K = 0$ levels. Detailed examination of the rotational energy matrices and their eigenvectors confirms that the $K = 2$ and $K = 3$ levels should not interact. The vibrational wavefunctions for these levels are, to a good approximation,

$$\begin{aligned}
 K = 2 : & \quad (2)^{-1/2} \left[|4^2\rangle^{(0)} - |6^2\rangle^{(0)} \right], \\
 K = 3 : & \quad (2)^{-1/2} |4^1 6^1\rangle^{(0)} + \frac{1}{2} \left[|4^2\rangle^{(0)} + |6^2\rangle^{(0)} \right]
 \end{aligned}
 \tag{5.12}$$

The b -axis Coriolis coupling between them would involve the matrix element

$$\langle 4^1 6^1 |^{(0)} \hat{G}_b \left[|4^2\rangle^{(0)} - |6^2\rangle^{(0)} \right],
 \tag{5.13}$$

where the two terms cancel exactly, to give zero. On the other hand, $\Delta K = \pm 3$ interactions between the $K = 3$ level and the two $K = 0$ levels arise from vibrationally allowed cross-terms between the asymmetry and the b -axis Coriolis coupling.

Here, we note that the interactions described above demonstrate that, despite the systematically large matrix elements that couple states within a B^n polyad, the vibrational levels cannot be described as “fully mixed.” That is, each eigenstate of the polyad Hamiltonian has characteristics that are unique, though these characteristics may not be obvious from the normal mode–asymmetric top labels. The fact that such systematic (as opposed to statistical) characteristics can be identified points to the fact that there likely exists a better zero-order basis in which to consider this rovibrational problem. In this better basis, the state labels would indicate the properties of the eigenstates. Although we do not offer a description of a better basis in this work, it seems likely that it would be related to the angular momentum properties of two degenerate harmonic oscillators, as in the description of the vibrational levels of

the linear electronic ground state of acetylene.

With seven of the nine K -stacks with $K = 0 - 2$ assigned, there are enough data for a least squares fit to the upper state term values. A simple model was chosen for the rotational structure. The rotational constants A , $\frac{1}{2}(B+C)$, and $B-C$ were varied just for the overtones 4^2 and 6^2 , and it was assumed that the rotational constants for the combination level 4^16^1 were the averages of those for the two overtones. For the coupling terms, the two Coriolis parameters $2A\zeta^a$ and $B\zeta^b$ and the Darling–Dennison parameter K_{4466} were varied initially, though it was later found that adding a centrifugal distortion correction to K_{4466} improved the fit considerably. This was taken as

$$K_{4466}^{\text{eff}} = K_{4466}^{(0)} + K_{4466,D}K_a^2. \quad (5.14)$$

The vibrational parameters required some care. Since the $K' = 0$ stack of the combination level is not seen, there are only two observable band origins, corresponding to the overtones 4^2 and 6^2 , heavily mixed by the Darling–Dennison interaction. In the end it was decided to include the $J = K = 0$ energies of the two fundamentals ν'_4 and ν'_6 (from the work of Utz *et al.*[2]), and to adjust, by least squares, ω'_4 , ω'_6 , and two of the three anharmonicity parameters x'_{44} , x'_{46} , and x'_{66} . The value of x'_{66} was then fixed at -4.22_6 cm^{-1} , as obtained from combining the position of the ν'_6 fundamental with the deperturbed origin of the 6^3 overtone (described in Section 5.4.2). The fit is extremely good, with an rms error of 0.011 cm^{-1} , which is comparable to the accuracy of the line measurements. The results are given in Table 5.4.1.

The most surprising result is the large size of the parameters x'_{46} and K_{4466} . These are made up of contributions from the vibrational angular momentum and the anharmonic force field, and in both cases the vibrational angular momentum contribution is the larger. It is interesting to compare the anharmonic contributions with those calculated from the anharmonic force field of Ref. [106]. For the Darling–Dennison parameter K_{4466} , where the experimental value, -51.68 cm^{-1} , includes

Table 5.1: Rotational constants from least squares fitting of the B^2 polyad of the \tilde{A}^1A_u state of C_2H_2 . Values are in cm^{-1} .

Vibrational parameters				Rotational parameters			
				6^2		4^2	
ω'_6	772.497	± 0.032	A	13.356	± 0.128	12.857	± 0.138
ω'_4	764.709	0.075	$\frac{1}{2}(B+C)$	1.0806	0.0077	1.0743	0.0080
x'_{66}	-4.226	fixed	$(B-C)$	0.1262	0.0077	0.0530	0.0088
x'_{46}	11.385	0.080					
x'_{44}	0.191	0.047	$2A\zeta_{46}^a$		18.449	0.005	
K_{4466}	-51.678	0.020	$B\zeta_{46}^b$		0.7980	0.0023	
$K_{4466,D}$	0.0381	0.0281					
rms error = 0.0112 cm^{-1}							

The $J = K = 0$ levels lie at 43 700.85 cm^{-1} (6^2 , 1503.28 cm^{-1} above T_{00}), 43 742.13 (4^16^1 , 1544.56), 43 752.57 (4^2 , 1555.00). Derived Coriolis constants: $\zeta_{46}^a = 0.7038$, $\zeta_{46}^b = 0.7111$; $(\zeta_{46}^a)^2 + (\zeta_{46}^b)^2 = 1.001$. The only correlation coefficients with magnitudes over 0.9 are $\frac{1}{2}(B+C)$ (6^2)/ $\frac{1}{2}(B+C)$ (4^2) -0.996 , $A(6^2)/A(4^2)$ -0.981 , and ω'_4/x'_{44} -0.949 .

-28.24 cm^{-1} from the vibrational angular momentum (meaning that the anharmonic contribution -23.44 cm^{-1}) a calculation using Eq. 5.11 gives -16.6 cm^{-1} . Similarly, for x'_{46} , where the anharmonic contribution is -2.73 cm^{-1} , a calculation using the symmetry-allowed terms from Mills' perturbation theory expression [153],

$$x'_{46} = \frac{1}{4}\phi_{4466} - \frac{1}{4}\sum_k \phi_{44k}\phi_{k66}/\omega_k, \quad (5.15)$$

gives $+1.08 \text{ cm}^{-1}$. At the same time experimental anharmonicity parameters x'_{44} and x'_{66} in Table 5.4.1 are quite small, which suggests that the pure bending motions are comparatively harmonic, once allowance is made from the vibrational angular momentum.

As for the Coriolis coupling parameters, these are almost unchanged from the values found in the fundamentals [2], where $2A\zeta^a = 18.47 \text{ cm}^{-1}$ and $B\zeta^b = 0.787 \text{ cm}^{-1}$. It is interesting to see how accurately the zeta sum rule (Eq. 5.5) holds in the B^2 polyad. The derived values of ζ_{46}^a and ζ_{46}^b are given in Table 5.4.1; the sum of their

squares is 1.001, compared to the theoretical value of 1.

The variation in the A rotational constants with v'_4 and v'_6 appears to be much smaller for the overtones (Table 5.4.1) than for the fundamentals [2], where $A(4^1) = 11.36(8) \text{ cm}^{-1}$ and $A(6^1) = 14.59(13) \text{ cm}^{-1}$. However, we note that the average of $A(4^1)$ and $A(6^1)$ is close to the value of the zero-point level, $13.057(5) \text{ cm}^{-1}$. [118] It is known from the N_2H_2 spectrum [140] that there is almost 100% correlation between the A constants of two strongly a -axis Coriolis-coupled levels, such that only their sum is well-determined. This may have also affected the determinations for the C_2H_2 fundamentals. In the overtones the correlation is less severe because there are more vibrational levels to provide data. On subject of correlation, we may also note that our fitting models incorporate only the frequency information contained in the spectra and not the intensity information. Using the intensity information in the spectra, if it were meaningful, would allow the model to distinguish energy level shifts due to variation in the diagonal energy terms, including the rotational constants, from energy level shifts due to off-diagonal terms such as the Coriolis ζ constants. Unfortunately, the intensity information in our LIF spectra is complicated by a number of factors that affect the relative detection efficiencies of the populated states, in addition to the pulse-to-pulse fluctuations in laser power that conspire to render intensity information qualitative at best.

An interesting minor point is that the (deperturbed) asymmetry parameter ($B - C$) is much smaller in the 4^2 level than it is in the 6^2 level. This is consistent with the C_2H_2 molecule becoming nonplanar on average as the torsional vibration is excited. The rationale is as follows. Since the inertial b and c axes interchange when C_2H_2 is twisted from *trans*-bent to *cis*-bent, there must be a point near a twisting angle of 90° where it is accidentally a symmetric top, with $B - C = 0$. The prototype molecule for this effect is H_2S_2 , which is 90° twisted and accidentally almost exactly a symmetric top [6, 154].

5.4.2 The $v'_4 + v'_6 = 3$ polyad (B^3)

The B^3 polyad consists of four vibrational levels, 4^3 , 4^26^1 , 4^16^2 and 6^3 . Their symmetries are a_u , b_u , a_u and b_u respectively. Two spectra of the polyad have been recorded by IR-UV double resonance. In one, the ground state ν_3'' fundamental ($\ell'' = 0$) was used as the intermediate level in order to observe the $K' = 1$ levels. In the other, the $\nu_3'' + \nu_4''$ combination level ($\ell'' = 1$) was used to observe the $K' = 0$ and 2 levels. Because of the strong b -axis Coriolis coupling, some of the K' levels appear in both spectra.

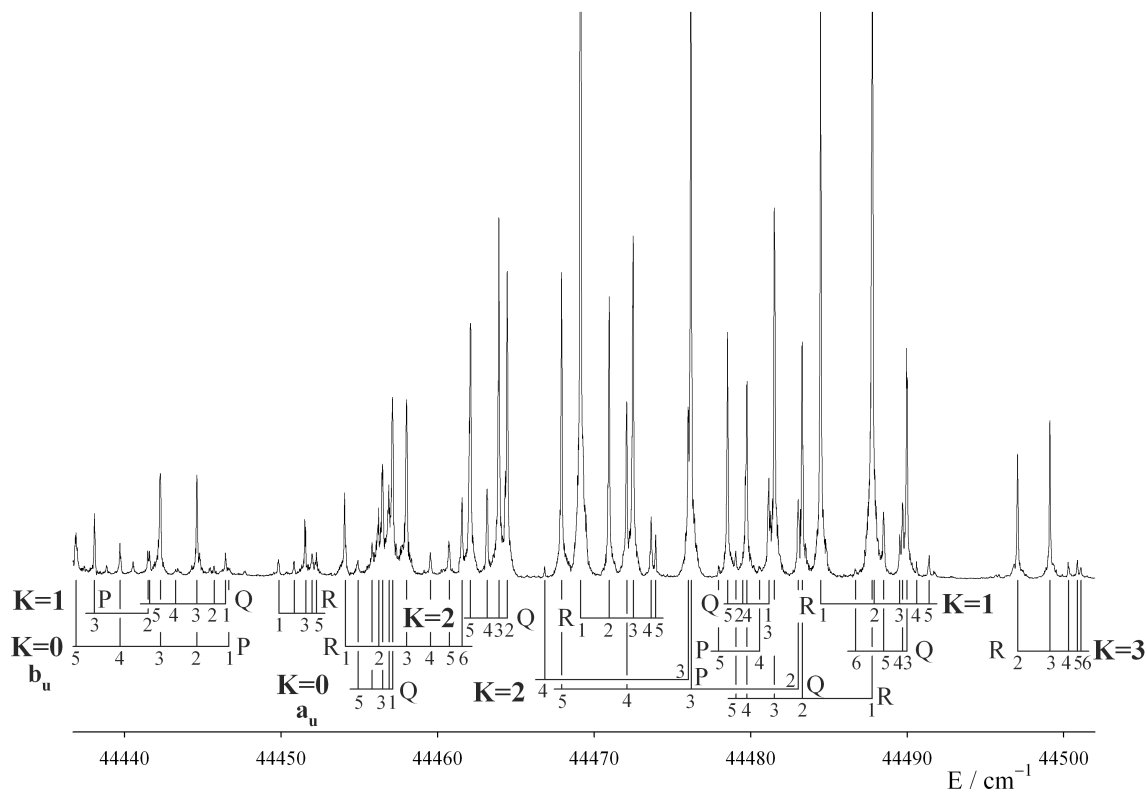


Figure 5-5: Low energy part of the $v_4 + v_6 = 3$ (B^3) polyad of the \tilde{A}^1A_u state of C_2H_2 , as observed in IR-UV double resonance via the $Q(1) - Q(5)$ lines of the ground state $\nu_3 + \nu_4$ combination band (3897.16 cm^{-1}).

The low energy part of the polyad is illustrated in Fig. 5-5, as seen following IR pumping of the Q branch of the $\nu_3'' + \nu_4''$ band at 3897.16 cm^{-1} . This branch is

very compact, so that when the IR laser is tuned to its head the first five lines are excited simultaneously, populating the $J = 1f - 5f$ rotational levels. This allows the complete double resonance spectrum to be recorded in one scan, though it loses the state-selectivity of pumping individual rotational lines. Nevertheless the line assignments could be made straightforwardly, using lower state combination differences. To assist with the assignments a scan was also taken via the $P(3)$ line of the band, which populates the $J = 2e$ levels. This was valuable in distinguishing the $K' = 0$ subbands, since the branch structures depend on the parity of the intermediate levels, as described above.

The strongest features in Fig. 5-5 are two close-lying $K' = 2$ subbands. The upper states interact with each other, and with nearby $K' = 1$ and 3 levels, inducing extra subbands. At the low energy side are two $K' = 0$ subbands separated by 8 cm^{-1} . They form a pair with b_u and a_u symmetries. There is also another weak Coriolis-induced $K' = 1$ band.

The central part of the B^3 polyad is illustrated in Fig. 5-6. It contains the other two $K' = 0$ subbands, again as a b_u/a_u pair, but this time separated by only 0.7 cm^{-1} . Also present are another strong $K' = 2$ subband and weaker Coriolis-induced $K' = 1$ and 3 bands. The remainder of the polyad, not illustrated, consists of a $K' = 1$ subband at $44\,614 \text{ cm}^{-1}$ and a $K' = 2$ subband at $44\,703 \text{ cm}^{-1}$. These latter lie well above the rest of the polyad, and are not perturbed.

The K - and J -structures of the B^3 polyad are illustrated in Fig. 5-7. The left-hand side shows clearly how the Darling–Dennison resonance groups the four $K = 0$ levels into a_u/b_u pairs, separated by about 100 cm^{-1} . As expected from the near degeneracy of the ν'_4 and ν'_6 fundamentals, the four zero-order basis levels lie quite close to each other, with the overtones below the combinations by an amount $2x'_{46}$. However, their separations are much smaller than the Darling–Dennison matrix element. The result is that one level of each symmetry is pushed up, and the other down, by the amount of

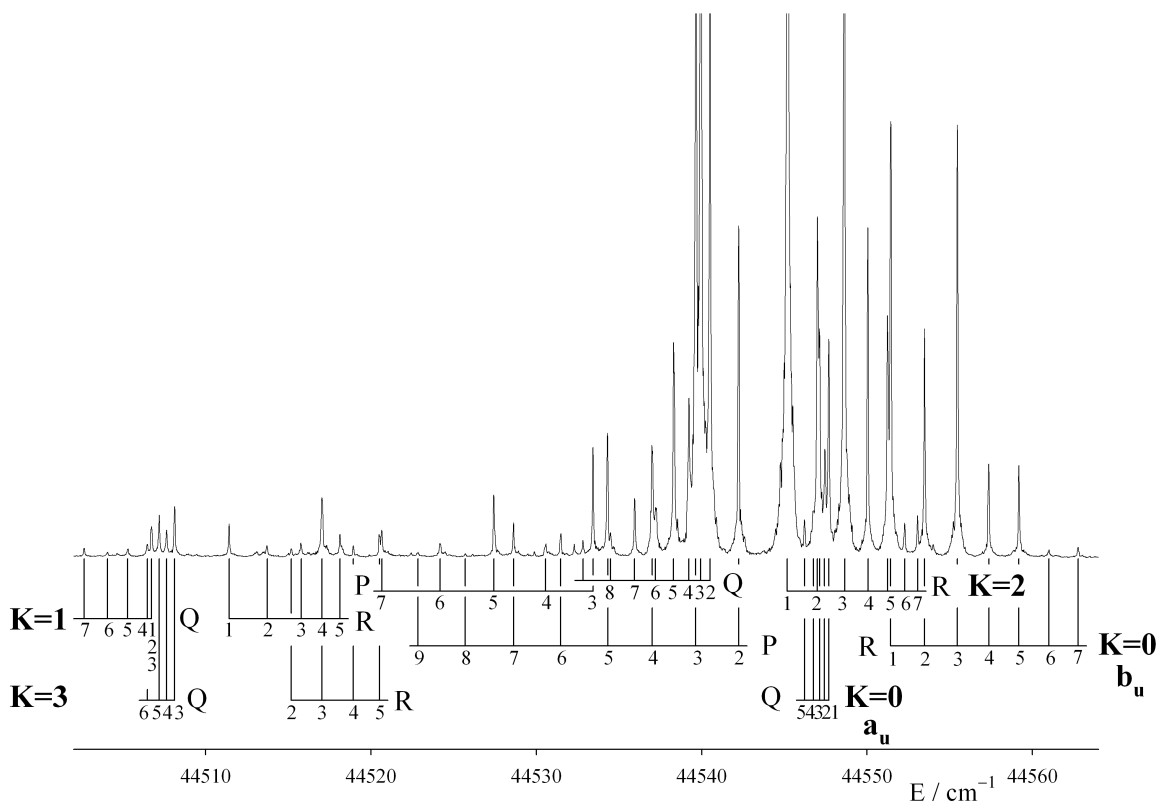


Figure 5-6: Central part of the B^3 polyad. This spectrum is a continuation of Fig. 5-5 to higher energy. The two $K' = 0$ subbands appear to be a single subband with R , Q and P branches but closer examination shows that the Q branch ($K = 0, a_u$) is shifted up by 0.73 cm^{-1} relative to the R and P branches ($K = 0, b_u$).

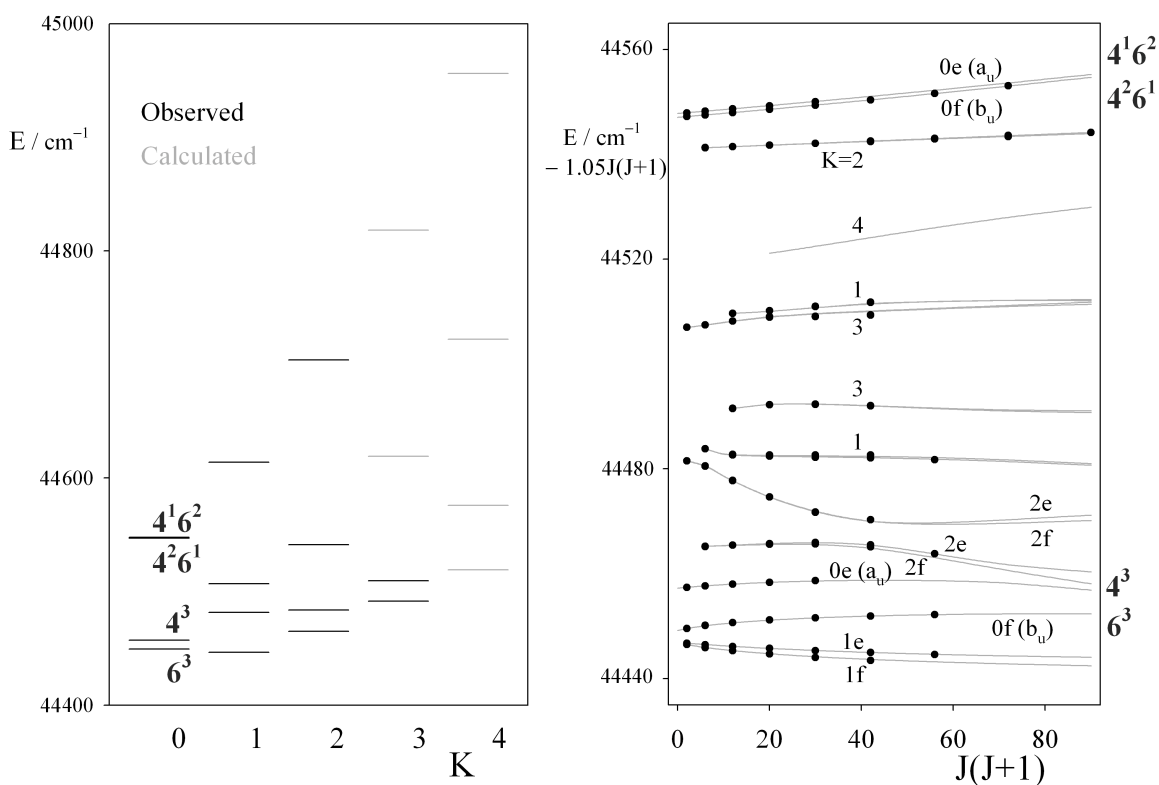


Figure 5-7: (a) K -structure of the B^3 polyad of the \tilde{A}^1A_u state of C_2H_2 , with the observed levels shown in black and the calculated levels shown in gray. Vibrational assignments are marked for the $K = 0$ levels, as given by their leading eigenvectors coefficients. For $K \geq 1$ levels the harmonic basis functions are so mixed that it is meaningless to give assignments. (b) J -structure of the 13 lowest energy K -stacks. Observed levels are shown as dots, calculated levels as gray lines. Two major avoided crossings occur: one between the $K = 1$ and 3 levels near 44150 cm^{-1} and the other involving the second $K = 2$ level, which interacts with the lowest $K = 2$ and second $K = 1$ levels.

the coupling matrix element, which in this case is 50 cm^{-1} . The patterns for higher K values are not so simple, though in first approximation that Coriolis coupling between the combination levels 4^16^2 and 4^26^1 pushes one of the levels far above the others.

The J -structure patterns show a number of local avoided crossings caused by the b -axis coupling elements. These follow $\Delta K = \pm 1$ selection rules in the rigid rotator basis, and therefore act to destroy the goodness of the quantum number K as a label. At the same time the Darling–Dennison resonance and the a -axis coupling, though diagonal in K , scramble the harmonic oscillator basis levels, so that the resulting patterns are often quite surprising. An example is given by the lowest two $K = 2$ levels. The upper of these two, which begins near $44\,480 \text{ cm}^{-1}$, is almost degenerate with the second $K = 1$ levels, and it gets pushed down strongly by b -axis coupling with it. As in the B^2 polyad, the R branch going to it degrades entirely to the red (see Fig. 5-5). At $J = 6$, this $K = 2$ level undergoes an avoided crossing with the lowest $K = 2$, after which it goes on to perturb the two $K = 0$ levels at the bottom of the pattern. Very clearly the K quantum number loses all meaning, as was noted by Utz *et al.*[2] in their analysis of the fundamentals, though it is retained here as a convenient label. Another unexpected avoided crossing occurs between the $K = 1$ and 3 levels near $44\,510 \text{ cm}^{-1}$.

Fourteen K' stacks have been identified, representing all the stacks with $K = 0-2$ together with two $K' = 3$ stacks. This has allowed a detailed least squares treatment, of which the results are given in Table 5.4.2. As might be expected from the density of perturbations, the main problem encountered was that of matching the eigenvalues of the Hamiltonian to the observed upper state term values. After some experimentation, the tactic adopted was to transform the Hamiltonian matrix in several steps. In the first step the Darling-Dennison resonance and the a -axis Coriolis coupling elements were diagonalized, after which the full Hamiltonian matrix was transformed by the resulting eigenvectors. Since the elements eliminated were diagonal in K , the

transformed basis states preserved the values of K . In the second step the asymmetry elements ($\Delta K = \pm 2$) were diagonalized, such that the next set of transformed functions still retained the odd- or even- K character of the original basis functions. Finally the doubly transformed Hamiltonian matrix was diagonalized, eliminating the b -axis coupling, and the eigenvalues sorted according to their eigenvector coefficients. Even so, it was found that the sorting was not always accurate at the most severe avoided crossings, so that the stacks with a given nominal K -value were then placed in ascending order.

Table 5.2: Rotational constants from least squares fitting of the B^3 polyad of the $\tilde{A} \ ^1A_u$ state of C_2H_2 . Values are in cm^{-1} . The band origins (T_0) are given relative to T_{00} ($\tilde{A} \ ^1A_u$) = 42 197.57 cm^{-1} , from Ref. [118].

Vibrational parameters				Rotational parameters			
				6^3		4^3	
T_0 (4^3)	2295.008	± 0.102	A	13.000	± 0.050	13.121	± 0.051
T_0 (4^26^1)	2321.592	0.068	$\frac{1}{2}(B + C)$	1.0870	0.0028	1.0685	0.0030
T_0 (4^16^2)	2314.791	0.087	$(B - C)$	0.1406	0.0072	0.0798	0.0102
T_0 (6^3)	2279.470	0.086	A_Δ		-0.398	± 0.050	
			$2A\zeta_{46}^a$		18.363	0.009	
$K_{4466}^{(0)}$	-51.019	0.009	$2A\zeta_D^a$		-0.0228	0.009	
$K_{4466,D}$	0.224	0.008	$B\zeta_{46}^b$		0.8024	0.0029	
rms error = 0.0282 cm^{-1}							

The $J = K = 0$ levels lie at 44 457.26 cm^{-1} (4^3), 44 547.04 (4^26^1), 44 547.77 (4^16^2), 44 449.15 (6^3). Derived Coriolis constants: $\zeta_{46}^a = 0.703_0$, $\zeta_{46}^b = 0.708_3$; $(\zeta_{46}^a)^2 + (\zeta_{46}^b)^2 = 0.996$. The parameter A_Δ raises the A constant of 4^26^1 (and lowers that of 4^16^2) relative to its value as interpolated between those for 4^3 and 6^3 . The only correlation coefficients with magnitudes over 0.9 are $\frac{1}{2}(B + C)$ (6^3)/ $\frac{1}{2}(B + C)$ (4^3) -0.948, $A(6^3)/A(4^3)$ -0.978, and $2A\zeta^a/A_\Delta$ -0.934.

Again, a simple model was used for the rotational energy, where only the A , $\frac{1}{2}(B + C)$, and $B - C$ constants for the overtones 4^3 and 6^3 were varied, with those for the combinations being interpolated between those of the overtones. As in the B^2 polyad, the coupling terms used were K_{4466} , $2A\zeta^a$, and $B\zeta^b$, though the first two were allowed centrifugal distortion corrections as in Eq. 5.14. No attempt was made

to write the band origins in terms of anharmonicity parameters, instead the four deperturbed origins were taken as adjustable parameters.

The final fit was not quite as good as that for the B^2 polyad, but there are other factors to consider. The first is the possibility of Fermi resonance between the B^3 polyad and the 2^1B^1 polyad, which lies about 100 cm^{-1} below. In fact, with the strong a -axis Coriolis coupling in both polyads the K -structure of 2^1B^1 catches up rapidly to that of B^3 , such that its upper $K = 2$ level lies only 40 cm^{-1} below the lowest $K = 2$ of B^3 . An attempt was made to allow for interpolyad interactions by extending the rotational matrices to include this Fermi resonance, but the results were inconclusive, presumably because the small perturbation shifts could be absorbed into effective constants for the B^3 polyad. Another factor is that the interpolation of the rotational constants for the combination levels reduces the flexibility of the model. An additional parameter representing the shift in the A rotational constant for the two combination levels, up and down from their interpolated values, was eventually added. It made a considerable improvement in the quality of the fit.

A comparison of Tables 5.4.1 and 5.4.2 shows that the coupling parameters and rotational constants are essentially the same in the B^2 and B^3 polyads, to within their error limits. As was found in the B^2 polyad, the asymmetry parameter $B - C$ is smaller for the 4^3 overtone than for the 6^3 overtone, again suggesting that excitation of the torsional vibration ν_4 makes the molecule significantly nonplanar. The line assignments for the B^3 polyad are included in Table 5.4.

5.4.3 The B^4 and B^5 polyads

Given the vibrational and rotational constants from the B^2 and B^3 polyads, the structures of the higher bending polyads can be predicted with fair accuracy. The bands are weak, since higher order anharmonicity terms are required to provide their intensity, but it has been possible to identify portions of both the B^4 and B^5 polyads.

The B^4 polyad consists of five *gerade* vibrational levels, 4^4 , 4^36^1 , 4^26^2 , 4^16^3 and 6^4 , whose $K = 0$ rotational levels are calculated to be spread over the energy range of $45\,170 - 45\,365\text{ cm}^{-1}$. A search of the one-photon LIF spectra immediately identified the two lowest $K' = 1$ subbands, within 2 cm^{-1} of their predicted positions, together with a Coriolis induced subband. These are illustrated in Fig. 5-8. Also appearing in Fig. 5-8 is the top $K' = 1$ member of the 2^1B^2 polyad, which is expected to be in Fermi resonance with the B^4 polyad. The fact that the B^4 levels are so close to their expected positions indicates that the effects of the Fermi resonance are quite small. Examination of the spectra taken with a warmed beam then allow identification of the lowest $K = 0$ level and the second $K' = 2$ level, as hot bands from ν_4'' . These levels lie within 1 cm^{-1} of their predicted positions.

All five $K' = 1$ levels of the B^4 polyad can be identified. The two lowest are illustrated in Fig. 5-8, while the top three lie at $45\,276$, $45\,301$, and $45\,446\text{ cm}^{-1}$, all within $1 - 2\text{ cm}^{-1}$ of their calculated positions. The levels at $45\,276$ and $45\,446\text{ cm}^{-1}$ have not been observed before, but the $45\,301\text{ cm}^{-1}$ level, which is almost coincident with the $3^3\ K = 1$ level, had been seen earlier by Scherer *et al.*[3] The $45\,301\text{ cm}^{-1}$ level has since been identified as a bending level [2], but it is now possible to assign it unambiguously as the second-highest $K' = 1$ member of the B^4 polyad. The evidence for the assignment is very clear. First, it has essentially no asymmetry splitting. Drabbels *et al.*[155] give the effective value of $B - C$ as $-0.001(3)\text{ cm}^{-1}$, while our calculation gives $B - C = 0.006\text{ cm}^{-1}$. In comparison, the zero-point level of the $\tilde{A}\ ^1A_u$ state has $B - C = 0.0931\text{ cm}^{-1}$ [118]. Second, it lies a mere 0.3 cm^{-1} from its predicted position. It can be argued that its position is affected by the presence of the nearby 3^3 level but, since the two level lie only 0.4 cm^{-1} apart, any shift caused by interaction between them must be small. In fact, a reanalysis[155] of the two interacting levels led to the conclusion that the best fit resulted when the interaction strength was set equal to zero.

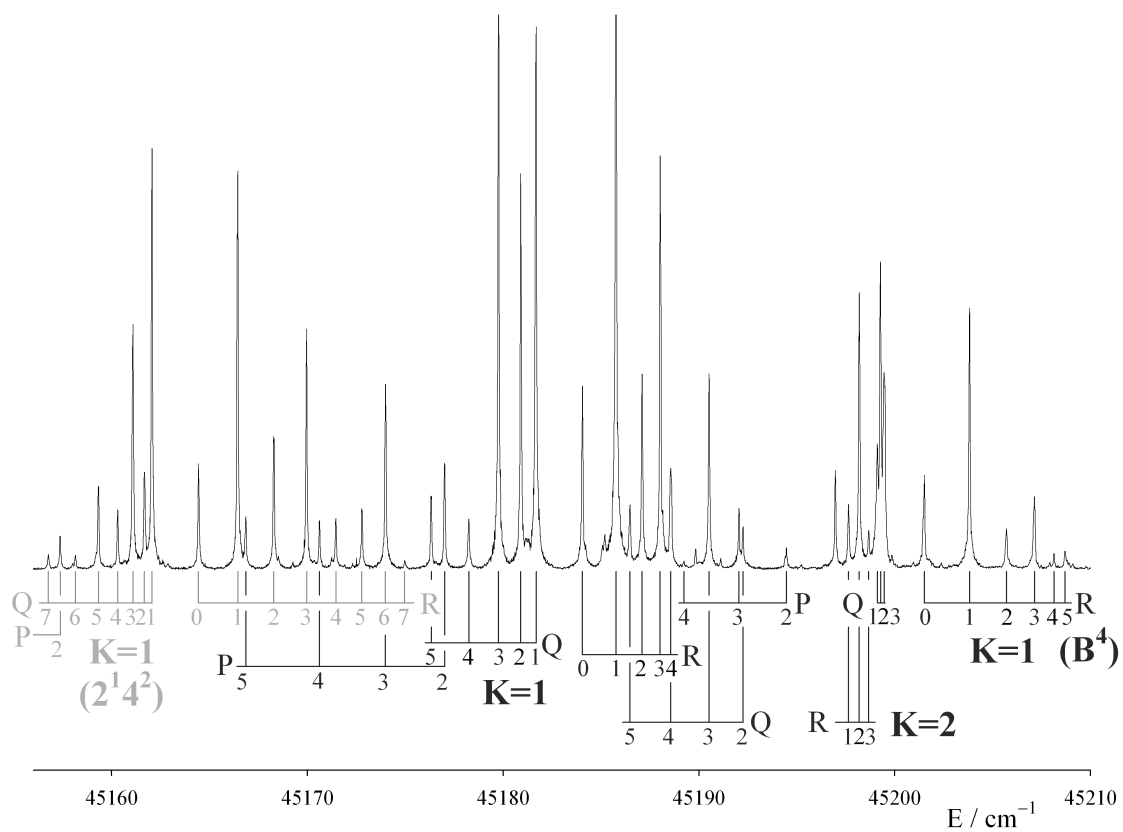


Figure 5-8: Three of the lowest energy subbands of the B^4 polyad, as seen in one-photon laser excitation. There is a weak Fermi resonance with the $K=1$ level of $2^1 4^2$ (assignments shown in gray).

No attempt has been made to fit the levels of the B^4 polyad by least squares because only eight of the fifteen stacks with $K' = 0 - 2$ have been found, and it is clear that at least two of the stacks are perturbed. For reference, the calculated level pattern is given in Table 5.3. It is interesting to note how the $K = 1$ asymmetry splittings vary erratically in these bending polyads: the pattern in the zero-point level is that the $J = 1e$ level lies 0.09 cm^{-1} above the $J = 1f$ level, but in the B^4 polyad the $J = 1e$ levels are calculated to lie below $J = 1f$ for the lowest two a_g levels, while for the two uppermost $K = 1$ levels the asymmetry splitting is close to zero.

Table 5.3: Calculated $J = K$ rotational levels of the B^4 and B^5 polyads (cm^{-1}). A quantity $1.074 \times J(J + 1)$ has been subtracted in order to facilitate comparison with Q branch positions in the spectra.

	$K = 0$	$K = 1e$	$K = 1f$	$K = 2$
B^4	45 171.80 (a_g)	45 180.76	45 180.79	45 191.23
	45 206.94 (b_g)	45 197.94	45 197.84	45 220.97
	45 239.79 (a_g)	45 275.13	45 275.18	45 266.46
	45 361.62 (b_g)	45 301.63	45 301.63	45 346.16
	45 363.22 (a_g)	45 447.64	45 447.64	45 556.89
B^5	45 894.42 (b_u)	45 896.13	45 896.46	45 912.06
	45 914.48 (a_u)	45 928.16	45 928.18	45 937.90
	46 006.85 (b_u)	45 979.55	45 979.56	46 006.98
	46 017.50 (a_u)	46 076.83	46 076.84	46 058.26
	46 192.59 (b_u)	46 113.30	46 113.30	46 166.75
	46 192.68 (a_u)	46 296.23	46 296.23	46 423.83

The B^5 polyad consists of six *ungerade* vibrational levels, whose $K' = 0$ subbands are calculated to lie in the region $45\,890 - 46\,200 \text{ cm}^{-1}$. This is an extremely crowded region of the double resonance spectrum, where five polyads overlap. Besides B^5 , bands are expected from 3^3B^1 , 3^15^1 , 1^1B^1 , and 2^1B^3 . The 3^3B^1 polyad gives the most intense bands, and has already been assigned by Mizoguchi *et al.* [138], the 3^15^1 band has been assigned by Tobiasson *et al.*[137] Reasonable predictions can then be made for the K -structures of the other two polyads, based on the properties of the B^1 and B^3 polyads. These indicate that there will be no structure with $K' = 0 - 2$

from overlapping polyads above $46\,150\text{ cm}^{-1}$.

As seen in double resonance via the ground state $\nu_3'' + \nu_4''$, the region of $46\,150 - 46\,240\text{ cm}^{-1}$ contains six subbands. It is immediately possible to identify three of these as belonging to the B^5 polyad since they lie within 2 cm^{-1} of the positions calculated from the constants of the B^2 and B^3 polyads (see Table 5.3). These three are the close pair of $K' = 0$ levels and the $K' = 2$ level illustrated in Fig. 5-9. The calculations predict that the two topmost $K' = 0$ levels of the B^5 polyad will form an a_u/b_u pair with the a_u member higher in energy 0.09 cm^{-1} . What is observed is an a_u/b_u pair with the a_u member higher by 0.3 cm^{-1} . (The small difference between the observed and calculated positions is not considered significant.) The reason why the topmost $K' = 0$ levels of a bending polyad form a close pair is that they correlate with what would be the component of highest vibrational angular momentum if the molecule were linear. For such a state, a perturbation would only lift the degeneracy in high order.

Given that the predictions of the levels of the B^5 polyad appear to be correct within a few cm^{-1} , it should be possible to identify more of them in the crowded region at lower energy. Some likely candidates can be picked out but, until the various resonances between the overlapping polyads are better understood, a discussion of them would be premature.

Two other subbands appear in Fig. 5-9. One of these is the axis-switching-induced $K' = 3$ subband of the 3^15^1 level, the position of which is consistent with the constants for that level given by Tobiasson *et al.*[137] The other is a $K' = 0$ (b_u) subband at $46\,175\text{ cm}^{-1}$, which seems to be associated with a $K' = 2$ subband at $46\,227\text{ cm}^{-1}$ (not shown). Near this energy, every level of the \tilde{A}^1A_u state that should exist has been accounted for, and it seems that these subbands may represent levels of the *cis*-well of the $\tilde{A}(S_1)$ that tunnel through the *cis-trans* isomerization barrier and obtain some intensity through interactions with nearby levels of the *trans*-well.

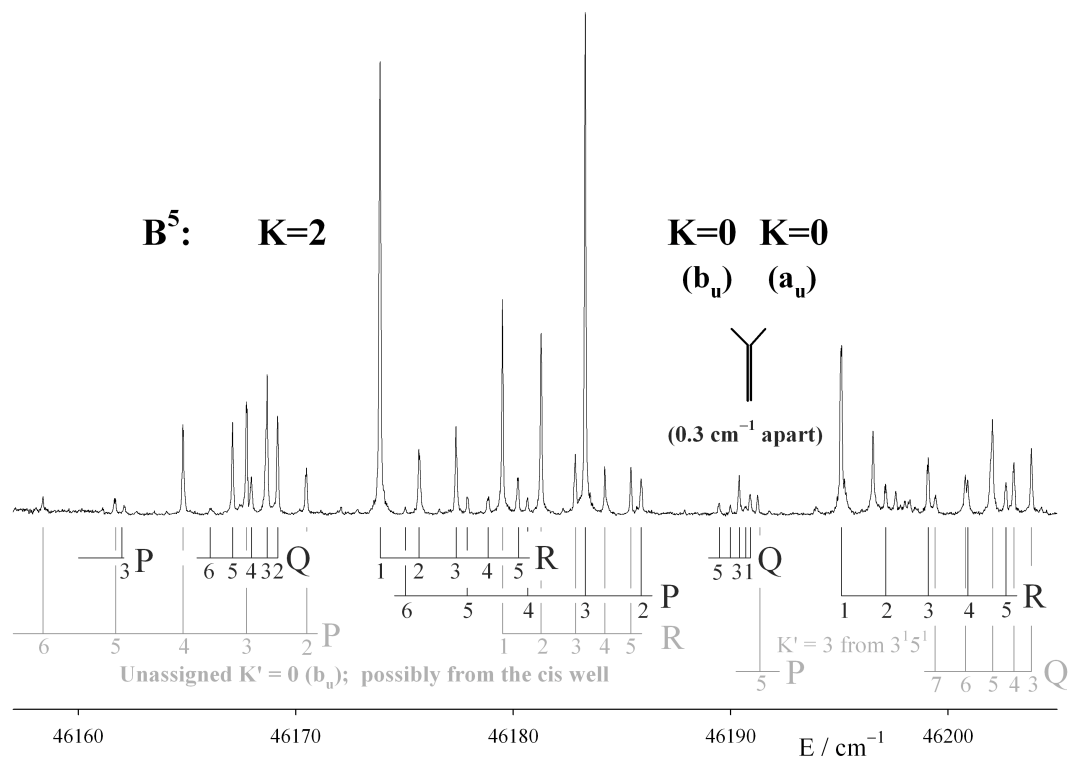


Figure 5-9: The two topmost $K' = 0$ subbands of the B^5 polyad, as seen in IR-UV double resonance via the Q branch of $\nu_3 + \nu_4$ at 3897.16 cm^{-1} . These form a very close pair, with the $K' = 0 (a_u)$ state lying 0.30 cm^{-1} above the $K' = 0 (b_u)$ state. The R and P branches belong to the b_u state, and the Q branch to the a_u state. Also shown, with assignments marked in black, is the second highest $K' = 2$ subband. Two other subbands, marked in gray, are the $K' = 3$ subband of $3^1 5^1$ and an unidentified $K' = 0$ subband which might possibly represent a level of the S_1 *cis*-well.

5.5 Discussion

In this work, detailed rotational analyses of the pure bending polyads with $v'_4 + v'_6 = 2$ and 3 have been carried out for the \tilde{A}^1A_u state of acetylene. The $v'_4 + v'_6 = 2$ polyad (B^2) was recorded in high sensitivity one-photon laser-induced fluorescence spectra, while the $v'_4 + v'_6 = 3$ polyad (B^3) polyad was recorded by IR-UV double resonance, using the ground state ν''_3 fundamental and $\nu''_3 + \nu''_4$ combination level as intermediates. The bands are weak because they are Franck–Condon forbidden; their intensity comes from anharmonic mixing of their upper states with the Franck–Condon-allowed levels of the 3^n and $2^m 3^n$ progressions.

The structures of the higher bending polyads are unexpectedly complicated because, in addition to the Coriolis coupling that was recognized[2] in the fundamentals, they suffer from unusually strong Darling–Dennison resonance, where the parameter K_{4466} is no less than -51 cm^{-1} . Its effect is that, even for $K = 0$, the members of a polyad with the same vibrational symmetry are pushed apart by amounts on the order of $50 - 100 \text{ cm}^{-1}$, even though the fundamentals themselves are almost degenerate. For $K \geq 1$ the a -axis Coriolis coupling causes the vibrational levels with different symmetry to interact with each other, following $\Delta K = 0$ selection rules, while the b -axis Coriolis coupling cause local interactions between close-lying levels with different K -values.

An interesting result of the strong a -axis Coriolis coupling is that the asymmetry splitting in the higher $K = 1$ member of a bending polyad is almost zero. The reason for this is that their wavefunctions contain nearly equal mixtures of basis states with a and b vibrational symmetries, so that the equal an opposite asymmetry splittings cancel in the heavily Coriolis-mixed levels.

As can be seen from Eqs. 5.9 and 5.11, the strengths of the Coriolis coupling and Darling–Dennison resonance both depend on the vibrational quantum numbers, which means that they becomes extremely large in the higher polyads. Nevertheless

the dependence is perfectly regular, so that it is possible to predict the level structures of the polyads with $\nu'_4 + \nu'_6 = 4$ and 5 with good accuracy, and to identify some of their K -stacks. The bands involved are extremely weak, as might be expected since the intensity is transferred to them from the Franck–Condon-allowed bands only by high order mixing terms. Once allowance is made for the Darling–Dennison resonance, the pure bending vibrational motion is found to be comparatively harmonic. The underlying level structure can be represented by the following constants:

$$\begin{aligned} \omega'_4 &= 764.71, & \omega'_6 &= 772.50, & x'_{44} &= 0.19, \\ x'_{66} &= -4.23, & x'_{46} &= 11.39 \text{ cm}^{-1}, \end{aligned} \tag{5.16}$$

where, as discussed below, the value of x'_{46} arises mostly from the Coriolis coupling.

The Coriolis coupling is a symptom that vibrational angular momentum is present. As Eq. 5.16 shows, the two bending vibrations ν'_4 and ν'_6 have almost the same frequency. If the molecule were linear they would coalesce into the degenerate *cis*-bending vibration (ν_5, π_u) of the linear configuration, with its associated vibrational angular momentum. This angular momentum does not go away in the bent molecule, but instead appears as a coupling of the two nearly degenerate vibrations. In the rotational structure it gives rise to the *a*- and *b*-axis Coriolis coupling, while in the vibrational structure it adds to the Darling–Dennison resonance parameter K_{4466} and the anharmonicity parameter x'_{46} . Remarkably, the vibrational angular momentum contributes the larger portion of both these parameters, which are usually considered to arise from the anharmonic force field. Specifically, it adds a quantity $2 [A(\zeta_{46}^a)^2 + B(\zeta_{46}^b)^2] = 14.1 \text{ cm}^{-1}$ to x'_{46} , and -2 times this quantity to K_{4466} . The zeta sum rule, given as Eq. 5.5, is found to hold very accurately in the bending polyads.

The analysis of the lowest bending polyads of the $\tilde{A} \ ^1A_u$ state has important

consequences for the understanding of the higher vibrational levels, particularly for those approaching the barrier to *cis-trans* isomerization. A significant result is that the singlet state vibrational level which appears to interact [3] with the low- J levels of the 3^3 , $K' = 1$ stack can now be definitively assigned. This state has been found to interact via $\Delta K = 0$ selection rules, albeit with a very small matrix element [155], suggesting that the mechanism involves a -axis Coriolis coupling or anharmonic resonance. Based on their assignment of the ν'_4 and ν'_6 fundamentals, Utz *et al.*[2] suggested that the interacting state was one of the vibrationally a_g members of the B^4 polyad, 4^4 , 4^26^2 , or 6^4 . With the accurate simulation of the B^4 polyad available from the present work, the interacting level is now seen to be the second-highest $K = 1$ member of the B^4 polyad. This is a combination level with nominal b_g vibrational symmetry, though the strength of the a -axis Coriolis coupling is so great in this polyad that for $K > 0$ the resulting levels are complete mixtures of a_g and b_g vibrational basis states.

The patterns found in the B^2 and B^3 pure bending polyads can be extended to the analyses of combination polyads such as 2^1B^2 and 3^1B^2 . That is, the Coriolis/Darling–Dennison polyad model for the pure-bending polyads establishes a template for the expected energy-level patterns in the remainder of the spectra. The vibrational identities of the higher lying combination states are best understood in terms of to which polyad they belong. Those states that do not fit within the polyad structure, established in this chapter, stand out as unique and must be accounted for by a zero-order state not belonging to the S_1 *trans*-well. One such state, suspected to be a vibrational level belonging to the S_1 *cis*-well, has been identified in this chapter, and several others will be discussed in the chapters that follow.

Table 5.4: Assigned rotational lines of the pure bending polyads of the \tilde{A}^1A_u state of C_2H_2 . The members of the upper state polyads are labeled with Roman numerals in order of increasing energy for each K -value. Blended lines are marked with an asterisk (*).

The $v'_4 + v'_6 = 2$ polyad, B^2											
I: $K = 0 - 1$				III: $K = 0 - 1$				III: $K = 0 - 0$			
J	R	Q	P	R	Q	P	Q	R	Q	P	Q
1	43093.26	43088.97	43086.81	43145.27	43140.78	43138.53	43752.43				
2	95.00	88.56	84.22	47.32*	40.58	36.04*					
3	96.53	87.99	81.45	49.23	40.27	33.46	51.93				
4	97.83	87.17	78.47	51.14	39.89 ₅	30.78					
5	98.95	86.20	75.25	53.05	39.47*	28.01	51.13 ₅				
6	99.78	85.02		54.93*		25.19					
7	43100.50*	83.59			38.74	22.38					
8	00.91	81.98		58.77		19.56*					
9		80.11									
I: $K = 1 - 0$				II: $K = 1 - 0$				II: $K = 1 - 1$			
J	R	Q	P	R	Q	P	R	Q	P	Q	P
0	43715.08			43724.05							
1	17.13	43712.64		28.64	43721.75		43117.01			43109.96*	
2	19.03*	12.15	43708.02	31.33	24.05*	43716.70*	19.68?			12.36*	
3	20.69	11.39	05.37	33.27 ₃	24.47	16.80*	21.63			12.79	43105.10*
4	22.40*	10.36 ₃	02.55 ₃	34.56	24.31		22.85			12.79?	
5	23.78*	09.40	43699.53	35.28	23.34	12.15*				11.68	
6		07.78	96.50								
7			93.19								

The $v'_4 + v'_6 = 2$ polyad, B^2 , cont'd.

III: $K = 1 - 0$			I: $K = 2 - 0$			III: $K = 2 - 1$			
J	R	Q	P	R	Q	P	R	Q	P
0	43798.89			43722.45			43110.80		
1	43800.94	43796.51		21.91	43717.76		10.30	43106.06	
2	02.82	96.16	43791.83	21.34	14.93	43710.70	09.66	03.30	43098.95*
3	04.57 ₅	95.66	89.17				08.72 _{ee}	00.19 _{ef}	
4	06.15	94.95 ₅	86.36				07.73 _{ee}	43096.85* _{fe}	
5	07.59	94.10	83.38 ₅		08.55	00.16	06.40 _{ff}		
6	08.90	93.08	80.26						
7	10.06	91.83*	77.00						
8		90.49							

I: $K = 2 - 0$			II: $K = 2 - 1$						
J	R	Q	P	R _{ee}	R _{ff}	Q _{ef}	Q _{fe}	P _{ee}	P _{ff}
1	43753.15 ₅			43141.48					
2	54.915	43748.44		43.21		43136.77			
3	56.48	47.84 ₅	43741.39	44.80		36.20 ₅		43129.75	
4	57.82	47.04 ₅	38.43	46.11		35.31	35.41	26.69	
5	59.00	46.08	35.28*	47.32*		34.29	34.44	23.68	23.53
6	60.01			48.30*	48.18	33.06	33.29	20.33?	20.13
7	60.72			49.12	48.91*		31.93	16.82	16.54
8						29.96			

The $v_4' + v_6' = 3$ polyrad, B^3

J	I: $K = 0(b_u) - 1$		II: $K = 0(a_u) - 0$		III: $K = 0(b_u) - 1$		IV: $K = 0(a_u) - 1$		I: $K = 1 - 1$	
	R_{ff}	P_{ff}	Q_{ef}	R_{ff}	P_{ff}	Q_{ef}	R_{ff}	Q_{ef}	R_{ff}	P_{ff}
1	44454.11	44446.65?	44457.14	44451.43	44547.68	44449.86	44446.45			
2	56.24	44.63*	56.90	53.47	44542.24	50.85	45.73	44441.50		
3	58.03	42.30	56.49	55.47	39.64	51.58	44.63*	38.08		
4	59.55	39.72	55.82	57.37	37.01*	51.98	43.26	34.34		
5	60.76*	36.91	54.92	59.18	34.32	52.26	41.61	30.36		
6	61.57			61.00	31.47			26.13		
7	62.11*			62.77	28.63					
8					25.69					

J	II: $K = 1 - 1$			III: $K = 1 - 1$			IV: $K = 1 - 1$		
	R_{ff}	Q_{ef}	P_{ee}	R_{ff}	Q_{ef}	Q_{fe}	R_{ff}	Q_{ef}	P_{ff}
1	44484.48	44481.18*		44511.42	44506.73*		44618.13	44613.73	
2		79.77*	76.62	13.72	06.73*	44506.73			
3		81.18*		15.78	06.73*				44606.36
4		79.77*		18.92	06.48*				
5	$R_{ee}(2)$	78.53	$Q_{fe}(2)$	20.53	7.19	$R_{ee}(2)$			
6	88.22		79.85		06.48*	13.76			

The $v'_4 + v_6 = 3'$ polyad, B^3 , cont'd.

J	I: $K = 2 - 1$			II: $K = 2 - 1$			III: $K = 2 - 1$		
	R_{ff}	Q_{ef}	R_{ee}	R_{ff}	Q_{ef}	P_{ff}	R_{ff}	Q_{ef}	P_{ff}
1	44469.14			44487.76			44545.17		
2	70.97	44464.46	44470.99	83.32	44483.05		47.01	44540.51	
3	72.51	63.93		81.52	76.21	44476.03	48.65	39.94	33.43
4	73.65	63.18		79.77*	72.10	66.85	50.06	39.23	30.55
5	73.94	62.10*		79.06	67.93		51.24	38.30	27.43
6							52.28	37.21	24.17
7							53.07	35.94	20.65
8			$Q_{fe}(2)$			$Q_{fe}(2)$		34.49	
9			64.43			83.11		32.82	

J	IV: $K = 2 - 1$			I: $K = 3 - 1$			II: $K = 3 - 1$		
	R_{ff}	Q_{ef}	P_{ff}	R_{ff}	Q_{ef}	P_{ff}	R_{ff}	Q_{ef}	R_{ee}
1	44707.97								
2	09.82	44703.26		44497.06			44515.18		44415.23
3	11.46	02.75	44696.23	99.12	44489.99		17.04*	44508.12	
4	12.95	02.05	93.33	44500.32	89.71	44480.57	17.04*	07.63	
5	14.30	01.21	90.29	00.89	88.50	77.95	18.13	05.28	
6	15.46	00.22		01.10	86.7			04.07	
7	16.46	44699.01						02.65?	

Table 5.5: Upper state term values, observed in IR-UV double resonance via the ground state ν_3^0 fundamental. UV laser is grating-tuned, resulting in less accurate calibration of line positions ($\sim 0.1 \text{ cm}^{-1}$).

The $\nu_4 + \nu_6 = 3$ polyad, B^3											
	I: $K = 0f$	II: $K = 0e$	III: $K = 0f$	IV: $K = 0e$	I: $K = 1e$	I: $K = 1f$	II: $K = 1e$	II: $K = 1f$			
1	44451.64	44459.37		44549.98	44448.90	44448.57	44483.55	44483.61			
2	56.44	64.01		54.51	52.72	52.22	86.67	86.82			
3	63.26	70.58		61.30	58.72	57.86	95.20	95.34			
4	72.18	79.31		44569.55	66.79	65.65	44503.42	44503.63			
5	83.08	90.21		80.81	76.82	75.43	13.72	14.14			
6	95.98	44503.41*		94.47	89.07	87.53	26.18	26.72			
7		17.72?			44503.37?		40.52				
	III: $K = 1e$	III: $K = 1f$	IV: $K = 1e$	IV: $K = 1f$	I: $K = 2e$	I: $K = 2f$	II: $K = 3e$	II: $K = 3f$			
1	44509.03	44508.99	44616.01	44616.07							
2	13.80	13.63	20.52	20.32	44471.49	44471.56					
3	20.67	20.65	27.05	27.14	77.9	77.97				44522.21?	
4	29.95	29.83	35.93	35.84	86.58	86.53	44531.23?			31.09	
5	42.47	42.41	46.93	46.92	97.43	97.21	40.99			40.89	
6	55.93	55.72	60.14	60.23	44509.61	44509.11	54.04			53.33	
7	71.18		75.56		22.60		69.09				
	II, $K = 2, J = 2e$: 44 4490.16, $J = 2f$: 44 490.21										

Table 5.6: Assigned rotational lines of the higher pure bending polyads of the \tilde{A}^1A_u state of C_2H_2 . The members of the upper state polyads are labeled with Roman numerals in order of increasing energy for each K -value. Blended lines are marked with an asterisk (*).

The $v'_4 + v'_6 = 4$ polyad, B^4												
I: $K = 0(a_g) - 1$				I: $K = 1 - 0$				II: $K = 1 - 0$				
J	R	Q	P	R	Q	P	R	Q	P	R	Q	P
0				45184.05			45201.52					
1	44564.97	44560.66	44558.50*	85.77	45181.69		03.83	45199.12*				
2	66.60	60.27	55.92	87.10	80.90	45177.02	05.71	99.12*	45194.47			
3	68.08	59.58	53.14	88.02	79.77	73.99	07.14	99.28	92.05			
4	69.27	58.74*	50.08	88.56*	78.25	70.62	08.14	99.46*	89.24			
5		57.64	46.97*	88.56*	76.33	66.86	08.70					
6				73.99*								
7				71.25								
V: $K = 1 - 0$				I: $K = 2 - 0$				II: $K = 2 - 1$				
J	R	Q	R	Q	R	Q	R	Q	R	Q	R	Q
0	45448.21											
1	50.33	45445.84	45196.97		45226.47		44614.83*					
2	52.22	45.54	97.65	45192.26	28.45	45221.80	16.79	44610.14				
3	53.98	45.11	98.20	90.52	30.36	21.38	18.69	09.73				
4	55.60	44.53	98.68	88.56		20.81		09.14*				
5	57.10	43.76		86.48		20.12		08.49				
6								07.46?				
7								06.35?				

The $v_4^l + v_6 = 5'$ polyad, B^5

J	V: $K = 0(b_u) - 1$		VI: $K = 0(a_u) - 1$		V: $K = 2 - 1$	
	R	P	Q	R	Q	
1	46195.09		46190.90	46173.88		
2	97.13		46185.88	90.69	46175.67	
3	99.09	83.32	90.40	77.37	68.69	
4	46200.90	80.66	89.99	78.84	67.96	
5	02.66	77.88	89.48	80.24	67.10	
6		75.04				
7		72.08				

V, $K = 2 - 1$, P(2): 46162.10

Chapter 6

Vibrational assignments in the S_1 state of acetylene, II:

Totally symmetric modes

The work in this chapter resulted from a collaborative effort between myself, Dr. Hans A. Bechtel, and Prof. Anthony Merer. The results in this chapter have been published in *Molecular Physics* (Ref. [156]).

6.1 Introduction

The electronically excited states of polyatomic molecules, even those which can be reached by a one-photon excitation from the ground state, are, as a rule, less completely characterized and less well understood than the corresponding ground electronic states. Access to excited states is limited by a number of factors, including restrictive spectroscopic selection rules (particularly in the presence of high symmetry), Franck-Condon overlap, and large variations in the detectability of vibrational levels in the excited state manifold due to nonradiative processes, most notably predissociation. Though not immune to these difficulties, the $\tilde{A} \ ^1A_u$ state of acetylene, C_2H_2 , is among the best understood of all polyatomic molecule excited states. This

can largely be attributed to the fact that it has been the subject of numerous experimental approaches including high-resolution absorption [118, 119, 122], infrared-ultraviolet double-resonance [2, 157, 138], and H-atom action spectroscopy [117, 158].

Pioneering work on this state focused on the change of geometry upon excitation from the ground state [108, 109, 121]. The $\tilde{A} \ ^1A_u$ excited state was demonstrated to arise from a $\pi_g^* \leftarrow \pi_u$ electronic excitation and to be characterized by a *trans*-bent equilibrium geometry. In recent years emphasis has moved toward developing an understanding of the vibrational dynamics of *trans-cis* isomerization in the excited state [127] and the role of specific classes of vibration in mediating the coupling between the $\tilde{A}(S_1)$ state and the manifold of triplet states [159, 160, 161]. These efforts require a nearly complete understanding of the vibrational energy level structure in order to interpret the spectra in regions well above the vibrational fundamentals, where anharmonic and Coriolis interactions may have grossly distorted the expected energy level patterns. However, even for a state of such prototypical nature, the complete set of the fundamental vibrational levels has yet to be observed. The symmetric C–H stretching fundamental, ν'_1 , has remained undetected despite more than a half-century of spectroscopic investigation. Furthermore, only a relatively small number of the binary combinations and overtones are known, making it difficult to determine the magnitudes of anharmonic contributions to the observed vibrational energies.

In order to be sure that our pictures of the vibrational dynamics are correct, we need to establish the vibrational assignments for as many of the \tilde{A} state levels as possible, building the vibrational assignments at higher energy upon a sound foundation. The main obstacle to making a complete set of assignments at low energy is the strength of the hot bands arising from the ground state ν''_4 level and its overtones. These are greatly enhanced, relative to cold bands observed at a similar frequency, by the Franck-Condon principle and by the variation of the electronic transition moment with bending angle (which goes to zero at the linear configuration). As a result,

the hot bands mostly obscure the weaker cold bands at the long wavelength end of the absorption spectrum [162]. Thus many states, which either have poor Franck-Condon factors for excitation from the ground vibrational state, or which are only weakly allowed through anharmonic interactions with members of the Franck-Condon active progressions, are likely to escape detection. As part of a continuing effort to describe the vibrational dynamics of \tilde{A} -state acetylene, up to and including the onset of *trans-cis* isomerization, we have recorded high resolution jet-cooled laser induced fluorescence spectra in the region around 45 000 cm^{-1} . Although barely detectable in the jet-cooled survey spectra of Ref. [139], several analyzable bands were found in this region. One of them, assigned as 2_0^2 , is straightforward to assign. The others consist of complicated structure resulting from interactions between the 1^1 fundamental and the 2^1B^2 polyad, where $\nu'_B = \nu'_4 + \nu'_6$. The lower-state J values could be assigned from population-labeling double resonance experiments, using an infrared laser to depopulate selected ground-state rotational levels. A least squares fit has provided an accurate value for $\nu'_1 = 2880.08 \text{ cm}^{-1}$, in agreement with the results from Ref. [139], as well as anharmonicity parameters describing the interactions of the symmetric C-H stretching vibration with the polyad-forming low-frequency bending modes.

The new value determined for ν'_1 implies that some of the currently accepted assignments above 47 000 cm^{-1} are in error. As a consequence, the interpretation of dynamics studies, which have relied on the accepted spectroscopic assignments, must be revisited. In particular, the pioneering studies of state-selective photodissociation by Mordaunt *et al.*[163] used the assignment of a vibrational level at 47 206 cm^{-1} to identify ν'_1 as a promoting mode for a dissociation mechanism involving direct S_1/T_1 crossing. In light of the current results, this mechanism is more likely to be promoted by one or other of the low-frequency bending modes: ν'_4 , torsion (a_u) and ν'_6 , in-plane bend (b_u).

6.2 Experimental details

Laser induced fluorescence spectra were recorded in an unskimmed pulsed jet expansion of neat acetylene gas. No attempt was made to remove residual acetone, which is present as a stabilizer. Acetylene was expanded through a pulsed valve (General Valve, Series 9), with a 0.5 mm orifice from a backing pressure of 200 kPa. The ultimate vacuum achieved in the apparatus was 2×10^{-7} Torr, which was reduced to 5×10^{-5} Torr under normal gas load. The laser radiation intersected the pulsed jet ~ 3 cm downstream from the orifice.

The radiation was the frequency-doubled output of a Lambda Physik 3002E dye laser, pumped by the third harmonic of a Nd:YAG laser (Spectra-Physics DCR-3). The majority of the power from the dye laser was doubled in a β -barium borate (BBO) crystal, and routed to the molecular beam chamber, while the residual fundamental was attenuated and passed through a heated gas cell containing $^{130}\text{Te}_2$ vapor for calibration ($\pm 0.02 \text{ cm}^{-1}$ accuracy).

Fluorescence from the excited acetylene was observed in a direction that is perpendicular to both the laser beam and the jet axis. The fluorescence was collected by a lens system and routed to a photomultiplier tube (PMT) assembly (Hamamatsu R331). Before impinging on the PMT, the fluorescence was passed through a dichroic mirror, which is coated for use at 193 nm and at an incident angle of 45° . Used at 0° , we have found that this mirror does an excellent job of suppressing scattered laser light near 220 nm, while transmitting the majority of the fluorescence in the near-ultraviolet and visible regions.

6.2.1 Hot band promotion

The $\tilde{A}^1A_u - \tilde{X}^1\Sigma_g^+$ transition obeys c -type selection rules: $K'_a = \ell'' \pm 1$. This means that, under beam conditions where most of the molecules are in the vibrationless

level of the ground state, transitions go only to levels with $K' = 1$. The selection rule is relaxed by axis-switching [121], but the resulting additional lines only have appreciable intensity for J greater than about 5, where the population in the cold molecular beam is already quite small. Therefore, the jet spectra usually only give part of the asymmetric top rotational structure of a vibrational band, and do not allow the A rotational constant to be determined. This is unfortunate since Merer *et al.*[139] have stressed how the apparent A constant can be used to distinguish between vibrational levels where only the totally symmetric modes are excited and those where even quanta of the low-frequency non-totally symmetric modes ν'_4 and ν'_6 are excited.

In order to observe more of the K structure, the experiment was modified so as to record hot bands arising from the $\nu''_4 = 1(\ell'' = 1)$ level. While this could be accomplished by recording spectra in a static cell as in Ref. [139], we have found that weak hot bands are easily obscured by the high J lines of nearby bands with more favorable Franck-Condon factors.

With the goal of populating the ν''_4 level while maintaining reasonably low rotational temperatures, the distance between the nozzle and the intersection of the laser with the pulse of molecules was reduced from ~ 30 mm to ~ 5 mm. Additionally, the relative timing of the pulsed valve and laser was adjusted so that the laser radiation intersected the leading edge of the gas pulse, where the effective vibrational temperature is higher.

6.2.2 Absolute lower state J -numbering

Utz *et al.* [2] demonstrated that strong a - and b -axis Coriolis effects in \tilde{A} -state C_2H_2 destroy the regular energy level patterns upon which spectroscopic assignments are often based. They were able to assign the spectra of the coupled ν'_4/ν'_6 system (B^1 polyad) because their IR-UV double resonance experiments gave a series of spectra

originating from known J'' , thereby simplifying the assignment of J' .

In order to assign J' in complicated spectra terminating on *gerade* vibrational levels, spectra have been recorded using a population-labelling technique. An IR laser is tuned to a selected rotational line within the ground state $\nu_3''/(\nu_2'' + \nu_4'' + \nu_5'')$ dyad. The IR laser has sufficient power to saturate the line partially and therefore reduce the lower state population for a selected value of J'' . While the laser is tuned to a particular rovibrational line in the IR, the UV spectrum of interest is scanned with a second laser. The repetition rate of the IR laser is reduced to half that of the UV laser, so that every other UV laser shot samples the depleted lower state population. The detection electronics average the difference between each pair of consecutive shots, returning a spectrum that only contains features that originate from the rotational level that has been selectively depleted by the IR laser.

A similar effect can be achieved by recording the spectrum under conditions of a temperature-regulated static gas cell [162] or by systematically varying the expansion conditions in order to alter the effective rotational temperature of the sample. However, in the case of significant overlap between lines originating from different values of J'' , differing temperature-dependence of the underlying structure often precludes any clear assignment. We therefore favor the more definitive, population-labelling technique, which returns an essentially binary answer to the question: is any significant intensity at this UV laser frequency due to population in the selected value of the lower state J'' ?

The IR radiation for this experiment was generated by difference frequency generation (DFG) in a lithium niobate (LiNbO_3) crystal by mixing the 1064 nm fundamental of an injection-seeded Nd:YAG laser and the output of a dye laser (Lambda Physik FL 2002) operating with LDS 798. The infrared radiation was then amplified by optical parametric amplification (OPA) in a second LiNbO_3 crystal to provide approximately 3 mJ of infrared light. The IR and UV light are spatially and temporally overlapped

at the sample, with the precise timing of the IR laser set to optimize a depletion signal on a line with a known lower state while minimizing the intensity of satellite peaks due to collisions that occur in the time between the IR and UV pulses.

6.3 Theory: Matrix elements for the interacting 1^1 and 2^1B^2 vibrational levels

The interaction between the 1^1 fundamental and the 2^1B^2 polyad can be modeled by adding the function $|v_1\rangle$ to the basis set of Eqs. 5.8 and 5.9, and including matrix elements for the anharmonic interactions. The operator for these latter was taken as

$$\hat{H}_{\text{anharm}} = K_{1244}\hat{q}_1\hat{q}_2\hat{q}_4^2 + K_{1266}\hat{q}_1\hat{q}_2\hat{q}_6^2. \quad (6.1)$$

The relevant matrix elements of this operator, which are diagonal in J and k , are

$$\begin{aligned} \langle v_1 = 1 \ v_2 = 0 \ v_4 = 0 \ v_6 | \hat{H}_{\text{anharm}} | v_1 = 0 \ v_2 = 1 \ v_4 = 2 \ v_6 \rangle &= \frac{1}{2\sqrt{2}}K_{1244} \quad (6.2) \\ \langle v_1 = 1 \ v_2 = 0 \ v_4 \ v_6 = 0 | \hat{H}_{\text{anharm}} | v_1 = 0 \ v_2 = 1 \ v_4 \ v_6 = 2 \rangle &= \frac{1}{2\sqrt{2}}K_{1266}. \end{aligned}$$

As in Ref. [106], a similarity transformation was applied to the matrices to remove the imaginary matrix elements of the first order Coriolis coupling. The effect of this on the matrix elements of Eq. 6.2 is that the terms in K_{1266} have their signs changed, but those involving K_{1244} remain unchanged. This becomes important in determining the relative signs of K_{1244} and K_{1266} from the experimental data.

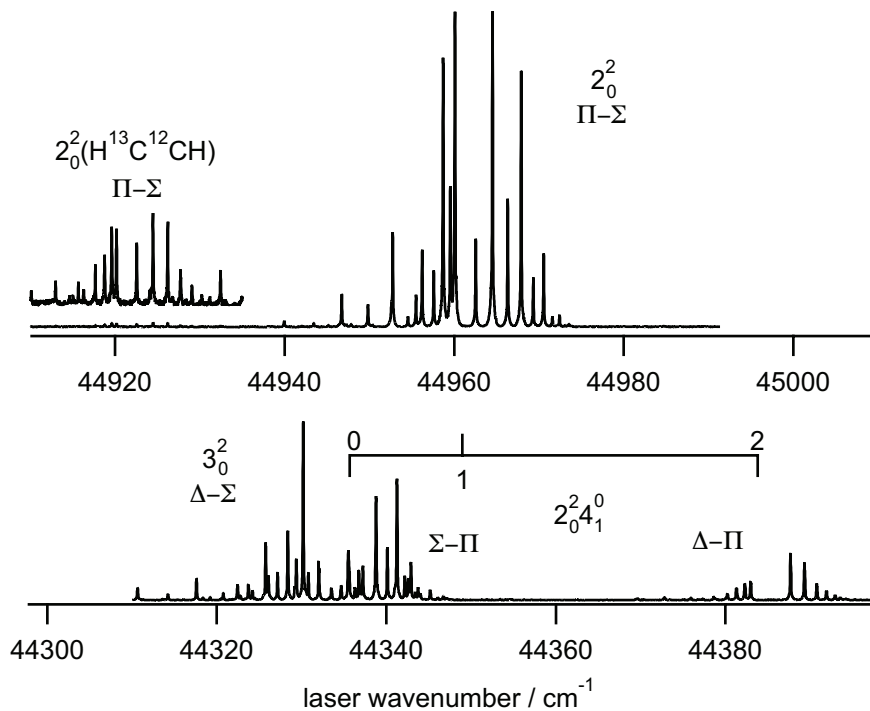


Figure 6-1: Laser-induced fluorescence spectra of jet-cooled C_2H_2 in the region of the 2_0^2 (upper panel) and $2_0^2 4_1^0$ bands (lower panel). The lower spectrum is offset by 612 cm^{-1} , the ground state ν_4'' fundamental frequency, in order to display the asymmetric top K_a -structure in the 2^2 vibrational level. The $44\,910 - 44\,935\text{ cm}^{-1}$ portion of the spectrum is expanded by $\times 20$ to show the corresponding 2_0^2 band for the $H^{13}C^{12}CH$ isotopologue, present at its natural abundance.

6.4 Results

6.4.1 The 2^2 level

Although the survey spectrum shown in Figure 3 of Ref. [139] contains no discernible features in the region near $45\,000\text{ cm}^{-1}$, our high-sensitivity measurements reveal several bands of detectable strength in this region. The lowest energy band, displayed in Figure 6-1, lies at $44\,960\text{ cm}^{-1}$ and is of clear $\Pi - \Sigma$ type. In order to complete the rotational analysis of the upper state of this transition, the jet conditions were adjusted to favor hot bands originating from the ν_4'' level of the ground state, and a spectrum was recorded approximately 612 cm^{-1} lower in energy in order to locate the associated K -structure. Although it is overlapped by the stronger $3_0^2 K_0^2$ axis-

switching transition, a $\Sigma - \Pi$ type band could be identified at $44\,337\text{ cm}^{-1}$ with a corresponding $\Delta - \Pi$ band at $44\,385\text{ cm}^{-1}$. The upper state term values were fitted by least squares using Watson’s A-reduced Hamiltonian and gave the constants listed in Table 6.4.1. Line positions for all bands described in this section are provided at the end of the chapter.

Table 6.1: Rotational constants (in cm^{-1}) for the 2^2 vibrational level of the \tilde{A}^1A_u state of C_2H_2 . The error limits are the 3σ uncertainties derived from the fit.

T_0	44948.681	0.033
A	12.757	0.045
B	1.1060	0.0012
C	1.0155	0.0015
Δ_K	0.0031	0.0099
Δ_{JK}	0.00017	0.00057
Δ_J	0.28×10^{-5}	fixed
r.m.s. error	0.0117	

The 1047 cm^{-1} interval between this level and the level 2^23^1 at $45\,995.65\text{ cm}^{-1}$, previously assigned in Ref. [139], strongly supports the assignment of the $44\,948.68\text{ cm}^{-1}$ level as 2^2 . This assignment is confirmed by the vibrational dependence of the rotational constants. In particular, the ν'_2 fundamental is the only level observed by Watson *et al.*[118] that has a smaller A_v rotational constant (12.902 cm^{-1}) than the vibrationless level (13.057 cm^{-1}). Our fitted value of A_v for the $44\,948\text{ cm}^{-1}$ band very closely matches the extrapolation from the observed ν'_2 fundamental.

It should be noted that these observations are only possible given the simplification afforded by jet cooling. Watson *et al.*[118] have studied this region of the spectrum previously at high resolution in absorption, but identified only numerous hot bands, mostly involving the K -structure of the strongly Franck-Condon allowed levels $\nu'_2 + 2\nu'_3$ and $4\nu'_3$.

The high sensitivity of our jet LIF measurements is demonstrated by the presence of an additional $\Pi - \Sigma$ type band at $44\,920\text{ cm}^{-1}$, which is approximately one percent

as intense as the band at $44\,960\text{ cm}^{-1}$. This band lacks the characteristic 3:1 intensity alternation caused by the nuclear spins of the equivalent hydrogen atoms. In addition, its ground state combination differences are about 3 percent smaller than those for the zero-point level of C_2H_2 , consistent with an assignment to the 2_0^2 band of the $\text{H}^{13}\text{C}^{12}\text{CH}$ isotopic species. No spectra of the $\tilde{A} \leftarrow \tilde{X}$ transition for this isotopologue are available in the literature, though the vibrational structure of its ground electronic state has been investigated in great detail [164].

6.4.2 Deperturbation of the $1^1/2^1B^2$ interaction

Between $45\,000$ and $45\,170\text{ cm}^{-1}$ there is significant structure in the spectrum that has not previously been observed. With the $44\,949\text{ cm}^{-1}$ level assigned as 2^2 from its A rotational constant, the only remaining level involving excitation of just the a_g symmetry normal modes that could lie in this region is the ν'_1 fundamental. As for combinations involving the low frequency bending modes (ν'_4 , torsion (a_u) and ν'_6 , in-plane bend (b_u)), the $\nu'_4 + \nu'_6 = 2$ polyad (B^2 , for short) was shown in Chapter 5 to lie near $43\,720\text{ cm}^{-1}$, so that the 2^1B^2 polyad should lie near $45\,100\text{ cm}^{-1}$. The B^4 polyad can be discounted since its lowest $K = 1$ level lies at $45\,182\text{ cm}^{-1}$.

The observed spectrum consists of two clear $\Pi - \Sigma$ bands at $45\,078\text{ cm}^{-1}$ and $45\,162\text{ cm}^{-1}$, together with a collection of moderately strong but confused lines near $45\,090\text{ cm}^{-1}$. The $\Pi - \Sigma$ bands strongly resemble the lowest and highest components expected for a B^2 -type polyad. The remaining structure could initially be interpreted only as being induced by pervasive Coriolis interactions.

In order to establish secure rotational assignments for the remaining lines, the spectrum was re-recorded using the population-labeling technique described in section 6.2.2 for $J'' = 0 - 5$. An example of the results of this technique is shown in Figure 6-2 for the highly congested region of 2^1B^2 near $45\,090\text{ cm}^{-1}$. The downward going lines in the lower trace are the LIF depletion signal recorded with the IR laser tuned

to the $R(1)$ line of the $\nu_3 \leftarrow$ GS band at 3299.52 cm^{-1} .

Only after the lower-state rotational numbering had been established could we identify the various branches making up the spectrum. Of particular note is that two lines with lower state $J'' = 0$ are located only 4.34 cm^{-1} apart. These must both be $R(0)$ lines, showing that there are two close-lying $J = 1e, K = 1$ levels present. They can be immediately assigned to the 1^1 and 2^1B^2 (middle polyad component) vibrational levels.

However, the branch structure associated with these lines is unexpectedly complicated because the lower energy $J' = 1$ level is strongly perturbed. Among the remaining lines it is possible, given the lower-state J -numbering, to assign a sub-band containing abnormally strongly degraded Q - and R -branches, the first lines of which show that it has $K' = 2$. The resulting energy level pattern is shown, plotted against $J(J + 1)$, in Figure 3. As the figure shows, this $K = 2$ level interacts, by very strong b -axis Coriolis coupling, with the 2^1B^2 $K = 1$ (middle) level, which in turn interacts with the 1^1 $K = 1$ level via anharmonic resonance. By accident the 1^1 $K = 1$ level happens to lie exactly in the middle of the Coriolis pattern, so that its level structure gets severely disrupted at $J = 2$, where the Coriolis interaction sets in. The Coriolis mixing is essentially complete, which means that the 2^1B^2 $K = 1$ character is spread equally between the nominal 2^1B^2 $K = 1$ and 2 levels. The 1^1 $K = 1$ level, lying between them, then feels equal and opposite perturbations from the two 2^1B^2 levels, so that its level structure appears to be regular at higher J values.

As in the case of the 2^2 level, the corresponding hot band region for the $1^1/2^1B^2$ levels has been recorded with the jet conditions adjusted to favor hot bands. The degree of congestion and spectral overlap is significantly worse in this region, but it is possible to identify hot bands terminating on the $K' = 0$ sublevels of 2^1B^2 (lower), 2^1B^2 (upper), and 1^1 . In addition, the corresponding $K' = 2$ sublevels have been located for the 2^1B^2 (lower), 2^1B^2 (middle), and 1^1 states.

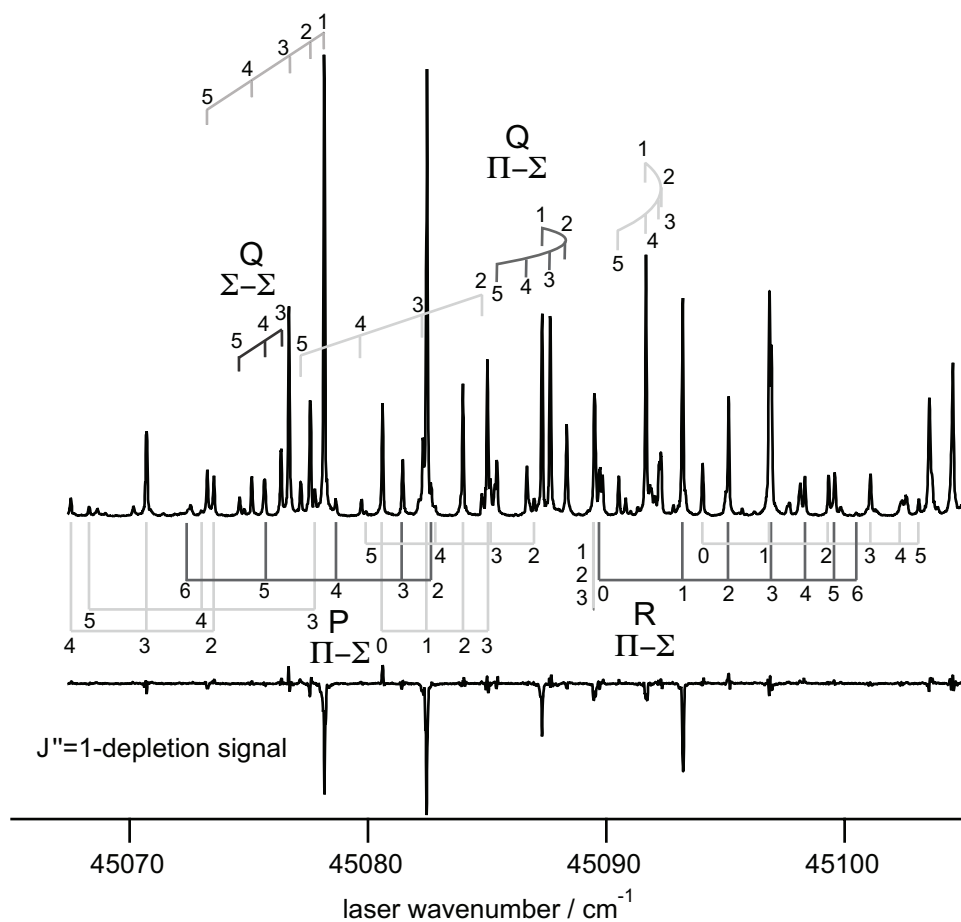


Figure 6-2: A portion of the LIF spectrum of the $1^1/2^1 B^2$ polyad. The normal LIF spectrum (upper trace) is shown with peaks pointing upwards. The depletion signal (lower trace) obtained by comparing the LIF signal with the IR laser on vs. off is shown with the population-labelled peaks pointing downwards. The population-labelled peaks correspond to peaks in the LIF spectrum whose lower state is the $J'' = 1$ level of the ground vibrational state. Rotational assignments are given for the $1^1/2^1 B^2$ polyad with the assignment markers in black for the nominal 1^1 band and in gray for the nominal $2^1 B^2$ bands.

The term energies of the states from the 10 identified sublevels (out of 12 possible with $K' = 0 - 2$) were fitted by least squares to the Hamiltonian described in section 6.3. The results are given in Table 6.4.2. The reported value of $T_0(1^1)$ corresponds to a vibrational energy of $+2880.08(16)$ cm^{-1} with respect to the vibrationless level of the \tilde{A} state. A complete account of the structure of the 2^1B^2 polyad and its relation to other $2^n3^mB^2$ polyads follows in the next chapter.

Table 6.2: Term values, rotational constants, and coupling parameters determined from the fit to the Coriolis/anharmonic model for the $1^1/2^1B^2$ vibrational levels described in section 6.3. The values of the rotational constants for the $2^14^16^1$ level are fixed to the averaged values of the 2^14^2 and 2^16^2 levels. The error limits correspond to the 3σ uncertainties from the fit.

Level	1^1		2^16^2		$2^14^16^1$		2^14^2	
T_0	45 077.65	± 0.48	45 097.98	± 0.72	45 108.33	± 0.66	45 089.16	± 0.36
A	12.672	0.021	13.535	0.180	12.906	fixed	12.277	0.210
\bar{B}	1.0741	0.0012	1.0670	0.0054	1.0667	fixed	1.0664	0.0054
$B - C$	0.0989	0.0051	0.1184	0.0141	0.0885	fixed	0.0585	0.0141
K_{1266}	8.922	± 1.223		$2A\zeta_a^{46}$	17.956	± 0.021		
K_{1244}	-1.854	4.036		$B\zeta_b^{46}$	0.790	0.006		
K_{4466}	-51.39	0.48						
r.m.s. error	0.023							

6.4.3 Vibrational assignments up to $+4500 \text{ cm}^{-1}$

With the assignments of the 1^1 and 2^2 vibrational levels, we are able to make reliable predictions for the other vibrational levels with excitation in the totally symmetric modes, ν'_1, ν'_2 and ν'_3 . Using the term values and A rotational constants of 2^1 and 2^2 , we predict that the $2^3 K = 1$ sublevel will lie at $46\,302.83 \text{ cm}^{-1}$. The one-photon LIF spectrum in this region is dominated by the very intense $3_0^4 K = 1 - 0$ band. However, just beyond the R -branch of this band, and extending a little way into it, are two series of lines which, based on their intensity patterns, appear to be another R - and Q -branch pair terminating on a $K = 1$ level at $46\,302.51 \text{ cm}^{-1}$. A least squares fit, shown in Table 6.4.3, gave values for the upper state B and C rotational constants

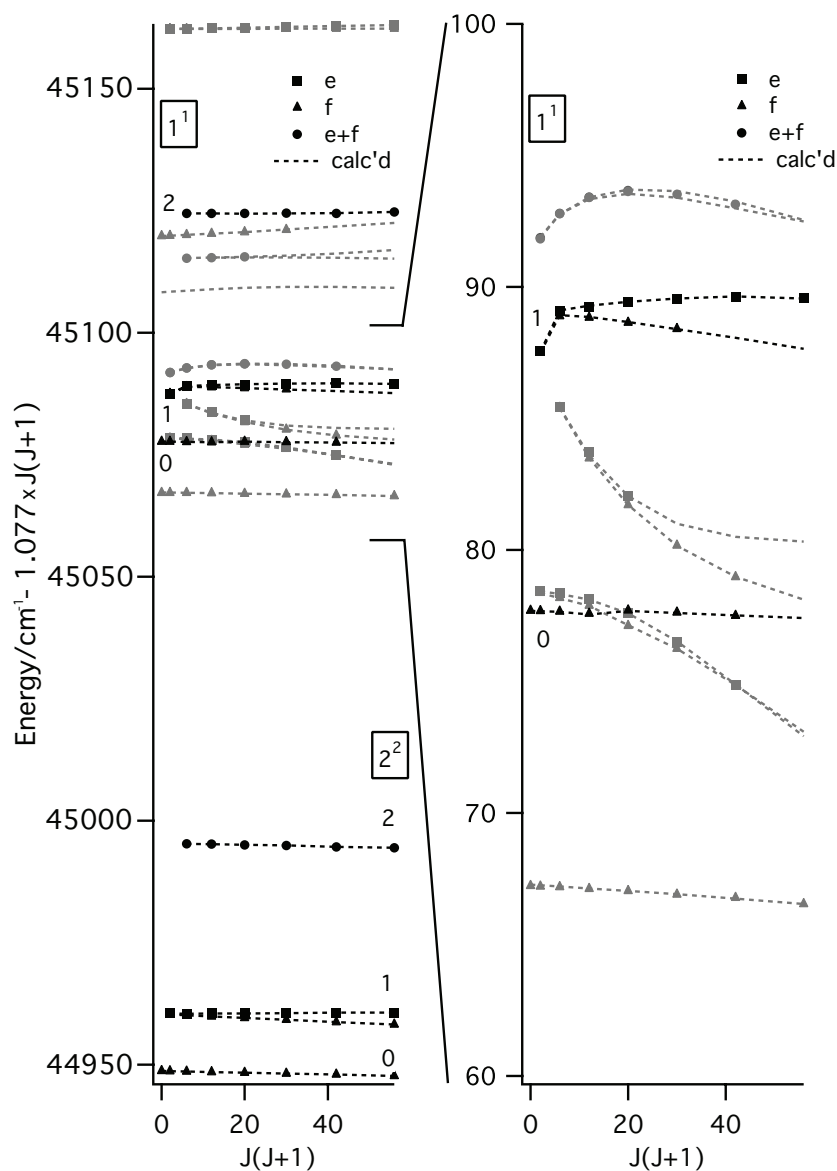


Figure 6-3: Reduced term value plots of the $K = 0 - 2$ levels of acetylene in the $45\,000\text{ cm}^{-1}$ region. Solid squares mark the positions of e -symmetry levels, triangles mark the f -symmetry levels, and circles mark positions where the e - and f -symmetry levels are unresolved in our experiments. The dashed lines represent the energy levels calculated from the Hamiltonian of section 6.3, with fit parameters given in Table 6.4.2. The energy scale for the left panel covers the range of $+2750\text{--}2965\text{ cm}^{-1}$ of energy above the A state origin. The right-hand panel is an expansion of the term value plot corresponding to the spectral region illustrated in Figure 6-2. States belonging to the 2^2 and nominal 1^1 levels are plotted in black, while the nominal 2^1B^2 states are plotted in gray. The kink at $J = 1$ in the reduced term value curve for the nominal 1^1 $K = 1$ level is caused by the multistate interaction with the 2^1B^2 polyad described in section 6.4.2.

that are completely consistent with extrapolations from the constants of the 2^1 and 2^2 levels, confirming that the upper state is the 2^3 , $K = 1$ level.

Table 6.3: Rotational constants (in cm^{-1}) for the 2^3 vibrational level of the \tilde{A}^1A_u state of C_2H_2 . Only $K_a = 1$ data are included in the fit, and the A rotational constant is fixed to the value extrapolated from the 2^1 and 2^2 levels. The error limits are the 3σ uncertainties derived from the fit.

T_0	46 290.94	0.014
A	12.622	fixed
B	1.0966	0.0013
C	1.0095	0.0039
r.m.s. error	0.0090	

The remaining level of those containing excitation only in the totally symmetric modes is 1^12^1 . From the level positions of 1^1 and 2^1 , we predict the 1^12^1 level to lie at $46\,464.55\text{ cm}^{-1}$, with an A rotational constant of 12.517 cm^{-1} . We find a relatively strong $K = 1 - 0$ band in the one-photon LIF at $46\,474.95\text{ cm}^{-1}$. However, it is difficult to interpret the hot band spectra for this region, in which there appear to be two $K = 0$ sublevels at $46\,460.53$ and $46\,467.85\text{ cm}^{-1}$ and a $K = 2$ level at $46\,509.41\text{ cm}^{-1}$. It seems that this is another example of the K_{12bb} interaction that we have successfully deperturbed in the $1^1/2^1B^2$ region. Here the near-degeneracy occurs between the $K = 0$ sublevels of 1^12^1 and one component of 2^2B^2 , thus obscuring the expected asymmetric top structure for the 1^12^1 band. However, if we assume that the perturbation only affects the $K = 0$ sublevel, it is possible to fit the remaining data from $K = 1$ and 2 in order to extract a zero-order vibrational energy of $+4265.91\text{ cm}^{-1}$. The results of the fit are given in Table 6.4.3. The vibrational origin of 1^12^1 extrapolated from the fit would place it very near the midpoint of the two observed $K = 0$ sublevels. The magnitude of the separation between the two resulting $K = 0$ eigenstates is consistent with the matrix elements derived from the $1^1/2^1B^2$ interaction, listed in Table 6.4.2.

Table 6.4: Rotational constants (in cm^{-1}) for the $1^1 2^1$ vibrational level of the $\tilde{A}^1 A_u$ state of C_2H_2 . Data from the $K_a = 0$ sublevel are excluded because of a strong perturbation by a member of the $2^2 B^2$ polyad. The error limits are the 3σ uncertainties derived from the fit.

T_0	46463.481	0.027
A	12.544	0.012
B	1.1095	0.0009
C	1.0313	0.0012
Δ_K	0.000	fixed
Δ_{JK}	0.00059	0.00033
Δ_J	0.000	fixed
r.m.s. error	0.0177	

6.5 Vibrational parameters for the totally symmetric modes

Our deperturbation of the $1^1/2^1 B^2$ interaction provides the definitive value of

$$\nu'_1 = 2880.08(16) \text{ cm}^{-1}, \quad (6.3)$$

in essentially complete agreement with the conclusions of Ref. [139]. As foreshadowed in Ref. [139], this resolves the discrepancy between the earlier assigned value of $\nu'_1 \approx 3040.6 \text{ cm}^{-1}$ given in Ref. [118], and the normal mode analysis of Tobiasson *et al.*[137] The agreement between our revised value and the result from the normal mode analysis ($\nu'_1 \approx 2954 \text{ cm}^{-1}$) is not perfect, but much of the discrepancy can be attributed to the uncertain partitioning of the observed term energies into harmonic and anharmonic contributions. Unfortunately, the 1^2 vibrational level is expected to lie above $47\,500 \text{ cm}^{-1}$, in a region of very high state density. This factor, coupled with the anticipated poor Franck–Condon factor for the transition from the ground state, makes it unlikely that an experimental value for x'_{11} will be determined before significant advances have been made.

The measurement of the ν'_1 fundamental frequency is in good agreement with the *ab initio* vibrational perturbation theory treatment presented in Ref. [139] ($\nu'_1 \approx 2940 \text{ cm}^{-1}$) and the recent MULTIMODE result[165] ($\nu'_1 \approx 2903.28 \text{ cm}^{-1}$). It is noteworthy that, in conjunction with the measurements of Refs. [118], [2], and [157], all of the upper state fundamentals have now been directly observed and rotationally analyzed. Such completeness is very rarely achieved for a molecule with more than three atoms. Furthermore, with our assignment of the $1^{12}1$ and 2^3 levels, all the vibrational states involving excitation of the totally symmetric modes have now been established up to 4500 cm^{-1} of vibrational energy.

From our direct measurement of the 2^2 level, we have been able to determine a value of

$$x'_{22} = -11.35 \text{ cm}^{-1}. \quad (6.4)$$

This value is again consistent with the previous determination ($x'_{22} = -12.13 \text{ cm}^{-1}$) from [139]. It also supports the assumption made in Ref. [137] that anharmonicities can be transferred according to the isotopic relation

$$x_{ii}^* = (\omega_i^*/\omega_i)^2 x_{ii}, \quad (6.5)$$

in which the starred quantities refer to vibrational parameters of an unmeasured isotopologue. Using this relation, Tobiasson *et al.* [137] derived $x'_{22}(\text{C}_2\text{H}_2) = -10.5 \text{ cm}^{-1}$ using the measured anharmonicity of C_2HD .

Similarly, from our measurement of the $1^{12}1$ vibrational level, we obtain a value of

$$x'_{12} = -1.07 \text{ cm}^{-1}. \quad (6.6)$$

In fact, all of the x'_{ij} parameters for the totally symmetric modes are now well known,

with the exception of the diagonal anharmonicity, x'_{11} . The vibrational energy formula

$$G(v_1, v_2, v_3) = \sum_i \omega_i(v_i + \frac{1}{2}) + \sum_{i \geq j} x_{ij}(v_i + \frac{1}{2})(v_j + \frac{1}{2}) \quad (6.7)$$

can be parameterized to the observed (and, in the case of 1^1 , deperturbed) vibrational term energies of the \tilde{A} -state vibrational levels with up to two quanta of excitation in the a_g symmetry modes. The resulting parameters are given in Table 6.5.

Table 6.5: Vibrational parameters for the a_g symmetry vibrational modes of \tilde{A}^1A_u state of acetylene.		
	$\omega_1 + 2x_{11}$	2885.89
	ω_2	1410.26
	ω_3	1070.34
	x_{22}	-11.35
	x_{33}	-8.70
	x_{12}	-1.07
	x_{13}	-10.55
	x_{23}	-0.24

6.6 Vibrational assignment of previously observed levels

With this knowledge of the vibrational level structure, we can assign several previously observed a_g combination levels up to at least $+5000 \text{ cm}^{-1}$. The parameterized vibrational energy formula implies positions for the 2^23^2 , 1^13^2 , and $1^12^13^1$ $K = 1$ levels of $47\,039$, $47\,148$, and $47\,513 \text{ cm}^{-1}$ respectively. Although not rotationally analysed in Ref. [139], a $K = 1 - 0$ band is apparent in their overview spectra near $47\,044 \text{ cm}^{-1}$. Based on the agreement with our predicted vibrational energy, we tentatively assign the upper state of this band as 2^23^2 . Between $47\,100$ and $50\,500 \text{ cm}^{-1}$, Yamakita *et*

al. [158] have analysed a large number of bands in LIF and H-atom action spectra. They observed a $K = 1 - 0$ band with a value of $T_0 + A = 47\,512.47\text{ cm}^{-1}$. We tentatively assign the upper state of this band as $1^12^13^1$.

Most notably, on the basis of the assignments of 1^1 in this work and 1^13^1 in Ref. [139], it is clear that the assignment in Ref. [119] of 1^13^2 $K = 0$ at $47\,194.80\text{ cm}^{-1}$, with the corresponding $K = 1$ at $47\,206.31\text{ cm}^{-1}$ should be re-examined. As shown in Ref. [139], the known anharmonicity constants are consistent with the assignment of the $K = 1$ level at $47\,146.92\text{ cm}^{-1}$ as 1^13^2 . It is also likely that assignments at yet higher energy, based upon following the vibrational intervals up from the erroneous ν'_1 energy, may prove incorrect, specifically the $K = 1$ level observed at $48\,160\text{ cm}^{-1}$ assigned as 1^13^3 in Ref. [119], and the higher members of the 1^13^n progression assigned in Ref. [122].

6.7 Impact of reassignment on our understanding of S_1 predissociation

The reassignment of ν'_1 may have significant impact on the current interpretation of the near-threshold photodissociation of acetylene. Mordaunt *et al.* [163] argued that excitation of ν'_1 enhanced the probability of dissociation through a direct ($S_1 \rightarrow T_1 \rightarrow \text{C}_2\text{H} + \text{H}$) channel relative to nearly isoenergetic states with excitation in the Franck-Condon active modes, which favor dissociation through an indirect ($S_1 \rightarrow T_3 \rightarrow T_2 \rightarrow T_1 \rightarrow \text{C}_2\text{H} + \text{H}$) pathway. This argument was based on the comparison of the C_2H product state distributions, derived from total kinetic energy release measurements, arising from the vibrational state-selected excitation of \tilde{A} -state C_2H_2 . In particular, bimodal product state distributions were noted by comparing photolysis energies of $47\,265.0\text{ cm}^{-1}$, terminating on the 3^5 level of the \tilde{A} state, and $47\,212.5\text{ cm}^{-1}$, accessing the level then assigned as 1^13^2 and currently under question. From the enhanced low-

J population present in the dissociation via the lower energy state and the associated H-atom recoil anisotropy, they concluded that this state decays by a mechanism that is both more direct and that imparts less torque to the C_2H fragment than the mechanism which dominates the decay of other states, particularly those at lower energy.

They interpreted these results in light of the *ab initio* calculations of Cui and Morokuma [166, 167] who tabulated stationary point energetics for various low-lying singlet and triplet states and, in addition, the minima of the seams of intersection between these electronic potential energy surfaces. While the indirect channel can, in large part, be rationalized by a mechanism resulting from sequential crossings from the S_1 to T_3 to $T_{2/1}$ and eventual dissociation over a late barrier on the T_1 surface, the mechanism controlling product formation for the more direct channel is not as clear. It is argued that the barrier which determines the product formation is half-linear, where the bond fission occurs for the C-H bond which is aligned with the CC bond, and therefore provides little torque to the departing C_2H fragment. The origin of the barrier is postulated to be the direct S_1/T_1 crossing, which may be invoked in the mechanism because the crossing is calculated to occur at a similar energy. However, the S_1/T_1 minimum of the seam of intersection (MSX) is calculated to have C_s symmetry and an out-of-plane structure with a dihedral angle of $\sim 140^\circ$. Mordaunt *et al.* point out that the MSX structure does not resemble what they anticipate for a dissociation transition state structure, but they do not discuss how the MSX structure and the expected half-linear structure would both appear to be unrelated to the observation that ν'_1 serves as a promoting mode for this channel.

Since ν'_1 is the symmetric C-H stretching mode, it is not expected to provide access to either out-of-plane or semi-linear geometries invoked in the argument of Ref. [163]. However, in light of the recent reassignment of $1^13^2 K' = 1$ to a lower energy band at 47147 cm^{-1} [139], the vibrational character of the level accessed in photolysis

at $47\,212.5\text{ cm}^{-1}$ is currently unknown. As we have mentioned, the assignments of vibrational levels containing excitation in only the totally symmetric, a_g , vibrational modes are considered secure up to $+4500\text{ cm}^{-1}$ ($46\,700\text{ cm}^{-1}$) and can be extended with some certainty up to $+5000\text{ cm}^{-1}$ ($47\,200\text{ cm}^{-1}$). The lowest energy state formed from totally symmetric modes which has not been at least tentatively assigned is 2^33^1 , the $K' = 1$ level of which is expected to lie near $47\,348\text{ cm}^{-1}$, some 140 cm^{-1} above the observed level position. Therefore, the upper state of this transition must involve excitation in the non-totally symmetric modes, belonging to either a $2^n3^mB^2$ or $2^n3^mB^4$ polyad. From energetic considerations, the most likely polyads to which the state may belong are $2^13^2B^2$, 3^2B^4 , or 3^4B^2 . Merer *et al.* [139] have suggested that the abnormally low value reported for A_v for this level in Ref. [119] was consistent with asymmetric top structure that had been distorted by Coriolis interactions, which are characteristic of the polyads formed by the low-frequency bending modes.

The plausible assignments of the $47\,206\text{ cm}^{-1}$ level can be viewed in light of the analysis of photodissociation results. The two geometric structures, out-of-plane with 140° dihedral angle and half-linear, implicated in the direct S_1/T_1 dissociation channel can each be associated with one of the two low-frequency bending vibrations. Reaching the out-of-plane structure of the S_1/T_1 MSX requires excitation of the torsional mode ν'_4 . More interestingly, the half-linear structure, postulated on account of the low- J population of C_2H fragments, bears strong resemblance to the calculated \tilde{A} -state *trans-cis* isomerization transition state. Reaching the isomerization transition state requires excitation in a superposition of the *cis*- (ν'_6) and *trans*-bending (ν'_3) normal modes. It is, therefore, possible that the state previously assigned as 1^13^2 may instead be one of the lowest members of a new class of states whose vibrational wavefunctions lie primarily along the isomerization coordinate, and the emergence of which is due to anharmonic interactions between the Franck-Condon active modes (ν'_2 , ν'_3) and the low-frequency bending vibrations (ν'_4 , ν'_6).

We will consider the precise nature of the $47\,206\text{ cm}^{-1}$ vibrational state and its relation to the onset of *trans-cis* isomerization in a later chapter.

Table 6.6: 2^2 upper state, $K'_a = 0$ and 1.

J	$\Sigma - \Pi$			$\Pi - \Sigma$			$\Sigma - \Sigma$
	R	Q	P	R	Q	P	Q_{fe}
0				44962.55			
1	44341.02*	44336.74	44334.66*	64.53	44960.09		44948.48
2	42.62	36.30	32.00	66.32	59.54	44955.50	47.96*
3	44.01	35.66*	29.18	67.90	58.69	52.74	47.28
4	45.14	34.66	26.07	69.33	57.60	49.83	46.35
5	46.06	33.49	22.78	70.57	56.23	46.74	45.19*
6	46.71	32.18*	19.22	71.59	54.55	43.45	43.76
7			15.40	72.44	52.64*	39.96	42.11
8				73.08	50.35	36.30	
9				73.55	47.84	32.45	
10				73.84	45.19*		

*Denotes a line that is blended or otherwise uncertain.

Table 6.7: 2^2 upper state, $K'_a = 2$.

J	$\Delta - \Pi$					
	R_{ee}	R_{ff}	Q_{fe}	Q_{ef}	P_{ee}	P_{ff}
1	44387.68					
2	89.31		44382.96			
3	90.78		82.28		44375.92	
4	91.92		81.26		72.80	
5	92.92		80.21	80.07	69.62	
6	93.50		78.88	78.62	65.92	
7	94.21		77.33	76.92	62.41	

Table 6.8: $2^2(\text{H}^{13}\text{C}^{12}\text{CH})$ upper state, $K'_a = 1$.

J	$\Pi - \Sigma$		
	R	Q	P
0	44922.57		
1	24.48	44920.18	
2	26.23	19.61	44915.67
3	27.73	18.78	13.01
4	29.07	17.68	10.14
5	30.22	16.31	07.03
6	31.21	14.65	

Table 6.9: 1^1 upper state, $K'_a = 0$ and 1.

J	$\Sigma - \Pi$			$\Pi - \Sigma$			$\Sigma - \Sigma$
	R	Q	P	R	Q	P	Q
0				45089.69			
1	44470.06	44465.79	44463.64	93.18	45087.31		
2	71.72	65.38	61.06	95.10*	88.29	45082.64	
3	73.78	64.70	58.26	96.90	87.64	81.42	45076.34
4	74.63	64.05		98.33	86.65	78.66	75.66
5	75.65	63.00		99.55	85.41	75.66	74.58
6		61.74				72.45	
7						68.97	

*Denotes a line that is blended or otherwise uncertain.

Table 6.10: 1^1 upper state, $K'_a = 2$.

J	$\Delta - \Pi$	
	$R_{ee,ff}$	$Q_{fe,ef}$
1	44516.92	
2	18.65	44512.18
3	20.21	11.64
4	21.56	10.72
5	22.74	09.89
6	23.80	

Table 6.11: $2^3 K'_a = 1$ upper state.

J	$\Pi - \Sigma$	
	R	Q
0	46304.67	
1	06.60	46302.21
2	08.36	
3	09.89	00.77
4	11.21	
5	12.35	
6	13.28	
7	13.96	

Table 6.12: $1^1 2^1 K'_a = 1$ and 2 upper states.

J	$\Pi - \Sigma$			$\Delta - \Pi$					
	R	Q	P	R_{ee}	R_{ff}	Q_{fe}	Q_{ef}	P_{ee}	P_{ff}
0	46477.14								
1	79.13	46474.73			45901.73				
2	80.96	74.21	46470.07		03.42		45897.03		
3	82.61	73.43	67.35		04.92		96.40		45890.00
4	84.10	72.41	64.50		06.15		95.45		86.91
5	85.41	71.15	61.47	07.29	07.17	94.46	94.30	83.74	
6	86.54	69.61	58.23	08.15	07.95		92.94		80.16
7	87.47	67.89	54.81				91.72		
8		65.97							72.58

Chapter 7

Vibrational assignments in the S_1

state of acetylene, III:

Combination polyads and the

approach to isomerization

The work in this chapter resulted from a collaborative effort between myself and Prof. Anthony Merer. A version of this chapter has been submitted as an article to the *Journal of Molecular Spectroscopy*.

7.1 Introduction

Multiple potential energy minima exist on the S_1 electronic surface of acetylene. The barriers separating these minima are relatively small (compared to the bond-breaking isomerization barrier on the ground state), a fact that suggests that the anharmonic vibrational interactions should become important at relatively low energy. In particular, the lowest energy path to *trans-cis* isomerization is calculated to occur through a half-linear geometry, where one of the CCH bond angles remains at 120° , while the

other hydrogen atom moves onto the C-C bond axis. This important geometry is not a point along any of the normal mode coordinates, but rather requires a superposition of the *trans* (ν'_3) and *cis*-bending (ν'_6) vibrations to be excited in order for it to be reached from the equilibrium geometry. The *trans*-bending mode is the primary Franck–Condon active mode in the $\tilde{A} \ ^1A_u - \tilde{X} \ ^1\Sigma_g^+$ transition. As a result, long progressions in ν'_3 are observed in the spectrum. In contrast, ν'_6 is of b_u vibrational symmetry and, therefore, forbidden to appear in the one-phonon spectrum. Weak overtones of ν'_6 have recently been observed on in the excitation spectrum (see Chapter 5), where they are found to be strongly mixed with the torsional mode, ν'_4 , which also has a nearly identical frequency. Coriolis interactions and Darling–Dennison resonance between these modes lead to the formation of polyads, which are characterized by unexpected rotational and vibrational patterns.

In this chapter, we describe the combination polyads, which contain excitation in the Franck–Condon active modes as well as the coupled low frequency modes. We aim to identify the effect that excitation of the Franck–Condon active modes has on the polyad structures in order to begin to characterize the effects of the *trans*–*cis* isomerization barrier. A second goal is to use the known polyad structures in order to securely assign all observed vibrational bands. Unassigned vibrational bands are of particular interest because they may involve vibrational levels of the unobserved *cis* well, transitions to which are forbidden by dipole selection rules.

7.2 Appearance of the spectra

The various vibrations involved in the combination polyads described in this chapter introduce considerable vibrational anharmonicity. As discussed below, this anharmonicity causes the simple model of Eqs. 5.8 and 5.9 to break down, though the basic structures of the polyads are not changed. We have not found a way to extend

the model to allow for the anharmonicity, and in our least squares fittings we have had to introduce, somewhat artificially, a number of centrifugal distortion terms and other corrections. These make minor adjustments to the K -structure, of the order of $1\text{--}2\text{ cm}^{-1}$, which then allow the rotational levels to be fitted with reasonable accuracy, though in some cases the values of these parameters are wholly unreasonable. These terms should be considered merely as fitting parameters, with no real physical meaning.

We refer to the bending polyads using the notation B^n . This notation means that the sum of the bending quantum numbers, v'_4 and v'_6 , for the vibrational levels making up the polyad is n ; for example the 2^1B^2 polyad consists of the three vibrational levels 2^14^2 , $2^14^16^1$ and 2^16^2 .

Figure 7-1 presents survey spectra of the $\tilde{A}^1A_u - \tilde{X}^1\Sigma_g^+$ system of acetylene as observed in jet-cooled excitation. The lower trace is the one-photon excitation spectrum from the ground vibrational level, which shows the $K' = 1$ levels of the Franck-Condon allowed (*gerade*) vibrational levels together with some of the bands involving the bending overtones. These latter are so much weaker than the Franck-Condon allowed bands that they are barely detectable at the long wavelength end of the spectrum. Leading lines show their positions. The upper trace shows the *ungerade* vibrational levels, as seen in IR-UV double resonance taken via the P(1) line of the ground state ν''_3 fundamental (which populates the $J'' = 0$ level). In this spectrum every vibrational band is reduced to a single R(0) line with $K' = 1$. The spectra are shown at the same horizontal scale, but displaced from each other by the average frequency of the upper state bending vibrations, so that the corresponding Franck-Condon allowed bands in the two spectra are roughly aligned vertically. The IR-UV double resonance spectrum becomes very complicated at about $46\,000\text{ cm}^{-1}$ and the vibrational assignments at higher energy have not been completed. Some one-photon bands are unavoidably present in these double resonance spectra; these

bands appear whenever the frequency of the UV laser happens to coincide with an absorption band. They are marked with asterisks in the figure.

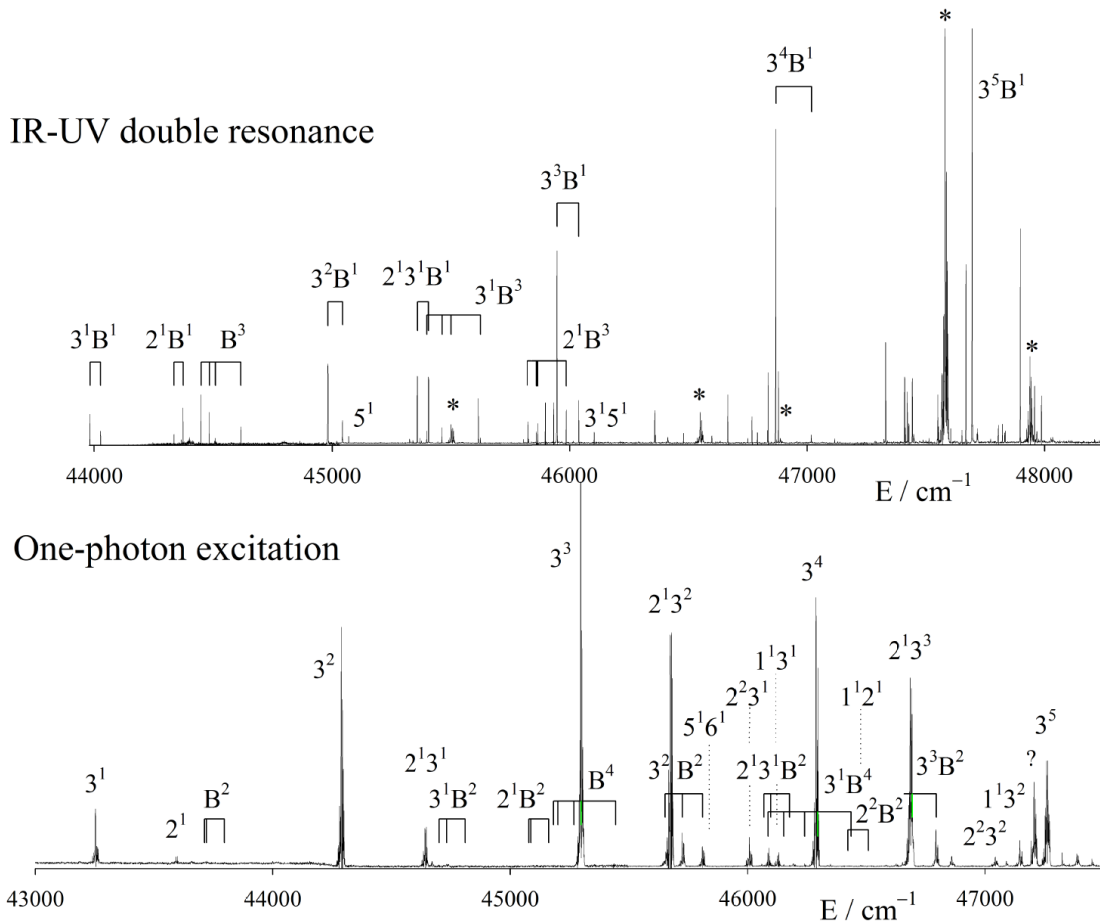


Figure 7-1: Survey spectra of the $\tilde{A} \ ^1A_u - \tilde{X} \ ^1\Sigma_g^+$ system of acetylene recorded with jet-cooling. Lower trace: One-photon excitation spectrum from the ground vibrational level, showing the $K' = 1$ levels of the Franck-Condon allowed *gerade* vibrational levels and some of the bending overtones. Upper trace: IR-UV double resonance spectrum of the *ungerade* vibrational levels, taken via the $J' = 0$ level of the ground state ν_3' fundamental. In this spectrum a vibrational band is reduced to a single R(0), $K' = 1$ line. Asterisks indicate one-photon artifacts.

Two points concerning the $3^n B^1$ polyads should be noted in Fig. 7-1, upper trace. First, the splitting between the two members of the polyads increases with excitation of ν_3' and, second, the lower members drop progressively below the corresponding one photon bands. In these polyads the nominal $3^n 6^1$ level always lies below the nominal $3^n 4^1$ level, providing clear evidence that the combinations of ν_3' and ν_6' are highly

anharmonic, as noted in Ref. [138]. Both traces in Fig. 7-1 show how the widths of the polyads, in energy terms, depend on the number of bending quanta that they contain. This is a result of the Darling-Dennison resonance term which, as Eq. 5.11 shows, has a strong vibrational quantum number dependence.

Some of the low-lying stretch-bend combination polyads of the \tilde{A}^1A_u state have already been described by other authors. Specifically, Mizoguchi et al. [138] reported analyses of the 3^2B^1 and 3^3B^1 polyads, and quoted unpublished results for the 3^1B^1 polyad. In Chapter 6, we have given some details of the 2^1B^2 polyad, since it interacts with the ν'_1 fundamental. The present chapter reports analyses of 2^1B^1 , 2^2B^1 , 2^2B^2 , 3^1B^2 , 3^2B^2 and the pairs of interacting polyads $2^13^1B^1/3^1B^3$ and $2^13^1B^2/3^1B^4$. We confirm the conclusion of Mizoguchi et al. [138] that the combinations of ν'_3 and ν'_6 are strongly anharmonic, though we find that excitation of ν'_2 has only a small effect on the structures of the bending polyads.

7.3 Combination polyads observed in IR-UV double resonance

7.3.1 The 2^1B^1 polyad

The 2^1B^1 polyad has been observed in IR-UV double resonance, with the IR laser tuned to individual P lines of the ν''_3 IR fundamental ($\ell'' = 0$) to record its $K' = 1$ levels and to the Q-branch head of the $\nu''_3 + \nu''_4$ combination band ($\ell'' = 1$) to record its $K' = 0$ and 2 levels. A weak Coriolis-induced band going to the lower $K' = 3$ level was also found in the second set of experiments. The Q-branch head of the $\nu''_3 + \nu''_4$ band is very compact, such that its first five lines lie within the line width of the IR laser; the levels $J'' = 1f - 5f$ can then be excited simultaneously. This reduces the time for data collection, but loses the J -selectivity of double resonance. However, the

line assignments could be made without difficulty by combination differences.

The structure of the 2^1B^1 polyad is similar to that of the B^1 polyad analyzed by Utz et al. [2], the main difference being that the 2^16^1 level lies 9.6 cm^{-1} above the 2^14^1 level, whereas 6^1 lies only 3.4 cm^{-1} above 4^1 . This is in contrast to the 3^nB^1 polyads, where the ν_6' member always lies below the ν_4' member [138]. There is no doubt about the assignments because the branch structures are unambiguous. Seen in double resonance via the f -symmetry component of the $\nu_3'' + \nu_4''$ combination level, the 2^16^1 level (b_u symmetry) gives a $K' = 0$ sub-band with R and P branches, while the $K' = 0$ sub-band of 2^14^1 (a_u symmetry) has only a Q branch.

Figure 7-2 is a reduced energy level plot showing the assigned upper-state term values together with the patterns calculated from the final least squares fit, described below. The strong b -axis Coriolis coupling between the two $K = 0$ levels and the lower $K = 1$ level is evident in the curvature of the plots for those levels. Interestingly, the largest asymmetry splitting occurs in the lower $K = 2$ level, presumably because of the proximity of the 2^16^1 , $K = 0$ level. The asymmetry splittings of the two $K = 1$ levels are smaller than expected for the \tilde{A}^1A_u state. In the absence of the a -axis Coriolis coupling, these two levels would have equal and opposite splittings, each about twice as large as is found. The a -axis coupling between them results in partial cancellation of their splittings.

The 2^1B^1 polyad lies just below the B^3 polyad and, with the strong a -axis Coriolis coupling pushing the uppermost level of each K' value some distance above the others, the upper $K = 2$ stack of the 2^1B^1 polyad lies only 40 cm^{-1} below the lowest $K = 2$ stack of the B^3 polyad. Obviously there must be Fermi resonance between the polyads, but the small shifts that result can be absorbed into sets of effective parameters for them.

The seven observed K -stacks of the 2^1B^1 polyad have been fitted by least squares to the Hamiltonian of Eq 5.8. The resulting parameters are given in Table 7.3.1. To

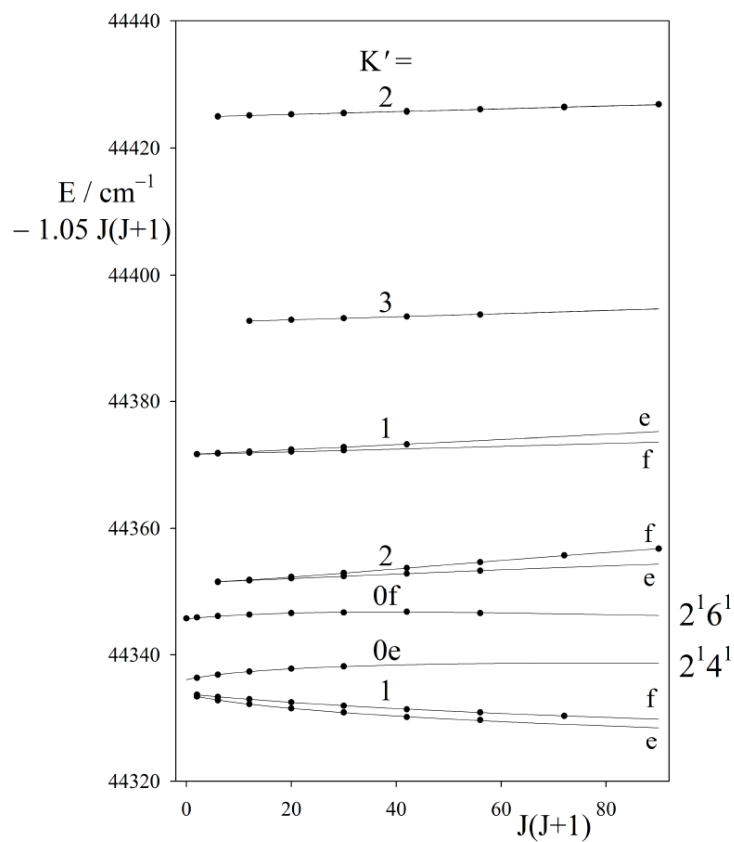


Figure 7-2: Reduced term value plot of the $2^1 B^1$ polyad, where the upper state energy levels, less $1.05 \times J(J + 1)$, are plotted against $J(J + 1)$. *A*-axis Coriolis interaction between the two $K' = 1$ levels pushes the lower $K = 1$ level (nominally $2^1 4^1$) below its $K' = 0$ level; *b*-axis Coriolis coupling between this $K' = 1$ level and the two $K' = 0$ levels is responsible for the curvatures in the plots. Points represent observed levels; lines are calculated from the results of the final least squares fit.

allow for the Fermi resonance with the B^3 polyad, a centrifugal distortion correction to the a -axis Coriolis constant, called $D(2A\zeta_{46}^a)_K$, was added to the parameter set. It reduced the r.m.s. error by about 30%. The rotational and Coriolis constants are found to be very similar to those determined by Utz et al. [39] for the B^1 polyad, though this is possibly fortuitous since there are extremely strong correlations between the two A rotational constants and the a -axis Coriolis parameters. We note that the mean of the two A constants, 12.894 cm^{-1} , is almost identical to the A constant of the 2^1 level, 12.902 cm^{-1} . With the rotational constants taken from the 2^1 level, the zeta sum rule [118],

$$(\zeta_{46}^a)^2 + (\zeta_{46}^b)^2 = 1, \quad (7.1)$$

holds very well, with the sum of the squares of the derived zeta parameters equal to 1.026.

Table 7.1: Rotational and Coriolis constants from a least squares fit of the \tilde{A} , 2^1B^1 polyad. Values in cm^{-1} .

Level	2^14^1		2^16^1	
T_0	44 336.08	± 0.04	44 345.69	± 0.03
A	11.411	0.50	14.376	0.50
\bar{B}	1.0750	0.0027	1.0601	0.0033
$B - C$	0.1080	0.0090	0.0813	0.0078
$2A\zeta_a^{46}$		17.928		± 0.13
$B\zeta_b^{46}$		0.821		0.009
$D(2A\zeta_a^{46})_K$		-0.0902		0.045
Δ_K		0.0060		0.0027
r.m.s. error	0.020			

The a -axis Coriolis coupling is defined as $2A\zeta_{46}^a + D(2A\zeta_{46}^a)_K K^2$. Derived values for the Coriolis parameters are: $\zeta_{46}^a = 0.695, \zeta_{46}^b = 0.737$. The centrifugal distortion parameter Δ_K is assumed to be the same for both vibrational levels. The following correlation coefficients have absolute values above 0.95: $A(2^14^1)/A(2^16^1)$, -0.998; $A(2^14^1)/2A\zeta_{46}^a$, 0.987; $A(2^16^1)/2A\zeta_{46}^a$, -0.981; $2A\zeta_{46}^a/D(2A\zeta_{46}^a)_K$, 0.954; $A(2^14^1)/D(2A\zeta_{46}^a)_K$, 0.988; $A(2^16^1)/D(2A\zeta_{46}^a)_K$, -0.994

7.3.2 The interacting $2^13^1B^1$ and 3^1B^3 polyads

Low resolution spectra of the overlapping $2^13^1B^1$ and 3^1B^3 polyads taken by IR-UV double resonance via the ν_3'' fundamental showed that there are seven $K' = 1$ stacks present, although only six are expected. We have therefore gone to some length to obtain a full analysis in order to clarify the vibrational assignments. It turns out that the extra stack is the highest of the seven in energy, and lies 8.2 cm^{-1} above the topmost $K' = 1$ stack of 3^1B^3 . There is no obvious vibrational assignment for the extra stack within the manifold of the S_1 -*trans* ($\tilde{A} \ ^1A_u$) state because every vibrational level expected in this energy region has been observed. Either it belongs to the S_1 -*cis* state, or it belongs to a higher S_1 -*trans* polyad where anharmonicity has pushed one of the component levels down by a huge amount. In either case, it presumably interacts with the 3^1B^3 levels, causing an energy shift, though this is hard to quantify.

The structure of the $2^13^1B^1$ and 3^1B^3 polyads is distorted because the ν_3'/ν_6' anharmonicity has a strong effect, particularly on the 3^1B^3 polyad. Excitation of the ν_3' vibration causes the vibrational level with the largest value of ν_6' (3^16^3) to drop considerably below the rest of the polyad. The result is that the lowest energy K -stacks of the 3^1B^3 polyad lie in the low- K region of the $2^13^1B^1$ polyad. A further complication is that there is non-negligible Fermi resonance between the two polyads.

The two interacting polyads have been recorded by IR-UV double resonance, using rotational levels of the ν_3'' fundamental and $\nu_3'' + \nu_4''$ combination level as intermediates, as described above for the 2^1B^1 polyad. Most of the analysis was carried out from spectra taken via the Q branch of the $\nu_3'' + \nu_4''$ band, which gave the whole $J'' = 1f - 5f$ spectrum in one recording, with consistent calibration. The line assignments could be made by combination differences, assisted for the crowded regions by spectra taken via the P(3) line of the $\nu_3'' + \nu_4''$ band (populating $J'' = 2e$). Various one-photon “artifact” bands, excited by the UV laser alone when its frequency happens to coincide with

an unrelated absorption band, could be distinguished by comparing the Q- and P-pumped spectra.

Figure 7-3 shows the rotational energy level structure of the two polyads, less $1.05 \times J(J + 1) \text{ cm}^{-1}$, plotted against $J(J + 1)$. Every assigned K -stack is shown, except the highest $K' = 2$ stack, which lies off the top of the figure near $45\,712 \text{ cm}^{-1}$. The K values of the various stacks, as given by the first lines of the branches, are marked in two columns, one for the $2^1 3^1 B^1$ polyad and the other for the $3^1 B^3$ polyad. The process of assigning the K -stacks to the polyads was complicated by the Fermi resonance and by the fact that some of the weaker sub-bands were not found until the late stages of the analysis.

Sizeable interactions occur among the levels in the central part of the structure. The most unexpected is the group of interacting $K = 1, 3$ and 4 levels near $45\,500 \text{ cm}^{-1}$. Their spectrum is shown in Fig. 7-4, as seen in double resonance via the Q branch of the $\nu_3'' + \nu_4''$ band. None of these levels should have given bands in Fig. 7-4 according to the selection rule $K' - \ell'' = \pm 1$, since the intermediate level has $\ell'' = 1$. It appears that the intensity comes from the very intense $K' = 0$ bands near $45\,540 \text{ cm}^{-1}$, and is transferred to the $K' = 1$ band by b -axis Coriolis coupling. The rotational level pattern shows that the $K' = 3$ stack gets its intensity by a combination of b -axis coupling with nearby $K' = 2$ stacks and asymmetry mixing with the $K' = 1$ stack. Finally, the $K' = 4$ stack interacts with the $K' = 3$ stack, again by b -axis coupling. Surprisingly, the $K' = 3$ stack does not appear in double resonance spectra taken via the ν_3'' fundamental ($\ell'' = 0$), although the $K' = 4$ stack gives quite strong lines. Evidently the K quantum number loses its meaning completely in the presence of the strong b -axis coupling. A similar situation was noted by Utz *et al.*[2] in their analysis of the B^1 polyad.

An interesting avoided crossing occurs between the $K' = 1$ and 2 stacks near $45\,460 \text{ cm}^{-1}$, illustrated in Fig. 7-5. In zero order the stacks belong to different

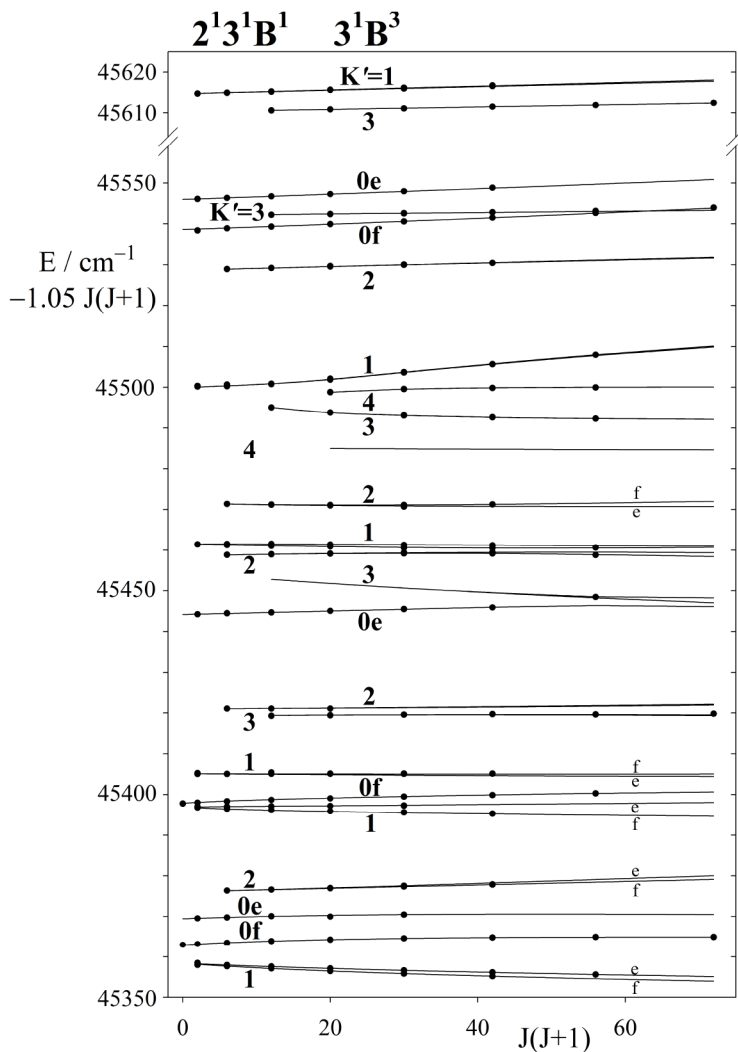


Figure 7-3: Energy levels of the interacting $2^1 3^1 B^1$ and $3^1 B^3$ polyads, less $1.05J(J+1)$, plotted against $J(J+1)$. The nominal K values of the rotational levels, as obtained from the first lines of the relevant branches, are indicated in two columns; left column, $2^1 3^1 B^1$ polyad, right column, $3^1 B^3$ polyad. Several avoided crossings between the K sub-levels occur in the central part of the figure. Points are observed rotational levels, lines are calculated from the results of the final least squares fit. All the observed K sub-levels are shown, with the exception of the highest $K' = 2$ sub-level, which lies near $45\,712\text{ cm}^{-1}$.

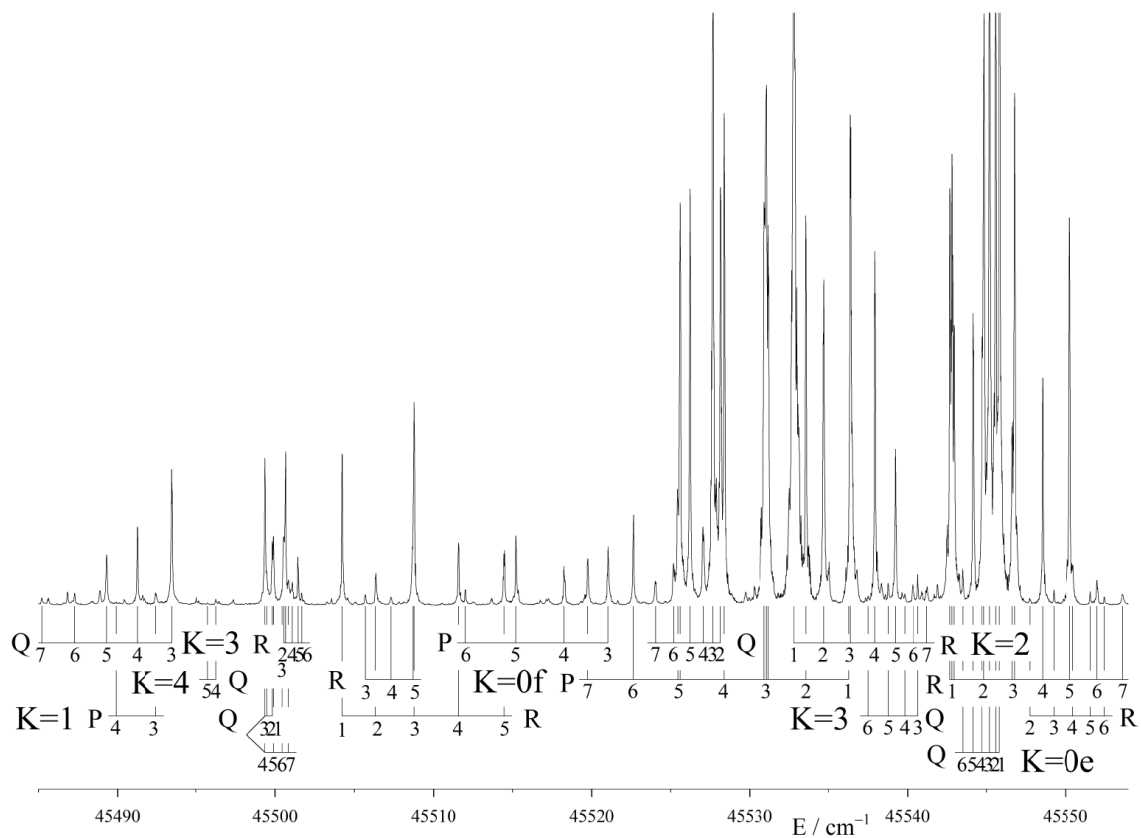


Figure 7-4: The region $45\,485\text{--}45\,554\text{ cm}^{-1}$ in the IR-UV double resonance spectrum of acetylene, showing seven overlapping sub-bands with $K' = 0 - 4$. The IR laser was tuned to the Q-branch head of the $\tilde{X}^1\Sigma_g^+$, $\nu_3'' + \nu_4''$ band ($\ell'' = 1$), populating the $J = 1f - 5f$ levels simultaneously. Some small splittings resulting from triplet perturbations can be seen in the $K' = 0f$ sub-band.

polyads, and have B values such that they cross through each other between $J = 5$ and 6. The minimum energy separation, which represents the strength of the Fermi resonances, is 1.36 cm^{-1} . A similar perturbation occurs between the $K' = 2$ and 3 stacks near $45\,420 \text{ cm}^{-1}$; there is clearly an avoided crossing, since the intensity is progressively transferred from the nominal $K' = 2$ stack to the nominal $K' = 3$ stack with increasing J , but the rotational levels diverge starting from the lowest J values. The lowest $K' = 3$ stack of the 3^1B^3 polyad, near $45\,450 \text{ cm}^{-1}$, could not be identified, although most of the other $K' = 3$ stacks appear weakly. However, its presence is shown by the avoided crossing with the $K' = 0e$ stack immediately below, where the $J = 7$ level is out of place.

Occasionally the rotational structures of two K -stacks cross through each other without a noticeable perturbation occurring. An example is the crossing between the upper $K' = 3$ stack of $2^13^1B^1$ and the upper $K' = 0f$ of 3^1B^3 near $45\,540 \text{ cm}^{-1}$. There are no measurable shifts at the crossing, and calculations of the level structure show that the shifts will be less than 0.01 cm^{-1} . Another example is the crossing of the upper $K' = 0e$ and the lowest $K' = 5$ of 3^1B^3 (not shown in Fig. 7-4) at $J = 7$; no measurable shifts are expected.

A few of the sub-bands, such as the upper $K' = 0f$ sub-band of the 3^1B^3 polyad illustrated in Fig. 7-5, show evidence of perturbations by triplet states. These take the form of small splittings of the lines into two or three components spread over up to about 0.4 cm^{-1} . The lines involved were not included in the final data set.

The results of a least squares treatment are given in Table 7.3.2. The levels of the $2^13^1B^1$ polyad were modeled with rotational constants A , $\frac{1}{2}(B + C)$ and $B - C$ for the two vibrational levels, together with Coriolis constants $2A\zeta_{46}^a$ and $B\zeta_{46}^b$. The operators for the Fermi resonances were taken as

$$\hat{H}_{\text{Fermi}} = k_{244}\hat{q}_2\hat{q}_4^2 + k_{266}\hat{q}_2\hat{q}_6^2 \quad (7.2)$$

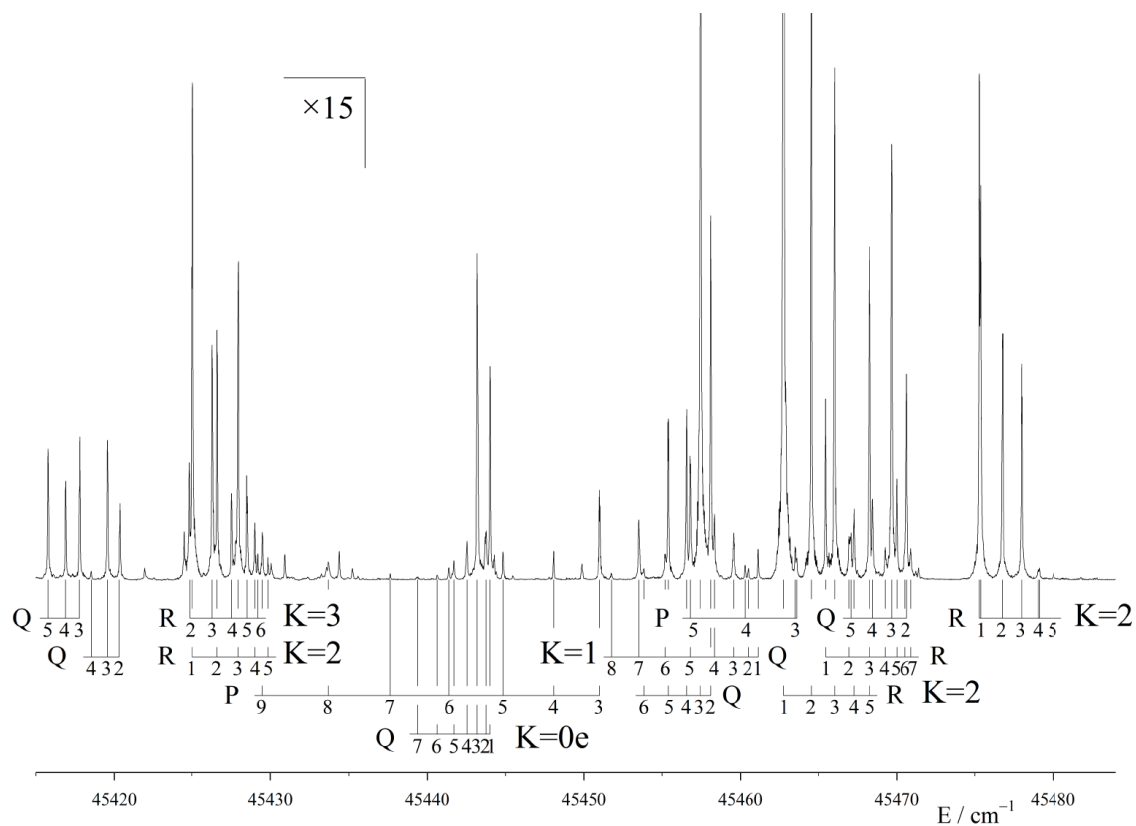


Figure 7-5: The region $45\,415\text{--}45\,484\text{ cm}^{-1}$ in the double resonance spectrum of acetylene, showing six overlapping sub-bands. This figure is a continuation of Fig. 7-4 to lower frequency. Below $45\,436\text{ cm}^{-1}$ the intensity scale of the spectrum has been expanded by a factor of 15 to show the weaker sub-bands in that region.

which gives matrix elements

$$\begin{aligned}
\langle 2^1 3^1 4^1 | \hat{H} | 3^1 4^3 \rangle &= \frac{\sqrt{3}}{2} k_{244} \\
\langle 2^1 3^1 4^1 | \hat{H} | 3^1 4^1 6^2 \rangle &= \frac{1}{2} k_{266} \\
\langle 2^1 3^1 6^1 | \hat{H} | 3^1 6^3 \rangle &= \frac{\sqrt{3}}{2} k_{266} \\
\langle 2^1 3^1 6^1 | \hat{H} | 3^1 4^2 6^1 \rangle &= \frac{1}{2} k_{244}
\end{aligned} \tag{7.3}$$

As explained in Section 6.3, the transformation that makes the Coriolis matrix elements real changes the signs of the k_{266} terms in Eq. 7.3, making them negative.

The ν'_3/ν'_6 anharmonicity complicated the fit of the $3^1 B^3$ polyad. It was found that the various avoided crossings in the J -structure could not be fitted satisfactorily until the K -structure was reproduced correctly, but in order to do this it was necessary to float the A constants for each of the four vibrational components and introduce a number of centrifugal distortion parameters. Some of these have unreasonable values, and should be treated just as fitting parameters, without physical meaning. The Δ_K parameters are a case in point. The parameters $\Delta_K(3^1 4^3)$ and $\Delta_K(3^1 6^3)$ were fitted by least squares, with the values of the Δ_K parameters for the other two vibrational levels of the polyad interpolated between them. The final values are far larger than expected, of opposite sign and also strongly correlated. Another unreasonable value is that for the parameter $D(2A\zeta_{46}^a)_K$ of the $2^1 3^1 B^1$ polyad. For the J -structure of the $3^1 B^3$ polyad, the parameters $\frac{1}{2}(B + C)$ and $B - C$ for the $3^1 4^3$ and $3^1 6^3$ levels were fitted, with the values for the other vibrational levels interpolated between them.

It was sometimes difficult in the least squares treatment to match the observed and calculated energies, particularly at the avoided crossings. The procedure adopted was to sort the energy levels by their nominal K values, which were then placed in ascending order. At the final stages, when the pattern of the K -structure had been established, the levels of each J and e/f symmetry were indexed by their energy

Table 7.2: Rotational and Coriolis constants from a simultaneous least squares fit of the \tilde{A} , $2^13^1B^1$ and 3^1B^3 polyads. Values in cm^{-1} .

$T_0(2^13^14^1)$	45 369.82	± 0.11	$T_0(3^14^3)$	45 502.16	0.71
$T_0(2^13^16^1)$	45 364.12	0.11	$T_0(3^14^26^1)$	45 517.43	0.17
$2A\zeta_{46}^a(2^13^1B^1)$	20.971	0.057	$T_0(3^14^16^2)$	45 487.64	0.67
$B\zeta_{46}^b(2^13^1B^1)$	0.7644	0.0108	$T_0(3^16^3)$	45 417.73	0.23
$A(2^13^14^1)$	10.709	0.228	K_{4466}	-57.865	0.123
$\frac{1}{2}(B + C)$	1.0784	0.0048	$K_{4466,DK}$	0.077	0.092
$(B - C)$	0.1235	0.0171	$2A\zeta_{46}^a(3^1B^3)$	20.596	0.050
$A(2^13^16^1)$	16.796	0.236	$B\zeta_{46}^b(3^1B^3)$	0.7788	0.0084
$\frac{1}{2}(B + C)$	1.0545	0.0036	$A(3^14^3)$	13.582	0.321
$(B - C)$	0.0868	0.0153	$\frac{1}{2}(B + C)$	1.0755	0.0036
$D(2A\zeta_{46}^a)_K(2^13^1B^1)$	-0.2701	0.0393	$(B - C)$	0.0934	0.0171
			$A(3^14^26^1)$	13.231	0.136
k_{244}	-7.36	1.14	$A(3^14^16^2)$	14.730	0.322
k_{266}	8.702	0.150	$A(3^16^3)$	14.873	0.080
			$\frac{1}{2}(B + C)$	1.0780	0.0042
			$(B - C)$	0.1532	0.0180
			$D(2A\zeta_{46}^a)_K(3^1B^3)$	-0.0589	0.0075
			$\Delta_K(3^14^3)$	0.0689	0.0243
			$\Delta_K(3^16^3)$	-0.0909	0.0240
			$K_{4466,DJ}$	-0.0035	0.0015
r.m.s. error	0.0453 cm^{-1}				

Error limits are three standard deviations.

The following correlation coefficients have absolute values above 0.95:

$$\begin{aligned}
 A(2^13^14^1)/A(2^13^16^1), & \quad 0.998; & T_0(3^14^3)/T_0(3^14^16^2), & \quad -0.985; \\
 A(3^14^3)/T_0(3^14^3), & \quad -0.975; & \Delta_K(3^14^3)/\Delta_K(3^16^3), & \quad -0.982; \\
 A(2^13^14^1)/D(2A\zeta_a^{46})_K(2^13^1B^1), & \quad 0.994; & A(2^13^16^1)/D(2A\zeta_a^{46})_K, & \quad -0.991; \\
 A(3^14^3)/T_0(3^14^16^2), & \quad 0.981
 \end{aligned}$$

The $J' = 0$ levels of the vibrational states are calculated to lie at:

e -symmetry: 45369.48 cm^{-1} ($2^13^14^1$); 45444.27 and 45545.87 cm^{-1} ($3^14^16^2$ and 3^14^3)

f -symmetry: 45362.99 cm^{-1} ($2^13^16^1$); 45397.81 and 45538.50 cm^{-1} (3^16^3 and $3^14^16^2$)

The differences between these values and those in the body of the table arise from the Fermi and Darling-Dennison resonances.

order. This method copes with the avoided crossings very well, but breaks down if a large change in a parameter interchanges the energy order of two K -stacks. In the end 216 rotational term values from 24 K -stacks were fitted with 33 parameters, giving an r.m.s. error of 0.045 cm^{-1} . It is very clear that the simple model of Eqs. 5.8 and 5.9 is starting to break down for these polyads. The line measurements are probably good to better than 0.03 cm^{-1} but, if no centrifugal distortion terms are included, the best fit to Eqs. 5.8 and 5.9 gives an r.m.s. error of about 0.12 cm^{-1} . Nevertheless, with the centrifugal distortion terms included, the courses of all the avoided crossings are reproduced with good accuracy.

One of the reasons for trying to get a good fit to the structure was to determine the Fermi resonance parameters, since these are important for extending the vibrational assignments to higher energy. It was found that the parameter k_{266} is quite well determined, though k_{244} is more approximate. Their absolute signs are not determinable, but their relative signs are opposite. To some extent their values must depend on the centrifugal distortion terms that were added in order to fit the K -structure. However, it was found that the value of k_{266} did not vary much from 8.7 cm^{-1} as these various terms were included.

As indicated at the beginning of this Section, the strong ν'_3/ν'_6 anharmonicity causes the 3^16^3 basis level of the 3^1B^3 polyad to drop a long way below the other three basis levels (see Table 7.3.2). As a result the Darling-Dennison resonance between the 3^16^3 and $3^14^26^1$ levels causes only a modest shift of 20 cm^{-1} (as can be seen from the calculated $J = 0$ energies in the Table). On the other hand the 3^14^3 and $3^14^16^2$ levels, which lie quite close in zero order, interact strongly, such that the nominal 3^14^3 state ends up as the top member of the polyad, 7 cm^{-1} above the nominal $3^14^26^1$ state. These two states form an a_u/b_u pair, of the type described in Chapter 5, which demonstrates the development of vibrational angular momentum patterns in the higher bending polyads. However, the effect is not as marked when ν'_3 is excited,

compared to the pure bending polyads, because the ν'_3/ν'_6 anharmonicity distorts the polyad structure.

7.3.3 The 2^2B^1 polyad

The 2^2B^1 polyad lies immediately above the 3^1B^3 polyad which, as just described, contains an “extra” $K' = 1$ stack. Another “extra” K -stack (this time with $K' = 0$, a_u symmetry) lies at $45\,735\text{ cm}^{-1}$, just above the predicted position of the 2^2B^1 polyad. It therefore becomes important to locate the 2^2B^1 polyad securely, in order to be sure that the “extra” stacks are not related to it. The 2^2B^1 polyad is expected to be much weaker than the 2^1B^1 polyad, since the 2^2_0 band (which was only found recently) is much weaker than the 2^1_0 band. We have searched for the $K' = 0$ and 2 levels of the 2^2B^1 polyad using IR-UV double resonance. Despite the poor signal-to-noise ratio it seems that the $K' = 0$ sub-band of 2^26^1 can be definitely identified, and the upper $K' = 2$ sub-band of the polyad possibly so. There is still some doubt about the 2^24^1 level.

The lines used for the IR pumping were isolated P branch lines of the $\nu''_3 + \nu''_4$ combination band. These populate the e -symmetry rotational levels of $\nu''_3 + \nu''_4$, such that levels of the \tilde{A} state with b_u vibrational symmetry give Q branches in IR-UV double resonance, and upper states with a_u symmetry give R and P branches. The 2^26^1 (b_u), $K' = 0$ sub-band, which appears as a weak Q branch at $45\,702.8\text{ cm}^{-1}$, is within 0.1 cm^{-1} of where it is predicted, based on anharmonicity constants derived from the known positions of 2^1 , 2^2 and the bending polyads B^1 and 2^1B^1 . The anharmonicity constants predict the 2^24^1 (a_u), $K' = 0$ sub-band to lie at $45\,687\text{ cm}^{-1}$. We have found nothing with the correct appearance near there, though a possible P and R branch pair lies at $45\,704.5\text{ cm}^{-1}$, some 17 cm^{-1} higher than predicted. This region is dominated by very intense lines from the highest $K' = 2$ sub-band of the 3^1B^3 polyad, and it could be that artifacts of the blending have confused the assignments,

despite the use of J -selected double resonance. The $K' = 1$ sub-bands of the 2^2B^1 polyad are not expected to appear in double resonance via an $\ell'' = 1$ intermediate level, and have not been looked for.

A calculation of the $K' = 2$ sub-band energies, based on the predicted $K' = 0$ origins together with rotational and Coriolis constants from the 2^1B^1 polyad, places them at 45 705 and 45 780 cm^{-1} . Nothing assignable as $K' = 2$ appears at the lower energy, but $K' = 2$ sub-bands are found at 45 777.9 and 45 790.8 cm^{-1} . It seems that the lower sub-band belongs to 2^2B^1 in zero-order, while the upper $K' = 2$ state is associated with the “extra” $K' = 0$ level at 45 735 cm^{-1} . No least squares fitting has been attempted for the 2^2B^1 polyad, since only three fragmentary sub-bands have been assigned.

The ν'_4 member of the various B^1 polyads is always weaker than the ν'_6 member, so that it is perhaps not surprising that we could not identify the 2^24^1 , $K' = 0$ sub-band securely. Nevertheless the good agreement of the position of the 2^26^1 , $K' = 0$ sub-band with the prediction from the anharmonicity constants suggests that there is nothing unusual about the 2^2B^1 polyad. The “extra” K stacks at 45 623 cm^{-1} ($K' = 1$) and 45 735 cm^{-1} ($K' = 0$, a_u) therefore appear not to belong to the 2^2B^1 polyad.

7.4 Combination polyads observed in one-photon laser excitation

With the a -axis Coriolis coupling disrupting the asymmetric top K -structure so severely, it is not possible to get a satisfactory least squares fit to a bending polyad without data from $K' = 0$, 1 and 2 stacks. As described above, two sets of experiments are needed to provide such data for the *gerade* bending levels, because of the rotational selection rule $K' - \ell'' = \pm 1$. The $K' = 1$ levels can be recorded in jet-

cooled laser excitation spectra from the ground vibrational state, where $\ell'' = 0$, but to record spectra of the $K' = 0$ and 2 levels it is necessary to warm the jet so that there is sufficient population in the ν_4'' fundamental, where $\ell'' = 1$. High sensitivity experiments with a cold jet have been carried out for the region up to $47\,000\text{ cm}^{-1}$, though with decreasing efficiency at the highest frequencies because of predissociation. Experiments with a warmed jet have so far not been attempted beyond $46\,000\text{ cm}^{-1}$.

7.4.1 The 3^1B^2 polyad

The 3^1B^2 polyad, near $44\,700\text{ cm}^{-1}$, has the simplest spectrum of all of the B^2 -type polyads observed in one-photon LIF. It lies at sufficiently low energy that it does not suffer from overlap with other polyads, while the anharmonicity between ν_3' and ν_6' causes the lowest member of the polyad (nominally 3^16^2) to drop well below the other members. Compared to the B^2 polyad, the anharmonicity greatly reduces the damaging effect of the b -axis Coriolis resonance on the qualitative appearance of the spectrum. All three $K' = 1$ bands are readily recognizable and sufficiently free from overlap with other bands to allow straightforward rotational analyses. The low frequency part of the polyad, as seen in laser excitation from the ground vibrational level, is illustrated in Fig. 7-6. The lowest two $K' = 1$ bands lie between the intense 3^34^1 , $\Sigma - \Pi$ and $\Delta - \Pi$ hot bands.

There is, in fact, a systematic coincidence between the strong hot bands of the type 3^n4_1 and weaker cold bands going to the $3^{n-2}B^2$ polyads. This can cause confusion when low resolution spectra are examined. For example, in the survey spectra of Ref. [139] there are bands with barely detectable intensity close to the expected positions for B^2 and 3^1B^2 . Upon closer inspection, despite the low temperature of the free-jet expansion, the positions of these bands are found to match those of the known 3^n4_1 hot bands and do not correspond to polyads formed from the low-frequency bending

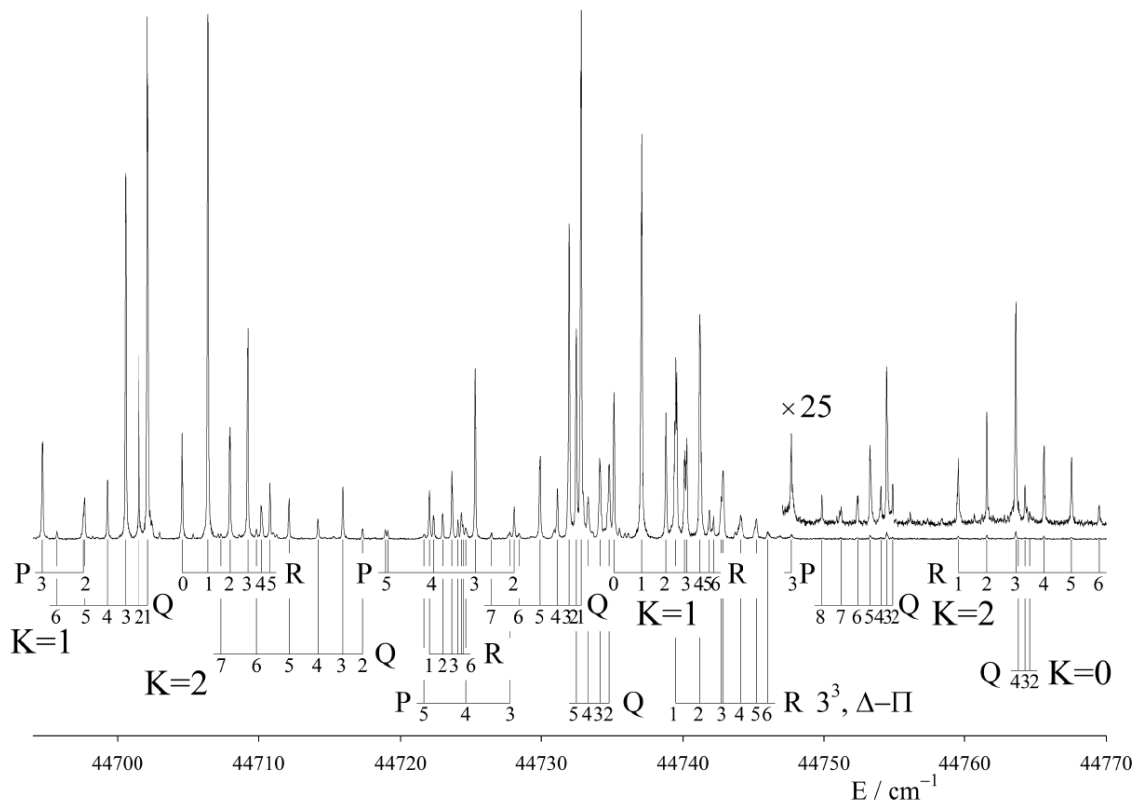


Figure 7-6: Low frequency part of the $3^1 B^2$ polyad of acetylene, as seen in jet-cooled laser excitation from the ground vibrational level. The comparatively intense, and very strongly red-degraded $K = 2 - 0$ sub-band near $44\,719\text{ cm}^{-1}$ gets its intensity by b -axis Coriolis coupling with the $K = 1 - 0$ sub-band near $44\,733\text{ cm}^{-1}$. The intensity scale of the spectrum has been expanded by a factor of 25 at the high frequency end in order to show the weak Coriolis-induced $K = 2 - 0$ and $0 - 0$ sub-bands near $44\,760\text{ cm}^{-1}$.

modes.

There are no low- J avoided crossings between the K stacks of the 3^1B^2 polyad members, but the b -axis Coriolis resonance is sufficiently strong that, despite the rotational selection rule $K' - \ell'' = \pm 1$, seven of the nine $K' = 0 - 2$ levels of the polyad appear in the cold jet spectrum; the exceptions are the middle $K' = 0$ level, which has b_g symmetry, and the highest $K'=2$ level, which lies 85 cm^{-1} above the highest $K' = 1$. As a result of the a -axis Coriolis interactions, the lowest vibrational level of the polyad has very compressed K -structure, with its $K' = 2$ sublevel only 16 cm^{-1} above its $K' = 1$. The $K' = 2$ sub-level is strongly affected by b -axis Coriolis resonance with the second $K' = 1$, so that the R branch going to it (near 44722 cm^{-1}) appears very compact in the spectrum. As Fig. 7-6 shows, the R(1)–R(6) lines fall within a span of only 2.5 cm^{-1} .

The middle $K' = 2$ sub-band and the uppermost $K' = 0$ sub-band appear in Fig. 7-6 as a result of the Coriolis interactions. Spectra recorded in a warmed beam confirm their assignments, but do not give evidence for any new sub-bands. The sub-band terminating on the highest $K' = 2$ level is predicted to lie hidden under the very intense $3_0^2K_0^1$ cold band, and has not been searched for.

The observed rotational term values of the seven observed K -stacks have been fitted to a Hamiltonian of the same form as that used for the B^2 polyad. The results of the fit are given in Table 7.3. Despite the lowering of the 3^16^2 level by the ν'_3/ν'_6 anharmonicity, no additional centrifugal distortion parameters were required to fit the data to within the measurement uncertainty. Comparing the parameters for 3^1B^2 and B^2 , the most significant difference is the 10% increase in the parameters K_{4466} and $2A\zeta_{46}^a$ on excitation of ν'_3 . The $B\zeta_{46}^b$ parameter undergoes a corresponding, but smaller percent decrease. Although the addition of one quantum of ν'_3 restores some of the regularity of the observed spectrum, it only slightly reduces the degree of mixing of the 3^14^2 and 3^16^2 normal mode basis states in the final vibrational eigenstates.

The reason for this is that the anharmonic shifts that separate the zero-order states are mostly offset by the larger value of the Darling–Dennison parameter, K_{4466} .

Table 7.3: Rotational and Coriolis constants from a least squares fit of the \tilde{A} , 3^1B^2 polyad. Values in cm^{-1} .

Level	3^16^2		$3^14^16^1$		3^14^2	
T_0	44 708.96	± 0.13	44 749.61	± 0.03	44 748.83	± 0.13
A	14.238	0.073	14.147	fixed	14.055	0.069
\bar{B}	1.0757	0.0012	1.0765	fixed	1.0772	0.0010
$B - C$	0.1153	0.0012	0.1112	fixed	0.1070	0.0029
$2A\zeta_a^{46}$			20.625	± 0.017		
$B\zeta_b^{46}$			0.784	0.005		
K_{4466}			-60.101	0.166		
r.m.s. error	0.032 cm^{-1}					

The $J' = K' = 0$ levels are calculated to lie at 44 692.84 (3^16^2), 44 749.61 ($3^14^16^1$) and 44 764.96 (3^14^2) cm^{-1} .

After the measured $K' = 0 - 2$ stacks had been fitted, it was noticed that the lowest $K' = 3$ sublevel of 3^1B^2 was predicted to lie at almost exactly the same energy as the $K' = 3$ sublevel of 2^13^1 , which had been reported as perturbed by Watson *et al.*[118] The near-degeneracy is quite striking: the predicted values given by Watson *et al.* for 2^13^1 $K' = 3$, based on fitting the unperturbed $K = 0 - 2$ sublevels, coincide with the predictions of our model for the $K' = 3$ sublevel of 3^1B^2 to better than 0.5 cm^{-1} . On this basis, we can now assign the lowest $K' = 3$ sublevel of 3^1B^2 as the perturbing partner to 2^13^1 $K' = 3$. Watson *et al.*[118] noted that this perturbation was the lowest energy perturbation that they found in the \tilde{A}^1A_u state.

A reduced term value plot for the perturbed levels is given in Fig. 7-7. The predicted term values of 3^1B^2 and 2^13^1 are shown, together with term values derived from measured line positions that were communicated privately to us by Dr. J.K.G. Watson. The observed components of the doubled band lie approximately 6.4 cm^{-1} apart and are symmetrically distributed around the predicted zero-order positions, indicating a coupling matrix element of about 3.2 cm^{-1} . An independent estimate

of this value can be obtained from the anharmonic parameters k_{244} and k_{266} derived from the interacting $2^1 3^1 B^1 / 3^1 B^3$ polyads (see Table 7.3.2). The eigenfunction of the lowest $J' = K' = 3$ state, considering just the Darling-Dennison and a -axis Coriolis interactions, and allowing for the phase factor for the v'_6 levels, is

$$|3^1 B^2, K = 3, I\rangle = 0.62 |3^1 4^2\rangle + 0.70i |3^1 4^1 6^1\rangle - 0.35 |3^1 6^2\rangle. \quad (7.4)$$

The Fermi resonance matrix element has only two terms, by symmetry:

$$\langle 2^1 3^1 | \hat{H} | 3^1 B^2, K = 3, I\rangle = 0.62 \langle 2^1 3^1 | \hat{H} | 3^1 4^2\rangle - 0.35 \langle 2^1 3^1 | \hat{H} | 3^1 6^2\rangle, \quad (7.5)$$

where the two integrals on the right hand side are $\frac{1}{2}k_{244}$ and $\frac{1}{2}k_{266}$, respectively.

Taking $k_{244} = -7.36$ and $k_{266} = 8.70 \text{ cm}^{-1}$ from Table 7.3.2, we obtain

$$\langle 2^1 3^1 | \hat{H} | 3^1 B^2, K = 3, I\rangle = -3.8 \text{ cm}^{-1}. \quad (7.6)$$

Total agreement is not expected, in view of the uncertainties in the determination of the k_{244} and k_{266} parameters, but the agreement with the (unsigned) value of 3.2 cm^{-1} from Fig. 7-7 seems very reasonable. The fact that the observed matrix element is small compared to k_{244} and k_{266} themselves is explained by the large amount of $|3^1 4^1 6^1\rangle$ character in the eigenfunction of Eq. 7.5, which does not contribute to the Fermi resonance matrix element.

A further perturbation in a single rotational level should be noted here. The $J' = 2e$ level of the highest $K' = 1$ member of the $3^1 B^2$ polyad exhibits quantum beats with nearly 100% modulation and a beat frequency of approximately 5 MHz. The large modulation depth combined with a slow beat frequency implies a weak interaction of $< 0.002 \text{ cm}^{-1}$. It is not surprising then, that the adjacent lines in the band appear to be unaffected by the perturbation and exhibit regular fluorescence decays. In

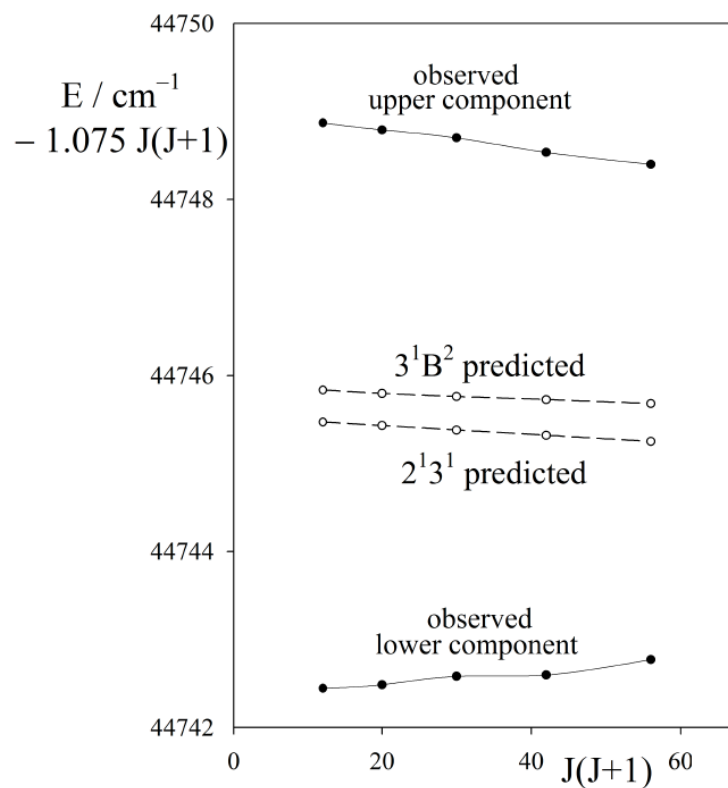


Figure 7-7: Observed and predicted rotational level structure at the perturbation between the $K' = 3$ stacks of the 2^13^1 and 3^1B^2 polyads, plotted against $J(J + 1)$. The predicted zero-order level positions, as obtained from least squares fits to lower- K stacks, are shown in the centre of the figure; the observed levels (from measurements communicated to us by Dr. J.K.G. Watson) are shown at the top and bottom of the figure.

hindsight we note that the R(1) line of this sub-band is very slightly asymmetrical, but this would not have been noticed without the quantum beat information. The perturbing state is presumably a member of the triplet manifold.

7.4.2 The 3^2B^2 polyad

The spectrum of the 3^2B^2 polyad is centered near $45\,700\text{ cm}^{-1}$, a region dominated by intense bands terminating on the 2^13^2 vibrational level. The 3^2B^2 polyad bands are themselves significantly more intense than the other B^2 -type polyads described in this work, a fact that is consistent with the observed trend of increasing intensity with higher excitation in the Franck-Condon active *trans*-bending mode ν'_3 . As a result, bands terminating on two of the three $K' = 1$ levels of the polyad can be seen in the survey spectrum of Ref. [139], where the upper state of the band at $45\,811\text{ cm}^{-1}$ is labeled as 3^24^2 .

The 3^2B^2 bands look quite similar to those of the 3^1B^2 polyad described above. There are no low- J avoided crossings between the polyad members, so the rotational assignments of the states are not complicated by b -axis Coriolis interactions. The most obvious feature is the relatively intense $45\,811\text{ cm}^{-1}$ band, which goes to the highest $K' = 1$ level. The sub-band terminating on the middle $K' = 1$ level, at $45\,726.12\text{ cm}^{-1}$, is nearly coincident with a hot band at $45\,726.93\text{ cm}^{-1}$ terminating on $3^4 K' = 2$, but is easily recognized from its intensity and the contrast between its fluorescence lifetime and that of the overlapping band. Coriolis-induced bands going to the middle $K' = 2$ and the highest $K' = 0$ levels lie in the clear and are readily recognized. The lowest $K' = 0$ sublevel of the 3^2B^2 polyad was located using spectra recorded with a warmed beam. Despite severe blending, the $K = 0 - 1$ sub-band was found to lie near $45\,032\text{ cm}^{-1}$, in the tail of the $K = 0 - 1$ hot band of 2^13^2 .

The lowest energy $K' = 1$ member of the polyad, at $45\,653.24\text{ cm}^{-1}$, was significantly more challenging to identify because of overlap by no less than four other

sub-bands. These four are the tail of the intense $2_0^1 3_0^2 K_0^1$ sub-band, its accompanying K_0^0 axis-switching band, the analogous $K' = 1$ transition of $\text{H}^{13}\text{C}^{12}\text{CH}$ and the $3^4 4_1 K_1^0$ hot band. The bands are illustrated in Fig. 7-8. Once the lines of these four bands are accounted for, only a few strong isolated lines remain, in particular the series at 45 655.31, 45 657.20, and 45 658.83 cm^{-1} . Since no clear combination differences could be found to number these lines, stimulated emission pumping (SEP) spectra were recorded using their upper states as the intermediate levels. Specifically, spectra were recorded to the $[N''_{\text{resonance}} = 13, N''_{\text{stretch}} = 1]_g$ polyad of the ground state, which lies near 8300 cm^{-1} . This region was chosen because it was known that the 45 811 cm^{-1} level emits strongly to this polyad, and it was assumed that the other $3^2 B^2$ levels should do so as well, though not necessarily to the same vibrational components.

Because the vibration-rotation structure of the electronic ground state of acetylene is well understood, the patterns in SEP spectra [168] can be used to label the rotational level of the $\tilde{A} \ ^1A_u$ state used as an intermediate. In particular, in the absence of axis-switching or accidental coincidences, the SEP spectrum via a $J' > 2$ R-branch PUMP transition contains 5 lines terminating on rotational levels of the $\Sigma_g^+(\ell'' = 0)$ and $\Delta_g(\ell'' = 2)$ components of every ground state vibrational level to which transitions are allowed. Q-branch PUMP transitions ($J' > 2$) give rise to 4 lines in the SEP spectrum. At lower values of J' , there are fewer lines because of the restriction $J'' \geq \ell''$. In all cases, the upper-state assignment follows from the final-state combination differences observed in the spectrum. The three isolated lines in the LIF spectrum described above could be identified as R(0-2) since their SEP spectra contain intervals of approximately $6B''$, $10B''$, and $14B''$, where B'' is the rotational constant for the ground vibrational level of C_2H_2 . Once the R-branch of the 45 653 cm^{-1} band had been recognized, the P and Q lines could be picked out, though in many cases they are severely blended. In particular the Q(1) line, at 45 652.91 cm^{-1} ,

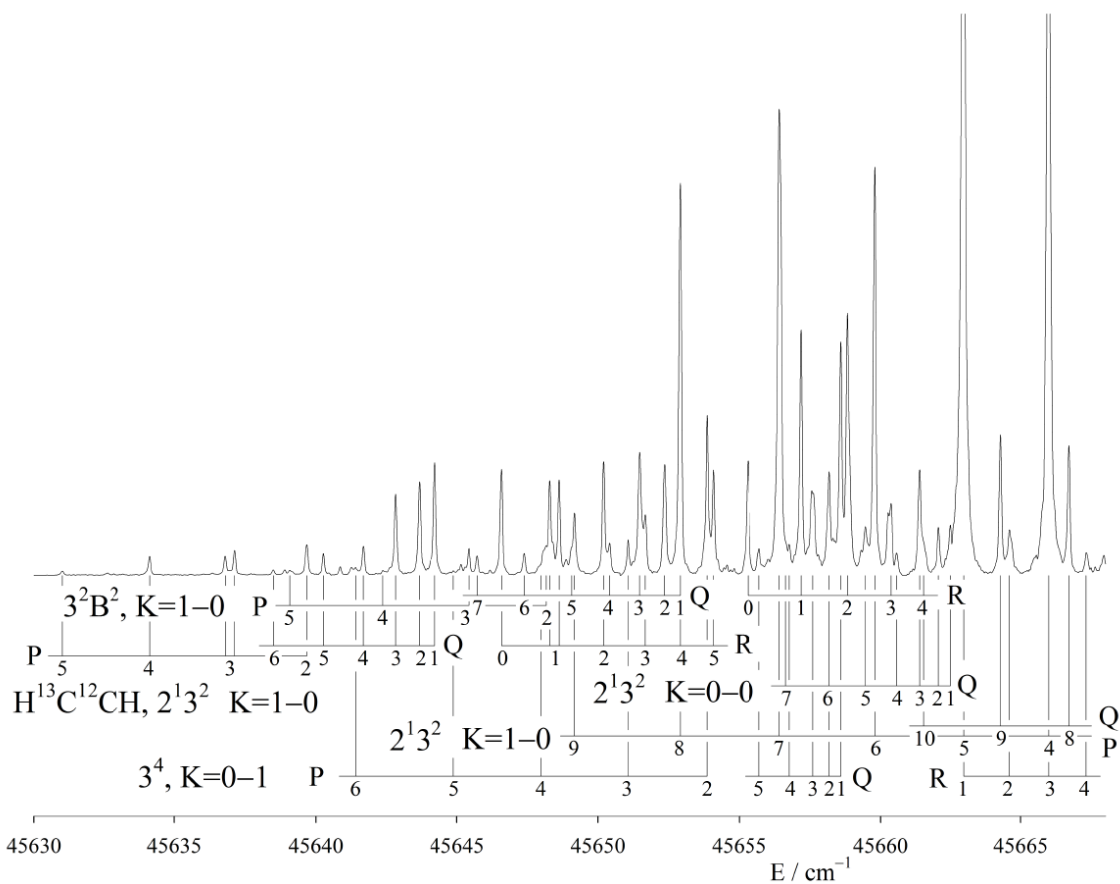


Figure 7-8: The lowest $3^2B^2, K' = 1$ sub-band of acetylene, overlapped by four other sub-bands. The strong structure is the tail of the $2^1_03^2_0, K = 1 - 0$ sub-band; weaker lines belong to the $H^{13}C^{12}CH$ isotopologue, the $2^1_03^2_0, K = 0 - 0$ axis-switching sub-band, and a hot band terminating on 3^4 .

coincides with the P(8) line of the strong $2^13^2K_0^1$ band. The assignment of Q(1) has been confirmed by recording an SEP spectrum using it as a PUMP transition.

The six observed sublevels of the 3^2B^2 polyad (of the nine with $K' = 0 - 2$) have been fitted to the Hamiltonian given in Eqs. 5.8 and 5.9. The results of the fit are given in Table 7.4. Addition of a second quantum of ν_3' continues the trend noted in the 3^1B^2 polyad: the Darling–Dennison and a -axis Coriolis coupling parameters increase yet further, while the b -axis coupling is slightly reduced. The increase in the Darling–Dennison parameter is more than offset by the increased separation of the 3^24^2 and 3^26^2 basis states as a result of anharmonicity, so that the mixing of the basis states by the Darling–Dennison resonance is actually less than it is in the B^2 polyad. To be exact, the $J' = K' = 0$ eigenstates receive over 90% of their character from a single basis state. The fit model indicates only slightly more mixing for the lowest $J' = K' = 1$ eigenstate, though the upper two states form a very strongly Coriolis-coupled a_g/b_g pair.

Table 7.4: Rotational and Coriolis constants from a least squares fit of the \tilde{A} , 3^2B^2 polyad. Values in cm^{-1} .

Level	3^26^2		$3^24^16^1$		3^24^2	
T_0	45 653.95	± 0.40	45 736.07	± 0.02	45 756.86	± 0.40
A	16.178	0.208	15.395	fixed	14.611	0.212
\bar{B}	1.0808	0.0012	1.0768	fixed	1.0727	0.0012
$B - C$	0.1080	0.0043	0.1034	fixed	0.0989	0.0027
$2A\zeta_a^{46}$			23.559	± 0.112		
$B\zeta_b^{46}$			0.808	0.014		
K_{4466}			-66.502	0.122		
r.m.s. error	0.024 cm^{-1}					

The $J' = K' = 0$ levels are calculated to lie at 45 644.14 (3^26^2), 45 736.07 ($3^24^16^1$) and 45 766.67 (3^24^2) cm^{-1} .

A further advantage of SEP spectra is that they give the distribution of b_g vibrational character among the polyad members. Since a_g and b_g correlate respectively with the Σ_g^+ and Σ_g^- representations of $D_{\infty h}$, the Franck–Condon-allowed levels of

the $\tilde{A} \ ^1A_u$ state, with a_g vibrational symmetry, will emit to $\ell'' = 0$ states with Σ_g^+ (e) symmetry, while levels with b_g vibrational symmetry will emit to $\ell'' = 0$ states with Σ_g^- (f) symmetry. Since the e/f symmetry is reversed in Σ_g^- states, compared to Σ_g^+ states, the pattern of emission lines in transitions to them is also reversed: for $J' > 2$, Q-branch pumping gives a five-line pattern and R-branch pumping a four-line pattern. It is therefore simple to identify Σ_g^- vibrational levels in SEP spectra, and thereby assess the amount of b_g character in a given vibrational level of the $\tilde{A} \ ^1A_u$ state.

SEP spectra have been recorded via the $J' = 1f$ (Q(1)-pumped) levels of the three $K' = 1$ stacks of the 3^2B^2 polyad. In all three SEP spectra, a feature is observed near an internal energy of 8320 cm^{-1} , terminating on what is believed to be a $J'' = 2$, $\ell'' = 2$ state. Just above this transition, but only in the spectra from the two highest energy $K' = 1$ intermediate levels, are two lines separated by approximately $6B''$. The final states of these transitions are assigned as $J'' = 0$ and 2 of a Σ_g^- vibrational level with an energy of 8322.3 cm^{-1} . To our knowledge, this state has not previously been observed, though the predictions of the multiresonant polyad Hamiltonian place a Σ_g^- member of the $[13, 1]$ polyad at 8322.5 cm^{-1} [169], in excellent agreement with our observation. The lack of intensity into this final state from the lowest $K' = 1$ polyad member is consistent with our model, which predicts $< 10\%$ b_g character in this sublevel. In general, levels of the $\tilde{A} \ ^1A_u$ state with dominant b_g vibrational character could prove useful in SEP experiments for identifying further Σ_g^- vibrational levels of the ground state, which are presently undersampled relative to the other symmetry species.

A final note on this polyad is that many of the lines in the highest $K' = 1$ sub-band ($45\,811 \text{ cm}^{-1}$) appear to be significantly broadened and structured, presumably because of interactions with the manifold of low-lying triplet states. While all lines are affected to some degree, the broadening is particularly severe for $J' = 5 - 8$, with

the FWHM of the observed linewidth increasing to over 0.3 cm^{-1} at $J' = 6$, compared to the width of 0.06 cm^{-1} in the narrowest lines observed in our study. The splittings in the higher- J R lines of this band are illustrated in Fig. 7-9.

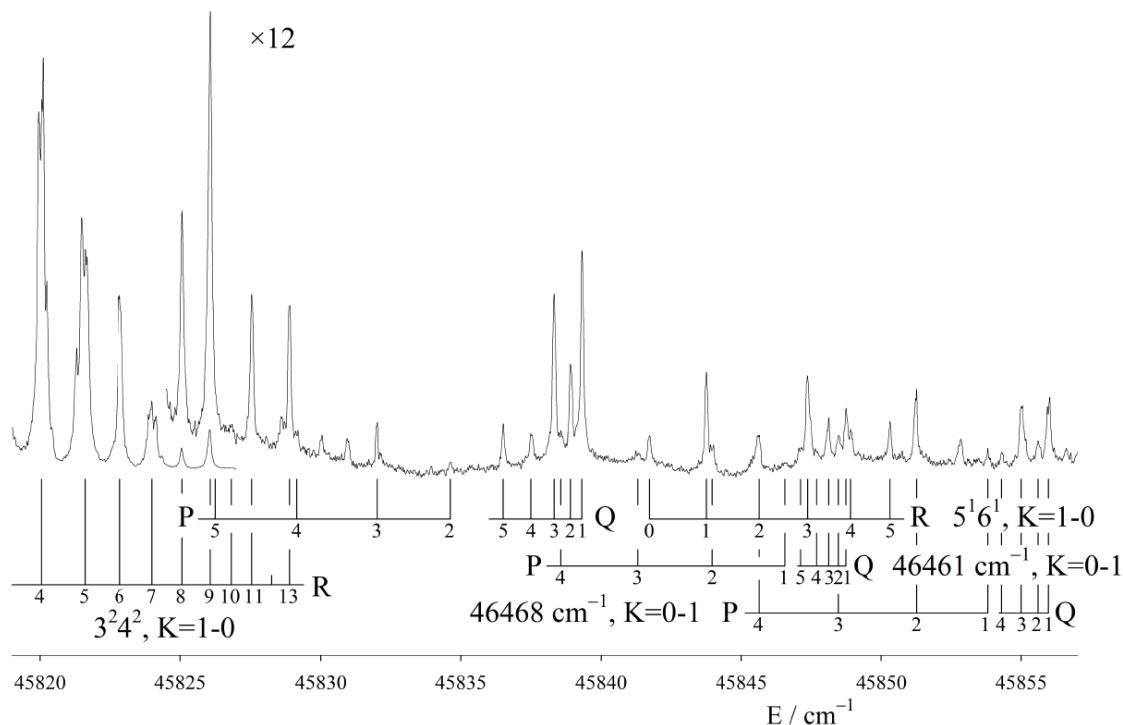


Figure 7-9: LIF spectrum of jet-cooled acetylene in the region of $45\,819\text{--}45\,857 \text{ cm}^{-1}$. At the low frequency (left) side are the higher- J R lines of the $3^2 4^2$ band ($45\,811 \text{ cm}^{-1}$), showing structure resulting from perturbations by triplet states. The central part of the spectrum contains the $5^1 6^1, K' = 1$ sub-band, and the two sub-bands at the high frequency side are $K = 0 - 1$ hot bands going to the interacting $2^2 B^2$ and $1^1 2^1, K' = 0$ levels; these hot bands are labeled by the energies of their upper states ($45\,461$ and $45\,468 \text{ cm}^{-1}$).

7.4.3 The $3^3 B^2$ polyad

The $3^3 B^2$ polyad lies above the onset of predissociation, and experiments with a warmed jet have not so far been carried out in this region. However, spectra taken with a cold jet have allowed assignment of the upper two $K' = 1$ sub-bands for this polyad. As in the $3^1 B^2$ and $3^2 B^2$ polyads, the lowest $K' = 1$ sub-band is weaker than the other two and has not been identified yet. Bands from three other polyads,

1^1B^2 , 2^1B^4 and B^6 , are expected in the same region, making vibrational assignments challenging.

The highest energy $K' = 1$ sub-band, at $46\,794.29\text{ cm}^{-1}$, was already recognized in Ref. [139]. It is a fairly strong band which continues the obvious 3^n4^2 progression found in the 3^1B^2 and 3^2B^2 polyads. Because it lies so far above the other $K' = 1$ stacks of its polyad, the asymmetry splitting of the upper state is only minimally affected by the a -axis Coriolis coupling, and its magnitude ($B - C = 0.074\text{ cm}^{-1}$) is not much reduced from that of the zero-point level. Another, rather weaker, $K' = 1$ sub-band (as yet unassigned vibrationally) lies just below it, at $46\,790.74\text{ cm}^{-1}$. No local interactions between the two upper states occur in the observable range of J' values, though an avoided crossing between the f -symmetry components is predicted to occur at much higher J . In contrast to the $45\,811\text{ cm}^{-1}$ band, discussed in the previous section, the $46\,794\text{ cm}^{-1}$ band does not appear to be strongly affected by triplet perturbations.

The middle $K' = 1$ sub-band, at $46\,692\text{ cm}^{-1}$, lies 5 cm^{-1} above the $2^13^3K_0^1$ sub-band, and appears to have caused some confusion in the rotational assignment of the latter [119]. With the advantage of jet-cooling it is possible to recognize that two bands are present, though their branches overlap severely. The reduced upper state energies are shown plotted against $J(J + 1)$ in Fig. 7-10. It is clear from this figure that the senses of the asymmetry splitting are opposite in the two levels. This is as expected, since the 3^3B^2 level in question is the middle component of its polyad. The largest contributor to its wavefunction is the $3^34^16^1$ basis state, which has bg vibrational symmetry; the sense of its asymmetry splitting is therefore opposite to that of the 2^13^3 level, which has a_g symmetry. The figure shows that, in contrast to the analysis of Ref. [119], the asymmetry splitting of the $2^13^3, K' = 1$ level is quite small at low J . Blending has made some of the measurements for the $3^34^16^1$ levels less certain, but it appears that the $K'_c = J' - 1$ (e -symmetry) components

of the two vibrational levels undergo an avoided crossing at about $J' = 5$, with an interaction matrix element of roughly 1.6 cm^{-1} , while the separation of the $K'_c = J'$ (f -symmetry) components changes only slightly with J . The size of the interaction matrix element is consistent with the energies of the K -stacks of the 2^13^3 level given in Table XI of Ref. [119], where it can be seen that the $K' = 1$ level is about 1 cm^{-1} lower than would be expected from the energies of the $K' = 0$ and 2 stacks because they will be more detuned from resonance.

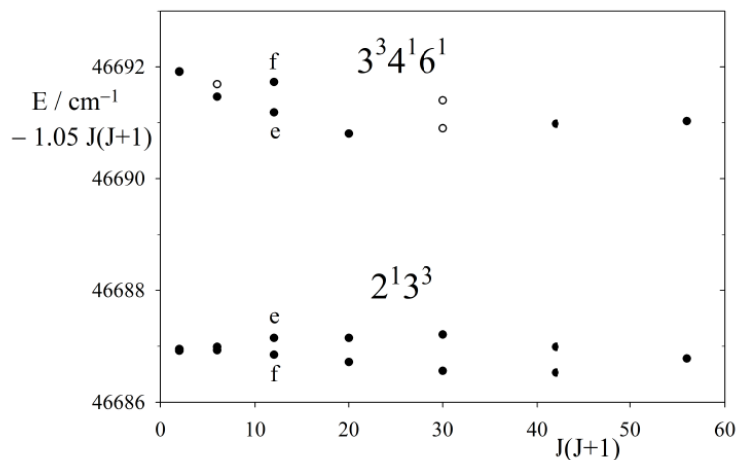


Figure 7-10: Rotational energies of the interacting 2^13^3 and $3^34^16^1$, $K' = 1$ levels, less $1.05J(J+1)$, plotted against $J(J+1)$. The levels of e symmetry undergo an avoided crossing near $J' = 5$. Open circles represent data points from blended lines.

If there were no a -axis Coriolis coupling in the 3^3B^2 polyad, there would be no perturbation, since the 2^13^3 level has a_g vibrational symmetry and the $3^34^16^1$ level has b_g symmetry. However the Coriolis coupling mixes 3^34^2 and 3^36^2 character into the nominal $3^34^16^1$ level for $K' \neq 0$, which then allows the Fermi resonance operators of Eq. (4) to cause local perturbations. Since the K -structure of the 3^3B^2 polyad is very different from that of the 2^13^3 level, the other K -stacks of 2^13^3 will be less affected.

Rotational constants from a band-by-band fit to the $K' = 1$ sub-band at $46\,795 \text{ cm}^{-1}$ are listed in Table 7.5.

Table 7.5: Rotational constants from band-by-band fits to miscellaneous levels of the \tilde{A}^1A_u state of acetylene. Values in cm^{-1} .

	T_0	$\frac{1}{2}(B + C)$	$B - C$	rms
$5^16^1, K' = 1$	45 839.52 ± 0.02	1.0867 ± 0.0014	0.0426 ± 0.0014	0.014
$2^2B^2/1^12^1, K' = 0, \text{I}^{(a)}$	46 460.58	1.1112	0.0016	0.076
$2^2B^2/1^12^1, K' = 0, \text{II}^{(a)}$	46 467.83	1.0843	0.0010	0.027
$2^2B^2, K' = 1, \text{III}$	46 505.46	1.0757	0.0011	0.016
$3^3B^2, K' = 1, \text{III}$	46 794.29	1.0869	0.0041	0.026

(a) These two levels arise from anharmonic interaction between the upper $K' = 0$ level of 2^2B^2 and $K' = 0$ of 1^12^1 ; the mixing is almost 50:50.

7.4.4 The 2^1B^2 and 2^2B^2 polyads

The 2^1B^2 and 2^2B^2 polyads were discussed briefly by in Chapter 6. The 2^1B^2 polyad is of interest because the ν'_1 fundamental lies near its center and causes perturbations as a result of anharmonic resonance. The rotational structure is unusually complicated because the $K' = 1$ stack of the ν'_1 fundamental happens to lie exactly where the middle $K' = 1$ and the lowest $K' = 2$ stacks of 2^1B^2 are involved in a very strong b -axis Coriolis resonance so that, with the two resonances competing, the resulting level pattern is very disorganized. We could only assign this region with the help of population labeling, where an IR laser was used to deplete the population of a selected rotational level of the ground state, modulating the fluorescence excited by the UV laser for those lines coming from the selected level. Analysis of the hot bands showed that further small perturbations occur between the $K' = 0$ stack of ν'_1 and the lowest $K' = 1$ stack of 2^1B^2 , but that the $K' = 2$ stack of ν_1 lies about 10 cm^{-1} above the middle $K' = 2$ stack of 2^1B^2 and is not locally perturbed. An energy level diagram and the results of least squares fitting are given in Chapter 6.

The 2^2B^2 polyad is weaker than the 2^1B^2 polyad, and only two of its sub-bands can be securely identified. These are the highest and lowest $K' = 1$ sub-bands, at $46 505.46$ and $46 419.04 \text{ cm}^{-1}$. It is clear that the $46 419 \text{ cm}^{-1}$ level undergoes strong Coriolis interactions with unseen $K = 0$ and 2 levels because it has an unusually low

B value, and its asymmetry splitting is highly irregular, reversing its sense at $J' = 6$. Some unusual structure near $45\,850\text{ cm}^{-1}$ had prompted us to carry out experiments with a warmed beam in that region, and led to the assignment of two $K = 0 - 1$ hot bands, with upper states at $46\,460.58$ and $46\,467.83\text{ cm}^{-1}$. The Q and P branches of these hot bands are illustrated in Fig. 7-9. As explained in our Chapter 6, these result from anharmonic resonance between the highest $K' = 0$ stack of 2^2B^2 and the $K' = 0$ stack of 1^12^1 . The $K' = 1$ and 2 stacks of 1^12^1 appear to be unperturbed, and a least squares fit to them alone predicts that the $1^12^1, K' = 0$ stack should lie at $46\,463.48\text{ cm}^{-1}$. This would place the highest $K' = 0$ stack of 2^2B^2 at $46\,464.93\text{ cm}^{-1}$ in zero order, with an interaction matrix element of 3.6 cm^{-1} .

A global least squares fit to the 2^2B^2 polyad has been attempted, but with only three K -stacks observed, one of which is involved in an anharmonic resonance, it is of limited value. Somewhat surprisingly though, the fit is very good ($\sigma = 0.011\text{ cm}^{-1}$), and reproduces the unusual asymmetry splitting of the $46\,419\text{ cm}^{-1}$ level faithfully. The position predicted by the fit for the middle $K' = 1$ sub-band coincides with the highest $K' = 1$ sub-band of the 3^1B^4 polyad, at $46\,434.37\text{ cm}^{-1}$. This is quite a strong band, but there are not enough unassigned lines remaining to allow clear assignments of the 2^2B^2 branches. Rotational constants from a band-by-band fit to the uppermost $K' = 1$ level ($46\,505\text{ cm}^{-1}$) are given in Table 7.5. Interestingly, it is not possible to give sensible rotational constants for the lower $K' = 1$ stack from a band-by-band fit because Coriolis couplings with unseen levels affect the asymmetry splitting so strongly.

7.4.5 The $2^13^1B^2$ and 3^1B^4 polyads

The $2^13^1B^2$ and 3^1B^4 polyads, together with the 1^13^1 level, form a complex of nine interacting vibrational levels, of which the lowest K -stacks lie near $46\,060\text{ cm}^{-1}$. Fermi resonance is expected between the $2^13^1B^2$ and 3^1B^4 polyads, and perturbations are

expected between the 1^13^1 level and the $2^13^1B^2$ polyad, in similar fashion to the perturbations between the ν'_1 fundamental and the 2^1B^2 polyad. As it turns out, the K -stacks of the 1^13^1 level mostly fall in gaps in the K -structure of the $2^13^1B^2$ polyad, so that the effect of the anharmonic resonances is quite small and can be absorbed into effective constants for the levels involved. An analysis of the 1^13^1 band was given in Ref. [139]. A number of small perturbations were found in the 1^13^1 level, but none of them can be attributed to the $2^13^1B^2$ polyad.

Although only nine vibrational levels are expected in this energy region, ten $K' = 1$ stacks are found, showing that an “extra” level, of the type discussed in parts 7.3.2 and 7.3.3, is present. It is important to establish the detailed K -structures of these polyads so that the “extra” level can be identified securely. However, this is more difficult in one-photon spectra than it is in double resonance spectra. The $K' = 1$ levels are usually easy to find because they appear in excitation spectra from the ground level. The $K' = 0$ and 2 levels require warmed jet spectra, which are more capricious experimentally, and lack the selectivity of double resonance spectra. As a result, the weaker $K' = 0$ and 2 sub-bands are not always seen, so that there can be some uncertainty in identifying what is actually observed. Careful predictions of the K -structure are needed, basing them soundly on the levels observed at lower energy.

Comparison of the 2^1B^1 and B^1 polyads shows that the anharmonicity parameters x'_{24} and x'_{26} are quite similar. Also x'_{23} is only -0.24 cm^{-1} . It should therefore be possible to predict the structure of the $2^13^1B^2$ polyad to within a few cm^{-1} by adding the observed differences between corresponding levels of the 2^1B^2 and B^2 polyads to the observed energies of the 3^1B^2 polyad. This procedure assumes that x'_{23} is zero, and ignores the small shifts of up to about 3 cm^{-1} in the 2^1B^2 structure caused by the 1^1 level, but otherwise follows the usual Dunham expressions for the vibrational energies.

Because of the ν'_3/ν'_6 anharmonicity, the structure of the 3^1B^4 polyad cannot be

predicted in similar fashion by adding the ν'_3 interval to the energies of the B^4 polyad. (In any case only eight of the 15 stacks in the B^4 polyad with $K' = 0 - 2$ have been located. See Chapter 5.) Instead, a calculation based on Eqs. 5.8 and 5.9 is needed, with the zero-order vibrational energies extrapolated from anharmonicity constants derived from the 3^1B^n polyads, where $n = 0 - 3$. The Fermi resonance between the $2^13^1B^2$ and 3^1B^4 polyads will make small random corrections to the energies, but is probably not important for the predictions since there appear to be no pathological near-degeneracies between levels of the two polyads, of the type seen in Fig. 7-3.

To calculate the 3^1B^4 levels, the energies of the basis states of the 3^1B^n polyads, $n = 0 - 3$, were reduced to a set of vibrational parameters where the anharmonicity in ν'_3 is folded into effective bending parameters. These parameters, which are listed below Table 7.6, were then used to calculate the rotational structure. A comparison of the observed and calculated level structures of the $2^13^1B^2$ and 3^1B^4 polyads is given in Table 7.6. Included in the data set are two levels, with $K' = 1$ and 3, which are not seen in the jet spectra, but which cause perturbations in the 3^4 level at higher J values; they are described in Ref. [170]. It can be seen that the match between the observed and calculated level positions is very good, with 12 of the 18 observed levels predicted to within 3 cm^{-1} , and the other six predicted to within 10 cm^{-1} .

Confirmation of the $K' = 1$ assignments comes from the asymmetry splittings, where the observed and calculated values of the asymmetry parameter $B - C$, listed in Table 7.6, are seen to agree to within about 0.01 cm^{-1} . At first sight it may seem that there are two exceptions to this statement, but there are simple explanations for them. One of the exceptions is the $46\,152.4 \text{ cm}^{-1}$ level, where the calculations predict the large magnitude of $B - C$ correctly, but with the wrong sign. The reason is that the nearby $K' = 0$ level, which causes the large splitting (by b -axis Coriolis coupling), is calculated to lie just below it, rather than just above it. Since the b -axis coupling is almost a first order effect in this instance, the correct magnitude but incorrect sign

follow at once.

The other exception is the lowest $K' = 1$ level of the 3^1B^4 polyad, at $46\,086.8\text{ cm}^{-1}$, where the calculation predicts $B - C = -0.002\text{ cm}^{-1}$ while the observed splitting gives $B - C = 0.067\text{ cm}^{-1}$. It turns out that the reason for the discrepancy is that the calculation places this $K' = 1$ level 5.5 cm^{-1} too low. We find that the apparent asymmetry splitting in the lowest $K' = 1$ level of a B^4 polyad is a very sensitive function of the energy separation between it and the lowest $K' = 0$ level. When the input parameters for the calculation are adjusted so that the “ $J = 0$ ” energies of the two levels are reproduced exactly, the calculated value of $B - C$ changes to 0.069 cm^{-1} , in excellent agreement with the observed value.

No attempt has been made to obtain a full least squares fit to the nine interacting vibrational levels, comparable to that in Table 7.3.2. The data are by no means as complete, while preliminary fits to the individual polyads show that many correction terms would have to be added to cope with the ν'_3/ν'_6 anharmonicity effects. Instead, band-by-band fits have been carried out. The resulting parameters are given in Table 7.7, and the assigned rotational levels are shown plotted against $J(J+1)$ in Fig. 7-11.

Figure 7-12 illustrates two elegant examples of Coriolis coupling from the 3^1B^4 polyad. One is the pair of $K' = 0$ and 1 levels near $46\,153\text{ cm}^{-1}$, discussed above. The $K' = 0$ level has b_g vibrational symmetry, which is an unusual observation. In other *gerade* bending polyads the $K' = 0$ levels of b_g vibrational symmetry are not seen because transitions to them are forbidden by the symmetry selection rules. However, in this instance the strong b -axis coupling transfers intensity to the $K' = 0$ sub-band and generates an apparent asymmetry splitting in the $K' = 1$ level that is more than twice as large as that in the zero-point level. The b_g vibrational symmetry of the $K' = 0$ stack (e rotational symmetry) follows at once from the P- and R-branch structure of the $K = 0 - 0$ sub-band. The other example illustrated is the pair of $K' = 1$ and 2 levels near $46\,239.5\text{ cm}^{-1}$. For zero rotation these lie within 0.6 cm^{-1}

Table 7.6: Calculated and observed K -structures of the $2^13^1B^2$ and 3^1B^4 polyads in the $\tilde{A} \ ^1A_u$ state of acetylene. For the $K' = 1$ levels, the second entry is the value of $(B - C)$. Values in cm^{-1} .

Calculated ^a				Observed ^b			
$K' = 0$	$K' = 1$	$K' = 2$	$K' = 3$	$K' = 0$	$K' = 1$	$K' = 2$	$K' = 3$
46 347 a_g	46 434 0.003	46 550		–	46 434.4 0.003	46 559.2	
46 343 b_g	46 248 0.006	46 314	46 413	–	46 294.5 ^d ~ 0	–	46 419.7 ^d
46 211 a_g	46 238 0.060	46 255^c		46 209.7	46 240.2 ^e 0.061	–	
46 150 b_g	46 177 0.024	46 247		46 153.3 ^f	46 176.3 0.033	46 239.6 ^e	
46 133 a_g	46 152 0.234 ^g	46 172		46 129.5	46 152.2 –0.239	46 174.0	
46 116 b_g	46 103 –0.030	46 122		–	46 097.0 –0.017	46 121.3	
46 074 a_g	46 081 –0.002 ^g	46 100		46 075.4	46 086.8 0.067	–	
46 059 a_g	46 067 0.056	46 079		46 058.7	46 068.5 0.060	–	

(^a) Parameters for the calculation of the 3^1B^4 levels: $K_{4466} = -57.86$, $\omega'_4 = 752.00$, $\omega'_6 = 742.47$, $x'_{44} = -0.405$, $x'_{46} = 15.425$, $x'_{66} = -3.695$, $y'_{444} = 0.173$, $y'_{446} = 0.55$, $y'_{466} = -1.245$, $y'_{666} = -0.798$, $A = 14.0 \text{ cm}^{-1}$, $\zeta_{46}^a = 0.7028$.

(^b) Values for $K > 0$ extrapolated to “ $J = 0$ ”.

(^c) Values in bold face type belong to the $2^13^1B^2$ polyad.

(^d) Values from deperturbation of avoided crossings in 3^4 (see Ref. [170]).

(^e) Very strongly Coriolis-coupled.

(^f) Vibrational b_g level, obtaining its intensity from the $K' = 1$ level at $46 152.4 \text{ cm}^{-1}$ by b -axis coupling.

(^g) See text for explanation of the discrepancy between calculated and observed structure.

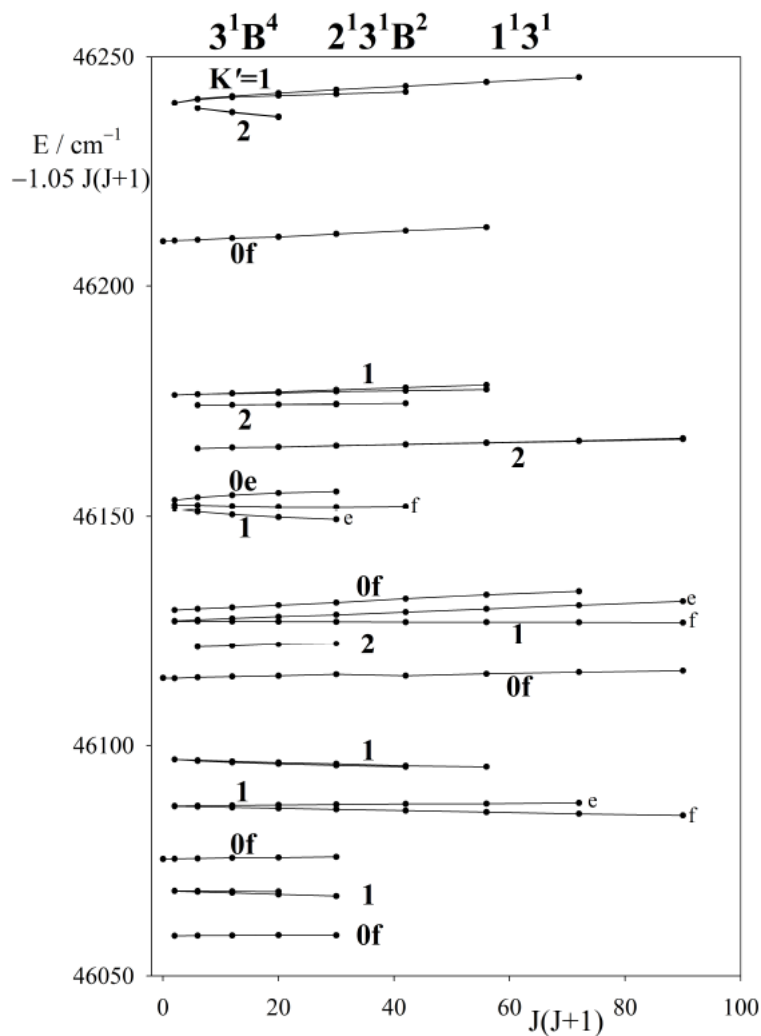


Figure 7-11: Observed rotational levels of the $1^1 3^1$, $2^1 3^1 B^2$ and $3^1 B^4$ vibrational states, less $1.05J(J+1)$, plotted against $J(J+1)$. The lines in the figure are drawn only to guide the eye because a full least squares fit has not been carried out. The four highest assigned vibrational states are not shown. These are the $K' = 1$ state at 46294.49 cm^{-1} and the $K' = 3$ state at 46419.67 cm^{-1} (both of which perturb 3^4), the topmost $K' = 1$ state (46434.37 cm^{-1}) and the topmost $K' = 2$ state (46559.22 cm^{-1}).

Table 7.7: Rotational constants for the $2^13^1B^2$ and 3^1B^4 polyads from band-by-band least squares fits. Values in cm^{-1} .

K'	T_0		$\frac{1}{2}(B+C)$		q^c		D		rms
$2^13^1B^2$									
0f	46 058.69	± 0.04	1.0540	± 0.0025					0.018
1	46 068.47	0.02	1.0258	0.0018	0.0302	± 0.0020			0.011
1	46 248	0.14	1.0025	0.0129	-0.0084	0.0046	-0.00026	± 0.00024	0.064
2	0.006	0.03	1.0813	0.0018					0.011
0f	46 238	0.17	1.1136	0.0125			0.000057	0.000056	0.073
1	0.060	0.06	1.0811	0.0021	0.0163	0.0027			0.047
3^1B^4									
0f	46 075.38	0.05	1.0646	0.0031					0.023
1	46 086.84	0.04	1.0437	0.0010	0.0333	0.0014			0.034
1e	46 151.94 ^a	0.32	0.8987	0.0507			-0.0022	0.0015	0.092
1f	46 152.48	0.11	1.0183	0.0178			-0.00046	0.00054	0.033
0e	46 153.30 ^a	0.29	1.1847	0.0460			0.0022	0.0014	0.083
2	46 174.04	0.03	1.0639	0.0037	0.00012	0.00004	0.00012	0.00009	0.009
0f	46 209.70	0.05	1.1039	0.0015					0.026
2	46 239.59 ^b	0.21	0.8718	0.0364	0.00035	0.00025	-0.0016	0.0014	0.025
1	46 240.16 ^b	0.34	1.1368	0.0241	0.0306	0.0116	0.0004	0.0004	0.164
1	46 434.40	0.03	1.0099	0.0013	0.0015	0.0017			0.019
2	46 559.23	0.04	1.0342	0.0094	-0.0004	0.0005			0.019

^(a) Strong b -axis Coriolis coupling between these levels leads to uncertainties in the parameters; the $K' = 1e$ and $1f$ levels have been fitted separately.

^(b) Strongly interacting levels; the parameters are not well determined.

^(c) The K -doubling has been taken as $\pm \frac{1}{2}q[J(J+1)]^K$ for the e/f levels; q corresponds to $\frac{1}{2}(B-C)$ for the $K' = 1$ levels.

of each other, and repel each other exceptionally strongly. The asymmetry splitting of this $K' = 1$ level is not affected by the interaction and is calculated correctly.

Not counting the 3^4 , 2^3 and 1^13^1 levels (which have been reported elsewhere), and the lowest $K' = 1$ component of 2^2B^2 at $46\,419\text{ cm}^{-1}$, the structure listed in Table 7.6 accounts for every observed level in this region except for a $K' = 1$ level at $46\,192.20\text{ cm}^{-1}$ (mentioned above) and a $K' = 0$ (a_g) level at $46\,113.78\text{ cm}^{-1}$. These two appear to be “extra” levels, since no other S_1 -*trans* levels are expected in the region.

7.4.6 The 5^1B^1 polyad

Just to the high energy side of the intense $45\,811\text{ cm}^{-1}$ band ($3^24^2, K' = 1$), and partially overlapping the hot bands of the 2^2B^2 polyad, is a comparatively weak $K' = 1$ sub-band that can be identified as belonging to the 5^1B^1 polyad. It is illustrated in Fig. 7-9.

The 5^1B^1 polyad should have two components, 4^15^1 and 5^16^1 , with vibrational symmetries b_g and a_g , respectively. The “ $J = 0$ ” energy of the observed upper state is $45\,839.52\text{ cm}^{-1}$ ($T_{00} + 3641.95\text{ cm}^{-1}$), and the sense of its asymmetry splitting is that the e -symmetry component lies above the f -component, with an apparent value of $B - C = 0.045\text{ cm}^{-1}$. This value of $B - C$ is about half what would be expected for a level that is free from Coriolis effects, and shows that the upper state is part of a bending polyad. Since the position of the band rules out a combination involving ν'_1 , ν'_2 or ν'_3 , the only other combinations that could appear in one-photon laser excitation spectra according to the g/u selection rules are those involving the antisymmetric C–H stretching vibration ν'_5 (b_u) with the *ungerade* bending vibrations. The sum of the ν'_5 frequency (2857.47 cm^{-1} [157]) and the mean of the two bending frequencies, ν'_4 and ν'_6 [2], is 3624.05 cm^{-1} , so that the observed [2] band has to be the upper $K' = 1$ sub-band of the 5^1B^1 polyad. The sense of the asymmetry splitting, which is consistent with a vibrational level of a_g symmetry, indicates that the upper state has the zero

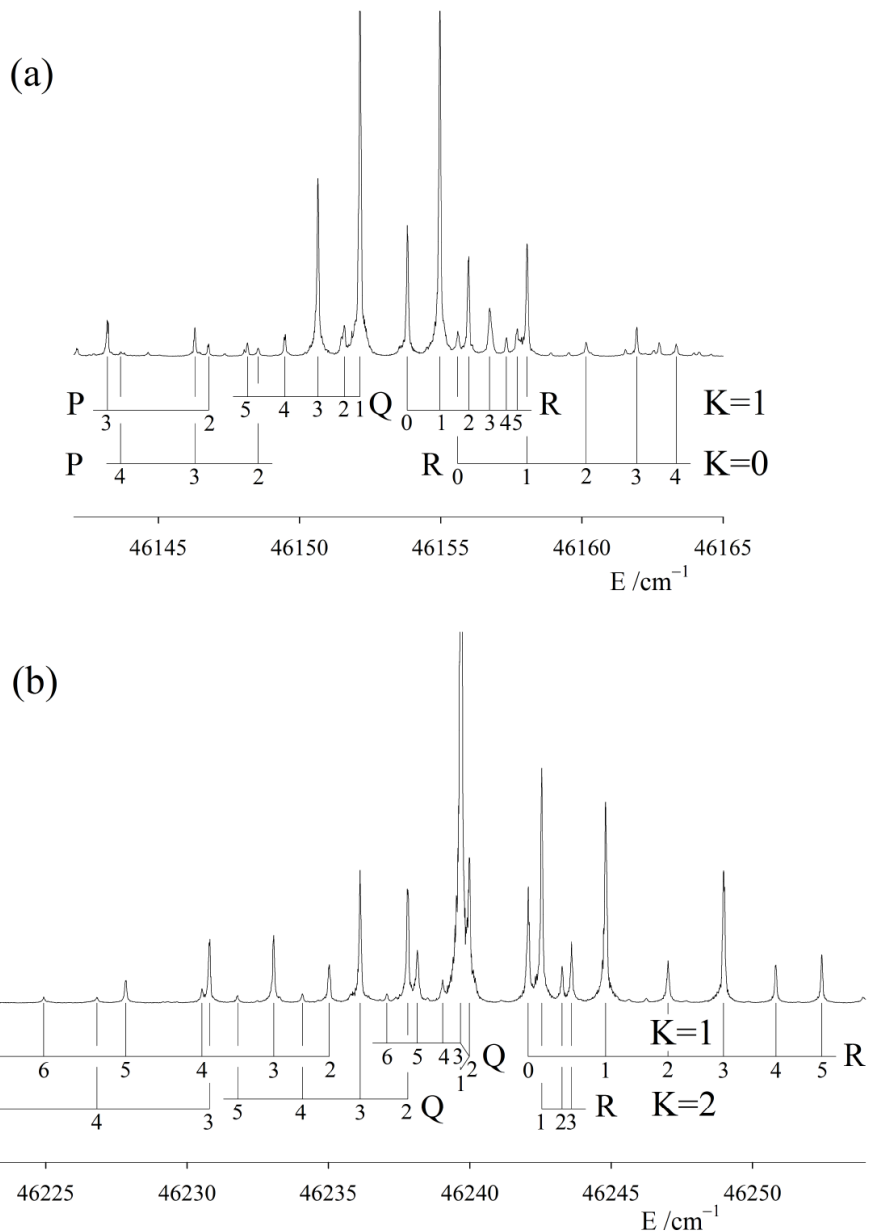


Figure 7-12: Coriolis interactions in the 3^1B^4 polyad of acetylene. (a) Interacting $K' = 0$ (b_g) and $K' = 1$ levels near 46150 cm^{-1} ; transitions to the $K' = 0$ (b_g) upper state are forbidden by the vibrational selection rules, but are induced by b -axis Coriolis interaction with the $K' = 1$ level. (b) Interacting $K' = 1$ and 2 levels near 46240 cm^{-1} ; the two K stacks are almost degenerate for zero rotation. The spectra in (a) and (b) are at the same horizontal scale.

order vibrational assignment 5^16^1 . The energy order of the vibrational components of the 5^1B^1 polyad, with 5^16^1 above 4^15^1 , is the same as the energy order of the fundamentals and the 2^1B^1 polyad, where the 2^16^1 level lies above the 2^14^1 level.

We are not able to assign the lower $K' = 1$ sub-band from our spectra. Assuming that the Coriolis coupling parameters are similar to those in other B^1 polyads, this band should lie near 45801 cm^{-1} . There are a few weak lines in this region, but it is not possible to pick out definite branches in between the very intense P and Q lines of the 45811 cm^{-1} band. With only one sub-band observed, little more can be said about the 5^1B^1 polyad, except that it lies slightly lower than expected; the sum of the x'_{45} and x'_{56} parameters is roughly 25 cm^{-1} .

7.4.7 ^{13}C isotope shift of the $K' = 1$ sub-bands

For some of the strong $K' = 1$ sub-bands, particularly those involving excitation of the C–C stretching vibration, ν'_2 , it is possible to assign the corresponding bands of $\text{H}^{13}\text{C}^{12}\text{CH}$ in natural abundance. A clear example is the 2_0^2 band, illustrated in Chapter 6. To our knowledge this was the first observation of a level of the \tilde{A}^1A_u state of $\text{H}^{13}\text{C}^{12}\text{CH}$, although its electronic ground state has been extensively studied. Table 7.8 lists the bands of $\text{H}^{13}\text{C}^{12}\text{CH}$ that have been identified in this work, and the corresponding isotope shifts. The largest isotope shifts are found for bands where quanta of ν'_2 are excited. It is fairly easy to pick out the $\text{H}^{13}\text{C}^{12}\text{CH}$ bands in these cases because they have no intensity alternation and the isotope shifts bring them well clear of the strong low- J P lines of the main bands, which are usually saturated under conditions where the $\text{H}^{13}\text{C}^{12}\text{CH}$ lines are observable. Since the saturated lines are often very wide, it can be difficult to pick out branches in the gaps between them. For bands with smaller isotope shifts it is not always straightforward to distinguish the isotopic lines from the axis-switching sub-bands [121] that lie in the same region. These latter are $\Delta K = 0$ sub-bands that arise because of a small rotation of the

inertial axis system on electronic excitation. In particular, the strong Franck–Condon-allowed $K = 1 - 0$ sub-bands of the principal progressions always have a $K = 0 - 0$ axis-switching sub-band just below them, separated from them by the rotational constant $A - \frac{1}{2}(B + C)$.

Table 7.8: ^{13}C isotope shifts for the $K' = 1$ sub-bands for the $\tilde{A}^1A_u - \tilde{X}^1\Sigma_g^+$ system of acetylene identified in this work. Values in cm^{-1} .

Assignment	T_0	$\Delta\nu$ ($\text{H}^{12}\text{C}^{12}\text{CH}-\text{H}^{13}\text{C}^{12}\text{CH}$)	
4^2	43 801.77	-5.10	
2^13^1	44 622.26	22.20	
3^14^2	44 810.71	0.43	
2^2	44 920.46	39.91	(Chap. 6)
2^13^2	45 644.49	32.09	
3^24^2	45 805.16	5.43	(^{12}C perturbed)
2^23^1	45 962.58	45.58	
1^13^1	46 125.54	1.61	
3^4	46 274.20	13.99	(perturbed)
1^12^1	46 453.92	21.07	
2^13^3	46 654.53	32.39	(^{12}C perturbed)

The T_0 values refer to the bands of $\text{H}^{13}\text{C}^{12}\text{CH}$.

Derived shifts per quantum: $\nu'_1 : 3.8 \text{ cm}^{-1}$; $\nu'_2 : 23.4 \text{ cm}^{-1}$; $\nu'_3 : 5.3 \text{ cm}^{-1}$; $\nu'_4 : 0.9 \text{ cm}^{-1}$.

Zero-point level shift ($K' = 1$): -6.8 cm^{-1} .

A very weak band at 46049.07 cm^{-1} appears to be the ^{13}C analog of the $2^13^1B^2$ band at 46068.47 cm^{-1} , though the assignment is not certain.

Three of the bands for which the isotope lines were easy to identify were 4^2 , 3^14^2 and 3^24^2 . These are comparatively intense isolated bands and, since they are the highest $K' = 1$ members of B^2 polyads, where the K -structure is distorted by the a -axis Coriolis interaction, they have no accompanying $K = 0 - 0$ axis-switching sub-bands. We have also identified the 3^4 band of $\text{H}^{13}\text{C}^{12}\text{CH}$. The reason for interest in this band was to locate a component of the 3^1B^4 polyad that is predicted to lie nearby. Because of the great intensity of the 3^4 band and its axis-switching structure, special experiments with a seeded beam were carried out in order to cool the acetylene as much as possible. It turns out that the 3^4 band of $\text{H}^{13}\text{C}^{12}\text{CH}$ contains triplet

perturbations at low J values, of the type identified by Drabbels *et al.*[155] in the 3^3 and 3^4 levels of $\text{H}^{12}\text{C}^{12}\text{CH}$. As a result it is only possible to give an approximate value for the isotope shift.

Comparison of the shifts in Table 7.8 shows that, with the exception of that for 2^13^2 , the observed shifts are additive to within $1\text{--}2\text{ cm}^{-1}$. Discounting the 2^13^2 level, where the line assignments are not in doubt, but the isotope shift is anomalous for reasons that we do not understand, the values in Table 7.8 allow the shifts per quantum to be derived for ν'_1 through ν'_4 ; these are listed below the table, along with the electronic isotope shift. The derived shifts agree quite closely with the values we calculate from the harmonic force field of Tobiasson *et al.*[137] For example, the shift per quantum of ν'_2 (23.38 cm^{-1}) compares well with the harmonic force field value (23.1 cm^{-1}). For ν'_3 the harmonic force field value (7.9 cm^{-1}) is possibly slightly too large, since the majority of the numbers in Table 7.8 indicate a shift per quantum of close to 5.3 cm^{-1} .

It can be argued that the shift per quantum for ν'_4 , which has been derived from levels of B^2 polyads where Darling-Dennison resonance is known to be strong, should be corrected for the effects of this resonance. In fact, any such correction must be very small, since the ν'_4 and ν'_6 vibrations have almost the same frequency, and their harmonic force field isotope shifts are calculated to be the same to within 0.1 cm^{-1} . Different degrees of mixing of the ν'_4 and ν'_6 basis states caused by the Darling-Dennison resonance will therefore have almost no effect on their isotope shifts.

7.5 Discussion

This work was motivated by ab initio calculations [114, 116] that the S_1 state of acetylene has a comparatively low barrier to *trans-cis* isomerization of about 4700 cm^{-1} . Only the *trans* well of the S_1 state (\tilde{A}^1A_u) is observable spectroscopically,

since the *cis* well transforms as 1A_2 , to which absorption transitions from the ground state are forbidden. Nevertheless, the possibility exists that levels of the *cis* well near the top of the barrier can tunnel through it and give rise to observable bands, picking up intensity by interaction with nearby *trans*-well levels. Obviously a search for levels of this type requires a very detailed understanding of the level structure of the $\tilde{A} {}^1A_u$ state in order to identify any “extra” levels that do not belong to the *trans* isomer. With this aim in mind we report rotational analyses of a number of newly-discovered vibrational bands at the long wavelength end of the $\tilde{A} {}^1A_u - \tilde{X} {}^1\Sigma_g^+$ system of acetylene. Specifically we have focused on the combination levels involving the a_g vibrations of the \tilde{A} state with the low-lying bending vibrations, ν'_4 and ν'_6 . Together with the results from previous work, analyses are now available for some parts of more than 75 vibrational levels of the \tilde{A} state, including every predicted level up to a vibrational energy of 3500 cm^{-1} . Four suspected *cis*-well levels have been found, but further studies are required to confirm their identities and give their vibrational assignments.

There are various reasons why such a complete cataloguing of the vibrational structure has been possible. On the experimental side, the main reason has been the very large dynamic range of the recorded spectra, which results from the way the laser-induced fluorescence has been gated so as to minimize the scattered laser light. Without this, the very weak bands at the long wavelength end of the band system would never have been detected. We have also made certain that full rotational analyses were carried out for those bands where pattern recognition methods break down because of the complexity of the rotational structure. In these cases the rotational assignments were made by stimulated emission pumping and population labeling experiments. On the theoretical side, we have gone to some length to understand the details of the Coriolis and Darling-Dennison resonances, which have allowed us to obtain good quality constants from the lower energy bending polyads

that could be used to predict, reasonably accurately, the structures of some of the higher bending polyads. For the purpose of understanding these details, it has been essential to put equal weight on data from the one-photon UV spectra and the IR-UV double resonance spectra, since g/u symmetry considerations cause the members of a B^n progression to alternate between the two types of spectra. However, probably the most important reason for the completeness of the results is the emphasis we have placed on obtaining spectra of the $K' = 0$ and 2 rotational levels, both in the one-photon and the double resonance experiments. The c -type rotational selection rules ($K' - \ell'' = \pm 1$) strongly favor the collection of $K' = 1$ data, whether in cold jet one-photon spectra from the $v'' = 0$ level or via the intense ν_3'' fundamental in double resonance, but without $K' = 0$ and 2 data it would have been impossible to understand the Coriolis effects and, therefore, to make any sensible predictions of the structure at higher energy.

The most interesting result from the present work has been the surprising anharmonicity in the combinations of ν_3' (*trans* bend, a_g) and ν_6' (in-plane *cis* bend, b_u). This is shown very clearly by the structures of the $3^n B^2$ polyads. Figure 7-13 illustrates the three $K = 1$ sub-bands of the $3^n B^2$, $n = 0 - 3$ polyads, showing how the compact structure of the B^2 polyad opens up with excitation of ν_3' . (The lowest frequency component of $3^3 B^2$ has not been securely identified yet, but probably lies near $46\,550\text{ cm}^{-1}$.) The high frequency members of the polyads, nominally $3^n 4^2$, form a normal progression with regularly decreasing spacing, but the low frequency members ($3^n 6^2$) drop rapidly below the rest of the polyad: for example, the separation of the two lower $K' = 1$ sub-bands increases from 9 cm^{-1} in B^2 to 73 cm^{-1} in $3^2 B^2$. It is not easy to obtain the vibrational energies directly from the positions of the $K = 1$ sub-bands because of the Darling–Dennison and Coriolis resonances, but deperturbed values are given by the least squares fits of Tables 7.3 and 7.4 and those in Chap. 5. The results show that, while the 4^2 level lies 2.09 cm^{-1} above the 6^2 level in zeroth

order, the 3^24^2 level lies 102.91 cm^{-1} above the 3^26^2 level in zeroth order.

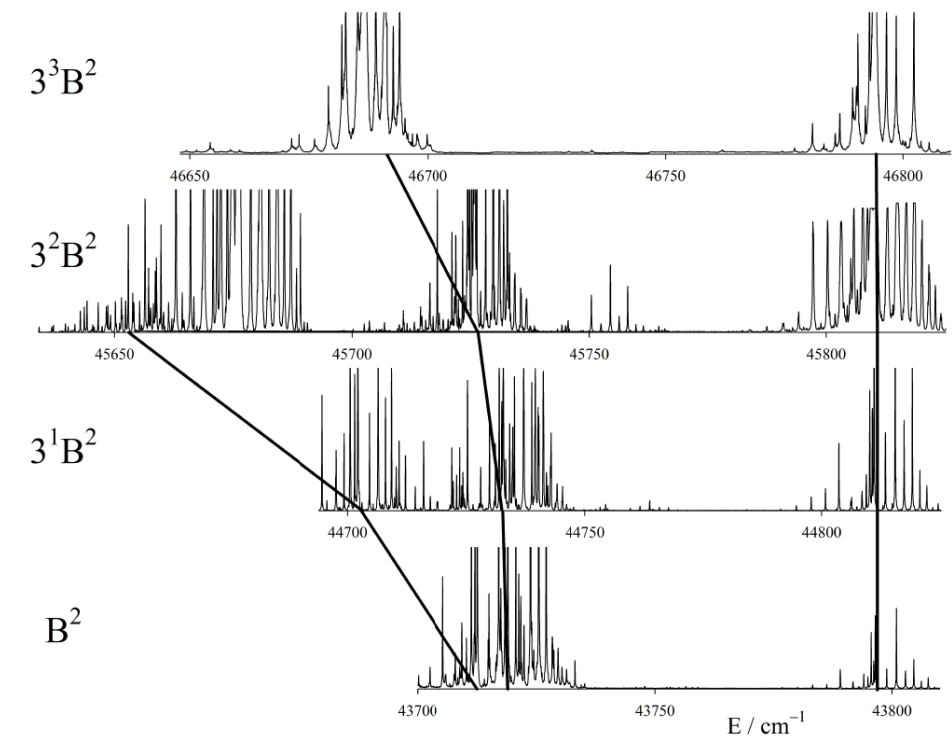


Figure 7-13: Jet-cooled excitation spectra showing the three $K' = 1$ sub-bands of each of the $3^n B^2$, $n = 0 - 3$ polyads. (The lowest energy sub-band of $3^3 B^2$ has not been definitely identified yet.) The spectra are all to the same horizontal scale, and arranged so that the highest frequency sub-bands (nominally $3^n 4^2$) are aligned vertically. Thick lines join the positions of the sub-band origins. The assignments of the overlapping bands are not marked.

The shape of the molecule at the *trans-cis* isomerization barrier is calculated to be half-linear [114, 116], which would correspond to simultaneous excitation of the ν'_3 and ν'_6 vibrations. Clearly the anharmonicity represents the molecule approaching the barrier, presumably with a change in the nature of the vibrational coordinates which contributes to the variation of K_{4466} with ν'_3 . The need for the many small correction terms in the least squares fits to the combination polyads, particularly $2^1 3^1 B^1$ and $3^1 B^3$, must arise from the same cause.

The resonance parameters $2A\zeta_{46}^a$ and K_{4466} increase unexpectedly quickly with excitation of ν'_3 . For example, the fitted value of $2A\zeta_{46}^a$ rises from 18.45 cm^{-1} in the B^2 polyad to 23.56 cm^{-1} in the $3^2 B^2$ polyad. However this increase is not related

to the ν'_3/ν'_6 anharmonicity (since the Coriolis constants are independent of the force field), but arises instead from the increase in the average $\angle\text{HCC}$ bond angle with excitation of ν'_3 . With $r_{\text{CC}} = 1.375 \text{ \AA}$ and $r_{\text{CH}} = 1.097 \text{ \AA}$ [120], the effective $\angle\text{HCC}$ bond angles for the members of the ν'_3 progression can be calculated from the A rotational constants reported by Watson *et al.*[118] The ζ_{46} constants corresponding to these angles can then be obtained by standard methods [171, 172]. For $\nu'_3 = 0$ and 2 the calculated values of ζ_{46}^a are 0.680 and 0.736, giving $2A\zeta_{46}^a = 17.76$ and 22.32 cm^{-1} , respectively. Although these calculated values are slightly lower than the observed, the trend is reproduced correctly: the large increase in $2A\zeta_{46}^a$ with ν'_3 occurs because both A and ζ_{46}^a increase as the molecule becomes more nearly linear.

The Darling-Dennison parameter, K_{4466} , depends on the force field as well as the A and B rotational constants and the Coriolis ζ parameters. To second order [152] it is given by

$$K_{4466} = \frac{1}{4}\phi_{4466} - 4[A(\zeta_{46}^a)^2 + B(\zeta_{46}^b)^2]\Omega^2 + \frac{1}{8} \sum_k \phi_{k44}\phi_{k66}\omega_k \times \left[\frac{1}{4\omega_4^2 - \omega_k^2} + \frac{1}{4\omega_6^2 - \omega_k^2} \right]. \quad (7.7)$$

The methods of the previous paragraph allow the Coriolis contribution to be calculated; it accounts for only about two thirds of the change in the value of K_{4466} , which implies that the second-order expression is beginning to break down. Specifically, the values of K_{4466} for the B^2 and 3^2B^2 polyads are -51.68 and -66.50 cm^{-1} , respectively, while the calculated values of $-4[A(\zeta_{46}^a)^2 + B(\zeta_{46}^b)^2]\Omega^2$ for $\nu'_3 = 0$ and 2 are -28.48 and -38.73 cm^{-1} . It is remarkable that the Coriolis effects make up more than half the value of K_{4466} , and also that this fraction increases with ν'_3 .

Several perturbations attributed to triplet electronic states have been identified in the course of this work. A summary of the most prominent perturbations is given in Table 7.9. Of the states that manifest splitting of the observed lines, anomalously long fluorescence lifetimes, or significant zero-field quantum beats, most have been subse-

quently studied by a combination of time-gated fluorescence and SEELEM (surface electron ejection by laser-excited metastables) techniques, demonstrating a variety of dynamics associated with vibrational state-specific intersystem crossing [173].

A number of exciting avenues for future work are suggested by the present results. One of the most interesting will be the vibrational assignment of the “extra” vibrational levels that have no place in the manifold of the S_1 -*trans* state. Already we have found that the $\text{H}^{13}\text{C}^{12}\text{CH} - \text{H}^{12}\text{C}^{12}\text{CH}$ isotope shift of the “extra” level at $46\,192\text{ cm}^{-1}$ is completely at odds with its apparent position in the *trans* well, suggesting that it lies at quite low energy in a state whose potential minimum lies above that of the *trans* well. A combination of isotope data with vibrational symmetry arguments, based on the rotational selection rules, should allow assignments to be made and give an estimate of the relative energies of the *cis* and *trans* wells. After that comes the problem of exactly what is the energy of the *trans-cis* isomerization barrier. The $46\,192\text{ cm}^{-1}$ “extra” level, which is the highest-energy “extra” level that we have found, appears to have an even-odd staggering in its K -structure of the type expected for tunneling through the barrier. The size of the staggering will be related to the classical frequency of this tunneling, carrying information about where the level lies relative to the top of the barrier. The spectra become increasingly confused in this energy region and the effects of predissociation start to become troublesome but, with careful systematic analyses, progress should be possible.

Table 7.9: Summary of \tilde{A} -state vibrational levels believed to be perturbed by triplet states in the absence of a magnetic field. Evidence (apart from observable splitting in the LIF spectrum) for the nature of the perturbation is provided by the experiments listed in the rightmost column. No claim of completeness is made, as the existing experiments are biased towards the strongest transitions and those perturbations observable at low J .

T_0	Assignment	Experiments
45300	$3^3, K' = 1$	high-resolution LIF ^a Zeeman quantum beats ^b SEELEM ^c
45347	$3^3, K' = 2$	SEELEM ^d
45423	$3^3, K' = 3, J' = 3 - 6, 8$	
45676	$2^13^2, K' = 1$	SEELEM ^d
46008	$2^23^1, K' = 1$	SEELEM ^d
46288 ^e	$3^4, K' = 1$	high-resolution LIF ^a Zeeman quantum beats ^b
44811 ^f	$3^1B^2, K' = 1, \text{III}, J' = 2e$	Zero-field quantum beats
45811 ^g	$3^2B^2, K' = 1, \text{III}$	SEELEM ^d
46192	“Extra”, $K' = 1$	SEELEM ^h
45539 ⁱ	$3^1B^3, K' = 0f, \text{II}$	
45938	$3^3B^1, K' = 0f$	SEELEM ^d
45947	$3^3B^1, K' = 1, \text{I}$	Zeeman quantum beats ^j
46040	$3^3B^1, K' = 0e$	SEELEM ^d

SEELEM = Surface Electron Ejection by Laser-Excited Metastables

Roman numerals represent energy rank of a given K sublevel within a polyad.

^aRef. [155]

^bRef. [174]

^cRef. [175]

^dRef. [173]

^eTriplet perturbations also noted in $\text{H}^{13}\text{C}^{12}\text{CH}$: see Section 7.4.7

^fsee Section 7.4.1

^gsee Section 7.4.2

^hRef. [161]. This state was preliminarily assigned as $2^13^1B^2, K' = 1, \text{III}$.

See analysis in Section 7.4.5 for reassignment.

ⁱSee Section 7.3.2

^jRef. [159]

Chapter 8

Observation of large amplitude bending eigenstates in S_0 acetylene

8.1 Motivation

The long-term goal of this research is to understand how the existence and energetics of the vinylidene minimum are encoded in the vibrational spectrum of acetylene. The acetylene vibrational levels most strongly affected by the presence of the vinylidene isomeric minimum will be those that are spatially localized near the isomerization barrier separating the acetylene and vinylidene regions of the potential energy surface. The barrier maximum is calculated to have a half-linear geometry, where one of the hydrogen atoms has migrated off-axis to a position above the C–C bond, while the other has remained essentially stationary. Large amplitude local vibrational motions have been predicted to exist on the acetylene S_0 surface by a number of techniques[176, 177, 178, 179, 180, 181]. If these states could be experimentally observed, they would serve as exquisite probes of the energetics along the acetylene \leftrightarrow vinylidene isomerization path.

Our current knowledge about these local-bending states is derived largely from

extrapolation. Though they are not directly observed, the local-bending eigenstates arise naturally from a spectroscopic effective Hamiltonian fit to the available data describing the bending vibrational dynamics of acetylene. Developing techniques by which these local-bending eigenstates may be experimentally probed is the primary motivation of this work.

Acetylene and vinylidene are very different chemical entities, yet their minima lie on the same electronic surface. It can be expected that, by exciting large amplitude vibrational motions, the electronic wavefunction (and therefore electronic properties) of the system can be highly distorted from that of its equilibrium configuration. The local-mode nature of the large amplitude vibrational states provides a further advantage in that the vast majority of vibrational eigenstates, particularly at low energy, are not well described in the local mode limit. The special properties of local mode vibrations can be used alongside the predicted electronic distortion to identify electronic signatures unique to these large amplitude motion states: dynamical symmetry breaking[182], a result of the systematic degeneracy of states possessing different rigorous symmetries, makes states in the local-mode limit *unique*; large distortions of the electronic wavefunctions guarantee that the electric dipole moments, normally zero by virtue of the molecular symmetry, will be *large*.

8.2 A local-bender reaction coordinate

Using the internal coordinate path method of Tew *et al.*[183], a one-dimensional reaction coordinate describing the acetylene \leftrightarrow vinylidene isomerization has been constructed. The internal coordinate path is defined in terms of a single large amplitude internal coordinate, which, for the current case of acetylene, is chosen to be the $\angle\text{HCC}$ bond angle. The large amplitude coordinate is scanned over a range of values. At each value of the large amplitude coordinate, all of the other internal degrees of

freedom are adjusted to minimize the energy. While retaining conceptual similarity with the true minimum energy path, the internal coordinate path has the advantage of numerical simplicity. Because of this formulation, the potential energy will be a single-valued function of the selected large amplitude degree of freedom. Results of applying this technique to the acetylene \leftrightarrow vinylidene isomerization have recently been reported[184], and the results of those calculations are summarized here.

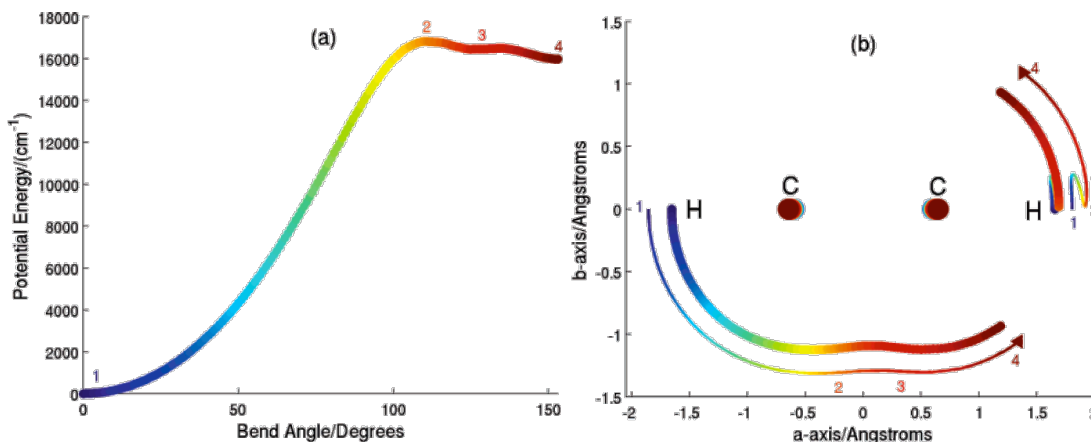


Figure 8-1: One-dimensional potential for acetylene \leftrightarrow vinylidene isomerization.

The one-dimensional internal coordinate path for the acetylene \leftrightarrow vinylidene isomerization is shown in Figure 8-1. In Fig. 8-1a, the vibrational potential energy, relative to the energy at the equilibrium geometry for HCCH, is plotted as a function of the \angle HCC bond angle parameter. The definition of the path, colored-coded to match the motion along the potential energy curve, is shown in Fig. 8-1b. Several important geometries along the path are noted. Between the equilibrium geometry (1), and the top of the barrier (2), the path consists almost exclusively of one hydrogen pivoting around the carbon atom to which it is bound. Between points (2) and (3), the hydrogen atom is transferred from the bonding sphere of its original carbon atom to the bonding sphere of the other carbon. Finally, between (3) and (4), the second hydrogen moves well off of the C-C axis, to a position associated with sp^2 hybridization of the CH_2 carbon. The most salient point of this analysis is that,

in the angular range $\angle\text{HCC} = 0 - 120^\circ$, essentially all of the vibrational motion is localized in one HCC bending motion, while the other CCH angle barely changes. Furthermore, the C-C distance is surprisingly constant. Over a large portion of its angular domain, the internal coordinate path description of the acetylene \leftrightarrow vinylidene isomerization closely resembles the type of motion expected in the local-mode picture of bending vibrations.

8.2.1 Local-bending energies from theory and experiment

Reduction of the reaction coordinate to a one-dimensional path is extremely useful, because it is straightforward to solve the vibrational problem for an arbitrary one-dimensional potential. What is not guaranteed is that the calculated eigenvalues and their associated vibrational wavefunctions have any bearing on the dynamics of the full-dimensional molecular system; the vibrational states obtained from this one-dimensional treatment may be diluted over an arbitrarily large number of full-dimensional vibrational eigenstates of the molecule. In acetylene, it has been shown that local-bending vibrations correspond to stable trajectories over a wide energy range and organize a considerable amount of the bending vibrational phase space [185]. As a result, many eigenstates of the spectroscopic effective Hamiltonian can be identified as possessing local-bending character.

In order to ascertain whether the local-bending eigenstates derived from the spectroscopic effective Hamiltonian are equivalent to the eigenstates of the internal coordinate path Hamiltonian, we compare the effective vibrational frequencies (energetic intervals) for the two representations of this large amplitude motion (Figure 8-2).¹ We find that the agreement is good despite the vastly different nature of these two models. Over the range of quantum numbers within which both models represent a local-bending motion of the the acetylene molecule, the approximate bending frequen-

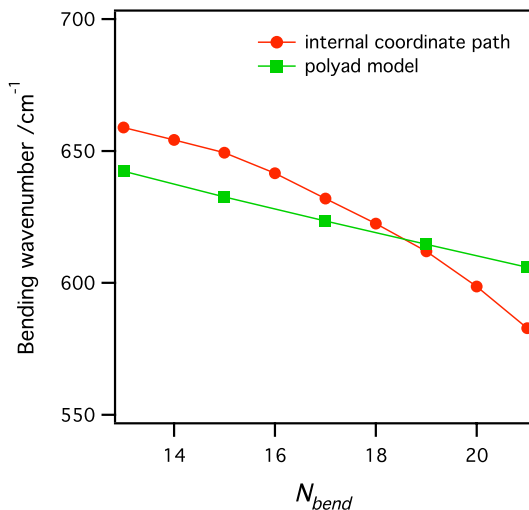
¹For the full-dimension molecular system, eigenstates with $\ell = 0$ exist for only even values of N_{bend} . The vibrational frequencies are, therefore, determined by $\frac{1}{2}[E(N_{\text{bend}} + 1) - E(N_{\text{bend}} - 1)]$.

cies agree to within 5%. The agreement breaks down at low energy, below $N_b = 14$, where the local-bending frequency is not well-defined in the polyad model because the eigenstates of the polyad Hamiltonian do not possess local-bending character. At high energy, above $N_b = 18$, the two models again diverge. The effective bending frequency of the internal coordinate path Hamiltonian drops rapidly due to the softening of the one-dimensional potential, as the molecule approaches the top of the isomerization barrier and experiences the effect of the possibility of tunneling through the barrier. The polyad model is fitted to data from levels that are well localized in the HCCH well, and do not sample the isomerization barrier. It is, therefore, unsurprising that the frequencies from this model do not mirror the steep decline observed in the *ab initio* data set. It is important to stress at this point that the data from the polyad model do not represent eigenstates that have so far been observed by experiment. We cannot, based on the data presented to this point, draw any conclusions about how relevant the higher energy eigenstates of the one-dimensional model are to the full-dimensional dynamics.

8.2.2 Electronic signatures: Electric dipole moments

In previous work [184], we have calculated the electric dipole moment along the *ab initio* internal coordinate path for the acetylene \leftrightarrow vinylidene isomerization. In order to identify the electronic signature of large amplitude vibrational excitation, we computed the expectation values by averaging the calculated dipole moment function over the one-dimensional wavefunctions. As discussed in Ref. [184], the expectation value of the dipole moment along the *b* inertial axis averages to zero, as the *b*-axis dipole moment function has the opposite sign when the hydrogen is above the C-C axis as it does when it is below the C-C axis. In contrast, the expectation value of the dipole moment along the *a*-inertial axis does not cancel over the period of vibration. It does not matter whether the hydrogen atom is above or below the C-C axis; at all

Figure 8-2: Comparison of effective bending frequencies from the experimentally polyad effective Hamiltonian and the one-dimensional *ab initio* internal coordinate path Hamiltonian. Over the quantum number range where both models represent local-bending of the acetylene molecule, good agreement is observed. Below $N_b = 14$, the eigenstates of the polyad Hamiltonian are not local in character. Above $N_b = 18$, the vibrational frequencies from the 1-D Hamiltonian drop rapidly due to the softening of the potential as the molecule approaches the top of the isomerization barrier and the effects of tunneling through the barrier to the vinylidene minimum. Because the polyad Hamiltonian is extrapolated from data representing localized HCCH vibrational levels, it cannot reproduce the effects of the barrier.



distorted geometries along the internal coordinate path, the a -axis component of the dipole moment is nonzero and oriented towards the distorted end of the molecule. The lowest order effect at play, for small deviations away from the equilibrium geometry, is simply the varying projection of the C-H bond dipole on the a -axis as a function of the CCH bend angle. However, this lowest order effect does not describe the gross changes in electronic structure at large geometric distortion. If the projection of the CH bond dipole was the only relevant contribution to the dipole moment function, the a -axis dipole at a CCH angle of 90° (where one CH bond has no projection onto the a axis) would be expected to be equivalent to that of the ethynyl radical (CCH). Instead, at this geometry, the dipole moment function assumes a much larger value, ~ 2 Debye, than that of CCH ($\mu = -0.75$ D). This behavior indicates that global electronic rearrangement is taking place on the way to the vinylidene configuration, which has a dipole moment of approximately 2.3 D.

The expectation value of the electric dipole moment has been calculated for each

eigenvalue of the one-dimensional isomerization path Hamiltonian. We find that there is an approximately linear trend in the expectation values as a function of number of quanta of excitation in the 1D system. Each additional quantum gives rise to an increase of 0.07 D in the dipole moment. While this change is small in an absolute sense, the dipole moments become quite significant (> 1 D) as the wavefunctions approach the barrier, because the number of quanta is high ($N_{\text{bend}} > 20$). This simple relationship is ideal because it is straightforward not only to identify that the observed state is a local-bending state, but also which local-bending state it is. Values for the dipole moments of vibrationally excited states have been updated since the publication of Ref. [184]. These updated values are provided later in this chapter, in Table 8.1.

8.2.3 Symmetry considerations for dipole moments in the local-mode limit

As noted above, the fact that acetylene possesses a center of inversion symmetry dictates that all of the rovibrational eigenstates of rigid acetylene (ignoring here the possibility of bond-breaking isomerization) have a well defined *gerade/ungerade* symmetry. The dipole operator has *ungerade* symmetry and, therefore, can only couple states of opposite *g/u* symmetry. As a consequence, it seems quite impossible for any vibrational state of acetylene to have a non-zero dipole moment. For the 1D calculations of the previous section, this aspect of the molecular symmetry has been ignored: *g/u* symmetry is not conserved by our Hamiltonian as the theoretical treatments of the two ends of the molecule are qualitatively different. In order to connect our one-dimensional (unsymmetrized) treatment of the molecule with the known symmetry properties of acetylene wavefunctions, we consider some results from the local-mode picture of molecular vibrations.

The vibrational energies of a molecule with two identical oscillators may be ex-

pressed in the conventional normal-mode picture or in the alternative local mode picture. Lehmann has shown that the two models are mathematically equivalent[148]. The local mode picture lends itself naturally to the consideration of wavefunctions that do not possess the complete symmetry of the molecule. For simplicity, we consider here the common case of a molecule with two identical bond oscillators (e.g. the two O-H stretching vibrations in water, or the two C-H stretching vibrations in HCCH). The treatment of bending vibrations is no different conceptually from that for stretching vibrations, but the presence of vibrational angular momentum in the bending modes requires additional notation. A local-mode basis function contains labels for the quanta of vibrational excitation in the two oscillators, taken here as the left oscillator, ν_l , and the right oscillator, ν_r . The state $|v_l v_r\rangle = |10 0\rangle$ has ten quanta of vibrational excitation in the left oscillator and zero quanta of excitation in the right oscillator. The left and right oscillators are indistinguishable, so a state of this kind does not have a well-defined symmetry with respect to the exchange of these two oscillators. Such a basis state is called unsymmetrized.

In order to create a basis state that is properly symmetrized, we take linear combinations of basis states as follows:

$$|0 10 \pm\rangle = \frac{1}{\sqrt{2}} [|0 10\rangle \pm |10 0\rangle] \quad (8.1)$$

The positive linear combination, $|0 10 +\rangle$, now is symmetric with respect to exchange of the two oscillators. Since, in our system, the body-fixed inversion operation exchanges the two oscillators, $|0 10 +\rangle$ has well-defined *gerade* symmetry. Matrix elements of the dipole operator can be evaluated between properly symmetrized states:

$$\langle 0 10 + | \mu | 0 10 - \rangle = \frac{1}{2} [\langle 0 10 | \mu | 0 10 \rangle - \langle 10 0 | \mu | 10 0 \rangle]. \quad (8.2)$$

Since, by symmetry, the two diagonal elements of the dipole operator for the left and

right local-bending states in the unsymmetrized states are of the same magnitude but of opposite sign,

$$\langle 0\ 10 | \mu | 0\ 10 \rangle = - \langle 10\ 0 | \mu | 10\ 0 \rangle, \quad (8.3)$$

the perturbation matrix element in the symmetrized basis can be expressed as a diagonal element in the unsymmetrized left/right basis:

$$\langle 0\ 10\ + | \mu | 0\ 10\ - \rangle = \langle 0\ 10 | \mu | 0\ 10 \rangle. \quad (8.4)$$

The two symmetrized states, $|0\ 10\ \pm\rangle$, make up a so-called local-mode pair and are systematically degenerate in the local-mode limit [149]. The transition (off-diagonal) dipole moment between the members of a local-mode pair can, as shown in Eq. 8.4, be interpreted as the permanent (diagonal) dipole moment of an unsymmetrized state.

The fact that the pair of local-mode states are systematically degenerate and are coupled by non-zero matrix elements of the dipole operator renders them exceptionally susceptible to symmetry-breaking perturbations [186]. In the presence of an electric field, the symmetrized local-mode states mix and the eigenstates of the system will resemble unsymmetrized local-mode basis functions. Because the vibrational excitation can remain essentially localized in one of the two oscillators for a long time² the associated phenomena are referred to as *dynamical symmetry breaking*[182]. The local-mode excited, symmetry-broken state will behave in ways entirely analogous to symmetry breaking by other means, such as isotopic substitution (e.g. HCCD): the state will exhibit regular quadratic Stark shifts, and it will be possible to excite “pure rotational” transitions³ in the millimeter-wave region.

Dynamical symmetry breaking makes eigenstates in the local mode limit unique, and should be exploitable as a means to recognize local-mode states among the vastly

²The classical frequency of the exchange of energy between the two oscillators is $\frac{1}{h}$ times the inverse of the energetic splitting between the two members of the local-mode pair.

³These transitions, which behave as rotational transitions in the unsymmetrized local-mode basis, may alternatively be thought of as vibration-rotation transitions in the symmetrized basis.

more numerous states of highly mixed, “ergodic” character.

8.3 Dipole moments from a full-dimensional description of acetylene vibrations

One-dimensional models of vibrational behavior are physically appealing, because they allow us to draw a direct connection between the observed states in a vibrational spectrum and a large amplitude reaction coordinate. For acetylene, the spectroscopic effective Hamiltonian provides evidence that local-mode states correspond to stable classical mechanical trajectories. However, the spectroscopic effective Hamiltonian describes the vibrations in a state space, rather than a coordinate space.⁴ The agreement between the effective frequencies of vibration from the polyad model and from the one-dimensional internal coordinate path model is a compelling indication that the coordinate of the 1D model is the same as the local coordinate of the eigenfunctions of the polyad model. This agreement is less obvious than it may seem, as the local-bending vibration could follow any number of paths, whether rectilinear (moving perpendicular to the C-C axis) or curvilinear (following, for example, the circular defined with respect to the C-C center of mass).

In order to show conclusively that the one-dimensional model captures the bending dynamics of the real molecular system, we seek to demonstrate that the properties of the one-dimensional wavefunctions are preserved in calculations performed using the full-dimensionality of the molecule. Our collaborators at the University of New Mexico have obtained the solutions to the full six-dimensional vibrational Hamiltonian calculated using an *ab initio* potential energy hypersurface. As expected, the calculations reveal local-bending behavior, as evidenced by (1) systematic degenera-

⁴For this reason, wavefunctions plotted from the analysis of a spectroscopic Hamiltonian are plotted against dimensionless (and often unlabeled) coordinates.

cies between wavefunctions of opposite g/u symmetry and (2) the qualitative shape of the associated wavefunctions, slices of which are shown in the top panels of Figure 8-3. These pictures resemble the wavefunctions derived from the spectroscopic effective Hamiltonian, as reported by Jacobson *et al.*[187] The vibrational normal coordinates, corresponding to the *cis* and *trans* bending modes, lie along the diagonals of these plots. It is clear that the nodal structure does not remotely resemble that of the normal mode basis states but rather lies along the isolated bond angle coordinates.

Unlike our reduced-dimension model of the bending dynamics, the 6D Hamiltonian properly obeys the symmetry of the molecular Hamiltonian, with eigenfunctions that possess well-defined g/u symmetry. However, the local-mode nature is most easily visualized by forming unsymmetrized states from the positive and negative linear combinations of the computed eigenfunctions. The unsymmetrized states are shown in the bottom panels of Fig. 8-3.

Our one-dimensional model has identified the electric dipole moment as a property that will serve as a spectroscopic probe of progress along the isomerization path. The transition dipole moments are calculated between the members of a given polyad of *gerade* symmetry and the corresponding (same N_{bend}) polyad of *ungerade* symmetry. These dipole moments are given in Table 8.1 along with the corresponding values from the one-dimensional model. During the course of these calculations, it was realized that quantitative agreement for the dipole moment required using the same *ab initio* method for the six-dimensional and one-dimensional calculations. The primary difference between the results using different *ab initio* methods is the shape of the dipole moment surface at highly distorted geometries, far from both the acetylene and vinylidene minima. We note good agreement, within approximately 10%, over the range of expected validity of the 1D model. Perhaps the most significant difference between the calculated dipole moments from the 6D and 1D models is that in the full-dimensional calculations the dipole increases at a decreasing rate at higher N_{bend} ,

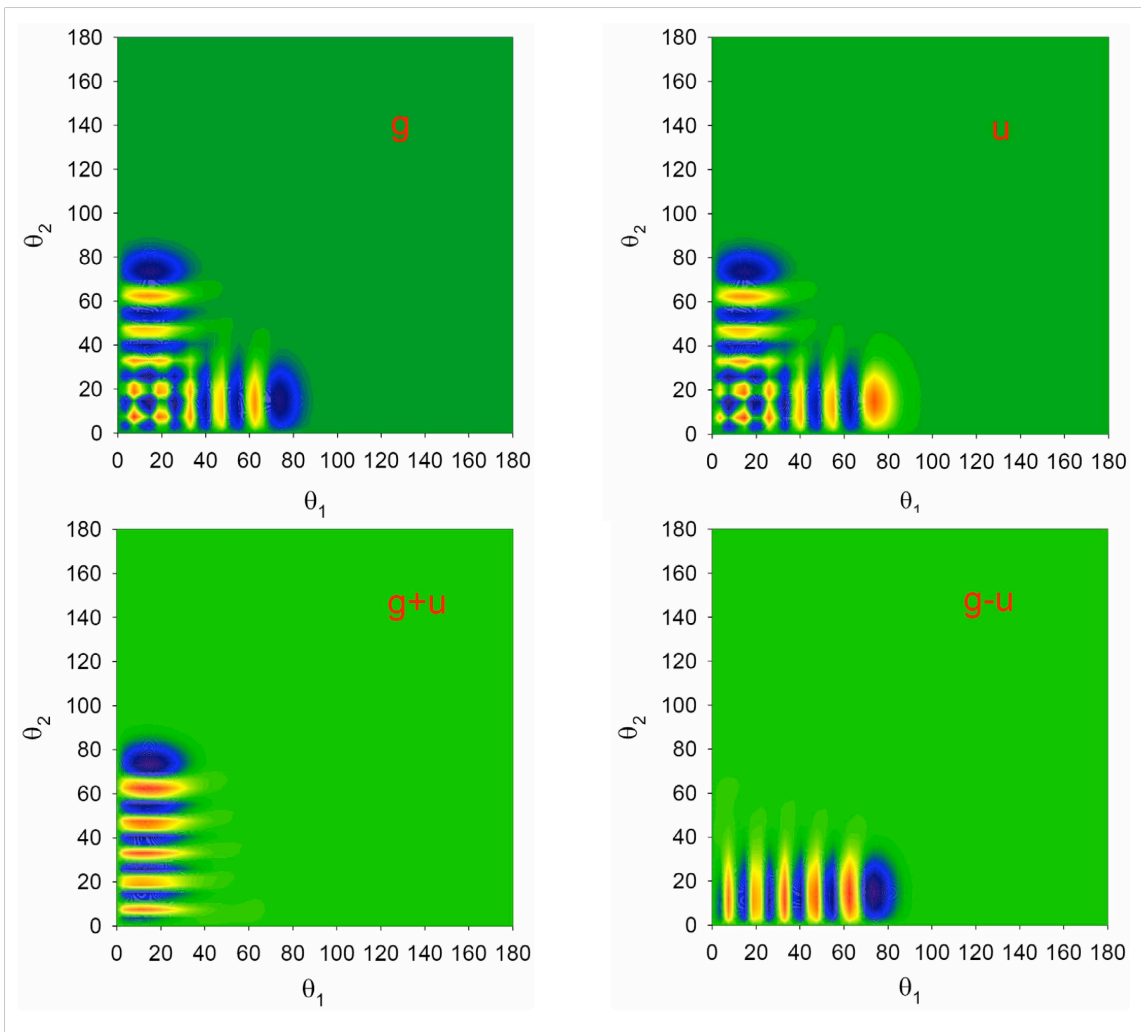


Figure 8-3: Symmetrized and unsymmetrized local-bending wavefunctions from a full-dimensional *ab initio* calculation at $N_{\text{bend}} = 20$. The symmetrized wavefunctions belong to the Σ_g^+ (left) and Σ_u^+ (right) representations of $D_{\infty h}$. The sum and difference of the symmetrized wavefunctions do not have well-defined g/u symmetry and are best thought of as left and right local-bender wavefunctions. Calculations were performed by our collaborator, Prof. Hua Guo, Professor of Chemistry at the University of New Mexico.

while the trend in the 1D model is essentially linear over the range studied. This discrepancy is a point of continuing interest.

Table 8.1: Dipole moments calculated using six-dimensional and one-dimensional Hamiltonians for the local-bending levels of S_0 acetylene. Energies are in cm^{-1} . Dipoles are in units of Debye.

N_{bend}	E_{6D}		$\langle \Psi_{\Sigma_g^+} \mu \Psi_{\Sigma_u^+} \rangle_{6D}$		$\langle \Psi_{\Sigma_g^+} \mu \Psi_{\Sigma_u^+} \rangle_{1D}$	
	g	u	CCSD(T)	CASSCF	CCSD(T)	CASSCF
6	3769.17	3819.38	0.175	0.171	-	-
8	5076.40	5107.75	0.199	0.195	-	-
10	6405.51	6483.71		0.240	-	-
12	7749.08	7750.69	0.398	0.389	-	-
14	9087.78	9087.78	0.586	0.572	0.657	0.600
16	10422.13	10422.13	0.716	0.697	0.761	0.703
18	11753.85	11753.85	0.822	0.800	0.875	0.780
20	13083.30	13083.30	0.913	0.887	0.996	0.905

The full-dimensional calculations also enable us to test the assertion that the local-bending states have distinct signatures in the electric dipole moments. The wavefunctions of the six-dimensional calculation have been used to calculate the transition dipole moments between each member of a g -symmetry polyad and all of the members of the corresponding u -symmetry polyad. This has been carried out in energy regions both below and above the expected onset of the normal-to-local transition, with vastly different results (Figure 8-4). In the low energy region (*left*) the calculation transition dipoles all have relatively small magnitudes. As none of the members of this polyad possess large amplitude bending character, no characteristically large dipole moments are noted. Additionally, there are no systematic degeneracies in this region, so the resulting Stark coefficients for the tuning of the states in an electric field will be exceedingly small. The behavior in the high energy region is precisely as predicted by qualitative arguments. A single transition dipole moment stands out, that between the lowest energy members of the $N = 20g$ and $N = 20u$ polyads, corresponding to the expectation value of the unsymmetrized local

mode wavefunction.

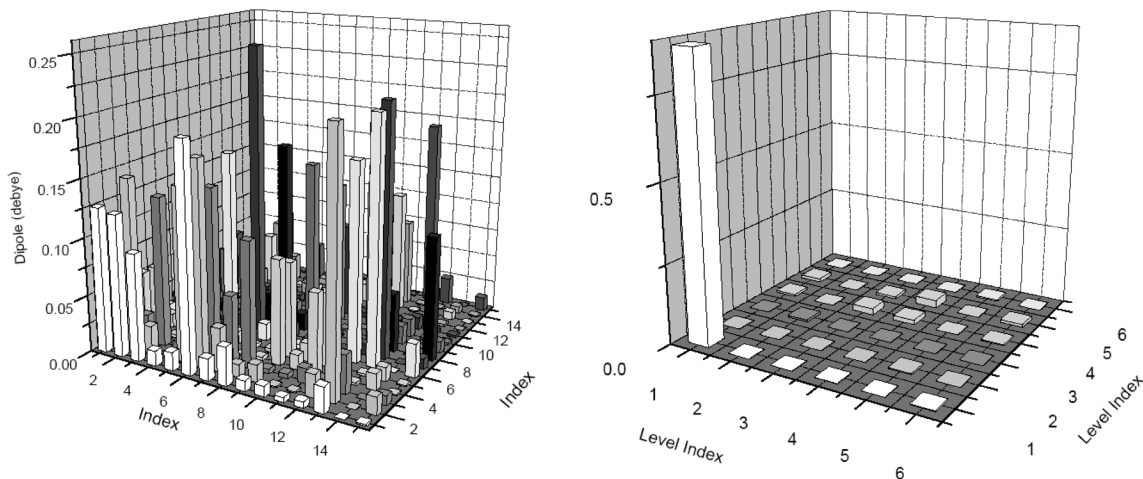


Figure 8-4: Transition dipole moments between g - and u -symmetry polyads at low (*left*, $N_b = 10$) and high (*right*, $N_b = 20$) vibrational excitation. The transition dipole matrix elements are shown graphically, with the energetic ranks the states shown on the horizontal axes. Only the low energy end of the $N_b = 20$ polyad is shown. Transition dipole moments between the members of Σ_g^+ and the corresponding Σ_u^+ polyads are small and random at low vibrational excitation. In the local mode limit, all of the dipole intensity is focussed into a transition connecting the lowest states of g - and u -symmetry polyads. Calculations were performed by our collaborator, Prof. Hua Guo, Professor of Chemistry at the University of New Mexico.

8.4 Experimental observation of the local-bending eigenstates

In the investigation of large amplitude vibrational dynamics, the nature of the spectroscopic “pluck” is crucial. The character of the pluck, that is which basis states are “bright” in a spectrum, is determined by both the experimental technique (and its associated selection rules) and by the nature of the initial, or “launch”, state of the transition. The flexibility of the pluck in determining what dynamics are sampled is one of the primary advantages of the stimulated emission pumping technique (SEP) over the more restrictive conventional techniques of infrared absorption and

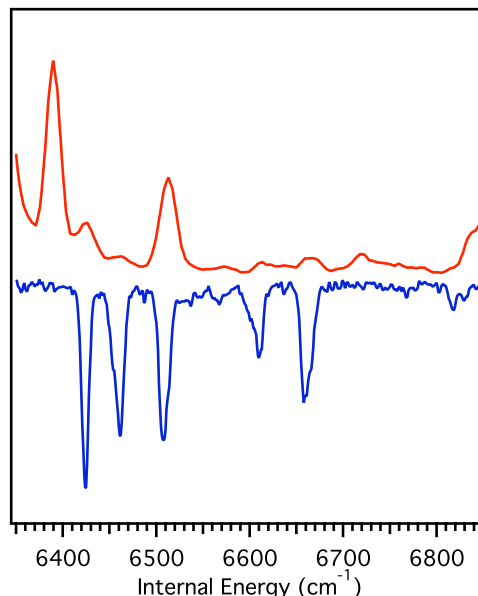
raman spectroscopy [95]. In an SEP experiment, the change in geometry between the ground and excited (intermediate) electronic states is generally thought to determine the dynamics sampled in the spectrum. As the S_1 state of acetylene is *trans*-bent ($\angle\text{CCH} = 122.5^\circ$) with an elongated C-C bond ($r_{\text{CC}} = 1.375 \text{ \AA}$) at its equilibrium geometry [120], large amplitude *trans*-bending dynamics are sampled in the SEP spectrum recorded from this intermediate state. That is, in SEP spectra, the zero-order bright states have excitation in the *trans*-bending mode (ν_4'' , π_g) and to a lesser extent the C-C stretching mode (ν_2'' , σ_g^+).

The *trans*-bending dynamics are not, ultimately, what we wish to study. Consequently, it becomes necessary to discard the Franck–Condon-active vibrational levels as the intermediate states in our experiments. The study of the weakly-allowed transitions into Franck-Condon-forbidden vibrational levels of the \tilde{A} state, described in previous chapters of this thesis, provides us with a wealth of possible intermediate states and, therefore, dramatically extends the range of the dynamics that we are able to sample on the ground standing surface.

8.4.1 A local-bender pluck of \tilde{X} -state dynamics

Dispersed fluorescence spectra have been recorded using one of the Franck–Condon-forbidden intermediate levels of the $\tilde{A} \ ^1A_u$ state described in Chapter 7, 3^2B^2 , III. As the low-frequency bending modes ν_4' and ν_6' both correlate with the linear molecule *cis*-bending mode, ν_5'' , we anticipate a propensity rule for transitions between S_0 and S_1 that will conserve the number of quanta of these modes, that is: $\nu_4' + \nu_6' = \nu_5''$. This propensity rule is borne out in the absorption spectra of the $\tilde{A} \ ^1A_u - \tilde{X} \ ^1\Sigma_g^+$ transition reported by Watson *et al.*[118]; by far the strongest transitions from the vibrationless level of the ground state ($\nu_5'' = 0$) go to vibrational levels of the excited state with no excitation in the low-frequency modes. Recall that it required sensitive LIF measurements, described earlier in this thesis, to locate the much weaker transitions into the

Figure 8-5: Dispersed fluorescence spectra of the $N_b = 10$ polyad recorded from a normal Franck–Condon-active vibrational intermediate (upward going), and from a Franck–Condon-forbidden combination level, 3^2B^2 , III (downward going). The relative intensity distribution within the polyad are different in the two spectra, reflecting the fact that the dynamics are initiated in different ways.



these Franck–Condon-forbidden vibrational levels. In emission, the intensities from the Franck–Condon active progression are well-modeled by considering bright states with $v_5'' = 0$.

A portion of a DF spectrum, from a member of the $2^m 3^n$ progression, is shown in Figure 8-5 (upper trace). The region shown is of a pure-bending polyad with $N_b = 10$. The intensity distribution in this spectrum is well-described by the zero-order bright state $(0, 0, 0, 10^{0/2}, 0^0)$. Although these states are at an energy below the onset of local-mode behavior, intensity is transferred by anharmonic interactions to several members of the polyad. The lowest energy, most intense feature in the spectrum is the eigenstate with the most overlap with the zero-order bright state. A DF spectrum of 3^2B^2 , III (nominally 3^24^2), in the same energy region, is shown in the lower trace of Fig. 8-5. Several of the same eigenstates are observed in the two DF spectra, but the intensity patterns are quite different. The DF spectrum of 3^2B^2 , III, has essentially no intensity into the nominal bright state of the upper spectrum. The intensity distribution of the lower spectrum is not as readily understandable as the upper spectrum, as a single normal-mode bright state does not successfully model the observed transition strengths. On the basis of the propensity rule, we may expect

intensity into the $8\nu_4'' + 2\nu_5''$ vibrational level. The presence of vibrational angular momentum results in multiple basis states with this vibrational character, namely $(0, 0, 0, 8^0, 2^0)$ and $(0, 0, 0, 8^2, 2^{-2})$. Each of these states may carry intensity in the spectrum, and the total intensity of an eigenstate can contain interfering contributions from multiple bright states[126].

Although we lack a complete model for the intensity distribution in the DF spectra of Franck–Condon forbidden levels, we observe that the intensity distribution resembles that predicted by a local-bending zero-order bright state (see Chapter 7 of Ref. [188]). This observation indicates that the Franck–Condon forbidden vibrational levels may serve as effective intermediates for populating the local-bending levels, once they emerge at higher energy. However, the relatively low resolution and complexity of the DF spectra prevent definitive identification of the local-bending levels. The dispersed fluorescence spectra previously recorded in this research group, for example, have a typical frequency resolution of approximately 7 cm^{-1} . Under these experimental conditions, transitions into the Σ ($\ell'' = 0$) and Δ ($\ell'' = 2$) components of a vibrational level are typically unresolved.

8.4.2 Stimulated emission pumping from Franck–Condon forbidden vibrational levels

High resolution SEP has the advantage over dispersed fluorescence that the rotational structure enables definitive assignment of the symmetry and vibrational angular momentum of each observed state. In order to record SEP spectra from the Franck–Condon forbidden vibrational levels, we have had to adopt a different experimental methodology from that previously used in our group[189]. Earlier experiments on acetylene[168, 190, 131] used two matched room temperature cells, both of which were PUMPed by one UV laser in order to promote transitions into the electronically excited state. A second DUMP laser was introduced into one of the two cells in order

to stimulate emission back to a ground state vibrational level and therefore reduce the intensity of observed spontaneous fluorescence. The SEP signal was derived from the difference in the fluorescence intensities in the two cells. As described earlier in this thesis, the majority of the Franck–Condon-forbidden vibrational bands are obscured in the LIF spectra recorded in a cell at room temperature. It is only with the simplification due to jet-cooling that these bands become observable. Therefore, the majority the Franck-Condon-forbidden levels are unusable in the standard SEP experiment.⁵ A common normalization technique in jet-cooled experiments is to use temporally separated PUMP and DUMP pulses[191], either by using an optical delay line or independently triggered lasers. The fluorescence decay, detected by a the PMT, is gated twice: once before the DUMP laser and once after. In the absence of a resonant DUMP transition, the intensities recorded by the two gates are trivially related to the properties of the (usually exponential) fluorescence decay. On resonance, the ratio of observed post-DUMP fluorescence to the expected level based on the pre-DUMP gate is used to determine the SEP signal (% dip).

In our experiments, the PUMP and DUMP dye lasers are pumped by two independent Nd:YAG lasers. The PUMP radiation is generated by an etalon-narrowed Lambda Physik 3002E, pumped by a Quanta-Ray DCR-3. The DUMP radiation is generated by a Sirah Cobra-Stretch dye laser, pumped by a Spectra-Physics PRO-270. The delay between the two lasers is set to approximately 100 ns, so that a reasonable pre-DUMP gate may be collected.

The transitions previously described in DF have been recorded by SEP, and the resulting spectra are displayed in Figure 8-6. In addition to (Franck–Condon active) 2^13^2 and 3^2B^2 , III, spectra are shown for the other two members of the 3^2B^2 polyad. While the spectra from the three polyad members are more similar to each other than they are to the spectrum from the Franck–Condon active level, the intensity patterns

⁵Some notable exceptions are: $B^4 K' = 1$, IV at 45301 cm^{-1} , and $3^2B^2 K' = 1$, III at 45811 cm^{-1} .

indicate that the different upper-state polyad members sample the bending dynamics of the ground state in different ways, though the propensity rule given above would treat all of the members of an upper-state polyad as identical. Rather, the differences between these spectra arise from two factors. As discussed in Chapter 7, the upper-state polyad basis states with b_g vibrational symmetry should give transitions into ground state levels of Σ_g^- symmetry, while the normal Franck–Condon active states and the Franck–Condon forbidden levels with a_g vibrational symmetry should give transitions into levels of Σ_g^+ symmetry. The levels observed near 6460 cm^{-1} are due to a Σ_g^- -symmetry state. The second factor consists of the unknown transition intensities into the multiple basis states that may carry the brightness in these experiments, as well as the the signs of interference effects between multiple intensity mechanisms for a given eigenstate.

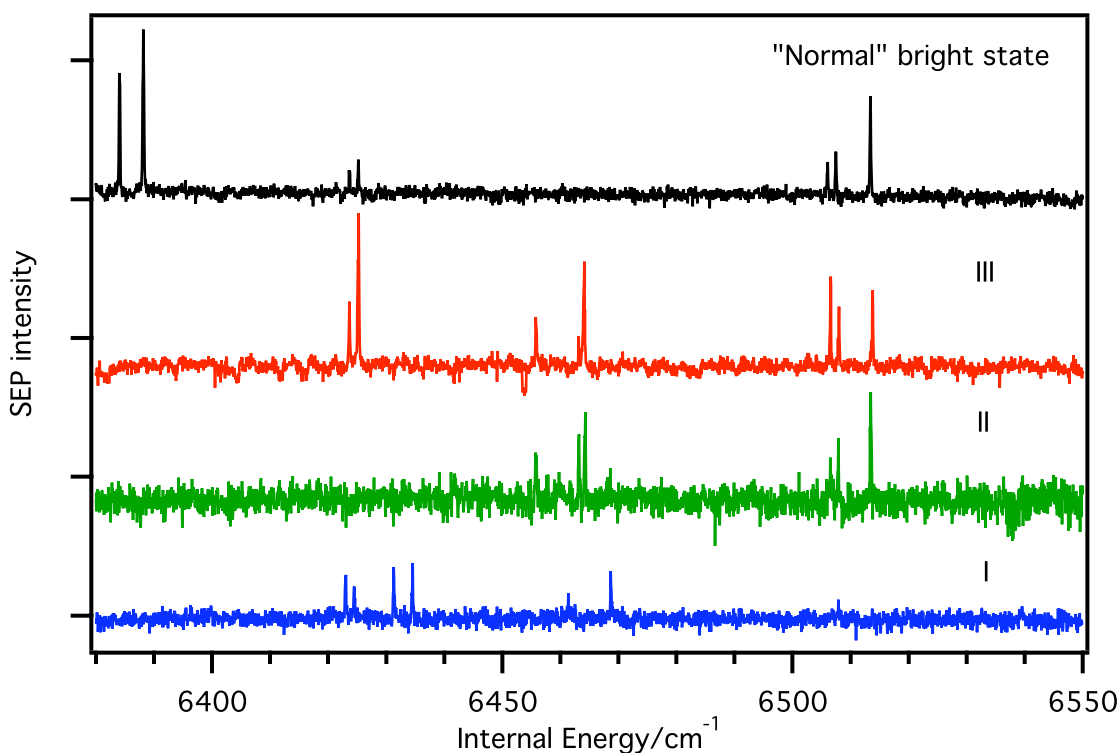


Figure 8-6: SEP spectra recorded from each member of the 3^2B^2 polyad, as well as from the 2^13^2 vibrational level. Roman numerals on the right hand side of the figure represent the energy rank of the $K = 1$ levels within the polyad.

The normal-to-local transition is calculated to occur in the range of $N_b = 10 - 14$. Over this range, the lowest member of a polyad shifts from primarily *trans*-bending in character to primarily local-bending. This shift coincides with a decrease of the intensity of the lowest polyad member, as observed from a Franck–Condon active vibrational level. The lowest member of the $N_b = 10$ and 12 polyads were easily observed in previous dispersed fluorescence experiments in our group[192], while the lowest member of the $N_b = 14$ polyad was too weak to be observed in these spectra. The $N_b = 14$ level is the lowest-energy level believed to possess primarily local-mode character, and therefore its observation is crucial to the understanding of the normal-to-local transition.

Although this crucial state has not previously been observed, the spectroscopic effective Hamiltonian that describes all of the observed data provides useful predictions of the $N_b = 14$ local-bender state. Using the $3^1B^4, I$ level as an intermediate,⁶ SEP spectra were recorded over the predicted position of the lowest-energy local-bender state. Strong signals were observed relatively easily, and spectra were recorded from a number of rotational levels in order to establish the rotational assignments of the lower state (Fig. 8-7). These measurements identify a $\Sigma_g^+(\ell = 0)$ state, at an energy ($J = 0$) of 8971.69 cm^{-1} , as well as its corresponding $\Delta_g(\ell = 2)$ state. A complete prediction of the energy levels in this region[169] gives four expected Σ_g^+ states in the energy region of $8960\text{--}8990 \text{ cm}^{-1}$, with the local-bender state predicted at the top end of this range, 8983 cm^{-1} .

Because the prediction of the local-bending energy is over ten cm^{-1} higher than our observed state, one critical observation is required to verify the assignment of the $N_b = 14$ local-bending level. This observation is related to the systematic degeneracy that is a hallmark of local mode behavior. Of the Σ_g^+ states predicted in this energy region, the only one predicted to be degenerate with a Σ_u^+ level is the local-bender.

⁶At the time of the of these experiments, the vibrational level at 46087 cm^{-1} was assigned as $2^13^1B^2, I$. The reasons for the reassignment are given in Section 7.4.5.

IR-UV dispersed fluorescence has identified a level with Σ_u^+ symmetry at 8971.76 cm^{-1} [126], however the authors of that work do not comment on the local-mode character of this state. Through these complementary experiments, two states are observed that are degenerate (within the experimental error) but possess opposite g/u symmetry. On this basis, these states can be assigned conclusively as the $N_b = 14$ local-bender pair.

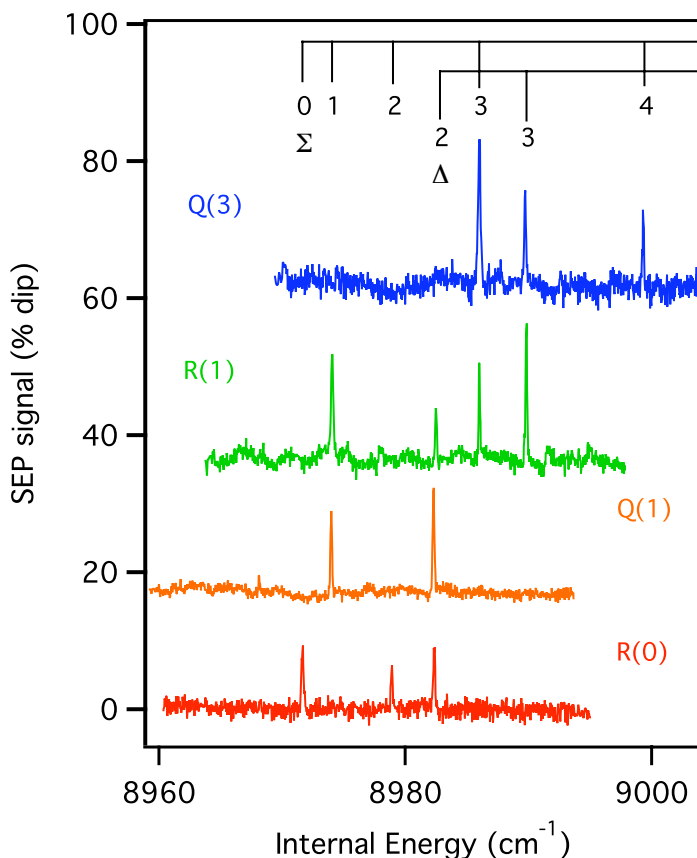


Figure 8-7: SEP spectra of the $N_b = 14$ local-bender state recorded from 3^1B^4 , I. Spectra are recorded from several rotational levels of the intermediate in order to label the lower-state J values.

Unfortunately, the information available for the *ungerade* manifold does not include local bender states of higher lying pure-bending polyads, so that assignments made on the basis of systematic degeneracies cannot be extended. We also note that the discrepancy between the observed energy of the local bender and that predicted

by a polyad model[169] is relatively large and expected to increase further for the higher energy states. Even the results of the model, which is fitted to data that includes the *ungerade* $N_b = 14$ local bender state, give this state as an outlier with a residual of over 3 cm^{-1} . Therefore we are somewhat unlikely to be able to make assignments based on extrapolation of the polyad model, particularly a model that is based on expansion of the force field in the normal coordinates. These models seem to predict systematically too high energies for the local-bending states. It is possible that the diagonal anharmonicity along the local-bending coordinate is poorly parameterized in such a model. Recently, Amano *et al.*[193] have proposed a spectroscopic fit model based on an expansion of the linear molecule Hamiltonian, which directly incorporates the vibrational angular momentum structure. The authors of that work have reported data up to $N_b = 12$, with excellent agreement, but it is not immediately clear that such a model will extrapolate well into the local-mode regime, since it is constructed from normal mode basis states. Alternatively, the data may be fitted to a Hamiltonian expressed in the local-mode basis[187]. Such a treatment should not be plagued with the systematic overestimation of the energies of local-bending states, but since so few local-bending states have been observed, the model will need to be parameterized to the energies of the low energy normal-mode states.

We have searched for the local-bend state in the $N_b = 16$ polyad using the same intermediate state as was used to observe the $N_b = 14$ local-bender state. The region $10\,200\text{--}10\,250 \text{ cm}^{-1}$ was searched by SEP, but only very weak features were located and these could not be assembled into meaningful rotational band structure. Unfortunately, this indicates that the $3^1B^4, I$ state cannot serve as a universal gateway into all of the local-bender levels: there is no universal local-bender pluck. This should not be surprising because higher energy local-mode basis states, expressed in the normal mode basis, require basis states with large numbers of quanta in both modes ν_4'' and ν_5'' . Based on the propensity rules expressed earlier in this chapter, the

brightness of states with a large number of quanta in ν_5'' necessitates an equal number of quanta in the two low-frequency bending modes in the excited state.

An alternative intermediate state, B^4 , I was also used in the attempt to locate the lowest $N_b = 16$ polyad member. The SEP spectra contained many of the weak features found in SEP from 3^1B^4 , indicating that they are real SEP features and not upward-going double resonance transitions. In addition, a new band is observed at an energy ($J = 0$) of $10\,218.9\text{ cm}^{-1}$. Clear branch structure is found in SEP spectra from multiple rotational levels of the intermediate state. Transitions into the lowest rotational levels of this state are shown in Figure 8-8d. While it is difficult to make a definitive vibrational assignment of this band, we tentatively assign it as the $N_b = 16$ local bender state. Evidence for this assignment is presented in Figure 8-8. The splitting between the $\Sigma(\ell = 0)$ and $\Delta(\ell = 2)$ components increases regularly for the series $N_b = 10, 12, 14$, as the bending structure makes the transition from being well-described in the normal-mode basis to being well-described in the local-mode basis. This large splitting can be rationalized in the local-mode limit as the molecule approaches the isomerization barrier. For a state with two quanta of vibrational angular momentum, some of the kinetic energy is directed perpendicular to the in-plane bending coordinate. This energy is “wasted” from the point of view of the isomerization reaction, so the wavefunction cannot explore the identical range of bending angle as the Σ state. As a result, the Δ state falls in energy less rapidly in response to softening of the potential along the local-bending coordinate. This pattern of increasing $\Sigma - \Delta$ separation provides some evidence that the state at $10\,218.9\text{ cm}^{-1}$ is the next member of the local-bender progression, though this assignment should be treated as somewhat speculative. We note that this is just under 30 cm^{-1} beneath the energy predicted by one of the commonly used spectroscopic effective Hamiltonians[169]. If our assignment is correct, this suggests a large deficiency in the predictive capability of this particular Hamiltonian.

The observation of the lowest local-bender state provides assurance that it is possible, by using SEP from a carefully chosen intermediate, to selectively populate this special class of large amplitude bending eigenstates. In order to extend these observations to the higher-lying local benders, spectroscopic signatures of the large-amplitude bending are required. The framework presented for using the electric dipole moment to identify the local-bending states will be useful for this purpose. The most direct method for determining the electric dipole moment of a highly vibrationally excited state, populated by SEP, is through the optical Stark effect. The Σ -symmetry states, which embody the large amplitude local-bending motions, are, despite the dynamical symmetry breaking in the local-mode limit, characterized by a quadratic Stark effect. Due to the nature of the quadratic Stark effect over a large energy gap ($2B'' \approx 2.4 \text{ cm}^{-1}$), very large fields (several tens of kV/cm) will be required to induce measureable energy shifts or to induce transitions into zero-field forbidden states. At the current time, we are incapable of generating large electric fields in our apparatus without causing breakdown of the gaseous sample. An alternative method, which will employ relatively low electric field strengths, is presented in the following section.

8.5 Chirped-pulse millimeter-wave spectroscopy

In the first half of this thesis, millimeter-wave spectroscopy was used to measure electronic signatures of large amplitude vibrational dynamics of HCN and HNC. The spectrometer used in that work was based on traditional, robust, relatively easy-to-use technology. However, it was unsuited to the task of recording large quantities of millimeter-wave spectra, particularly when used in combination with relatively unstable pulsed laser sources. In this section, a new spectrometer based on broad-band chirped-frequency sources is described.

In the last several years, Brooks Pate and his group at the University of Virginia

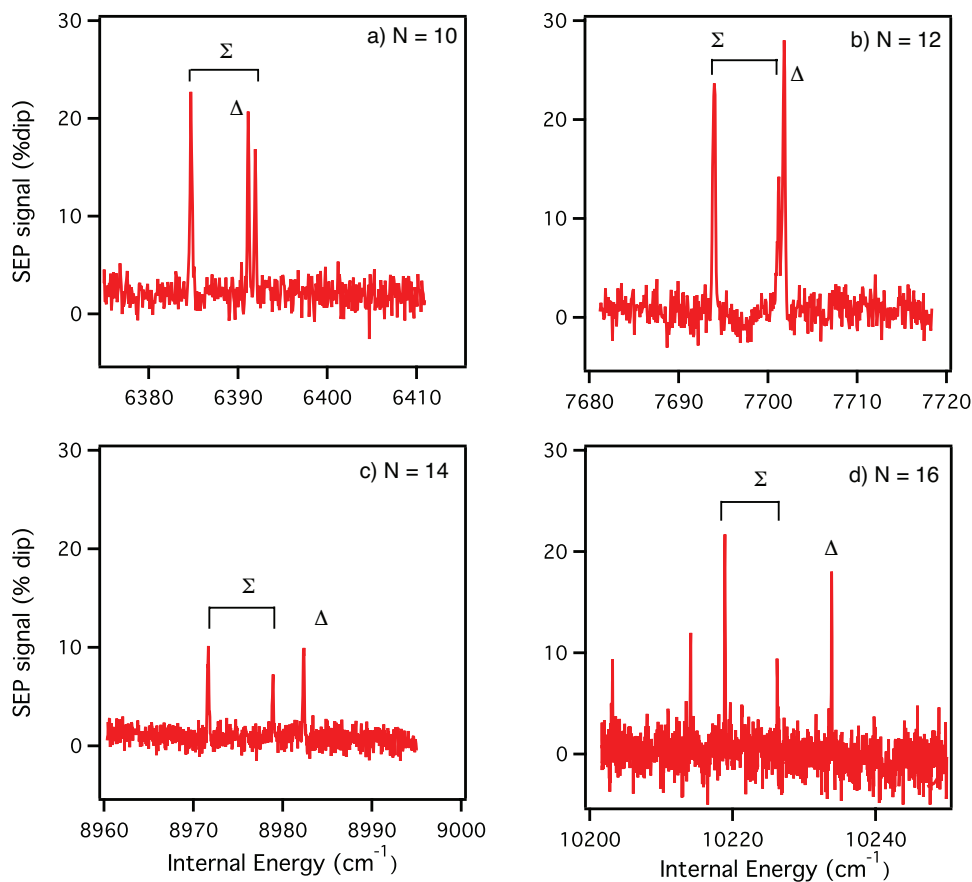


Figure 8-8: SEP spectra of the lowest members of the $N_b = 10 - 16$ polyads. Transitions into the $N_b = 10$ and 12 polyads are recorded from Franck-Condon-active intermediate levels. Transitions into the $N_b = 14$ and 16 polyads use Franck-Condon-forbidden levels as intermediates: the spectra of $N_b = 14$ is recorded from $3^1B^4, I$, and that for $N_b = 16$ is recorded from B^4, I . The pattern of the Σ/Δ splittings suggests that the state observed at 10218.9 cm^{-1} is the $N_b = 16$ local-bender Σ state.

have developed a revolutionary microwave spectrometer, capable of recording over 10 GHz of spectra in a single gas pulse[194, 195, 8]. The cavity-free chirped-pulse microwave (CPMW) spectrometer differs from the standard Balle-Flygare spectrometer by utilizing a linearly chirped microwave pulse to polarize the sample. As a chirped pulse is used to polarize the sample, rather than the standard fourier transform-limited pulse, the frequency bandwidth of the spectrometer is decoupled from the pulse duration and, therefore, the available power. The chief advantages of this spectrometer are an extremely high data rate and accurate relative intensity information across a wide spectral region.

Recently, in collaboration with Brooks Pate's research group, Barratt Park has constructed a chirped-pulse spectrometer at MIT operating in the millimeter-wave region ($\sim 70 - 100$ GHz). A schematic of the spectrometer is shown in Figure 8-9. The details of this spectrometer will be reported at a later time, but the a brief overview is given here. An arbitrary waveform generator outputs a linearly chirped pulse of a frequency up to 2 GHz. The output of the arbitrary waveform generator is mixed with a stable oscillator, and one of the sidebands is selected and actively multiplied $\times 8$ (that is, multiplied and amplified) into the millimeter-wave frequency region. In the process of the frequency multiplication, the frequency bandwidth of the experiment is also multiplied, enabling up to 10 GHz of spectra to be recorded simultaneously. The molecular sample, having been polarized by the chirped pulse, emits a free-induction decay that is detected by heterodyne mixing with the output from a Gunn oscillator. The downconverted signal is amplified and directly fed into a fast digital oscilloscope. The entire apparatus is locked to the output of a rubidium frequency standard so that each FID event can be detected in-phase and therefore coherently averaged in the time domain.

This spectrometer has been tested by recording rotational transitions of several small molecules, such as CH_3CN and SO_2 . We have found that the spectra of equiv-

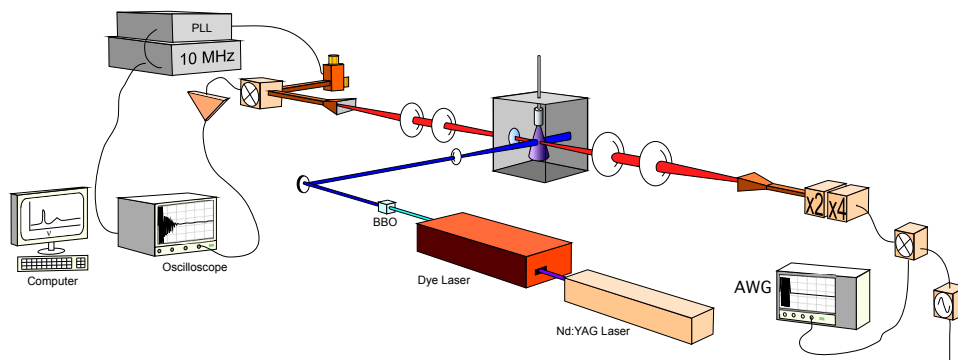


Figure 8-9: Schematic of the chirped-pulse millimeter-wave spectrometer.

alent quality to those recorded with the cw millimeter-wave spectrometer described earlier in this thesis can be recorded in $100\text{--}1000\times$ shorter times using the chirped-pulse method. The broad bandwidth of the spectrometer makes it ideal for studying pure rotational spectra of optically populated states. As a demonstration of the chirped pulse technique, we have repeated the experiment described in Section 2.3.3, in which we populate an excited triplet electronic state of CS with a UV laser beam and then record the rotational spectrum of the laser-excited state. The resulting spectra are shown in Figure 8-10. With a 1 GHz spectral bandwidth, the transition is easily recognized in fewer than 100 laser shots. Further averaging of the signal causes the incoherent baseline noise to average away, improving the signal-to-noise ratio to the desired level at a rate consistent with the expectations for coherent averaging.

Ultimately, this technique will be applied to SEP-populated vibrationally excited states of acetylene. As discussed earlier, dynamical symmetry breaking in the large amplitude local-mode bending levels will lead to the appearance of pure rotational transitions for these states. The magnitude of the dipole moment, which indicates the distortion of the electronic wavefunction and, therefore, the progress along the

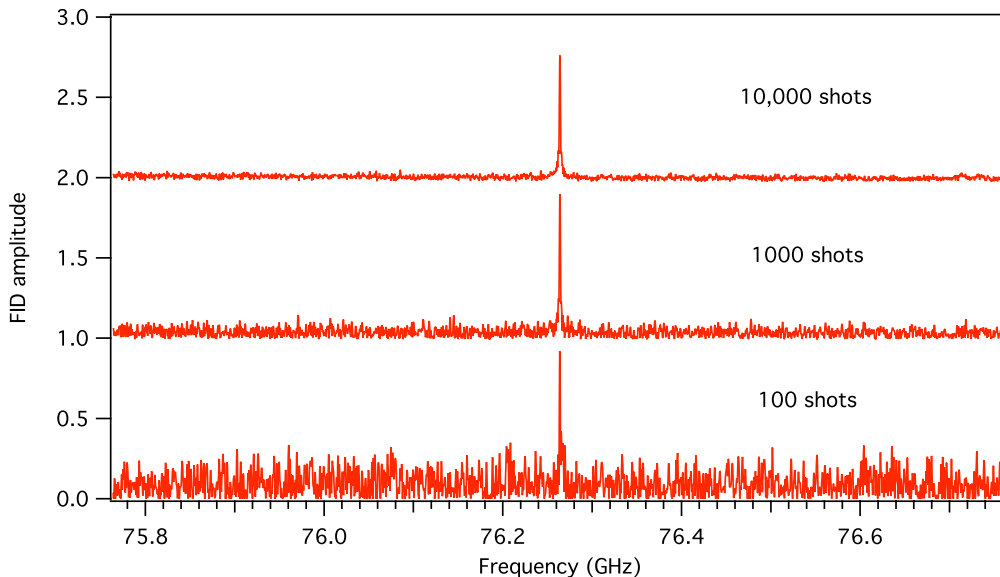


Figure 8-10: UV-CPmmW double resonance spectra of the $J' = 2, N' = 2 \leftarrow J' = 1, N' = 1$ transition of the $e\ 3\Sigma^-$ state of CS. The acquired free induction decays are averaged phase-coherently in the time-domain for each laser pulse. The 1GHz spectral bandwidth of these spectra is sufficient to cover the uncertainty in predicted transition frequencies based on pulsed laser measurements.

isomerization path, can be readily measured by applying a modest electric field to the interaction region in order to determine the Stark effect for the millimeter-wave transition. For the Σ ($\ell'' = 0$) components of the local-bender levels, the second-order Stark shift of the $J = 1 - 0$ transition is given by the expression used for linear molecules [6]:

$$\Delta\nu^{(2)}(\Delta M_J = 0, J = 0 \rightarrow 1) = \frac{8}{15} \frac{\mu^2 \mathcal{E}^2}{h^2 \nu_0}. \quad (8.5)$$

The predicted value of the dipole moment of the $N_b = 14$ local-bending level is approximately 0.6 D (Table 8.1). To shift the observed transition frequency by 100 kHz, an electric field of approximately 400 V/cm is required. Initial attempts have been made to observe the pure rotation transition in the $N_b = 14$ local-bender state, populated by SEP, but these experiments have not yet been successful in identifying transitions due to vibrationally excited acetylene.

Chapter 9

Ongoing work

9.1 Global vibrational structure of S_1 acetylene

In this thesis, we have described over 30 newly observed vibrational levels of the \tilde{A}^1A_u state of acetylene with the twin aims of (1) elucidating the effects of *trans-cis* isomerization in the S_1 state and (2) identifying suitable intermediate states from which to probe the local-bending levels most relevant to bond-breaking isomerization in the S_0 state. A few anharmonic resonances have been identified, but only one, K_{4466} , is large enough to have an effect on the global appearance of the spectra. The others, K_{12bb} and k_{2bb} , are small enough that they only disrupt the observed level structures locally, as has been observed in the 1^1 fundamental level. None of these anharmonic interactions resemble those expected to arise from the presence of a low barrier to *trans-cis* isomerization. Rather, we anticipate the existence of interactions between the *trans*- (ν'_3) and *cis*-bending (ν'_6) modes that give rise to motions that project onto the minimum energy isomerization path, through the predicted half-linear transition state [114].

The form of the interaction between modes ν'_3 and ν'_6 is not known *a priori*, however, so we would hope to be able to identify the effects of this interaction in the

spectrum. Unfortunately, unlike many anharmonic interactions, the ν'_3/ν'_6 interaction does not have an obvious lowest order term as a result of being nearly resonant: the frequencies of ν'_3 (1047 cm⁻¹ [118]) and ν'_6 (768 cm⁻¹ [2]) are not related by the small integer ratios associated with either Fermi (2:1) or Darling–Dennison (2:2) resonances. Even if the associated anharmonic force constants are large, these interactions will be very far from resonance in the spectrum.

Because the barrier to isomerization is quite low, only a few quanta of vibrational excitation in these modes is sufficient to reach it. In contrast to the situation in the ground electronic state, where the high isomerization barrier results in regular spectral patterns for many thousands of cm⁻¹, the vibrations on the excited state surface do not have a long region of regularity that is eventually broken by the existence of the isomerization barrier. As a result, the anharmonic interactions between modes ν'_3 and ν'_6 are sampled weakly and indirectly in the experimentally observed spectrum. We have identified the anharmonicity observed in the energies of the lowest members of the $3^n B^2$ polyads, described in Chapter 7, as one symptom of these interactions.

In order to address the changes in level structure due to the accessibility of the barrier to *trans-cis* isomerization, Josh Baraban has undertaken a series of discrete variable representation (DVR) [196] calculations on reduced-dimension models of the S_1 surface. These models are based on high quality *ab initio* potential energy surfaces calculated using equation-of-motion coupled-cluster theory [197]. The details of the methods used will be reported later. The results include the vibrational energies and wavefunctions of all states associated with the reduced-dimension surface. This is in contrast to the partial picture offered by computational approaches designed solely to simulate the observed spectrum, e.g. spectral quantization [198, 199], which determine energies and wavefunctions only for states that have significant intensity in excitation from an initially formed basis state (typically the vibrationless level of the ground electronic state). Earlier work by Köppel and coworkers [198, 199] has revealed

bifurcations in the shapes of the wavefunctions in the vicinity of the isomerization barrier. Due to the fact the spectral quantization method does not capture the “dark” states that lie below the isomerization barrier, forming a mechanistic picture of the isomerization from this limited data set seems quite impossible.

The most severe reduction of the dimensionality still expected to provide insight into the \tilde{A} -state vibrational dynamics is a planar model, where the only internal degrees of freedom allowed to vary are the two $\angle\text{CCH}$ bond angles. Three wavefunctions from the planar DVR calculation are reproduced in Figure 9-1. These wavefunctions represent vibrationally excited states that are localized in the *trans* well of S_1 . The two axes represent the two angle bends that give rise to the normal mode vibrations: ν'_3 along the main diagonal (top left to bottom right) and ν'_6 along the anti-diagonal (bottom left to top right). It is relatively easy to assign vibrational quantum numbers to the observed wavefunctions. Shown in Figure 9-1 are the (a) 6^2 , (b) 3^16^4 , and (c) 6^6 . The wavefunctions plotted here, while easy to assign, are clearly not identical to expected zero-order wavefunctions from a normal mode treatment. The nodal structures become elongated and curved, clear evidence of mixing of the normal mode basis states.

In order to attempt to explain the mechanism of this mixing, and the general shapes of the wavefunctions, we have fitted the assignable DVR energies to a simple effective Hamiltonian with diagonal terms,

$$\hat{H}_{\text{diag}}^{\text{eff}} = \omega_3 \hat{n}_3 + \omega_3 \hat{n}_3 + x_{33} \hat{n}_3^2 + x_{66} \hat{n}_6^2 + x_{36} \hat{n}_3 \hat{n}_6, \quad (9.1)$$

and resonance terms,

$$\hat{H}_{\text{res}}^{\text{eff}} = \frac{1}{2\sqrt{2}} K_{366} [a_3 a_6^\dagger a_6^\dagger + \text{c.c.}] + \frac{1}{8} K_{3366} [a_3 a_3 a_6^\dagger a_6^\dagger + \text{c.c.}]. \quad (9.2)$$

The precise values of the fit parameters are not considered to be physically meaning-

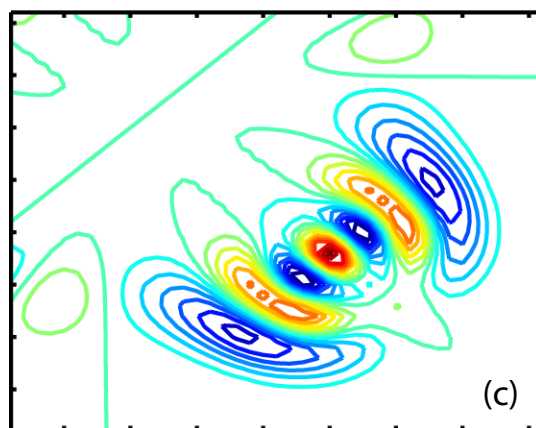
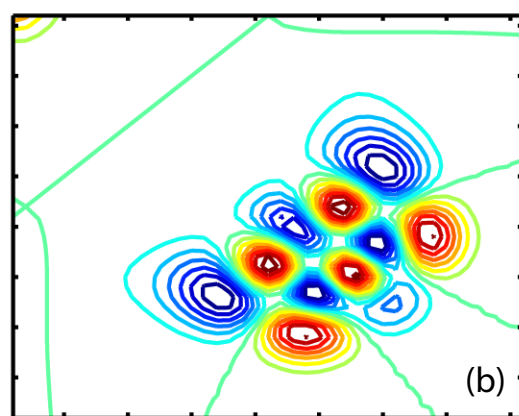
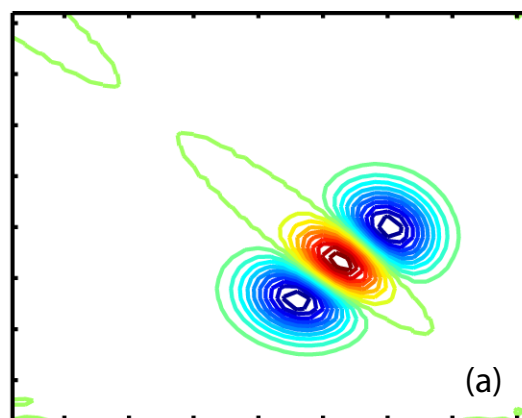


Figure 9-1: Three DVR wavefunctions of planar S_1 acetylene. The axes are the two CCH bond angles, so the two normal coordinates are the diagonals, top left to lower right (ν'_3), bottom left to top right (ν'_6), of each figure. Despite some distortions, the wavefunctions are straightforward to assign in the normal mode basis. (a) The 6^2 level. (b) The $3^1 6^4$ level. (c) The 6^6 level.

ful, due to the reduced-dimension approach, and are not reported fully here. (The magnitudes of the resonance parameters are approximately 158 and 66 cm^{-1} , for K_{366} and K_{3366} respectively.) Rather, by visual inspection of wavefunctions derived from the fitted Hamiltonian, we argue that both Fermi and Darling–Dennison resonances are necessary to reproduce the observed qualitative features. The wavefunctions from Figure 9-1 are reproduced as the top row of Figure 9-2. The second row are the wavefunctions resulting from the effective Hamiltonian fit described above. The \hat{H}^{eff} wavefunctions are calculated in a normal mode basis, so that the axes are the *cis*- and *trans*-bending normal coordinates. Accordingly, the figures have been rotated by 45° in order to achieve the closest resemblance between the DVR and \hat{H}^{eff} wavefunctions. The third and fourth rows of Figure 9-2 are the wavefunctions of the effective Hamiltonian with the Darling–Dennison and Fermi resonance terms, respectively, set to zero. In the wavefunctions derived from the \hat{H}^{eff} without the Fermi resonance, the nodal structure is symmetric: positive and negative displacements along the ν'_3 coordinate are identical. With the Fermi resonance set to zero, the wavefunctions are more asymmetric than those calculated using DVR: they are strongly bent but do not curve back onto themselves to form nearly circular nodal patterns. This analysis indicates that both Fermi and Darling-Dennison anharmonic interactions between modes ν'_3 and ν'_6 are significant in determining the nodal structure and, therefore, the vibrational dynamics of S_1 acetylene.

The fact that both anharmonic interaction mechanisms are important should not be surprising, considering that the ratio between the two normal mode frequencies (1:0.73) is almost exactly halfway between the Fermi (1:0.5) and Darling–Dennison limits (1:1). If both of these interactions are important in determining the position of the energy levels, it will have important consequences for the vibrational dynamics. One consequence is that none of the bending quantum numbers will be related to approximately conserved polyad quantum numbers [200]. The non-existence of polyads,

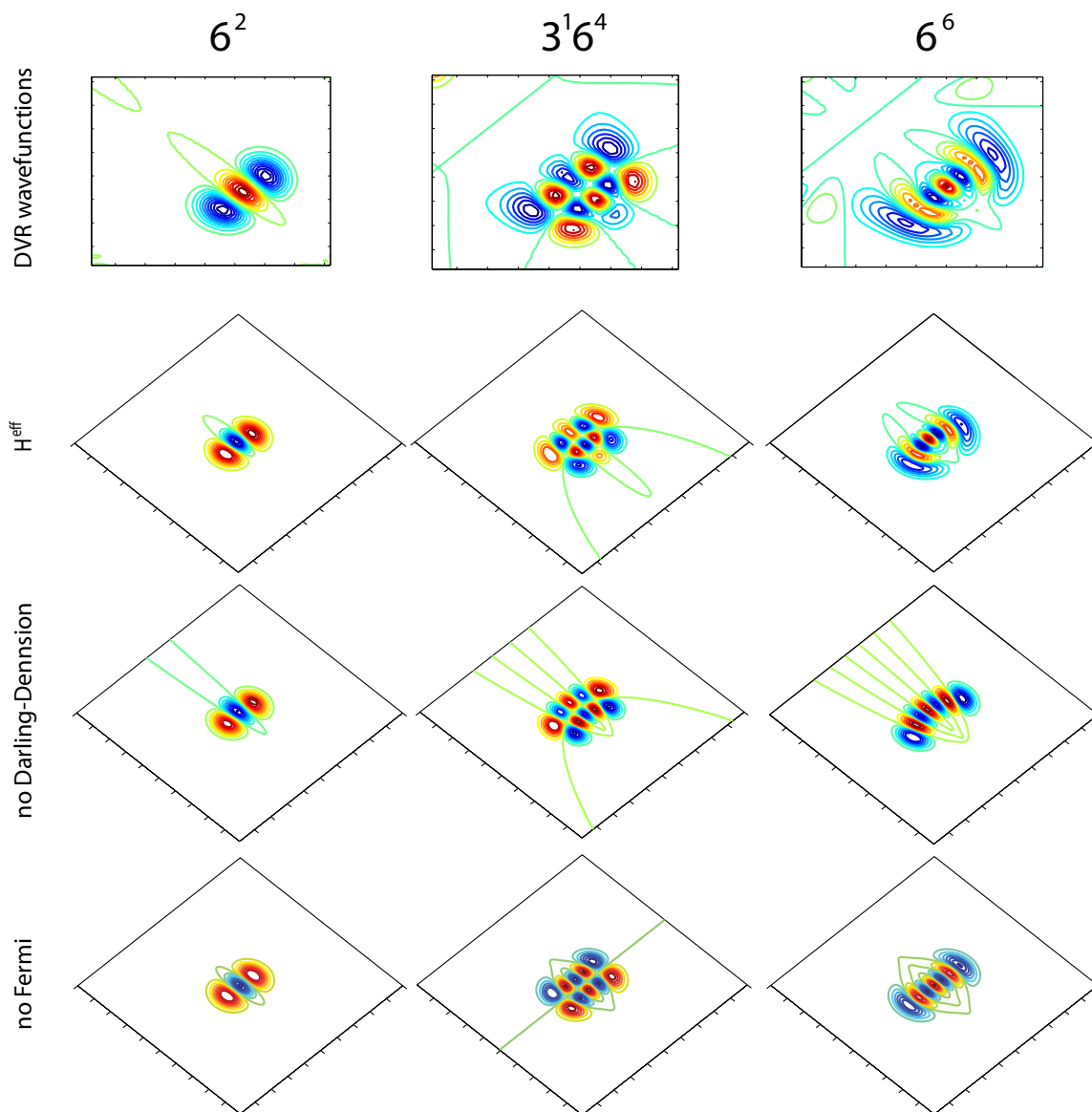


Figure 9-2: Comparison of DVR wavefunctions, from Figure 9-1, with wavefunctions derived from an \hat{H}^{eff} fit to the DVR energy levels of the *trans* well. The wavefunctions of the \hat{H}^{eff} resemble all of the qualitative features of the full DVR wavefunctions. If either the Darling–Dennison or Fermi resonance is turned off, the qualitative resemblance is lost.

due to the action of multiple resonances between the same vibrational modes, signifies the absence of dynamical bottlenecks in the phase space of the vibrations.

9.2 Strong, unassigned perturbing levels in S_1

As noted in the previous section, spectral quantization calculations [198, 199] predict a bifurcation in the qualitative shapes of the wavefunctions above the barrier to isomerization. Specifically, qualitatively new types of nodal structure are observed in the region of six quanta of the Franck-Condon active mode ν'_3 . Very similar nodal structures are observed in the DVR wavefunctions (not shown), and these structures are a subject of current interest. Relevant to the current discussion is the observation that the LIF and absorption spectra of acetylene have strong unassigned levels in the energetic regions corresponding to the onset of these novel structures. The unassigned levels, the lowest of which lies at $47\,206\text{ cm}^{-1}$, were previously assigned as states excited in the symmetric C-H stretching mode, ν'_1 [119, 122]. With the new and definitive assignment of the ν'_1 fundamental in Chapter 6, it is clear that the previous assignments are incorrect, and we have proposed a few possibilities for the vibrational assignments of the previous incorrectly assigned levels. As the predicted bifurcation and the correct assignment of these bands appear to be related to the possibility of *trans-cis* isomerization, this is one of the most significant unexplained points in the analysis of the spectrum of the $\tilde{A}^1A_u - \tilde{X}^1\Sigma_g^+$ transition.

What is most surprising about the band at $47\,206\text{ cm}^{-1}$ is its strength. In the overview spectra of Figure 7-1, this band appears at the very high end of the one-photon spectrum, indicated by a question mark. It is only slightly weaker than the Franck-Condon allowed 3^5 level, which lies only 50 cm^{-1} above it. Of course, we have stressed in this thesis that the relative intensities in LIF are not identical to the relative intensities observed in absorption, as a result of numerous factors includ-

ing predissociation. However, the earlier absorption work also indicates that these two bands have very similar intensities (see Figure 2 of Ref. [119]). If the 3^5 basis state carries all of the intensity in absorption at these energies, a very reasonable assumption based on the patterns observed at lower energy, the nearly equal intensities of the bands at 47 206 and 47 260 cm^{-1} indicate two strongly mixed (nearly 50:50) states with a matrix element between them of approximately 27 cm^{-1} . Normally, the patterns in the spectra can be usefully interpreted by shifting the entire spectrum by an amount equal to one quantum of the *trans*-bending vibration. However, while there are many weak features in the spectrum near 3^4 , there is no uniquely strong band which appears to steadily gain intensity as one goes from one member of the progression to the next. In fact, the sudden jump in intensity is quite unexpected when one considers that borrowed intensity usually varies quite smoothly from one member of the vibrational progression to the next as an effect of the quantum number scaling of anharmonic interaction matrix elements.

A possible explanation for the sudden intensity onset for the 47 206 cm^{-1} band may be related to the presence of multiple anharmonic interactions and, therefore, multiple pathways through which intensity may be transferred into this band. One assignment proposed for the 47 206 cm^{-1} band in Chapter 6 is 3^4B^2 , I. This assignment is appealing because we have argued that there exists a strong Fermi resonance between ν'_3 and ν'_6 , which would provide a large matrix element between the 3^5 and 3^46^2 basis states. The assignment is challenging, however, on the basis that the 3^3B^2 , I level has not yet been assigned. Therefore, we must extrapolate a significant way from the assignment of the 3^2B^2 , I level to make a prediction about where the 3^4B^2 , I level is likely to be found in the spectrum. Additionally, it has been demonstrated that the anharmonicity is strong in these polyads, pushing the lowest polyad member well below the others, as shown in Figure 7-13. As the lowest member detunes from the rest of the polyad, it also becomes relatively weak as compared to the other

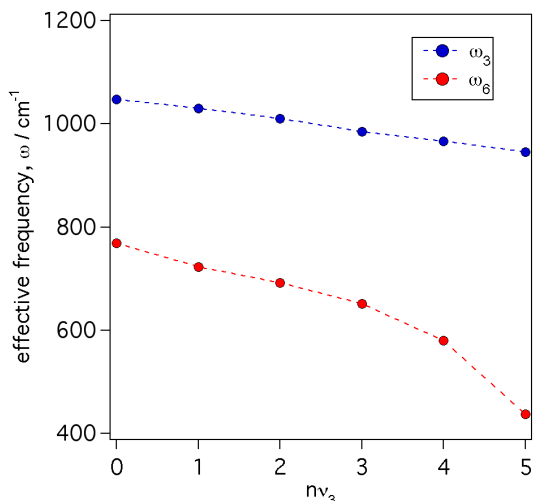


Figure 9-3: Effective frequencies of vibration for the *trans*- and *cis*-bending modes as a function of ν'_3 . Between $\nu'_3 = 4$ and 5, the effective frequencies of the two modes passes through a 2:1 ratio.

polyad members. This is likely the cause of the non-observation of 3^3B^2 , I. As an aid to the appropriate extrapolation of the 3^3B^2 energies, it is useful to consider the effective vibrational frequencies calculated from the positions of the lowest members of the 3^nB^1 polyads. A plot of the effective frequencies of the *trans*- and *cis*-bending vibrations is shown in Figure 9-3. The effective frequency of the $n\nu'_3$ progression decreases relatively slowly, while the effective frequency from the $n\nu'_3 + \nu'_6$ progression decreases much more rapidly. Importantly, between four and five quanta of excitation in the ν'_3 mode, the ratio of the effective frequencies appears to pass through the 2:1 ratio, which brings the Fermi interaction into perfect resonance.

A tentative argument for the assignment of the 47 206 cm^{-1} level is as follows. The lowest members of the 3^nB^2 progression, nominally 3^n6^2 , gets its intensity in the spectrum from multiple sources. The exact details of these intensity-borrowing mechanisms are not known. At low *trans*-bending excitation ($\nu'_3 = 0, 1$), 3^n6^2 has significant intensity because one of the intensity-borrowing mechanisms is close to resonance. The effects of anharmonicity, likely involving the K_{3366} interaction, cause the 3^n6^2 level to drop well below the other polyad members for intermediate values of ν'_3 . As this occurs, the two intensity-borrowing mechanisms become comparably strong but, having opposite signs, cancel and give 3^n6^2 very small net intensity in

the spectrum. At high v'_3 , the $3^n 6^2$ energy falls below the energy of 3^{n+1} . Once the energetic ordering of the two basis states has been reversed, the energy denominator of one intensity-lending interaction changes sign. The previously canceling contributions to the intensity now have the same sign and constructively interfere to give rise to a sudden enhancement of intensity in this state.

Three-dimensional DVR calculations have been carried out in order to capture most of the planar vibrational dynamics associated with the observed spectral features. The results of these calculations support assignment of the state that interacts with 3^5 as either $3^4 6^2$ or $2^1 3^2 6^2$. In fact, these two states appear to perturb each other, raising the possibility of a more complicated multi-state interaction. These two assignment possibilities should be distinguishable on the basis of the ^{13}C isotope shift for this band.

9.3 “Extra” levels and the *cis* well of S_1

The multiple minima on the S_1 state have been alluded to previously. Notably, a *cis*-geometry minimum exists on the S_1 surface, predicted to lie only about 3000 cm^{-1} above the *trans* minimum. Despite more than 50 years of spectroscopic investigation of the S_1 state, no transitions into vibrational levels of the *cis* well have been assigned. The non-observation of *cis*-well vibrational levels is due to symmetry restrictions on the dipole selection rules in the C_{2v} point group that prohibit transitions between of electronic states of A_1 and A_2 symmetry. Several “extra” levels were identified in Chapters 5 and 7 that may be due to *cis*-well vibrational levels that derive their intensity via interactions with the *trans*-well states.

The lowest observed “extra” level lies just above the highest $K' = 1$ member of $3^1 B^3$. Transitions to this level were previously observed by Nami Yamakita, prior to the analysis of the interactions in B^3 -type polyads. New high resolution IR-UV

LIF spectra of this region, recorded via several rotational levels of the ground state ν_3'' level, are shown in Figure 9-4. In the figure, the final states of two R-branches are labeled: transitions terminating on the highest $K' = 1$ member of 3^1B^3 are at lower energy in each spectrum, and the higher energy transitions into the “extra” vibrational level are marked by stars. The separation between the two labelled states in each spectra is quite constant with J , $\sim 8.3 \text{ cm}^{-1}$, indicating that the B and C rotational constants are quite similar for the two vibrational levels.

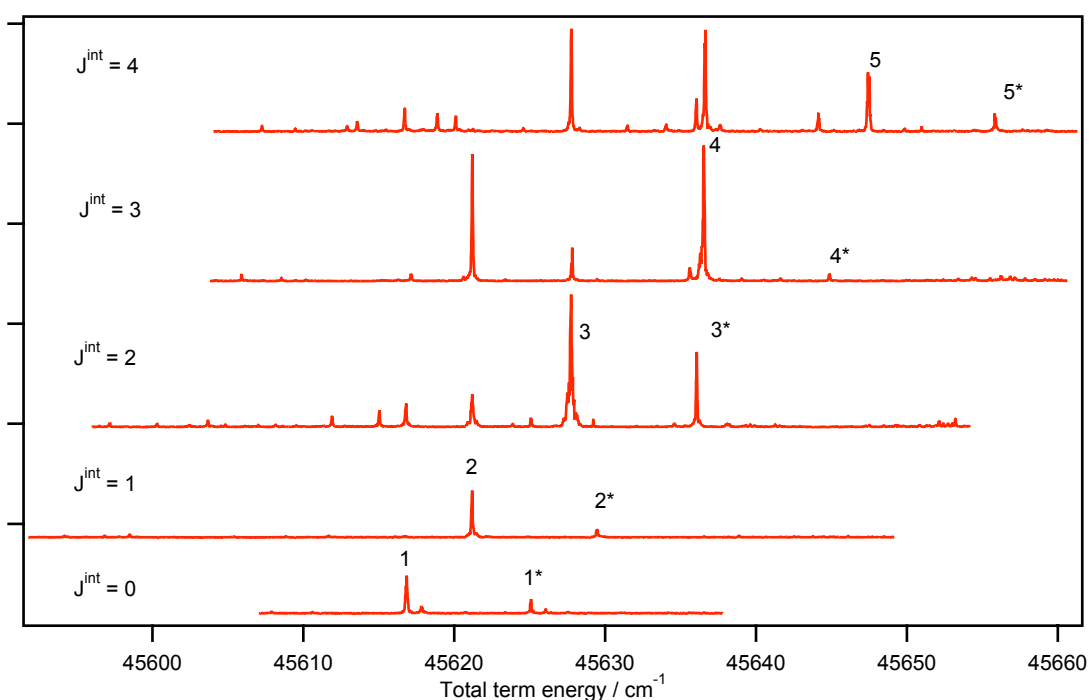


Figure 9-4: IR-UV LIF spectra showing an “extra” vibrational level near 3^1B^3 , $K' = 1$, IV. The lines of an R branch terminating on the highest-energy member of the 3^1B^3 polyad are labelled by the upper-state J -values. The associated transitions into the “extra” vibrational level are marked with stars.

This observed “extra” level lies only $\sim 3430 \text{ cm}^{-1}$ above the vibrationless level of *trans*- S_1 . If the energetic separation between the *trans* and *cis* minima is close to the expected value of $\sim 3000 \text{ cm}^{-1}$, the “extra” level must lie very low in the vibrational manifold of the *cis* well, likely with only one quantum of vibrational excitation. Arguments based on which *cis*-well levels are allowed, by symmetry, to

appear in the one-photon and IR-UV LIF experiments may be made, limiting the possible vibrational symmetries of the observed “extra” levels. The development of a model of the *cis*-well vibrations is ongoing. Isotope shifts are again expected to provide valuable evidence against which to weigh proposed vibrational assignments.

Appendix A

Cavity-ringdown spectroscopy of the $\tilde{A} - \tilde{X}$ transition of C_2H_2

[Cavity-ringdown spectroscopy of the $\tilde{A} - \tilde{X}$ transition of C_2H_2]

Quantitative understanding of the intensities of molecular transitions is desirable for a number of reasons. Chief among these is the ability to determine absolute number densities of species involved in a complex network of chemical reactions, for example, in a flame. Absolute intensity measurements also provide a means to address the fundamental interactions between molecules and radiation and the coupling between electronic and nuclear degrees of freedom within a molecule.

During the 1990s, cavity-ringdown spectroscopy (CRDS) emerged as an extremely popular tool for performing absolute intensity measurements on very weakly absorbing or highly rarefied samples. In CRDS,¹ the measured quantity is the decay rate of a high-finesse optical cavity. This decay rate is determined by the losses of the cavity mirrors and by any absorption or scattering of radiation by a molecular sample within the cavity. Being a direct measurement of the absorption by a molecular sample, CRDS is immune to the nonradiative processes (predissociation, fluorescence

¹See Ref. [201] for a review of techniques and applications.

quenching, intersystem crossing, internal conversion) that plague other highly sensitive measurement techniques based on fluorescence or ionization.

Ilya Dubinsky[202], Leah Ruslen[203], and Michelle Silva[204] implemented a modified version of the conventional CRDS experiment in order to extend the application of this technique into the ultraviolet region, where broadband dielectric coatings do not typically have the same high reflectivities available in the visible region. The primary modification consisted of the use of a fast detector (bipolar phototube, subnanosecond response) that enabled time resolution of each round trip of the laser pulse within the ringdown cavity. As a result, the cavity could be aligned to minimize the effects of spatial variations in gain across the detector surface. These authors report high sensitivity measurements of cavity loss despite the relatively short ($\sim 1 \mu\text{s}$) cavity decay times.

Silva has applied this UV-CRDS technique to the determination of the absorption cross sections of several vibronic bands in the $\tilde{A}^1A_u - \tilde{X}^1\Sigma_g^+$ system of C_2H_2 [204], which had been previously measured using classical techniques in the seminal work on acetylene by Ingold and King[108]. The intensity of this electronic transition is of considerable interest because it is forbidden at the Franck–Condon point (linear, $D_{\infty h}$) as well as at other high-symmetry geometries (*cis*-bent, C_{2v} ; diamond shaped, D_{2d}). Thus, the transition strength is highly dependent on the nuclear geometry, one of the hallmarks of vibronic coupling. Silva reported an oscillator strength, $f_v = 1.35 \times 10^{-9}$ for the $V_0^1K_0^1$ band. This determination is somewhat troubling because it disagrees strongly with the classically measured value of $f_v = 4.2 \times 10^{-8}$ [108]. If the CRDS measurement is correct, it may imply systematic errors in the cross-section measurements reported by King and coworkers for a number of molecules. However, the CRDS experiments were plagued by several inconsistencies, and the authors were unable to recommend adoption of their new values for the absorption cross-section of C_2H_2 . Silva and Ruslen both noted significant and unexplained dependence of

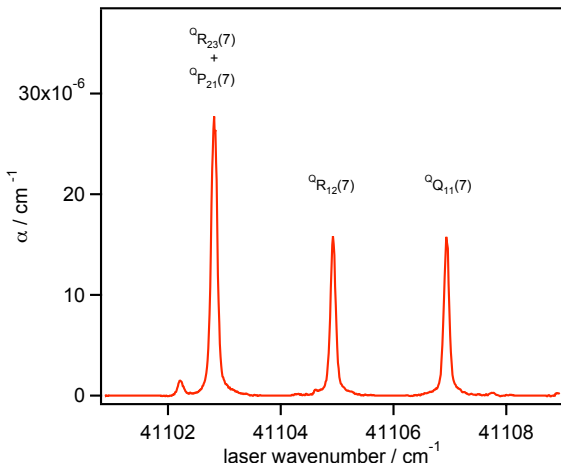


Figure A-1: A portion of the CRDS $A\ ^3\Sigma_u^+(v' = 11) - X\ ^3\Sigma_g^-(v'' = 0)$ spectrum. The O_2 pressure is 40 Torr. Rotational assignments are taken from Ref. [208].

the linestrengths on the laser scanning speed and step size. Furthermore, some of the recorded bands appear to have qualitative distortions in their intensity profiles, perhaps indicating that the CRDS measurements suffer from some form of saturation.

As an attempt to reconcile the measurements made by Silva with the earlier work of Ingold and King, we performed validation experiments using UV-CRDS to determine cross-sections of the well-characterized Herzberg I system of O_2 [205]. The absolute intensities of the bands in this system have been investigated by a number of authors and refined over the years[206, 207]. Ruslen[203] shows a spectrum of the $A\ ^3\Sigma_u^+(v' = 11) - X\ ^3\Sigma_g^-(v'' = 0)$ band but does not attempt quantitative comparison between her data and that of contemporary measurements of the absolute intensities of these bands.

The same CRDS apparatus was used for the current experiments as was used by Silva[204] and Ruslen[203], although the fast detector was replaced with a standard photomultiplier tube that is unable to resolve each pass of the ringdown cavity. Alignment was performed by maximizing the ringdown decay times while minimizing the residuals of a single exponential fit to the digitized ringdown transient. The portion of the O_2 band used for the intensity measurements is shown in Figure A-1. The ringdown time, τ , is inverted at each frequency to give a value for the frequency-dependent absorption coefficient, $\alpha(\omega)$. Integrated cross-sections for the observed lines are ob-

tained by integrating over $\alpha(\omega)$ after subtracting a background value corresponding to the baseline cavity loss between the resonances. We find that integrating the signal shown in Figure A-1 produces a cross-section for each line that is approximately 30% smaller than the best contemporary measurements of Mérienne *et al.*[207] and Yoshino *et al.*[206].

Unexpectedly low values for transition intensities are a common feature of the CRDS literature. Explanations for this phenomenon have been advanced by several authors, starting from the early work by Zalicki and Zare[209] and Jongma *et al.*[210]. Hodges *et al.*[211] stressed the importance of the relative linewidths of the laser radiation and the molecular absorption features. The fundamental, and frequently overlooked, assumption underlying the naive picture of cavity ringdown spectroscopy is that all frequencies injected into the ringdown cavity decay at the same rate. This assumption breaks down when the laser linewidth is not very narrow compared to the linewidth of the molecular feature being measured.

The sensitivity of cavity-ringdown techniques is due to the fact that the detection of absorption is shifted into the time-domain, rendering the technique immune to intensity fluctuations in pulsed lasers. However, this aspect also requires that all radiation in the cavity decay at the same rate in order to model the observed ringdown transient signal by a single-exponential decay. In standard linear absorption spectroscopy, the absorption spectrum is a convolution of the laser lineshape and the absorber lineshape. In CRDS, the spectrum is not a simple convolution, due to the properties of exponential decay: the average of several exponentially decaying functions with varying decay times, τ_i , is *not* an exponentially decaying function with the average decay time, $\bar{\tau}_i$. As a consequence of the more complex effects of laser linewidth when $\Gamma_{\text{laser}} \not\ll \Gamma_{\text{mol}}$, Hodges states that “when multimode lasers are used for CRDS, quantitative information can be extracted only when the laser’s actual mode structure is taken into account”[211].

Several strategies exist to incorporate a finite laser lineshape into the analysis, e.g. Refs [212, 213, 214]. Common to all of these solutions is that the deleterious effects of finite laser linewidth can be reduced both by selectively fitting the earliest portion of the decay transient and by artificially broadening the molecular transitions with the addition of a buffer gas. Our ringdown decays have been fitted using various time windows (data not shown), with windows on the early part of the decay (fitting only the region between 90% and 70% of the peak signal) giving rise to larger absorption signals in agreement with the general principles discussed above. Extrapolating the windowed fit data to shorter and shorter gate intervals is problematic as fast oscillations in the ringdown transient that appear due to “mode beating” effects become problematic and the resulting spectra become noisier.

We have also implemented a second general approach to compensate for the finite laser linewidth, intentionally pressure-broadening the molecular transition by the addition of a buffer gas. CRD spectra were recorded of a cell containing 40 Torr of O₂ gas. Nitrogen gas was then added to the cell in increments of roughly 150 Torr, up to a total pressure of 700 Torr. Three of the resulting spectra are shown in Figure A-2a.

It is clear from these spectra, which focus on only the ${}^Q R_{12}(7)$ line of the previously described transition, that the total transition intensity is not conserved as it would be in a purely linear measurement. While the peak height at the center frequency of the transition is similar for the spectra recorded at 0 and 270 Torr of added N₂ buffer gas, the peak is significantly broader in the 270 Torr spectrum ($\Gamma_{\text{FWHM}} = 0.14 \text{ cm}^{-1}$) than in the unbroadened case ($\Gamma_{\text{FWHM}} = 0.11 \text{ cm}^{-1}$). At higher buffer gas pressures, the peak intensity decreases as expected, while the line continues to broaden. The integrated cross-sections are shown in Figure A-2b, as a function of partial pressure of the N₂ buffer gas. As noted, the integrated intensity is not conserved despite the constant number density of absorbing molecules. In the unbroadened spectra, the

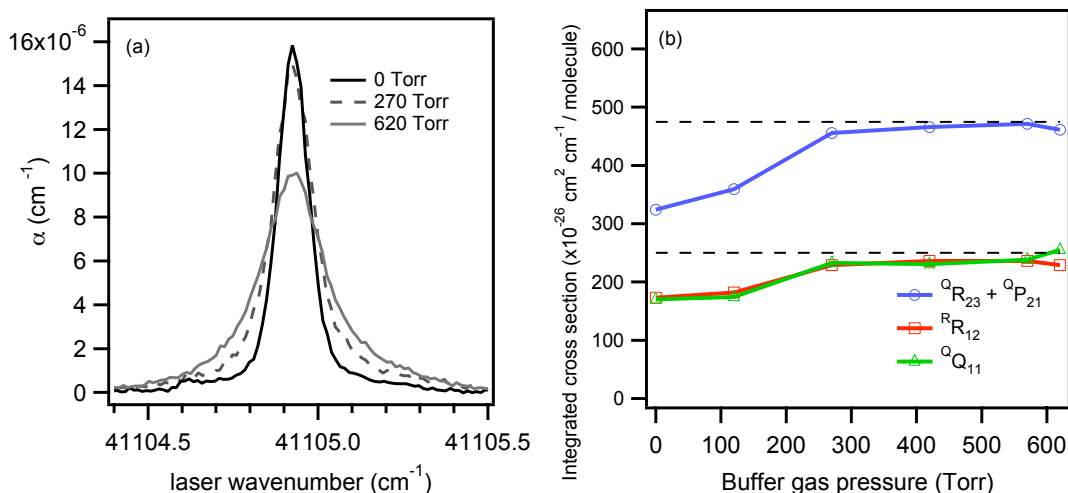


Figure A-2: Pressure-broadening of the transitions observed by CRDS in the Herzberg I system. (a) Observed CRD lineshape of the ${}^Q R_{12}(7)$ line of the Herzberg I ($v' = 11$) - ($v'' = 0$) band with addition of N_2 gas. (b) Integrated cross-section of three features in the CRD spectrum as a function of the added partial pressure of N_2 gas. The dashed horizontal lines represent the cross-sections measured by Mérieu *et al.*[207].

intensities are significantly too low ($\sim 30\%$) as compared to the best measurements of these transitions, which are represented visually by dashed horizontal lines in Figure A-2b. As the partial pressure of buffer gas is increased, the measured cross-sections increase, until at a partial pressure of approximately 300 Torr they level off. At this point, the linewidth of the molecular transition is approximately three times broader than the frequency width of the frequency-doubled dye laser radiation ($\Gamma_{\text{FWHM}} \approx 0.06 \text{ cm}^{-1}$). Although the agreement between our pressure-broadened cross-sections and those of Ref. [207] is not exact, the agreement to within better than 10% is promising in that it indicates that our general method is sound.

A second conclusion of these validation experiments, however, is that the underestimates of cross-sections due to finite-linewidth effects, under the conditions used in our CRD experiments, are relatively small. These effects will lead to underestimates of 50%, in the worst case, and cannot plausibly account for the factor of ~ 30 discrepancy between the oscillator strengths measured by Silva[204] and those measured by

Ingold and King[108]. The finite-linewidth effects should be of comparable magnitude for O₂ and for C₂H₂, due to their similar molecular weights and, consequently, their Doppler profiles.

Now that the UV-CRDS measurements have been validated, we return to the question of the absorption cross-section of the $V_0^1K_0^1$ band of the $\tilde{A}^1A_u - \tilde{X}^1\Sigma_g^+$ transition of C₂H₂. CRDS spectra of the $V_0^1K_0^1$ band, acquired using the methods described for O₂ above, are shown in Fig. A-3. The upper trace is the spectrum recorded at 3 Torr of acetylene vapor, and the lower trace is recorded with an additional 300 Torr of N₂ gas. The effects of the pressure-broadening are quite dramatic. The density of features in the spectrum is such that the pressure-broadening required to create a sufficient disparity between the transition linewidth and the laser linewidth causes most features in the spectrum to become blended with their neighbors. In the R branch, the blending is particularly acute, and only the first few lines are reasonably well resolved. This highlights one problem with the proposed application of pressure-broadened CRDS to the study of the absolute cross-section of the $\tilde{A}^1A_u - \tilde{X}^1\Sigma_g^+$ transition of C₂H₂. We wish to make line-by-line measurements of the intensity, in order to search for rotational effects beyond those contained within the Hönl-London factors. Lack of an obvious baseline, or regions where the intensity between resolved transitions drops to zero, is problematic for such efforts.

Difficulties defining the baseline in CRDS are quite vexing, as it is not immediately clear how to deal with frequency-dependent losses caused by scattering at the mirror surface or changes in alignment when the sample is introduced into the ring-down cavity. This is particularly true for broad spectra or continuum measurements, though some progress has been made in these directions recently[215]. In the spectra of acetylene, recorded at room temperature and at Doppler-limited resolution, there is very little “true” baseline. Rather, the observed baseline is made up of a somewhat inhomogeneous collection of blended lines due to hot-bands and perhaps to excita-

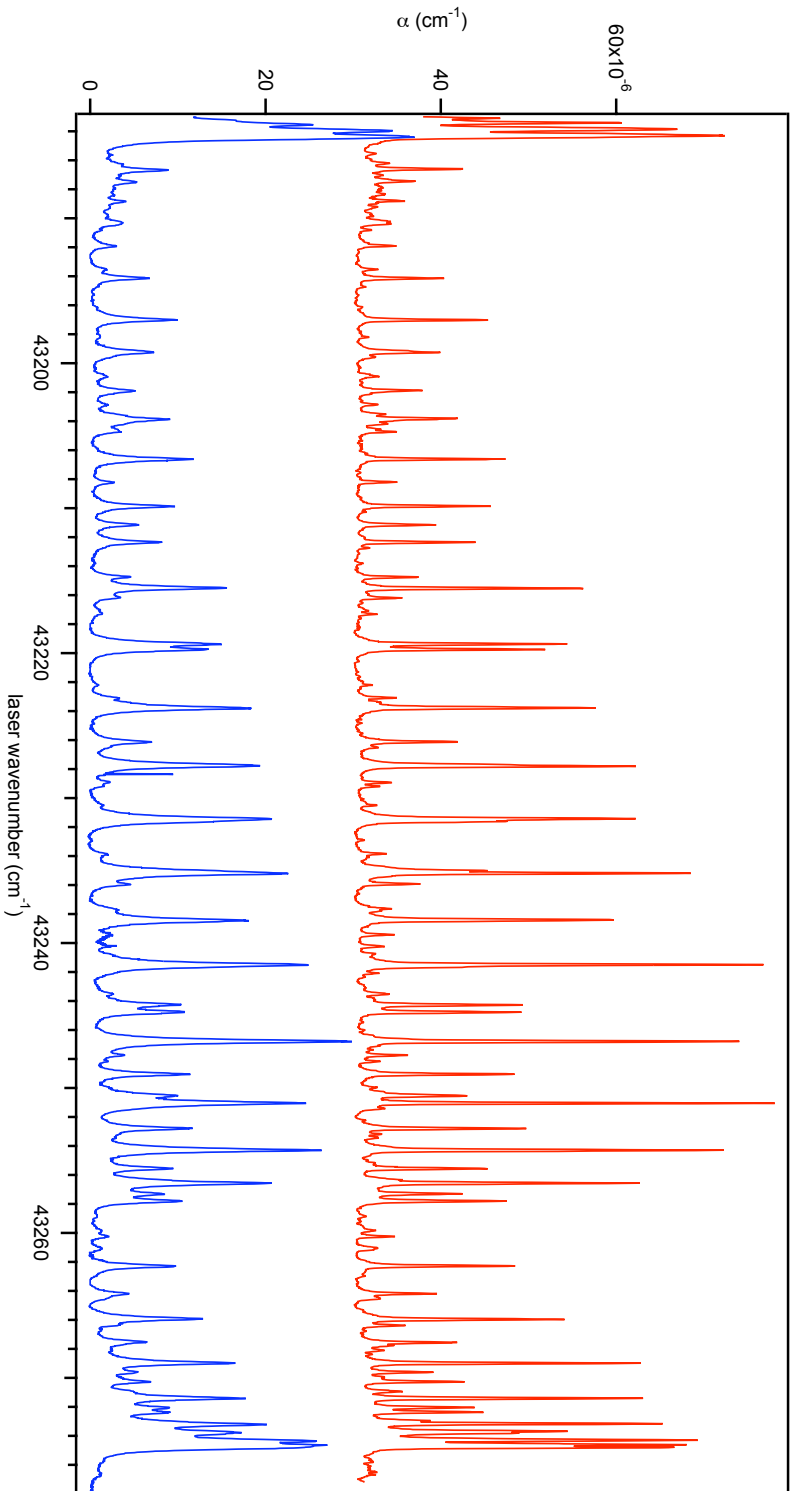


Figure A-3: Broad CRDS spectra of the $V_0^1 K_0^1$ band of the $\tilde{A}^1 A_u - \tilde{X}^1 \Sigma_g^+$ transition of C_2H_2 . For the upper trace, the cell contained 3 Torr of neat acetylene vapor. For the lower trace, the acetylene spectra was pressure-broadened by the addition of 200 Torr of N_2 gas. The upper trace is offset vertically by $30 \times 10^{-6} \text{ cm}^{-1}$. The units on the vertical axis are loss per centimeter of pathlength, not the common spectroscopic unit of wavenumber, the reciprocal centimeter. A large density of weak features causes a problem in identifying a definite baseline, as these features become blended with the transitions we seek to measure in the pressure-broadened spectrum.

tion of the dense manifold of triplet states. Pressure-broadening, in this case, only exacerbates the problem of separating the background absorption from the resonance absorption that we seek to measure.

Though there are some clear difficulties in applying the CRDS method to acetylene, we have repeated some of the measurements of Ruslen[203] and of Silva[204] in order to assess whether or not their measurements of the acetylene absorption cross-sections correctly point to a large flaw in the cross-section determined by Ingold and King[108]. The unbroadened CRD spectra of the $V_0^0 K_0^1$, $V_0^1 K_0^1$, and $2_0^1 V_0^1 K_0^1$ bands of the $\tilde{A}^1 A_u - \tilde{X}^1 \Sigma_g^+$ transition of C_2H_2 are shown in Figure A-4. As was done for the O_2 transitions, nitrogen gas was added to the ringdown cell in order to broaden the acetylene transitions. Approximately 200 Torr of N_2 was used in order to sufficiently broaden the lines until the integrated line intensities stopped increasing with increasing buffer gas pressure. Following the approach of Silva[204], the integrated line intensities were transformed into band oscillator strengths in order to compare these measurements with those of Ingold and King[108]. There are significant line-to-line variations in the calculated values of the band oscillator strengths, indicating that there may be significant ignored rotational intensity factors.

The average value for the band oscillator strength, f_v , determined from the Q(1–5) lines of the $V_0^1 K_0^1$ band is 6.4×10^{-9} . Our band oscillator strength is significantly larger than that reported by Silva[204] (1.35×10^{-9}), but significantly smaller than that reported by Ingold and King[108] (4.2×10^{-8}). Because our measurement is six times smaller than the classically measured value and five times larger than the previous CRD value, it does not provide any significant evidence to support either previous determination. As a result, no further quantitative measurements are reported here. At best, we may conclude that doubts remain about the original measurements by Ingold and King[108], but that the large discrepancy between the cavity ringdown measurements within our own group indicates that CRD is not the optimal tool for

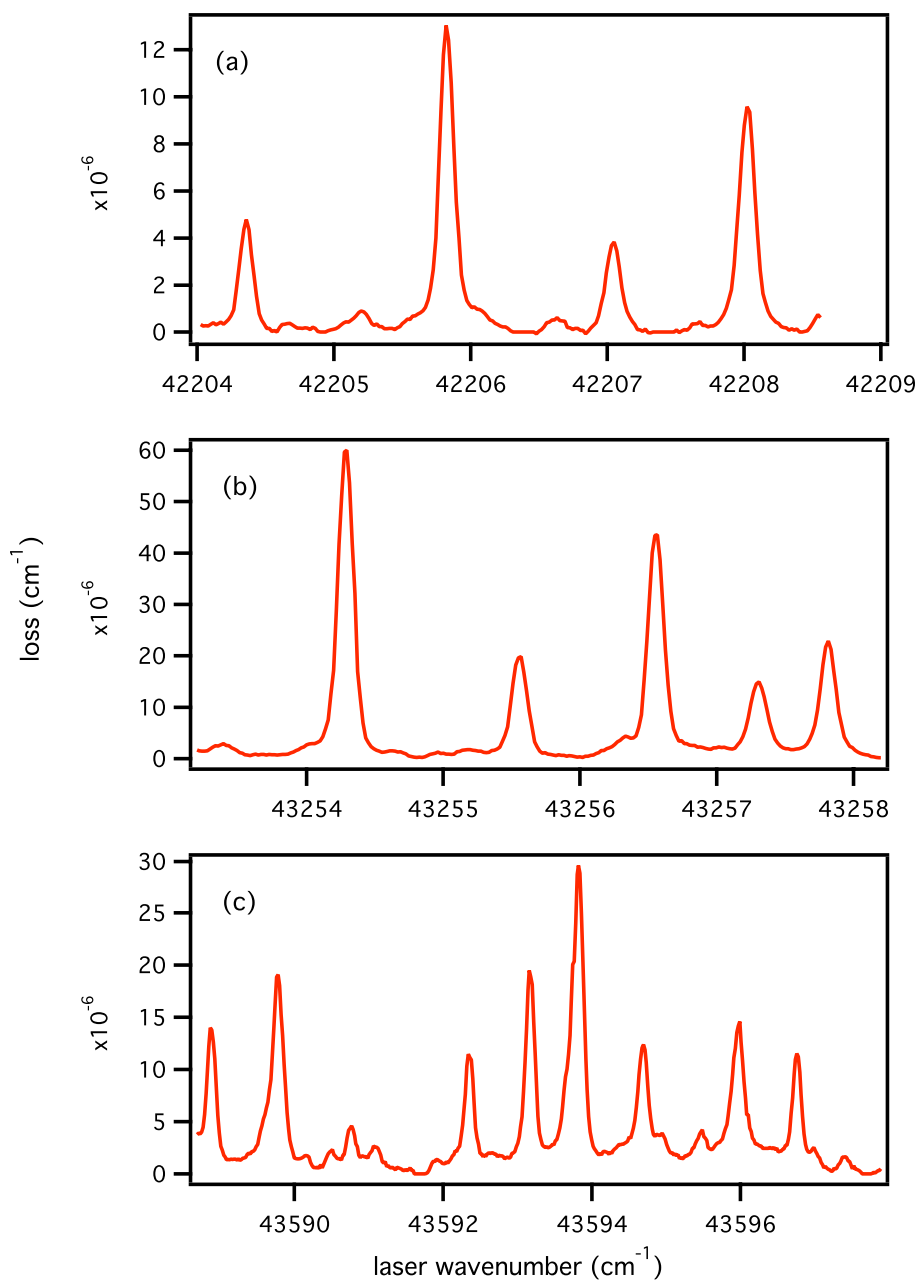


Figure A-4: CRD spectra of portions of the Q branches of the (a) $V_0^0 K_0^1$, (b) $V_0^1 K_0^1$, and (c) $2_0^1 V_0^0 K_0^1$ bands of acetylene. The pressures of acetylene in these spectra are 8, 3, and 4 Torr respectively. In (c), the transitions belonging to the $2_0^1 V_0^0 K_0^1$ band are overlapped by more intense hot-bands terminating on the $2\nu_3'$ vibrational level.

further investigation of this possible error.

There are several variants of the simple pulsed CRDS technique that more conclusively eliminate the effects of finite laser linewidth. The most obvious of these is to use a single-mode laser, though this is experimentally challenging in the deep UV [216]. Alternatively, the mutli-mode structure of the laser output may be analyzed and input into a complicated fit of the ringdown decay. Other modifications are equally arduous, requiring significant additional experimental complexity to guarantee more rigorously quantitative results. In addition to the finite-linewidth effects, which were certainly a cause for error in the measurements of Silva[204], there is some possibility that additional non-linearities[217] plague the CRDS measurements. The consistent measurements of the oscillator strength of the Herzberg I system in Refs. [206] and [207], identify UV fourier transform absorption spectroscopy as a highly capable alternative for making such measurements.

The $\tilde{A}^1A_u - \tilde{X}^1\Sigma_g^+$ transition of C_2H_2 is not ideally suited to the use of CRDS. In fact, the bands, particularly the higher members of the Franck–Condon progression are not weak enough to merit the use of CRDS, particularly since acetylene is a stable gas and measurements, therefore, of high column densities are trivial. Several groups have performed linear absorption spectroscopy on acetylene using conventional, relatively noisy, pulsed lasers with the particular application of studying the predissociation rate and mechanism[218, 219]. Further experiments along these lines are required to determine whether the cross-sections reported by Ingold and King[108] for bands in the $\tilde{A}^1A_u - \tilde{X}^1\Sigma_g^+$ transition of C_2H_2 are accurate.

Bibliography

- [1] Bowman, J.M., Irle, S., Morokuma, K. and Wodtke, A.M. *Journal of Chemical Physics*, **114**(18), 7923–7934 (2001).
- [2] Utz, A.L., Tobiasson, J.D., Carrasquillo, E., Sanders, L.J. and Crim, F.F. *Journal of Chemical Physics*, **98**(4), 2742–2753 (1993).
- [3] Scherer, G.J., Chen, Y.Q., Redington, R.L., Kinsey, J.L. and Field, R.W. *Journal of Chemical Physics*, **85**(11), 6315–6323 (1986).
- [4] Steeves, A.H., Bechtel, H.A., Coy, S.L. and Field, R.W. *Journal of Chemical Physics*, **123**(14), 141102 (2005).
- [5] Townes, C.H. and Dailey, B.P. *Journal of Chemical Physics*, **17**(9), 782–796 (1949).
- [6] Gordy, W. and Cook, R. *Microwave molecular spectra*, vol. XVIII of *Techniques of Chemistry*. Wiley (1984).
- [7] Douglass, K.O., Dian, B.C., Brown, G.G., Johns, J.E., Nair, P.M. and Pate, B.H. *Journal of Chemical Physics*, **121**(14), 6845–6854 (2004).
- [8] Dian, B.C., Brown, G.G., Douglass, K.O. and Pate, B.H. *Science*, **320**(5878), 924–928 (2008).
- [9] Theule, P., Callegari, A., Rizzo, T.R. and Muentner, J.S. *Journal of Chemical Physics*, **119**(17), 8910–8915 (2003).
- [10] Balle, T.J. and Flygare, W.H. *Review of Scientific Instruments*, **52**(1), 33–45 (1981).
- [11] Grabow, J.U. and Stahl, W. *Zeitschrift Fur Naturforschung Section A-A Journal of Physical Sciences*, **45**(8), 1043–1044 (1990).
- [12] Petkie, D.T., Goyette, T.M., Bettens, R.P.A., Belov, S.P., Albert, S., Helminger, P. and DeLucia, F.C. *Review of Scientific Instruments*, **68**(4), 1675–1683 (1997).
- [13] Surin, L.A., Dumesh, B.S., Lewen, F., Roth, D.A., Kostromin, V.P., Rusin, F.S., Winnewisser, G. and Pak, I. *Review of Scientific Instruments*, **72**(6), 2535–2542 (2001).

- [14] Ziurys, L., Barclay, W., Anderson, M., Fletcher, D. and Lamb, J. *Review of Scientific Instruments*, **65**(5), 1517–1522 (1994).
- [15] Amano, T. and Amano, T. *Journal of Chemical Physics*, **95**(4), 2275–2279 (1991).
- [16] Mccarthy, M., Gottlieb, C., Cooksy, A. and Thaddeus, P. *Journal of Chemical Physics*, **103**(18), 7779–7787 (1995).
- [17] Hepp, M., Jager, W., Pak, I. and Winnewisser, G. *Journal of Molecular Spectroscopy*, **176**(1), 58–63 (1996).
- [18] Uemura, K., Hara, A. and Tanaka, K. *Journal of Chemical Physics*, **104**(24), 9747–9753 (1996).
- [19] Linnartz, H., Motylewski, T., Maiwald, F., Roth, D., Lewen, F., Pak, I. and Winnewisser, G. *Chemical Physics Letters*, **292**(1-2), 188–192 (1998).
- [20] Tanaka, K., Toshimitsu, M., Harada, K. and Tanaka, T. *Journal of Chemical Physics*, **120**(8), 3604–3618 (2004).
- [21] Huiszoon, C. *Review of Scientific Instruments*, **42**(4), 477–481 (1971).
- [22] Drucker, S., Cooksy, A. and Klemperer, W. *Journal of Chemical Physics*, **98**(7), 5158–5183 (1993).
- [23] Drucker, S., Tao, F. and Klemperer, W. *Journal of Physical Chemistry*, **99**(9), 2646–2655 (1995).
- [24] Drouin, B., Maiwald, F. and Pearson, J. *Review of Scientific Instruments*, **76**(9), 093113 (2005).
- [25] Duffy, L. *Review of Scientific Instruments*, **76**(9), 093104 (2005).
- [26] Kinch, M.A. and Rollin, B.V. *British Journal of Applied Physics*, **14**(10), 672–676 (1963).
- [27] Pickett, H., Poynter, R., Cohen, E., Delitsky, M., Pearson, J. and Muller, H. *Journal of Quantitative Spectroscopy & Radiative Transfer*, **60**(5), 883–890 (1998).
- [28] Muller, H.S.P., Schloder, F., Stutzki, J. and Winnewisser, G. *Journal of Molecular Structure*, **742**(1-3), 215–227 (2005).
- [29] Lehmann, K. and Coy, S. *Journal of Chemical Physics*, **81**(8), 3744–3745 (1984).
- [30] Lehmann, K. and Coy, S. *Journal of Chemical Physics*, **83**(7), 3290–3296 (1985).

- [31] Coy, S., Lehmann, K. and Delucia, F. *Journal of Chemical Physics*, **85**(8), 4297–4303 (1986).
- [32] Nakajima, M., Sumiyoshi, Y. and Endo, Y. *Review of Scientific Instruments*, **73**(1), 165–171 (2002).
- [33] Douglass, K., Keske, J., Rees, F., Welch, K., Yoo, H., Pate, B., Leonov, I. and Suenram, R. *Chemical Physics Letters*, **376**(5-6), 548–556 (2003).
- [34] Wieman, C. and Hansch, T. *Physical Review Letters*, **36**(20), 1170–1173 (1976).
- [35] Teets, R., Feinberg, R., Hansch, T. and Schawlow, A. *Physical Review Letters*, **37**(11), 683–686 (1976).
- [36] Ernst, W. and Topping, T. *Physical Review A*, **25**(2), 1236–1238 (1982).
- [37] Ernst, W. and Topping, T. *Physical Review A*, **27**(2), 875–880 (1983).
- [38] Ernst, W. and Schroder, J. *Physical Review A*, **30**(1), 665–666 (1984).
- [39] Bergeman, T. and Cossart, D. *Journal of Molecular Spectroscopy*, **87**(1), 119–195 (1981).
- [40] Sanz, M., Mccarthy, M. and Thaddeus, P. *Journal of Chemical Physics*, **122**(19), 194319 (2005).
- [41] Shapiro, J. and Bloemhof, E. *International Journal of Infrared and Millimeter Waves*, **11**(8), 973–980 (1990).
- [42] Gerstenkorn, S. and Luc, P. *Atlas du spectre d'absorption de la molécule d'iode, 14800–20000 cm⁻¹*. CNRS (1978).
- [43] Demtröder, W. *Laser Spectroscopy : Basic Concepts and Instrumentation*. Springer (1996).
- [44] Milligan, D.E. and Jacox, M.E. *The Journal of Chemical Physics*, **39**(3), 712–715 (1963).
- [45] Arrington, C.A. and Ogryzlo, E.A. *Journal of Chemical Physics*, **63**(8), 3670–3671 (1975).
- [46] Northrup, F.J., Bethardy, G.A. and Macdonald, R.G. *Journal of Molecular Spectroscopy*, **186**(2), 349–362 (1997).
- [47] Maki, A.G. and Mellau, G.C. *Journal of Molecular Spectroscopy*, **206**(1), 47–52 (2001).
- [48] Mahon, C., Stampanoni, A., Luque, J. and Crosley, D. *Journal of Molecular Spectroscopy*, **183**(1), 18–24 (1997).

- [49] Jonas, D., Solina, S., Zhao, X., Field, R. and Kittrell, C. *Journal of Chemical Physics*, **96**(10), 7209–7217 (1992).
- [50] Schnell, M., Banser, D. and Grabow, J. *Review of Scientific Instruments*, **75**(6), 2111–2115 (2004).
- [51] Bechtel, H.A., Steeves, A.H. and Field, R.W. *Astrophysical Journal*, **649**(1, Part 2), L53–L56 (2006).
- [52] Casimir, H. *Physica*, **7**, 719 (1935).
- [53] Snyder, L. E. ; Buhl, D. *Bulletin of the American Astronomical Society*, **3**, 388 (1971).
- [54] Blackman, G.L., Brown, R.D., Godfrey, P.D. and Gunn, H.I. *Nature*, **261**(5559), 395–396 (1976).
- [55] Creswell, R.A., Pearson, E.F., Winnewisser, M. and Winnewisser, G. *Zeitschrift Fur Naturforschung Section A-A Journal of Physical Sciences*, **31**(3-4), 221–224 (1976).
- [56] Saykally, R.J., Szanto, P.G., Anderson, T.G. and Woods, R.C. *Astrophysical Journal*, **204**(3), L143–L145 (1976).
- [57] Goldsmith, P.F., Irvine, W.M., Hjalmarson, A. and Ellder, J. *Astrophysical Journal*, **310**(1), 383–391 (1986).
- [58] Harju, J. *Astronomy and Astrophysics*, **219**(1-2), 293–302 (1989).
- [59] Hirota, T., Yamamoto, S., Mikami, H. and Ohishi, M. *Astrophysical Journal*, **503**(2), 717–728 (1998).
- [60] Irvine, W.M. and Schloerb, F.P. *Astrophysical Journal*, **282**(2), 516–521 (1984).
- [61] Schilke, P., Walmsley, C.M., Desforets, G.P., Roueff, E., Flower, D.R. and Guilloteau, S. *Astronomy and Astrophysics*, **256**(2), 595–612 (1992).
- [62] Turner, B.E., Pirogov, L. and Minh, Y.C. *Astrophysical Journal*, **483**(1), 235–261 (1997).
- [63] Wootten, A., Evans, N.J., Snell, R. and Bout, P.V. *Astrophysical Journal*, **225**(3), L143–L148 (1978).
- [64] Hirota, T., Ikeda, M. and Yamamoto, S. *Astrophysical Journal*, **547**(2), 814–828 (2001).
- [65] Hirota, T., Ikeda, M. and Yamamoto, S. *Astrophysical Journal*, **594**(2), 859–868 (2003).
- [66] Snell, R.L. and Wootten, A. *Astrophysical Journal*, **228**(3), 748–754 (1979).

- [67] Turner, B.E. *Astrophysical Journal Supplement Series*, **136**(2), 579–629 (2001).
- [68] Wilson, T.L. and Rood, R.T. *Annual Review of Astronomy and Astrophysics*, **32**, 191–226 (1994).
- [69] Amano, T. and Zelinger, Z. *Journal of Molecular Spectroscopy*, **211**(2), 273–278 (2002).
- [70] Okabayashi, T. and Tanimoto, M. *Journal of Chemical Physics*, **99**(5), 3268–3271 (1993).
- [71] Pearson, E.F., Creswell, R.A., Winnewisser, M. and Winnewisser, G. *Zeitschrift Fur Naturforschung Section A-A Journal of Physical Sciences*, **31**(11), 1394–1397 (1976).
- [72] Thorwirth, S., Muller, H.S.P., Lewen, F., Gendriesch, R. and Winnewisser, G. *Astronomy and Astrophysics*, **363**(3), L37–L39 (2000).
- [73] Burkholder, J.B., Sinha, A., Hammer, P.D. and Howard, C.J. *Journal of Molecular Spectroscopy*, **126**(1), 72–77 (1987).
- [74] Maki, A.G. and Sams, R.L. *Journal of Chemical Physics*, **75**(9), 4178–4182 (1981).
- [75] Nezu, M., Amano, T. and Kawaguchi, K. *Journal of Molecular Spectroscopy*, **192**(1), 41–46 (1998).
- [76] Winter, M.J. and Jones, W.J. *Journal of Molecular Structure*, **80**(1-4), 43–46 (1982).
- [77] Walker, K.A. and Mckellar, A.R.W. *Journal of Molecular Spectroscopy*, **205**(2), 331–337 (2001).
- [78] McElmurry, B.A., Lucchese, R.R., Bevan, J.W., Leonov, I.I., Belov, S.P. and Legon, A.C. *Journal of Chemical Physics*, **119**(20), 10687–10695 (2003).
- [79] Grabow, J., Stahl, W. and Dreizler, H. *Review of Scientific Instruments*, **67**(12), 4072–4084 (1996).
- [80] Bardeen, J. and Townes, C.H. *Phys. Rev.*, **73**(2), 97 (1948).
- [81] Thaddeus, P., Krisher, L.C. and Loubser, J.H.N. *The Journal of Chemical Physics*, **40**(2), 257–273 (1964).
- [82] Pickett, H.M. *Journal of Molecular Spectroscopy*, **148**(2), 371–377 (1991).
- [83] Brunken, S., Muller, H.S.P., Thorwirth, S., Lewen, F. and Winnewisser, G. *Journal of Molecular Structure*, **780-81**, 3–6 (2006).
- [84] Delucia, F. and Gordy, W. *Phys. Rev.*, **187**(1), 58–65 (1969).

- [85] Ahrens, V., Lewen, F., Takano, S., Winnewisser, G., Urban, S., Negirev, A. and Koroliev, A. *Zeitschrift Fur Naturforschung Section A-A Journal of Physical Sciences*, **57**(8), 669–681 (2002).
- [86] Kukolich, S.G. *The Journal of Chemical Physics*, **57**(2), 869–871 (1972).
- [87] Kruger, M., Dreizler, H., Preugschat, D. and Lentz, D. *Angewandte Chemie-International Edition*, **30**(12), 1644–1646 (1991).
- [88] Pd, P. and Chandra, P. *Journal of Chemical Physics*, **114**(17), 7450–7460 (2001).
- [89] Snyder, L.E., Hollis, J.M. and Buhl, D. *Astrophysical Journal*, **215**(2), L87–L88 (1977).
- [90] Watson, W.D., Snyder, L.E. and Hollis, J.M. *Astrophysical Journal*, **222**(3), L145–L147 (1978).
- [91] Frerking, M.A., Langer, W.D. and Wilson, R.W. *Astrophysical Journal*, **232**(1), L65–L68 (1979).
- [92] Bechtel, H.A., Steeves, A.H., Wong, B.M. and Field, R.W. *Angewandte Chemie International Edition*, **47**(16), 2969–2972 (2008).
- [93] Layne, B.H., Duffy, L.M., Bechtel, H.A., Steeves, A.H. and Field, R.W. *Journal of Physical Chemistry A*, **111**(31), 7398–7403 (2007).
- [94] Kittrell, C., Abramson, E., Kinsey, J., McDonald, S., Reisner, D., Field, R. and Katayama, D. *The Journal of Chemical Physics*, **75**, 2056 (1981).
- [95] Silva, M., Jongma, R., Field, R.W. and Wodtke, A.M. *Annual Review of Physical Chemistry*, **52**, 811–852 (2001).
- [96] Lehmann, K.K. (2004). Private communication.
- [97] Wilhelm, M.J., Nikow, M., Letendre, L. and Dai, H.L. *The Journal of Chemical Physics*, **130**(4), 044307 (2009).
- [98] Tomasevich, G.R. *Molecular-Beam Electric-Resonance Studies of HCN and DCN*. Ph.D. thesis, Harvard University (1970).
- [99] Wong, B.M. *Quantum chemistry for spectroscopy : A tale of three spins ($S = 0, 1/2$, and 1)*. Ph.D. thesis, Massachusetts Institute of Technology (2007).
- [100] Yarmus, L. *Phys. Rev.*, **104**(2), 365–367 (1956).
- [101] Glendenning, E.D., Bdenhoop, J.K., Reed, A.E., Carpenter, J.E., Bohmann, J.A., Morales, C.M. and Weinhold, F. NBO 5.0. Tech. rep., Theoretical Chemistry Institute, University of Wisconsin, Madison (2001).

- [102] Rinne, M. *Advances in Nuclear Quadrupole Resonance*, vol. 1, chap. 27. Heyden (1974).
- [103] Cazzoli, G., Puzzarini, C. and Gauss, J. *Astrophysical Journal Supplement Series*, **159**(1), 181–188 (2005).
- [104] Huber, H. *Journal of Chemical Physics*, **83**(9), 4591–4598 (1985).
- [105] Wong, B.M. *Physical Chemistry Chemical Physics*, **10**(36), 5599–5606 (2008).
- [106] Merer, A.J., Yamakita, N., Tsuchiya, S., Steeves, A.H., Bechtel, H.A. and Field, R.W. *Journal of Chemical Physics*, **129**(5), 054304 (2008).
- [107] King, G.W. and Ingold, C.K. *Nature*, **169**(4313), 1101–1102 (1952).
- [108] Ingold, C.K. and King, G.W. *Journal of the Chemical Society*, 2702–2755 (1953).
- [109] Innes, K.K. *Journal of Chemical Physics*, **22**(5), 863–876 (1954).
- [110] Demoulin, D. and Jungen, M. *Theoretica Chimica Acta*, **34**(1), 1–17 (1974).
- [111] Lischka, H. and Karpfen, A. *Chemical Physics*, **102**(1-2), 77–89 (1986).
- [112] Yamaguchi, Y., Vacek, G. and Schaefer, H.F. *Theoretica Chimica Acta*, **86**(1-2), 97–113 (1993).
- [113] Vacek, G., Thomas, J.R., Deleeuw, B.J., Yamaguchi, Y. and Schaefer, H.F. *Journal of Chemical Physics*, **98**(6), 4766–4776 (1993).
- [114] Stanton, J.F., Huang, C.M. and Szalay, P.G. *Journal of Chemical Physics*, **101**(1), 356–365 (1994).
- [115] Malsch, K., Rebentisch, R., Swiderek, P. and Hohlneicher, G. *Theoretical Chemistry Accounts*, **100**(1-4), 171–182 (1998).
- [116] Ventura, E., Dallos, M. and Lischka, H. *Journal of Chemical Physics*, **118**(4), 1702–1713 (2003).
- [117] Mordaunt, D.H. and Ashfold, M.N.R. *Journal of Chemical Physics*, **101**(3), 2630–2631 (1994).
- [118] Watson, J.K.G., Herman, M., Vancraen, J.C. and Colin, R. *Journal of Molecular Spectroscopy*, **95**(1), 101–132 (1982).
- [119] Vancraen, J.C., Herman, M., Colin, R. and Watson, J.K.G. *Journal of Molecular Spectroscopy*, **111**(1), 185–197 (1985).
- [120] Huet, T.R., Godefroid, M. and Herman, M. *Journal of Molecular Spectroscopy*, **144**(1), 32–44 (1990).

- [121] Hougen, J.T. and Watson, J.K.G. *Canadian Journal of Physics*, **43**(2), 298 (1965).
- [122] Vancraen, J.C., Herman, M., Colin, R. and Watson, J.K.G. *Journal of Molecular Spectroscopy*, **119**(1), 137–143 (1986).
- [123] Solina, S.A.B., O'Brien, J.P., Field, R.W. and Polik, W.F. *Journal of Physical Chemistry*, **100**(19), 7797–7809 (1996).
- [124] Jacobson, M.P., O'Brien, J.P. and Field, R.W. *Journal of Chemical Physics*, **109**(10), 3831–3840 (1998).
- [125] Jacobson, M.P. and Field, R.W. *Journal of Physical Chemistry A*, **104**(14), 3073–3086 (2000).
- [126] Hoshina, K., Iwasaki, a., Yamanouchi, K., Jacobson, M.P. and Field, R.W. *Journal of Chemical Physics*, **114**(17), 7424–7442 (2001).
- [127] Tsuji, K., Terauchi, C., Shibuya, K. and Tsuchiya, S. *Chem. Phys. Lett.*, **306**, 41–47 (1999).
- [128] Orr, B.J. *International Reviews in Physical Chemistry*, **25**(4), 655–718 (2006).
- [129] Jonas, D.M., Solina, S.A.B., Rajaram, B., Silbey, R.J., Field, R.W., Yamanouchi, K. and Tsuchiya, S. *Journal of Chemical Physics*, **99**(10), 7350–7370 (1993).
- [130] Nesbitt, D. and Field, R. *Journal of Physical Chemistry*, **100**(31), 12735–12756 (1996).
- [131] Moss, D.B., Duan, Z.C., Jacobson, M.P., O'Brien, J.P. and Field, R.W. *Journal of Molecular Spectroscopy*, **199**(2), 265–274 (2000).
- [132] Silva, M.L., Jacobson, M.P., Duan, Z. and Field, R.W. *Journal of Molecular Structure*, **565**, 87–91 (2001).
- [133] Lundberg, J.K., Chen, Y.Q., Pique, J.P. and Field, R.W. *Journal of Molecular Spectroscopy*, **156**(1), 104–122 (1992).
- [134] Takahashi, M., Fujii, M. and Ito, M. *Journal of Chemical Physics*, **96**(9), 6486–6494 (1992).
- [135] Pratt, S., Dehmer, P. and Dehmer, J. *Journal of Chemical Physics*, **99**(9), 6233–6244 (1993).
- [136] Tang, S.J., Chou, Y.C., Lin, J.J.M. and Hsueh, Y.C. *Journal of Chemical Physics*, **125**(13) (2006).
- [137] Tobiason, J.D., Utz, A.L., Sibert, E.L. and Crim, F.F. *Journal of Chemical Physics*, **99**(8), 5762–5767 (1993).

- [138] Mizoguchi, M., Yamakita, N., Tsuchiya, S., Iwasaki, A., Hoshina, K. and Yamanouchi, K. *Journal of Physical Chemistry A*, **104**(45), 10212–10219 (2000).
- [139] Merer, A.J., Yamakita, N., Tsuchiya, S., Stanton, J.F., Duan, Z.C. and Field, R.W. *Molecular Physics*, **101**(4-5), 663–673 (2003).
- [140] Hegelund, F., Burger, H. and Polanz, O. *Journal of Molecular Spectroscopy*, **167**(1), 1–10 (1994).
- [141] Darling, B.T. and Dennison, D.M. *Phys. Rev.*, **57**(2), 128–139 (1940).
- [142] Wilson, E. and Howard, J. *Journal of Chemical Physics*, **4**(4), 260–268 (1936).
- [143] Wilson, E., Decius, J. and Cross, P. *Molecular Vibrations*. McGraw-Hill (1955).
- [144] Watson, J.K.G. *Molecular Physics*, **15**(5), 479–490 (1968).
- [145] Oka, T. and Morino, Y. *Journal of Molecular Spectroscopy*, **6**, 472 – 482 (1961).
- [146] di Lauro, C. and Mills, I.M. *Journal of Molecular Spectroscopy*, **21**(1-4), 386 – 413 (1966).
- [147] Mills, I. *Pure and Applied Chemistry*, **11**(3-4), 325–344 (1965).
- [148] Lehmann, K.K. *Journal of Chemical Physics*, **79**(2), 1098–1098 (1983).
- [149] Child, M. and Halonen, L. *Advances in Chemical Physics*, **57**, 1–58 (1984).
- [150] Mills, I.M. and Robiette, A.G. *Molecular Physics*, **56**(4), 743–765 (1985).
- [151] Lehmann, K.K. *Journal of Chemical Physics*, **96**(11), 8117–8119 (1992).
- [152] Lehmann, K. *Molecular Physics*, **66**(6), 1129–1137 (1989).
- [153] Mills, I.M. *Molecular Spectroscopy: Modern Research*, vol. 1, 115. Academic Press (1972).
- [154] Winnewisser, G., Winnewisser, M. and Gordy, W. *Journal of Chemical Physics*, **49**(8), 3465–3478 (1968).
- [155] Drabbels, M., Heinze, J. and Meerts, W.L. *The Journal of Chemical Physics*, **100**(1), 165–174 (1994).
- [156] Steeves, A.H., Merer, A.J., Bechtel, H.A., Beck, A.R. and Field, R.W. *Molecular Physics*, **106**(15), 1867–1877 (2008).
- [157] Tobiason, J.D., Utz, A.L. and Crim, F.F. *Journal of Chemical Physics*, **99**(2), 928–936 (1993).
- [158] Yamakita, N., Iwamoto, S. and Tsuchiya, S. *Journal of Physical Chemistry A*, **107**(15), 2597–2605 (2003).

- [159] Yamakita, N. and Tsuchiya, S. *Chemical Physics Letters*, **348**(1-2), 53–59 (2001).
- [160] Thom, R.L., Wong, B.M., Field, R.W. and Stanton, J.F. *Journal of Chemical Physics*, **126**(18), 184307 (2007).
- [161] Virgo, W.L., Bittinger, K.L., Steeves, A.H. and Field, R.W. *Journal of Physical Chemistry A*, **111**(49), 12534–12537 (2007).
- [162] Duan, Z., Field, R.W., Yamakita, N. and Tsuchiya, S. *Chemical Physics*, **324**(2-3), 709–720 (2006).
- [163] Mordaunt, D.H., Ashfold, M.N.R., Dixon, R.N., Loffler, P., Schnieder, L. and Welge, K.H. *Journal of Chemical Physics*, **108**(2), 519–526 (1998).
- [164] Fayt, A., Robert, S., Di Lonardo, G., Fusina, L., Tamassia, F. and Herman, M. *Journal of Chemical Physics*, **126**(11), 114303 (2007).
- [165] Rheinecker, J. and Bowman, J.M. *Journal of Physical Chemistry A*, **110**(16), 5464–5467 (2006).
- [166] Cui, Q., Morokuma, K. and Stanton, J.F. *Chemical Physics Letters*, **263**(1-2), 46–53 (1996).
- [167] Cui, Q. and Morokuma, K. *Chemical Physics Letters*, **272**(5-6), 319–327 (1997).
- [168] Chen, Y.Q., Halle, S., Jonas, D.M., Kinsey, J.L. and Field, R.W. *Journal of the Optical Society of America B-Optical Physics*, **7**(9), 1805–1815 (1990).
- [169] Herman, M., Campargue, a., El Idrissi, M. and Vander Auwera, J. *Journal of Physical and Chemical Reference Data*, **32**(3), 921–1361 (2003).
- [170] Merer, A.J., Duan, Z., Field, R.W. and Watson, J.K.G. *Canadian Journal of Physics*, in press (2009).
- [171] Meal, J.H. and Polo, S.R. *Journal of Chemical Physics*, **24**(6), 1119–1125 (1956).
- [172] Hedberg, L. and Mills, I. *Journal of Molecular Spectroscopy*, **160**(1), 117–142 (1993).
- [173] Bittinger, K.L. *Spectroscopic Signatures of Doorway-Mediated Intersystem Crossing*. Ph.D. thesis, Massachusetts Institute of Technology (2009).
- [174] Ochi, N. and Tsuchiya, S. *Chemical Physics*, **152**(3), 319–336 (1991).
- [175] Mishra, A.P., Thom, R.L. and Field, R.W. *Journal of Molecular Spectroscopy*, **228**(2), 565–579 (2004).
- [176] McCoy, A. and Sibert, E. *Journal of Chemical Physics*, **105**(2), 459–468 (1996).

- [177] Sibert, E. and McCoy, A. *Journal of Chemical Physics*, **105**(2), 469–478 (1996).
- [178] Rose, J. and Kellman, M. *Journal of Chemical Physics*, **105**(24), 10743–10754 (1996).
- [179] Xu, D., Chen, R. and Guo, H. *Journal of Chemical Physics*, **118**(16), 7273–7282 (2003).
- [180] Prosimiti, R. and Farantos, S. *Journal of Chemical Physics*, **118**(18), 8275–8280 (2003).
- [181] Tyng, V. and Kellman, M.E. *Journal of Physical Chemistry B*, **110**(38), 18859–18871 (2006).
- [182] Kellman, M.E. *The Journal of Physical Chemistry*, **87**(12), 2161–2167 (1983).
- [183] Tew, D., Handy, N., Carter, S., Irle, S. and Bowman, J. *Molecular Physics*, **101**(23-24), 3513–3525 (2003).
- [184] Wong, B.M., Steeves, a.H. and Field, R.W. *Journal of Physical Chemistry B*, **110**(38), 18912–18920 (2006).
- [185] Jacobson, M.P., Jung, C., Taylor, H.S. and Field, R.W. *Journal of Chemical Physics*, **111**(2), 600–618 (1999).
- [186] Schmid, G.M., Coy, S.L., Field, R.W. and Silbey, R.J. *The Journal of Chemical Physics*, **101**(2), 869–875 (1994).
- [187] Jacobson, M.P., Silbey, R.J. and Field, R.W. *Journal of Chemical Physics*, **110**(2), 845–859 (1999).
- [188] Jacobson, M.P. *Spectroscopic Patterns Encode Unimolecular Dynamics*. Ph.D. thesis, Massachusetts Institute of Technology (1999).
- [189] Kittrell, C. *Molecular Dynamics and Spectroscopy by Stimulated Emission Pumping*, vol. 4 of *Advanced Series in Physical Chemistry*, chap. 3, 109–147. World Scientific (1995).
- [190] Jonas, D.M., Solina, S.A.B., Rajaram, B., Silbey, R.J., Field, R.W., Yamanouchi, K. and Tsuchiya, S. *Journal of Chemical Physics*, **97**(4), 2813–2816 (1992).
- [191] Northrup, F.J. and Sears, T.J. *J. Opt. Soc. Am. B*, **7**(9), 1924–1934 (1990).
- [192] O’Brien, J.P., Jacobson, M.P., Sokol, J.J., Coy, S.L. and Field, R.W. *Journal of Chemical Physics*, **108**(17), 7100–7113 (1998).
- [193] Amano, T., Sako, T., Hoshina, K. and Yamanouchi, K. *Chemical Physics Letters*, **375**(5-6), 576–582 (2003).

- [194] Brown, G.G., Dian, B.C., Douglass, K.O., Geyer, S.M. and Pate, B.H. *Journal of Molecular Spectroscopy*, **238**(2), 200–212 (2006).
- [195] Brown, G.G., Dian, B.C., Douglass, K.O., Geyer, S.M., Shipman, S.T. and Pate, B.H. *Review of Scientific Instruments*, **79**(5), 053103 (2008).
- [196] Light, J.C., Hamilton, I.P. and Lill, J.V. *The Journal of Chemical Physics*, **82**(3), 1400–1409 (1985).
- [197] Stanton, J.F. and Bartlett, R.J. *Journal of Chemical Physics*, **98**(9), 7029–7039 (1993).
- [198] Malsch, K., Hohlneicher, G., Schork, R. and Koppel, H. *Phys. Chem. Chem. Phys.*, **3**, 5393–5407 (2001).
- [199] Schubert, B., Koppel, H. and Lischka, H. *Journal of Chemical Physics*, **122**(18), 184312 (2005).
- [200] Kellman, M.E. *Annual Review of Physical Chemistry*, **46**(1), 395–422 (1995).
- [201] Berden, G., Peeters, R. and Meijer, G. *International Reviews in Physical Chemistry*, **19**(4), 565–607 (2000).
- [202] Dubinsky, I. *Application of highly sensitive spectroscopic techniques to the study of intramolecular dynamics and remote sensing*. Ph.D. thesis, Massachusetts Institute of Technology (1998).
- [203] Ruslen, L. *Application of sensitive spectroscopic techniques to intramolecular dynamics and combustion kinetics*. Ph.D. thesis, Massachusetts Institute of Technology (2002).
- [204] Silva, M.L. *Spectroscopic investigations of the \tilde{X} and \tilde{A} state dynamics of $^{13}\text{C}_2\text{H}_2$* . Ph.D. thesis, Massachusetts Institute of Technology (2002).
- [205] Herzberg, G. *Canadian Journal of Physics*, **30**, 185–210 (1952).
- [206] Yoshino, K., Esmond, J., Murray, J., Parkison, W., Thorne, A., Learner, R. and Cox, G. *Journal of Chemical Physics*, **103**(4), 1243–1249 (1995).
- [207] Merienne, M., Jenouvrier, A., Coquart, B., Carleer, M., Fally, S., Colin, R., Vandaele, A. and Hermans, C. *Journal of Molecular Spectroscopy*, **202**(2), 171–193 (2000).
- [208] Jenouvrier, A., Mérienne, M.F., Coquart, B., Carleer, M., Fally, S., Vandaele, A.C., Hermans, C. and Colin, R. *Journal of Molecular Spectroscopy*, **198**(1), 136 – 162 (1999).
- [209] Zalicki, P. and Zare, R. *Journal of Chemical Physics*, **102**(7), 2708–2717 (1995).

- [210] Jongma, R., Boogaarts, M., Holleman, I. and Meijer, G. *Review of Scientific Instruments*, **66**(4), 2821–2828 (1995).
- [211] Hodges, J., Looney, J. and vanZee, R. *Applied Optics*, **35**(21), 4112–4116 (1996).
- [212] Naus, H., van Stokkum, I., Hogervorst, W. and Ubachs, W. *Applied Optics*, **40**(24), 4416–4426 (2001).
- [213] Yalin, A. and Zare, R. *Laser Physics*, **12**(8), 1065–1072 (2002).
- [214] Wachsmuth, U. and Abel, B. *Journal of Geophysical Research-Atmospheres*, **108**(D15), 4473 (2003).
- [215] Cormier, J., Hodges, J. and Drummond, J. *Journal of Chemical Physics*, **122**(11), 114309 (2005).
- [216] Sneep, M., Hannemann, S., van Duijn, E. and Ubachs, W. *Optics Letters*, **29**(12), 1378–1380 (2004).
- [217] Labazan, I., Rudic, S. and Milosevic, S. *Chemical Physics Letters*, **320**(5-6), 613–622 (2000).
- [218] Haijima, A., Fujii, M. and Ito, M. *Journal of Chemical Physics*, **92**(2), 959–968 (1990).
- [219] Suzuki, T. and Hashimoto, N. *Journal of Chemical Physics*, **110**(4), 2042–2050 (1999).

Curriculum Vitae

NAME: Adam H. Steeves

BIRTH DATE: March 17, 1980

EDUCATION: Williams College, B.A. with Highest Honors, *summa cum laude* (2002); Massachusetts Institute of Technology, Ph.D. (2009)

HONORS AND AWARDS: Coblenz Society Student Award (2007), National Defense Science and Engineering Graduate Fellowship, (2003–2006), MIT Presidential Graduate Fellowship (2002–2003), James F. Skinner Prize in Chemistry, Williams College (2002)

SELECTED PUBLICATIONS AND PRESENTATIONS:

A. H. Steeves, H. A. Bechtel, A. J. Merer, N. Yamakita and R. W. Field. “Stretch-bend combination polyads in the \tilde{A}^1A_u state of acetylene, C_2H_2 .” *Journal of Molecular Spectroscopy*, accepted (2009).

R. W. Field, A. J. Merer, **A. H. Steeves***, J. H. Baraban, H. A. Bechtel, G. B. Park III, B. M. Wong, J. F. Stanton, H. Guo, W. L. Virgo, K. L. Bittinger, E. M. Robertson, S. H. Lipoff. “Acetylene!” 236th American Chemical Society National Meeting, Philadelphia, PA, August 17–21, 2008.

A. H. Steeves, A. J. Merer, H. A. Bechtel, A. R. Beck and R. W. Field. “Direct observation of the symmetric stretching modes of \tilde{A}^1A_u acetylene by pulsed supersonic jet laser induced fluorescence.” *Molecular Physics*, **106**, 1867–1877 (2008).

A. J. Merer, N. Yamakita, S. Tsuchiya, **A. H. Steeves**, H. A. Bechtel and R. W. Field. “Darling–Dennison resonance and Coriolis coupling in the bending overtones of the \tilde{A}^1A_u state of acetylene, C_2H_2 .” *Journal of Chemical Physics*, **129**, 054304 (2008).

H. A. Bechtel, **A. H. Steeves**, B. M. Wong and R. W. Field. “Evolution of chemical bonding during HCN/HNC isomerization as revealed through nuclear quadrupole hyperfine structure.” *Angewandte Chemie International Edition*, **47**, 2969–2972 (2008).

A. H. Steeves, H. A. Bechtel, A. J. Merer, N. Yamakita, A. Beck and R. W. Field. “Acetylene: What happens when a well-behaved molecule gets bent out of shape?” Modern Optics and Spectroscopy Seminar Series, Cambridge, MA, May 8, 2007.

B. M. Wong, **A. H. Steeves** and R. W. Field. “Electronic signatures of large amplitude motions: Dipole moments of vibrationally excited local-bend and local-stretch states of S_0 acetylene.” *Journal of Physical Chemistry B*, **110**, 18912–18920 (2006).

A. H. Steeves, H. A. Bechtel, S. L. Coy and R. W. Field. “Millimeter-wave-detected, millimeter-wave optical polarization spectroscopy.” *Journal of Chemical Physics*, **123**, 141102 (2005).